Generation, Temporal Characterization and Applications of Femtosecond-/ Attosecond Extreme Ultraviolet Pulses

by

Isabell Thomann

Diplom Physik, ETH Zürich, 2001

A thesis submitted to the
Faculty of the Graduate School of the
University of Colorado in partial fulfillment
of the requirements for the degree of
Doctor of Philosophy
Department of Physics
2009

This thesis entitled:
Generation, Temporal Characterization and Applications of Femtosecond-/
Attosecond Extreme Ultraviolet Pulses
written by Isabell Thomann
has been approved for the Department of Physics

Margaret M. Murnane

Henry C. Kapteyn

Date

The final copy of this thesis has been examined by the signatories, and we find that both the content and the form meet acceptable presentation standards of scholarly work in the above mentioned discipline.

Thomann, Isabell (Ph.D., Physics)

Generation, Temporal Characterization and Applications of Femtosecond-/ Attosecond Extreme Ultraviolet Pulses

Thesis directed by Prof. Margaret M. Murnane

The work of this thesis is arranged into three parts:

(A) Generation and temporal characterization of extreme ultraviolet (EUV) attosecond pulses. In this work I present the generation and first temporal characterization of sub-optical cycle EUV radiation generated in a noble-gas filled hollow-core waveguide. Two regimes of EUV radiation were characterized, ranging from 200 attoseconds to ~ 1 femtosecond in duration. The first regime that was characterized distinguishes itself from EUV radiation generated by other methods by its narrow (~ 1 eV) spectral width, its simple energy tunability and its temporal confinement to ~ 1 femtosecond. In the second regime, single isolated pulses of 200 attoseconds duration (and accordingly larger bandwidth) were generated. In both regimes dynamic phase-matching effects create an extremely short time window within which efficient nonlinear conversion is possible, while it is suppressed outside this window. Temporal characterization of the generated EUV pulses was approached by two-color pump-probe photoelectron spectroscopy. Therefore an efficient photoelectron spectrometer was set up, detecting electrons in a 2π collection angle. For the interpretation of the experimental data, an analytical model as well as an iterative algorithm were developed, to allow extraction of complex EUV waveforms. The demonstrated radiation will allow for time-resolved studies of the fastest processes in molecules and condensed matter, while at the same time ensuring adequate energy resolution for addressing individual electronic states.

(B) Application of a COLTRIMS reaction microscope in combination

with femtosecond EUV pulses to questions in molecular physics. The combination of the sensitive detection capabilities of a COLTRIMS reaction microscope with the high time resolution of pump-probe experiments using femtosecond extreme-ultraviolet pulses makes it possible to answer very fundamental open questions in molecular physics such as the dependence of molecular photoionization on the molecular orientation. To this end, molecules were impulsively aligned by means of femtosecond pump pulses. The excited molecular rotational wavepacket experiences revivals that continue long after the pump pulse has left. During such revivals, the molecular axes change their orientation from parallel to perpendicular with respect to the polarization of the pump pulse within a few hundred femtoseconds. Therefore photoionization by femtosecond EUV pulses with variable delay during a revival is equivalent to photoionization of molecules with varying orientation. With this novel method the orientational dependence of single-photon photoionization of N_2 and CO_2 into non-dissociating channels, as well as for a long-lived state of CO_2^+ was measured for the first time.

(C) Carrier-envelope-phase (CEP) stabilization of a femtosecond chirped pulse amplifier. Lastly, CEP stabilization of intense laser pulses from a chirped pulse amplifier was realized. For amplifier systems containing a pulse stretcher and compressor based on diffraction gratings, an increased susceptibility to CEP fluctuations had been expected prior to this work. Therefore the pulse stretcher and compressor system were examined separately in a first step, and the introduced CEP fluctuations were found to be insignificant. The CEP stability of the full amplifier system was then characterized, and excellent long-term stability was shown. With this work a scaling of the energy of CEP-stabilized pulses into the joule range becomes possible. In contrast to absolute frequency measurements with low-energy femtosecond pulses which require stability in the frequency range, the interest in stabilized high-energy pulses is to control the entire electric field of intense laser pulses in the time domain with attosecond precision, to allow full control of the dynamics of electrons in intense light fields.

Dedication

To my grandparents, parents and Volker.

Acknowledgements

First of all I would like to thank my advisors Margaret Murnane and Henry Kapteyn for always giving me the opportunity to pursue the research I was interested in, for their generous advice, and for teaching me a lot about ultrafast physics. There are a number of people who have directly contributed to the work in this thesis: In the few months I worked with him, I have learned a lot from postdoc Wen Li. Thanks to Emily Gregonis for various contributions to the EUV temporal characterization setup, and to Robynne Lock for sharing her code and for doing calculations regarding the alignment of molecules. I thank Oren Cohen and Alon Bahabad for their collaboration, and for various supporting numerical calculations on EUV generation. Thanks also to everybody else in the group past and present, for their assistance and for making this Ph.D. enjoyable.

During this thesis I had various fruitful collaborations outside the group: Thanks to Jason Jones and Jun Ye, for giving me the opportunity to help explore novel phase stabilization techniques for ultrafast lasers. Thanks to Xuan Liu and Rick Trebino at Georgia Tech for a fruitful collaboration on numerical codes for the temporal characterization of EUV radiation. I also thank Farhad Salmassi, Andy Aquila and Yanwei Liu at Berkeley for fabricating the EUV mirrors used in my temporal characterization and COLTRIMS experiments. Last but not least, many thanks go to the people at NIST, where I spent a very interesting and rewarding time at the beginning of grad school: Leo Hollberg, Scott Diddams, Kristan Corwin, Albrecht Bartels, Nate Newbury and

Brian Washburn.

This work would not have been possible without the excellent support of the JILA electronics and machine shops, and the JILA computing staff and the JILA office staff: All of them significantly ease the life of a grad student! In particular I thank Terry Brown and James Fung-a-Fat for always being available for advice in the CEP stabilization project. Invaluable advice and assistance also came from David Alchenberger, Thomas Foote, Hans Green, J. R. Raith, Brian Lynch and Jeff Sauter. Thanks also to Dirk Mueller, Sterling Backus, and Kendall Read from KMlabs for their assistance.

I also thank family and friends.

Contents

Chapter

Tables

Table

Figures

Figure

Chapter 1

Introduction

The work in this thesis involved several topics ranging from the generation and temporal characterization of coherent ultrafast extreme-ultraviolet (EUV) radiation to its application in molecular physics. The fundamental light-matter interaction leading to the generation of this EUV radiation is the recollision of an electron with its parent ion after it was ejected and accelerated by an intense near-infrared laser field. In this recollision, the electron may give up its energy and emit a high-energy photon. This basic process has allowed the realization of table-top EUV sources which provide laser-like radiation with unique properties: femtosecond to attosecond pulse duration, good spatial and temporal coherence, energy-tunability, and temporal synchronization with the driving laser pulse which is essential for pump/probe experiments. The accessible energy range is suitable for probing outer and inner valence level (and not-too-tightly bound core level) atomic / molecular physics, as well as for studies of condensed matter systems. A very recent achievement is the generation of EUV pulses of sub-optical cycle duration, or even a single isolated attosecond EUV burst per laser pulse - the shortest manmade events to date. Isolated attosecond pulses have been produced either by an extremely short driving laser pulse, by driving pulses with time-varying polarization, or - as implemented for the first time in this thesis - by exploiting dynamic phase-matching effects between the driving laser and EUV pulse.

1.1 Background: Relevant Time Scales

Why are we interested in experimentally making attosecond timescales accessible? Ever shorter pulse durations allow us to make movies with unprecedented time resolution of ever faster processes occurring in nature. In the past this has led to time-resolved observations of nuclear motions, such as in molecular rotations, which happen on a picosecond timescale ($1\,ps = 10^{-12}$ seconds) or in molecular vibrations, which happen on a femtosecond ($1\,fs = 10^{-15}$ seconds) timescale, as well as in chemical reactions which evolve on a similar timescale as vibrations [179].

One challenge remains: Similar movies of electronic processes in inner atomic shells prove much more difficult, as these motions take place over tens to thousands of attoseconds ($1\,as = 10^{-18}$ seconds), e.g. the electron-orbit period for the ground state of the hydrogen atom is 150 as. Within the past years, scientists have begun to learn how to use femtosecond laser pulses to coherently manipulate electron motions in atoms and molecules, down to attosecond timescales. With the beginning of this new era of *attosecond science*, we now have the possibility of manipulating and measuring electronic wavefunctions. In addition to purely electronic motions, a very interesting regime of motions occurs on the order of a few femtoseconds: When the Born-Oppenheimer approximation [1] breaks down, the nuclear and electronic dynamics become coupled, as it occurs at conical intersections between molecular electronic potential surfaces. An overview of the timescales relevant to this thesis is given in Figure 1.1.

By the uncertainty principle, sub-femtosecond light pulses require a bandwidth larger than 10^{15} Hz, which is larger than the entire visible range of the spectrum. Therefore, to generate attosecond timescale radiation it is necessary to work with higher frequency radiation. High harmonic generation from intense near-infrared laser pulses can

---

[1] The Born-Oppenheimer approximation is often made in molecular physics. It assumes that electrons adjust their positions much faster than any motion of the nuclei. Within this adiabatic approximation the electronic energy eigenvalues can then be displayed as a function of nuclear distances aka potential energy surfaces.

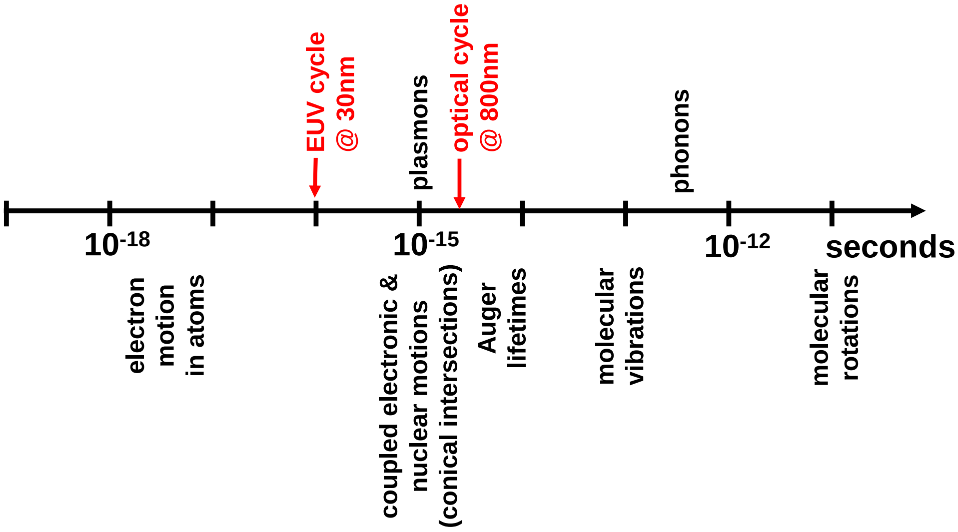

Figure 1.1: Time scales of matter and light relevant to this thesis.

certainly access these timescales. However it should be noted here, that manipulation of electron dynamics on the attosecond time scale does not require the use of isolated attosecond pulses. As an example, pulse shaping techniques of intense NIR femtosecond pulses can be used to manipulate electron trajectories in the continuum with a precision of 25 attoseconds [11].

1.2 Overview of work in this thesis

The temporal characterization, as well as many applications of ultrafast EUV radiation are typically done by a two-color cross correlation with the fundamental light, and detected by making use of the ionizing nature of the radiation. In this thesis, I have set up a beamline for the generation and temporal characterization of EUV pulses, including a hollow-waveguide setup for high-harmonic generation, a piezoelectric delay stage with attosecond resolution, and a photoelectron spectrometer allowing efficient $2-\pi$ photoelectron collection. I have generated and temporally characterized two different regimes of EUV radiation, producing 1.4 femtosecond (fs) pulses as well as 200 attosecond (as) pulses. The 1.4 fs pulses will be particularly useful, because they are close to the Fourier transform limit, meaning in addition to their short pulse duration we have sufficient energy resolution (~ 1 eV) for state resolved experiments in the congested molecular and materials energy bands in the EUV region. This regime also distinguishes itself by a high photon flux and easy energy tunability due to phase-matching in the high harmonic generation waveguide. The 200 as pulses have a correspondingly broader spectrum, and will thus have their applications in the study of even faster processes where state-selectivity is not required.

In the next project I used few-femtosecond EUV pulses in combination with the COLTRIMS detection technique for a basic molecular physics experiment: The measurement of the angular dependence of molecular photoionization. The experiments are performed in the gas phase, requiring an initial alignment step. Alignment is performed by impulsively torquing the molecules using a near-infrared femtosecond pulse. This new technique allows to study non-dissociative ionizations and dissociations that involve long-lived intermediate states, as we showed for dissociation of CO_2 at 43 eV excitation energy which likely proceeds through the long-lived $C\,4\sigma_g$ channel of CO_2^+.

At the beginning of this PhD a high-power femtosecond pulse train was realized which had its electric field oscillations stabilized underneath the pulse intensity envelope. Such carrier-envelope phase (CEP) stabilized amplified pulses will have many applications in strong-field physics and attosecond science.

In the following I will thus give an introduction to the topics of generation, temporal characterization and applications of ultrafast EUV radiation, as well as the CEP stabilization of high-power fs lasers.

1.3 A carrier-envelope phase (CEP) stabilized amplifier

The objective of the first project of my PhD work was to develop a laser system capable of generating high-power femtosecond laser pulses with a stable phase of the electric field oscillations under the pulse envelope (carrier-envelope phase, CEP, see

Figure 1.2). In conventional femtosecond laser pulse trains from a Ti:Sapphire oscillator (and thus also in amplified pulse trains seeded by such oscillators), the repetition period and the pulse envelope are stable in time. However the CEP is random from one pulse to the next, due to the differing group and phase velocities in the laser cavity. Highly nonlinear processes, such as EUV generation or other strong-field phenomena, can be very sensitive to the fluctuations of the CEP. For example, when very short driving pulses are used for high harmonic generation, the properties of the emitted EUV pulse can depend very sensitively on the position of the electric field oscillations of the fundamental pulse, not just on the envelope. A "cosine" driving pulse with one strongest half-cycle will generate a single attosecond pulse, whereas a "sine" driving pulse with two equally strong half-cycles will generate two attosecond pulses.

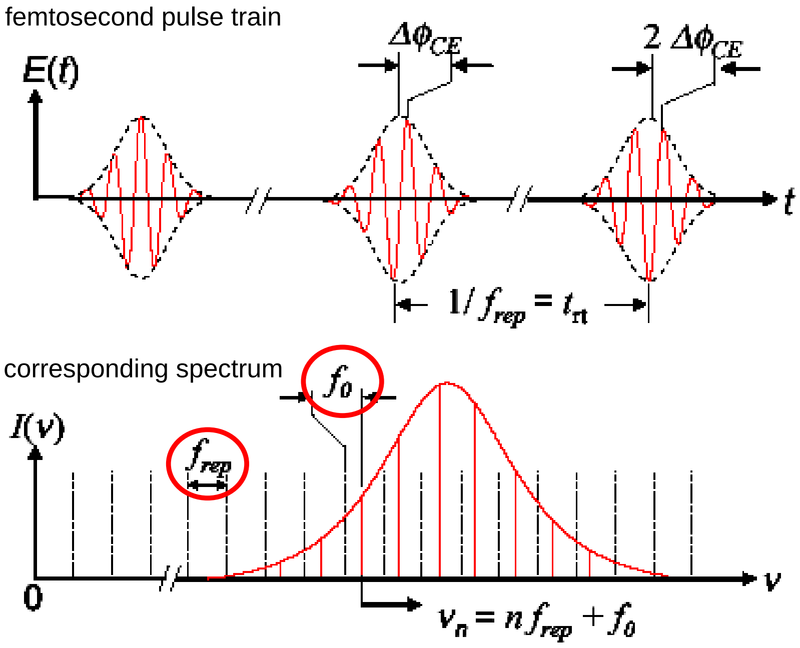

Figure 1.2: A femtosecond pulse train of period t_{rt} and its corresponding spectrum, a frequency comb of spacing $f_{rep} = 1/t_{rt}$. The carrier-envelope phase slip $\Delta\phi_{CE}$ between adjacent pulses is seen as the time-domain offset between the carrier oscillations and the pulse envelope. It is connected to a frequency-domain offset $f_0 = f_{rep}\frac{\Delta\phi_{CE}}{2\pi}$ (see text) of the frequency-comb from zero. This illustrates the importance of this parameter both for frequency measurements and strong-field phenomena such as attosecond control of electron dynamics. Adapted from [76].

The technique of stabilizing the CEP to a fixed value is nowadays reasonably straightforward for femtosecond oscillators [76]. However an oscillator only produces pulse energies on the order of a few nanoJoules. To reach intensities required e.g. to generate EUV light, an amplification by a large factor ($\sim 10^6$) is needed. A typical setup to achieve this uses the principle of chirped-pulse amplification [148] (see figure 1.3). For the CEP stabilization of such amplifier systems additional complications arise, which had to be addressed.

1.3.1 CEP stabilization of low-power femtosecond pulses

For low-power oscillator pulse trains there is a convenient way of detecting and controlling this phase slip in the spectral domain, as indicated in Figure 1.2. The spectrum of the pulse train consists of a mode comb, which has two degrees of freedom. The first is the offset frequency f_0 of the comb, which arises from dispersive elements in the laser cavity. The other degree of freedom is the repetition frequency f_{rep}, determined by the pulse round trip time in the laser cavity. For oscillator pulse trains this repetition rate is high enough to spectrally resolve the offset frequency. As will be shown in Chapter 2, the ratio f_0/f_{rep} determines the CEP pulse-to-pulse slip according to $f_0 = f_{rep}\frac{\Delta\phi_{CE}}{2\pi}$. By locking this ratio of two measurable radio-frequencies, the electric field under the envelope is fixed. Although we do not know the *absolute* CE-phase, there are physical phenomena that depend on this absolute phase, and therefore it is in principle possible to detect and control it. Examples include the work of Paulus et al. using above-threshold photoionization [118, 119], and the work in the Cundiff group on CEP-dependent photocurrent generation in semiconductors [132].

1.3.2 CEP stabilization of amplified ultrafast laser pulses

Figure 1.3 shows the generation of amplified femtosecond pulses by chirped-pulse amplification (CPA). A seed oscillator produces $\sim 4-9$ nJ, ~ 25 fs pulses. Amplification

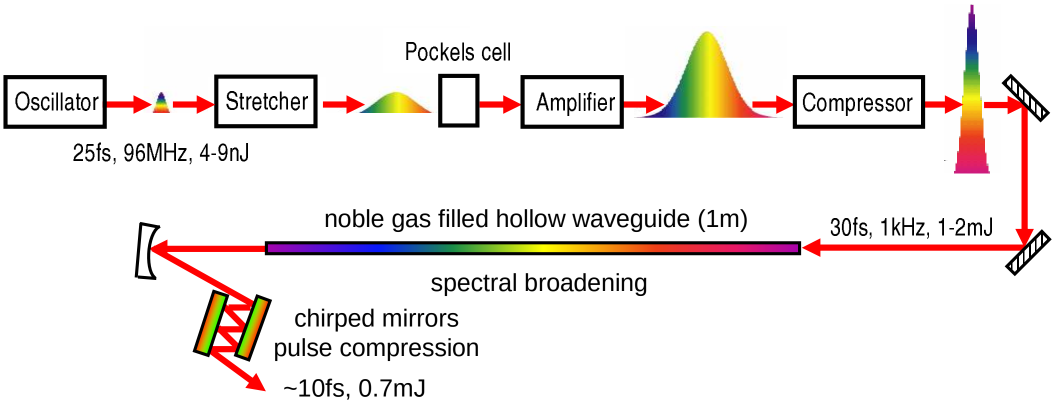

Figure 1.3: Femtosecond near-infrared light source for the experiments in this thesis. A pulse train from a femtosecond oscillator is amplified using chirped pulse amplification: pulses are stretched to $\sim$ 200 ps duration before amplification by a factor $> 10^6$, and then recompressed to $\sim 30fs$. The limited bandwidth of amplified pulses requires further spectral broadening in a "self-phase modulation" fiber [113, 149] to produce $\sim 10fs$ pulses.

proceeds via temporally stretching the pulses from $\sim$ 20 fs to $\sim$ 200 ps duration in a stretcher. This is required to avoid material damage in the amplifier gain medium. A Pockels cell selects pulses at a $\sim$ 1 kHz repetition rate for amplification. The stretched pulses are amplified to $\sim$ 3 mJ in a multipass cryo-cooled amplifier ring, and are then recompressed to $1-2$ mJ per pulse, $\sim$ 30 fs in the compressor before being sent to the EUV generation setup. For some experiments the limited bandwidth of amplified pulses requires further spectral broadening in a self-phase modulation fiber to produce $\sim$ 10 fs pulses. Figure 1.4 shows a spectrogram of $\sim$ 10 fs pulses exiting the SPM fiber, taken with a Grenouille apparatus used for routine temporal characterization of NIR pulses.

For stretching/compression in chirped pulse amplification there are two methods, which both introduce a frequency-dependent delay to stretch the pulse: material based stretcher-compressors and grating based stretcher-compressors. In material based stretcher-compressors, highly dispersive glasses are used for stretching, and pulse energies are limited to about 3 mJ. Grating based stretcher-compressors, on the other hand, introduce frequency-dependent beam paths in free space, and are scalable to $\sim$ 1000

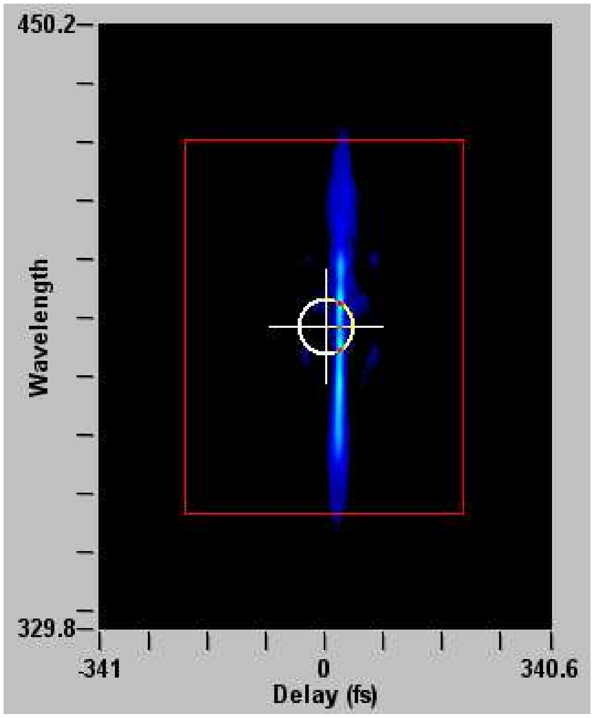

Figure 1.4: Spectrogram (taken with a Grenouille apparatus) corresponding to an amplified NIR pulse passing through a self-phase modulation fiber. The Fourier transform limit corresponds to 6.4 fs.

times higher pulse energies. For the first demonstration of amplification of CEP stable pulses, material based stretcher-compressors systems were used, while the grating-based stretcher and compressors used in our group had been predicted to be at a disadvantage for CEP stabilization, due to a strong conversion of beam-pointing fluctuations to CEP noise. Our strategy was thus to first investigate this claim by characterizing the CEP noise introduced in a separate stretcher/compressor system without the actual amplifier. Once we had shown that the introduced CEP noise was negligible, the full amplifier was set up and CEP stabilized.

For an amplifier with much lower repetition rate than an oscillator, the offset frequency f_0 is not readily resolvable, and another technique has to be used to detect the CEP and stabilize the pulse train: In this work we used spectral interferometry, a technique that encodes the CEP slip in a spectral offset of an interference pattern as I will show in chapter 2. Using this technique, we could demonstrate the intrinsic long-term CEP stability of our grating-based amplifier system.

In the early demonstrations of CEP stabilized amplifiers, stabilization is achieved by pre-compensating slow CEP fluctuations from the amplifier using actuators in the seed oscillator. In another more recent technique, slow CEP feedback control of an amplifier was demonstrated using feedback on the effective stretcher grating separation [94]. In the years since our own work was completed, the field of CEP stabilized amplifiers has continued to make great progress. CEP stabilized amplifiers up to several milliJoules are now commercially available. Nonetheless the use of CEP stabilized amplifiers will continue to be challenging due to the requirement of ensuring low levels of electronic, acoustic and vibrational noise in the lab.

1.4 Generation of coherent ultrafast extreme-ultraviolet radiation

As EUV generation is the basic tool for most experiments in this thesis, I will give here an overview of its generation. To understand EUV generation two points have to be considered: The first point is the single-atom description, which provides an understanding of the temporal structure, as well as a first estimate for the energy range of EUV emission. The second point is the macroscopic emission of an ensemble of atoms, where coherence between different emitters decides on the spatial and temporal coherence properties, the directionality of the emission, the overall signal strength, and also the final temporal structure of the macroscopic radiation.

1.4.1 The three-step model

An intuitive semiclassical model for the interaction of the intense laser field of a femtosecond pulse with atoms, leading to high harmonic generation, was given by Corkum [26] – the "three-step model" (see Fig. 1.5). When an intense laser pulse is focused onto atoms in the gas-phase, it may suppress the Coulomb potential sufficiently

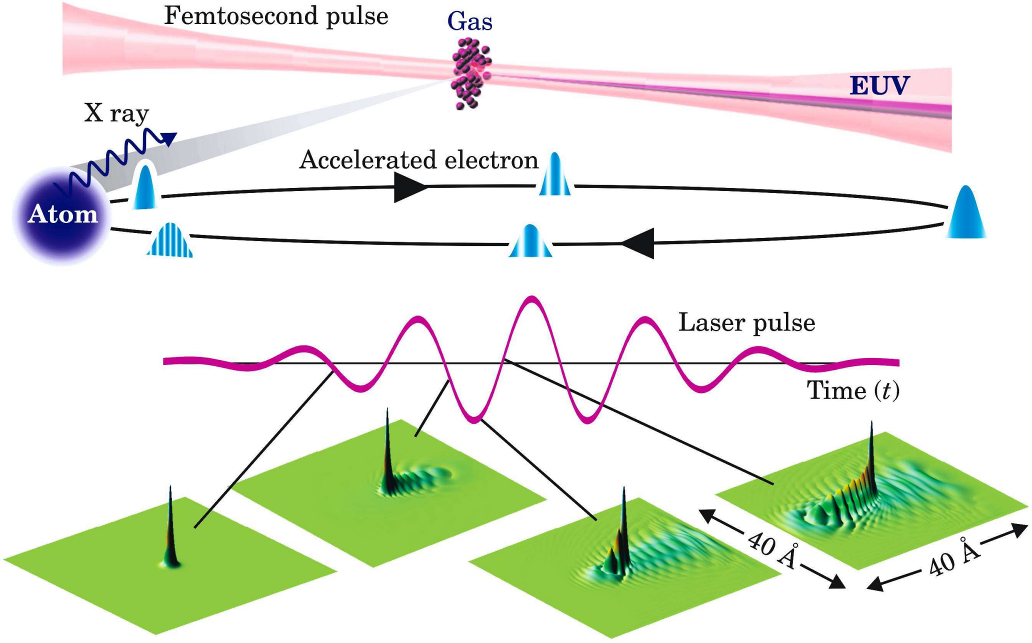

Figure 1.5: Schematic for the generation of extreme ultraviolet radiation: infrared radiation is focused into a gas target, leading to laser-like emission of EUV in the forward direction. Blue: in the three-step model of HHG, an electron is set free by tunnel ionization, and is then accelerated by the laser field gaining kinetic energy. When it returns to the nucleus it may recombine and emit EUV radiation. Lower panel: quantum mechanical simulations of electron wave packet propagation. In this picture of HHG the rapid spatio-temporal interference between returning electron wave packet and the portion remaining close to the nucleus generates a radiating dipole. From [82].

for electrons to tunnel. Thus, near each peak of the electric field of a femtosecond laser pulse a portion of an electron wave packet is set free from an atom through tunnel ionization. In this first step the probability of ionization as a function of the laser electric field is calculated using the ADK tunnel ionization model (see Section 1.4.1.1). The second step describes the classical electron trajectory after ionization, accelerated by the electric field of the fundamental pulse. In a linearly polarized laser field there is a significant probability for the free portion of the electron wave packet to reencounter its parent ion. In this third step, EUV radiation is emitted when the free portion of the wave packet recombines with the remaining part of the ground state wavefunction.

This EUV emission has a temporal periodicity of half the laser cycle ($T_L/2$), that follows the electric field strength of the fundamental laser pulse, generating an EUV attosecond pulse train. This in turn leads to a discrete spectral structure of the emitted radiation with a frequency spacing of twice the laser frequency ($2\omega_L$). Only odd harmonics are emitted because of a constraint on the n'th order nonlinear susceptibility $\chi^{(n)}$ in an isotropic gas: if the direction of the electric field is reversed, $E \to -E$, then also the polarization of the gas must reverse its sign: $P \to -P$. Because $P = \epsilon_0 \sum_n \chi^{(n)} E^n$, only odd orders $\chi^{(2m+1)}$ are allowed and only odd harmonics are generated.

In the following I will describe in detail the three steps of the model, as well as some of the most important predictions.

1.4.1.1 Step 1: ADK-model for the electron tunneling probability

A strong laser field suppresses the Coulomb potential, so that the electron may tunnel out of its potential well, or even escape over the barrier for sufficiently strong suppression. The tunneling probability T is

$$T = \left| \exp\left(-\int_a^b k dx \right) \right|^2 = \left| \exp\left(-\int_a^b \sqrt{\frac{2m(I_p - V(x))}{\hbar^2}} dx \right) \right|^2 \tag{1.1}$$

Here, k is the wave vector of the tunneling electron, a and b are the inner and outer edges of the tunnel barrier, $V(x)$ is the combined Coulomb and laser potential and Ip is the atom's ionization potential. To convert the probability into an ionization rate $R_{ion}(t)$ one multiplies by the attempt frequency, given e.g. in the Bohr model by twice the binding energy (or ionization potential) $2I_p/\hbar$.

The ADK model describes the ionization rate $R_{ion}(t)$ in a strong electric field $E(t)$ [145, 26]:

$$n^* = \sqrt{\frac{Ip_H}{Ip}} \tag{1.2}$$

$$C_{nl}^2 = 2^{2n^*}/(n^*\Gamma(n^*+1)\Gamma(n^*)) \tag{1.3}$$

$$R_{ion}(t) = \frac{Ip}{\hbar} C_{nl}^2 \left(\frac{4Ip\sqrt{2mIp}}{\hbar e|E(t)|} \right)^{(2n^*-1)} \exp\left(-\frac{4Ip\sqrt{2mIp}}{3\hbar e|E(t)|} \right) \tag{1.4}$$

Here, m and e are the electron's mass and charge, respectively, I_p and Ip_H are the ionization potential of the atom of interest and the hydrogen atom, respectively, and Γ is the Gamma function. This expression shows that ionization is strongly peaked around the maxima of the electric field. As we will see in step 2 of the model, the ionization time decides on the energy E available for EUV emission.

The time-dependent ionization rate $R_{ion}(t)$ also leads to a time-dependent plasma fraction $\eta(t)$ that increases during each half-cycle of the femtosecond laser pulse:

$$\eta(t) = 1 - \exp\left(-\int_{-\infty}^{t} dt' R_{ion}(t')\right). \tag{1.5}$$

This ionization fraction is important for dynamic phase-matching effects that allow the generation of single isolated attosecond pulses, as will be shown below.

Note that more advanced models of ionization [24] take into account nonadiabatic effects, leading for pulses shorter than ~ 25 fs to lower ionization rates than predicted by Eq. 1.4.

1.4.1.2 Step 2: Classical trajectories

From the time of tunneling, the electron is accelerated by the laser electric field. It is first driven away and when the electric field switches sign, it is accelerated back toward the nucleus. The motion is described by Newton's equations, and the solutions are given in [26]. Figure 1.6 shows three representative trajectories as a function of phase ωt where ω is the laser angular frequency. 0 degrees corresponds to a maximum of the electric field. The black trajectory, ionized at a phase $\phi_{ion} = \omega t_{ion} = 17°$, returns to the nucleus with maximum slope (velocity), generating the highest EUV energy possible. For all lower return energies, there exist two distinct electron trajectories returning to the nucleus with the same kinetic energy (and therefore generating the same harmonic). These are referred to as the 'long' and 'short' trajectories (red and blue curves, respectively).

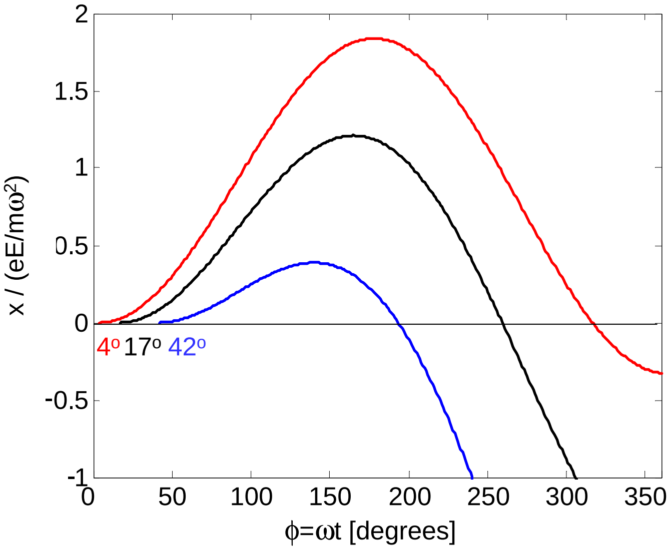

Figure 1.6: Representative classical electron trajectories [26] in a laser field. $x = 0$ is the position of the nucleus. The black trajectory, ionized at 17°, returns to the nucleus with maximum slope (velocity), generating the highest EUV energy possible $(3.17\,U_p + I_p)$ where U_p is given by Eq. (1.6). Blue and red trajectories, ionized at 42° and 4°, respectively, are representative long and short trajectories returning to the nucleus with identical energy, in this case generating radiation of $\sim 1.4\,U_p + I_p$. Electrons ionized between 90° and 180° (not shown) do not reencounter the nucleus and do not generate EUV radiation.

A characteristic energy scale in this classical electron motion is the ponderomotive potential

$$U_p = e^2 E_a(t)^2/(4m_e\omega_L^2) \tag{1.6}$$

which is the cycle averaged kinetic energy of the free electron in the electric field $E_L(t) = E_a(t)cos(\omega_L t + \phi_{CE})$ of envelope $E_a(t)$ and frequency ω_L. Here, ϕ_{CE} is the phase between the oscillations of the carrier frequency and the envelope maximum of the pulse ("carrier-envelope phase").

Fig. 1.7 shows three plots as a function of the phase of the laser field at which the electron tunnels. The blue curve gives the return kinetic energy in units of U_p. The black curve gives the return phase, and the red curve shows the difference between return phase and ionization phase, i.e. the time the electron spent in the continuum. Ionization for the long trajectories takes place between 0 and 17 degrees and the return

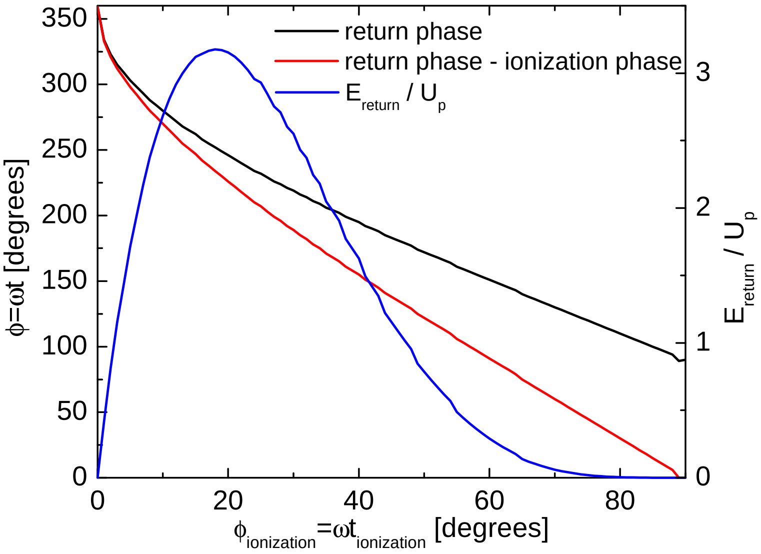

Figure 1.7: Blue: Kinetic energy of the electron returning to the ion, in units of the ponderomotive energy U_p. Black: Return phase. Red: Return phase - ionization phase.

phase is between 360 and 255 degrees. For the short trajectories ionization happens between 17 and 90 degrees and the return phase corresponds to 255 and 90 degrees. For the case of an electron ionized at 17 degrees, there is only one trajectory. In this case the electron spends a time corresponding to $\sim$ 238 degrees of laser phase in the continuum before returning to the nucleus with maximum kinetic energy, just before the sign of the electric field switches again to decelerate it.

Fig. 1.8 shows a logarithmic plot of the modulus of the electron position with respect to the nucleus, as a function of tunnel phase and return phase. The yellow color corresponds to the electron at the position of the nucleus. It shows that the electron returns to the nucleus for an initial phase of 0 to 90 degrees, but never returns for ionization phases larger than 90 degrees and smaller than 180 degrees. Therefore, no harmonics will be generated from electrons ionized between 90 and 180 degrees. After half a fundamental laser cycle the process repeats.

As can be seen from Figure 1.7, the ionization time t_i decides on the energy E available for EUV emission when the electron recollides. The ionization rate $R_{ion}(t)$ can

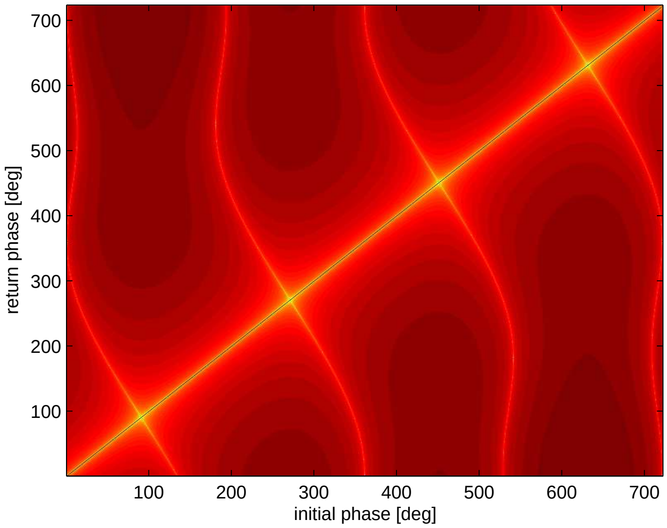

Figure 1.8: Logarithm of electron position w.r.t. ion core, versus the initial phase when the electron is ionized (x-axis), and versus its return phase (y-axis). Light red / yellow: electron position close to the ion core. Dark red: far from the ion core.

therefore be converted into a probability $dP(E)/dE = R_{ion}(t_i(E))(dt_i/dE)$ telling us how likely it is that the electron reencounters the nucleus with just the right energy to emit a photon of energy E. What remains to be calculated in step 3 is the probability that it will actually emit this photon.

1.4.1.3 Step 3: Recombination and EUV emission

When the electron returns to the nucleus, there is a probability for it to recombine into the ground state and to emit EUV radiation. The emission is calculated from the second time derivative of the expectation value of the dipole moment operator, and the spectrum is found by Fourier transform. The wave function is a superposition of a free portion and a portion remaining in the ground state. Only when $< \Psi_{ground}|e\mathbf{r}|\Psi_{free} >$ is nonzero, radiation will be generated. For Ψ_{ground} the unperturbed outermost atomic orbital may be assumed. $\Psi_{free}(t)$ is the returning electron wave packet. It can be expanded in a sum over contributions with the right momentum p_q to generate harmonic order q [26]:

$$\Psi_{free}(t) = \sum_q A_q \exp(ip_q x/\hbar) \exp\left(i\left(\frac{p_q^2}{2m} + Ip\right) t/\hbar\right) \tag{1.7}$$

where the normalization constant A_q depends on the ionization probability for electrons returning with suitable kinetic energy to create harmonic q, as well as the transverse spread of the electron wave function of $\sim 1.5\, Angstrom/fs$.

1.4.1.4 Predictions of the Model

Most importantly, the three-step model correctly predicts the maximum possible EUV photon energy, which is given by the sum of the atom's ionization potential I_p and and the maximum kinetic energy [26] the electron can receive from the laser field when returning to the nucleus. This cutoff energy of high harmonic radiation is therefore given by

$$E_{cutoff} = I_p + 3.17U_p \tag{1.8}$$

where U_p is the ponderomotive energy of the electron in the laser field. The model predicts that the maximum kinetic energy of $3.17U_p$ (and thereby the high harmonic cutoff) is gained when the electron is ionized at a phase of the electric field of ~ 17 degrees with respect to the the field maximum.

The model also predicts the existence of a plateau region where harmonic intensity remains almost independent of energy. Further, as already indicated in Figure 1.6, in each half-cycle two trajectories, 'long' and 'short', contribute to emission of any particular harmonic, in agreement with experiments.

The three-step model also predicts that even a small ellipticity of the fundamental polarization rapidly quenches EUV emission [25, 42]. In this case the electron trajectory is two-dimensional, and the probability of a reencounter with the parent ion is reduced significantly. This effect is used in the polarization gating technique for the generation of isolated attosecond pulses [25, 74].

1.4.1.5 The intrinsic phase of HHG

So far, the model has neglected a correct description of the phase properties of harmonic emission. During its motion in the continuum, the electron behaves like a wave and thus acquires a phase during its motion. When it recombines and emits a photon, this phase is imprinted on the radiation. These effects were first discussed by Lewenstein and coworkers [93], leading to a model that has since then successfully described many experiments [19, 123, 70].

The total phase Φ_{tot} of an electron that generates radiation at frequency ω is

$$\Phi_{tot} = \omega \cdot t_r + \Phi_{intrinsic} \tag{1.9}$$

It contains a term $\omega \cdot t_r$ corresponding to the return time, and the phase the electron accumulates on its trajectory, i.e. the "intrinsic" phase

$$\Phi_{intrinsic} = -S(t_i, t_r)/\hbar \tag{1.10}$$

Here, t_i is the release time of the electron, t_r is the return time, and $S(t_i, t_r)$ is the semi-classical action over the electrons trajectory as calculated using Step 2 of the three-step model

$$S(t_i, t_r) = \int_{ti}^{tr} dt \left(\frac{(p - A(t))^2}{2m} + Ip \right) \tag{1.11}$$

Here, p is the canonical momentum and $A(t)$ is the laser's vector potential. The semi-classical action S can be approximated as $S \approx U_p \tau$, where $\tau = t_r - t_i$ is the time between tunneling and recombination [137].

Equation 1.9 can be used to calculate the spectral phase properties $\phi(\omega)$ of EUV radiation, by evaluating it for the trajectories contributing to emission at frequency ω. An important consequence of Eq. (1.11) is that the phase properties of EUV radiation can be manipulated during the few-femtosecond trajectory of the electron driven by the laser field, e.g. by shaping the laser pulse [11].

1.4.2 Advanced single-atom models for HHG

Alternatively to using the three-step model based on ADK tunneling theory, classical electron trajectories, and recombination, or the Lewenstein model, one can describe the HHG process quantum mechanically, e.g. numerical simulations of the time-dependent Schroedinger equation [160]. The time-dependent electron wavefunction is calculated by split-step Fourier techniques. The dipole acceleration calculated from the time-dependent wavefunction then gives the EUV emission amplitude in time; Fourier transform to frequency domain gives the HHG spectrum.

To achieve the generation of a single attosecond pulse within a single-atom model of high-harmonic generation, the laser pulse must be short enough so that only few laser cycle peaks give rise to high harmonic generation (HHG). Then a single attosecond pulse can be isolated by spectrally filtering the highest energy radiation [22]. For longer pulses the EUV emission forms an attosecond pulse train with a temporal periodicity of $T_0/2$. This temporal periodicity leads to a discrete spectral structure of the emitted radiation with a frequency spacing of $2\omega_L$. This is shown in Figure 1.9.

However single-atom effects in general are not always sufficient to describe EUV generation. The next section describes how single-atom predictions will be modified by macroscopic effects. These macroscopic effects offer new routes to attosecond pulse generation.

1.4.3 Macroscopic effects on HHG emission: Phase matching

The macroscopic EUV radiation generated from many emitters can be different from the single-atom radiation due to propagation effects, such as phase-matching and absorption. These effects can be tailored to manipulate the properties of the emitted radiation.

If atoms should emit EUV radiation constructively over a long interaction length

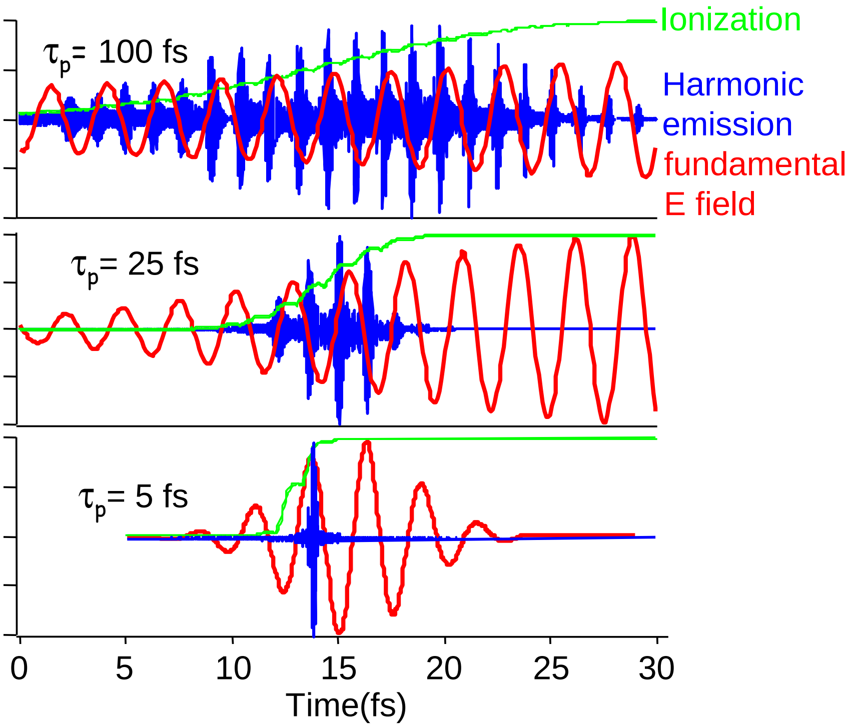

Figure 1.9: Simulations of EUV generation [22], based on numerical solution of the time-dependent Schroedinger equation. A long fundamental pulse duration τ_p results in an attosecond EUV pulse train. A short fundamental pulse, combined with spectral filtering, can result in an isolated attosecond pulse.

in a macroscopic generation medium, as e.g. in a hollow core waveguide, one must ensure that the harmonic radiation travels with the same phase velocity through the waveguide as the fundamental pulse. Such phase matching conditions can be effectively implemented in a gas-filled hollow-core waveguide, because the waveguide can tightly confine the light and enforce plane-wave propagation over a macroscopic length. By modifying the structure of the waveguide (e.g. using a tapered or corrugated waveguide) additional phase matching terms can be introduced [23, 116].

The phase mismatch between the q'th harmonic and the fundamental light is given by

$$\Delta k(t) = q \cdot k_{laser}(t) - k_q \tag{1.12}$$

where k_q is the wave vector of the q'th harmonic, and $k_{laser}(t)$ the fundamental laser wave vector. A general expression for the wave vector of light in a waveguide filled with gas is given by [135]

$$k(t) \approx 2\pi/\lambda + \frac{2\pi N(1-\eta(t))\delta(\lambda)}{\lambda} - N\eta(t)r_e\lambda - \frac{u_{nm}^2\lambda}{4\pi a^2} \tag{1.13}$$

Here, N is the total gas density (neutral gas plus plasma), $\eta(t)$ is the time-dependent ionization fraction (calculated using equation 1.5), $\delta(\lambda)$ describes the dispersive characteristics of the atom, r_e is the classical electron radius, a is the waveguide radius, and u_{nm} is the m^{th} root of the $(n-1)^{th}$ Bessel function of the first kind and depends on the transverse modes coupled into the waveguide. One finds that the influence of the waveguide and the plasma on the phase mismatch is q^2 smaller ($\lambda_q = \lambda_{fund}/q$). Also the neutral gas dispersion $\delta(\lambda)$ is in general small at x-ray wavelengths. The EUV radiation is thus not strongly affected by any of the three dispersion contributions, and its wave vector k_q in Eq. (1.12) is only slightly modified from its vacuum value.

If phase-matching is fulfilled, the generated radiation will interfere constructively along the whole generation region (limited only by absorption, see below). The intensity increases quadratically with the number of emitters. For EUV generation in a gas-filled waveguide we therefore get a quadratic dependence of phase matched emission with fiber length. On the other hand if $\Delta k \neq 0$, the signal will start to interfere destructively after a coherence length defined by $L_{coh} = \frac{\pi}{\Delta k}$. Coherence lengths for HHG in the presence of high levels of ionization are on the order of $\mu m - mm$.

To understand how one can influence the phase mismatch, consider the contributions to the k-vector (1.13). Neutral gas increases the k-vector, the waveguide and the plasma reduce the k-vector. As the harmonic k-vector is nearly unchanged from its vacuum value, the fundamental k-vector can be influenced independently to achieve phase-matching. For large ionization fractions η, the plasma term becomes dominant and destroys phase-matching (then the neutral gas term becomes small, and the waveguide anyway adds with same sign to the plasma term).

Not only phase matching but also EUV absorption can limit EUV generation: The electric field is attenuated with propagation length L according to Beer's law $E = E_0 \exp(-\alpha L)$ (Note: α is defined here as the field absorption coefficient.). A typical absorption length $L = 1/(2\alpha)$ is $\sim$ 30 mm for $\lambda = 25$ nm radiation in 10 torr Argon.

Empirically it had been found that the intensity of EUV radiation depends on the fundamental intensity as $I_{HHG} \propto I_F^{2s}$, where the effective nonlinearity $2s$ of the generation process is $2s \approx 11$. Durfee et al. [71] combine these three ingredients, effective nonlinearity, phase matching and absorption, to give an approximate formula for the EUV output:

$$I_{HH}(t) \sim N_A^2 I_{F(t)}^{2s} \left(\frac{1 + \exp(-2\alpha L) - 2\exp(-\alpha L)\cos(\Delta k(t) L)}{\alpha^2 + \Delta k_{(t)}^2} \right) \tag{1.14}$$

The term in brackets reduces to $sinc^2(\Delta k L/2)$ if absorption is neglected.

Finally we note that in a real waveguide there are several other contributions that need to be taken into account, such as e.g. a varying coherence length along the fiber due to losses from ionization (and Fresnel reflections) and mode beating of various coupled spatial modes.

1.4.4 Attosecond pulse generation in a hollow waveguide

Despite being oversimplified, equation (1.14) suggests different ways to achieve a single isolated attosecond pulse: The high-order $I_{F(t)}^{11}$ dependence suggests that EUV pulses are significantly shorter than their driving pulses, and that shortening the fundamental pulse to a few femtoseconds should localize EUV generation to less than a half-cycle (1.33 fs for 800 nm). Theoretical calculations [22] show that the use of 5 fs pulses, in combination with spectral filtering, allow for generation of an isolated attosecond pulse. However the generation and management of such few cycle pulses is technically very challenging.

Instead we can focus on the phase-matching contribution to Eq. (1.14) and engineer some process that limits EUV emission to a temporal window smaller than a half cycle of the driving fundamental field. The phase mismatch (1.12) has a very strong time-dependence due to the time-dependent ionization fraction $\eta(t)$ in (1.13). The fast sweep of the phase mismatch through zero can be used to generate single attosecond pulses even from relatively long ($\sim 15fs$) femtosecond driving pulses.

The upper graph in Fig. 1.10 shows the intensity of a NIR 13 fs driving pulse. (b) shows the corresponding electric field (blue). When sufficient field strength is reached, the field ionizes the gas in the fiber and creates a plasma. The red line shows how the ionization fraction in the gas rapidly increases. For the conditions here, nearly full ionization is reached around the pulse peak. The generated plasma gives a negative contribution to the phase mismatch, which varies rapidly in time. This phase mismatch is shown in red in (c). Initially the neutral gas causes a slight positive mismatch (the negative waveguide term does not compensate this). The growing plasma contribution sweeps the phase mismatch to zero and then to large negative values. Also shown in (c) is the summed-up intensity of $19^{th} - 31^{st}$ harmonic generated from 25 mm of Argon gas, calculated with the simple model (1.14), with the additional constraint that only fundamental intensities above the cutoff intensity for each harmonic, calculated from Eq. (1.8), contribute. Note that EUV emission does not peak at the fundamental intensity maximum but earlier. At late times $>\sim -5$ fs emission is suppressed by the large phase mismatch due to nearly complete ionization of the gas. At early times EUV emission is constrained by the low fundamental intensity. While this oversimplified model should not be taken too seriously, it predicts the generation of EUV pulses of order of 1 fs from a 13 fs driving pulse.

If we could now still add a constant offset to the phase mismatch in Fig. 1.10, then we could shift the phase-matching window in time toward the pulse peak, and phase match the highest harmonics. Even more importantly, the sweep of the phase mismatch through zero can be even more rapid, and create an even shorter temporal phase-

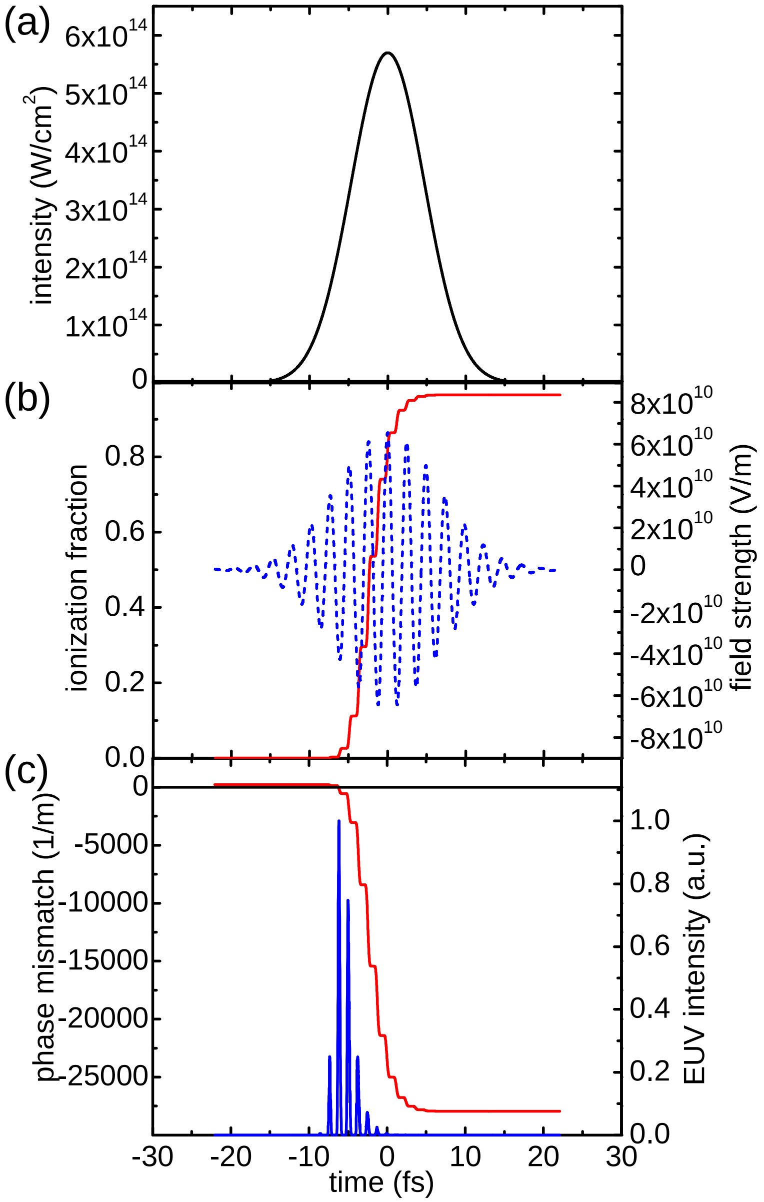

Figure 1.10: Dynamic phase-matching effects in EUV generation (parameters similar to section 3.9). (a) intensity envelope of a 13 fs fundamental pulse. (b) electric field (blue) and ionization fraction of the Argon gas (red). (c) phase mismatch for the 25^{th} harmonic in 10 torr of Argon (red), summed-up intensity of $19^{th} - 31^{st}$ harmonic from 25 mm of Argon gas, calculated with the simple model (1.14), with the additional constraint that only fundamental intensities above the cutoff (1.8) contribute to each harmonic. EUV emission does not peak at the fundamental intensity maximum but earlier: At late times $>\sim -5$ fs EUV emission is suppressed by the large phase mismatch due to full ionization of the gas, while at early times it is constrained by the low fundamental intensity.

matching window, facilitating the generation of a single phase-matched attosecond pulse. Such a constant offset can be introduced by quasiphasematching techniques, as was shown in our group [116]. This technique was however not pursued in this thesis.

1.5 Temporal Characterization of ultrafast EUV radiation

Not only the generation, but also the temporal characterization of ultrafast EUV radiation is an active field of research: In contrast to femtosecond NIR pulses, where nonlinear effects are easily exploited to generate an autocorrelation signal, EUV fluxes are low, and nonlinear experiments are difficult. However temporal characterization of short events can as well be achieved by a cross-correlation with another event. The most common method for characterization of EUV pulses is therefore a cross correlation with the electric field of a strong NIR pulse, based on "Laser Assisted Photoelectron Emission". Here EUV radiation and fundamental field are focused into a gas target with an adjustable delay. The EUV pulse causes photoionization, where the photoelectron wave packet can be viewed as a replica of the EUV pulse. The photoelectron will then receive a momentum shift (or, as we will see in section 3.4, a phase shift) by the fundamental laser field. The final photoelectron wave packet contains information on both amplitude and phase of the EUV pulse, allowing a complete reconstruction of its temporal structure.

When this cross-correlation signal is energy-resolved, a spectrogram results

$$S(\omega,\tau)=\left|\int_{-\infty}^{+\infty}E(t)g(t-\tau)\exp\left(-i\omega t\right)dt\right|^2 \tag{1.15}$$

where $E(t)$ is the electric field of the pulse to be measured and $g(t-\tau)$ is the gate function. The most common FROG technique for the characterization of NIR laser pulses, uses an amplitude gate. In contrast, laser assisted photoemission employs a phase gate $g(t-\tau)=\exp(i\phi(t-\tau))$ where the NIR pulse causes a phase-modulation of the photoelectron wave packet. Laser assisted photoemission, as well as our analysis of the recorded spectrograms are described in detail in Chapter 3.

1.6 Applications of femtosecond / attosecond pulses

1.6.1 Molecular physics

Femtosecond EUV radiation is ideally suitable to initiate or probe molecular dynamics by ionization. Figure 1.11 shows a molecular potential diagram and gives an overview of the energetics of EUV (energy $h\nu$) photoionization (green) $AB + h\nu \rightarrow AB^{+} + e^{-}$ of the photoexcited complex and photodissociation (red) $AB + h\nu \rightarrow AB^{+*} + e^{-} \rightarrow A^{+} + B + e^{-} + KER$, where KER is the total kinetic energy release after subtracting the internal energy of the A and B products. Of course, even the simplest diatomic molecules can have very congested energy diagrams with several potential energy curves possibly crossing each other and leading to the same final products. Time-resolved EUV-NIR pump-probe experiments with sufficient spectral resolution have shown great potential to initiate and probe nuclear motions, or correlated electron-nuclear motions. EUV radiation is particularly suitable for excitation to highly excited molecular states, which have been rarely studied in detail so far, both theoretically and experimentally.

1.6.2 Condensed matter systems

Just as in molecular systems, EUV radiation may initiate photoionization or Auger processes in condensed matter systems, such as surface-adsorbate systems. A proof-of principle experiment to observe such Auger decays in the time-domain was recently conducted in our group on noble gas atoms physisorbed on platinum [105]. From a time-delay between laser-assisted photoemission and laser-assisted Auger decay signals, a lifetime of 7 fs of the $4d^{-1}$ core level of Xenon on Pt(111) could be determined.

Not only Auger decays, but also excited-state lifetimes and charge transfer timescales

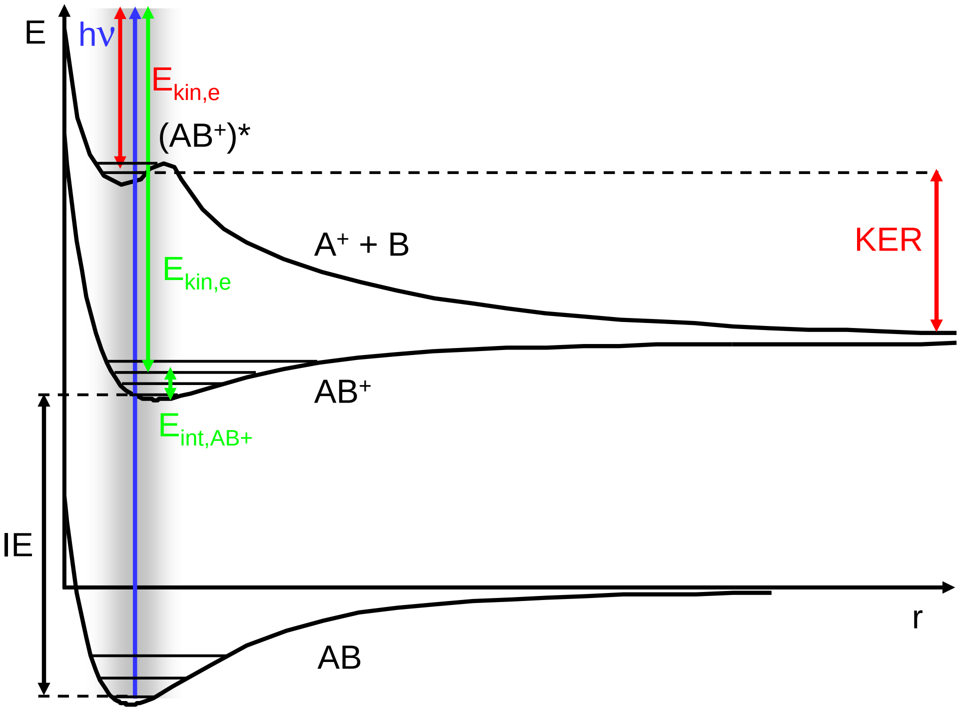

Figure 1.11: Basic energetics of EUV (energy $h\nu$) photoionization (green) and photodissociation (red) of molecules. Shaded area: Franck Condon region in which photoabsorption takes place.

of molecules chemisorbed onto a surface are expected to occur on femtosecond- or even sub-femtosecond timescales.

1.6.3 Strong-field physics

When an external electric field of comparable strength is superimposed on a nuclear field, there is a high probability for single or multiple ionization. An example is the study of double ionization of noble gas atoms leading to correlated electron emission [170]. The data showed electron-electron correlations for double ionization at low intensities, while supporting the picture of sequential ionization with no directional correlation of the electrons at high intensities. In the low intensity regime the data suggest that first one electron is ionized, accelerated by the field, and is then driven back to its parent ion where it transfers energy to eject the second electron.

A strong laser field can of course be applied to molecular systems as well. The mechanism of strong-field electron tunneling, acceleration and recollision with the parent ion, can now be used to induce electron diffraction from the molecule [103]. The high achievable return kinetic energies correspond to electron de Broglie wavelengths of ~ 1 Angstrom. One can therefore make use of the wave-nature of the returning electron wave packet to obtain information about the parent molecule. In addition to the elastically scattered electrons which reveal information on the positions of the nuclei in the molecule, the momentum distribution of electrons moving directly, without scattering to the detector reveals the symmetry of the highest occupied molecular orbital.

Another way to extract molecular information is a detailed analysis of the strength of EUV generation from molecules [95]. This technique was recently shown to yield dynamical information on coupled electronic-nuclear motions of polyatomic molecules [95]. Vibrations in N_2O_4 were excited and stronger high harmonic emission was observed at the outer turning point of the dimer, when tunneling to the ground state of the ion occurred, whereas weaker high harmonic radiation was observed when tunneling occurred to the first excited state of the ion at the inner turning point. Calculations supported the experimental findings and explained them by a larger recombination dipole (better electronic overlap) for high harmonic generation involving the ground state of the ion.

As pointed out in the last example, strong-field physics is not limited to electron motion alone. Strong-field ionization of molecules can start correlated electron-nuclear motions (when the equilibrium configuration of the ion is different from the neutral molecule). In a second step, electron recollision can lead to dissociation of the parent molecular ion, and thus act as a probe of the nuclear motion [111]. What is even more exciting is that the laser field can continue to act on the dissociating molecule, controlling the carrier-envelope sensitive localization of the remaining electron on one of the two dissociation products [85].

1.7 The COLTRIMS reaction microscope

COLTRIMS (COLd Target Recoil Ion Momentum Spectroscopy) [34] is a technique which has the capability of detecting in coincidence all charged particles emerging from a single reaction event. It also allows the reconstruction of the full 3D momentum of all particles. This technique has recently become very popular among the ultrafast community, beginning with strong-field experiments described above.

1.7.1 Opportunities of fs-EUV pulses combined with COLTRIMS detection

The combination of ultrafast EUV pulses with the COLTRIMS technique provides a powerful experimental tool, which allows one to extract a maximum amount of information from every event.

Applications include time-resolved studies combined with the capability of multiple coincidence detection. Such experiments have just begun to shed light on basic processes in highly excited molecules, such as autoionization [139].

The coincidence detection of ions and electrons also allows experiments with fixed-in-space gas-phase molecules: When simple molecules dissociate, the fragment ion momenta point along the molecular axis at the time of dissociation. COLTRIMS can measure such 3D momenta, and in addition measure momenta of electrons in coincidence with the ions. A major application of this technique is the measurement of molecular-frame photoelectron angular distributions. Such photoelectron angular distributions can be very complex and reveal detailed information e.g. about correlated electron dynamics in molecules [30]. One new approach for measuring molecular-frame photoelectron angular distributions in the case of nondissociating channels is described in this thesis.

1.8 Organization of this thesis

This thesis is organized as follows: Chapter 2 describes the realization of a high-power fs pulse train which had its electric field stabilized underneath the intensity envelope. In Chapter 3 of this thesis I will tell you about the generation and temporal characterization of extremely short EUV pulses: these pulses are shorter than one optical cycle of the driving radiation, yet they are spectrally narrow enough to do state-selective excitation in a condensed matter or molecular system. In the third part of the thesis, Chapter 4, I will tell you about one application experiment, which allowed us to measure the orientation of transition dipoles in small molecules.

Chapter 2

A carrier-envelope phase (CEP) stabilized amplifier

This chapter on the carrier-envelope phase stabilization of a femtosecond amplifier system contains material published in [157] and [50]. This project builds on my prior work at NIST in Leo Hollberg's group [158, 153, 28, 9] on the CEP stabilization of a Chromium Forsterite femtosecond oscillator, which allowed the extension of phase-stabilized frequency combs for absolute optical frequency measurements further into the infrared region ($\sim 1.1\,\mu m$ to $\sim 2.2\,\mu m$) relevant for telecommunications and infrared molecular spectroscopy.

During the course of this work I also participated in work in Jun Ye's group in which novel stabilization techniques of a femtosecond Ti:Sapphire oscillator to a reference cavity were explored [78]. In particular, it was explored how to lock the two degrees of freedom of the femtosecond frequency comb, f_0 and f_r, to the mode comb of the cavity. In particular the limitations due to the residual dispersion of the cavity were explored.

2.1 Introduction, Motivation and Difficulties

2.1.1 Motivation

The carrier-envelope phase (CEP) is defined as the phase difference between the carrier oscillations and the pulse envelope of ultrashort laser pulses. Its definition and relevance were shown in the introduction in Figure 1.2. In conventional femtosecond laser oscillators this phase fluctuates randomly from pulse to pulse. After the first demonstration of CEP stabilization of low-power femtosecond pulse trains in 2000 [76] this technique spread rapidly, driven by the huge interest in absolute frequency measurements and optical waveform synthesis, but remained restricted to low-power pulses. The amplification of carrier-envelope phase stabilized femtosecond (fs) laser pulses has only recently received considerable interest. One major driving force for this interest is that extreme nonlinear processes such as HHG driven by amplified laser pulses, exhibit a strong dependence on the driving laser field [11, 10, 22, 21], and are therefore sensitive to the CEP of the driving laser pulses [38, 118, 7].

Combination of pulse shaping techniques [178, 177] with methods of CEP control, [76, 29] offers the possibility of controlling the complete electric field of the ultrafast pulse in the time-domain, with attosecond precision. This allows us to access the fastest time-scales to date that are accessible with modern laser technology. It has thus become possible to manipulate electron dynamics with attosecond precision [11, 10, 21], to manipulate phase-matching of the HHG process,[23, 116] and to generate pulses of light with sub-femtosecond duration [84, 152].

Interesting applications of CEP stabilization can be expected in molecular physics and condensed matter systems. Using CEP control, it was e.g. possible to control electron localization in the dissociative ionization $D_2 \rightarrow D^+ + D$ [85]: CEP sensitive light-driven intramolecular electronic motion before dissociation decides on which nucleus the electron localizes. In solid-state systems, CEP stabilization allows the control of directional currents [4, 132], providing interesting perspectives for future ”opto-electronics” technologies.

2.1.2 Where do CEP fluctuations come from?

To understand why there are shot-to-shot fluctuations of the carrier-envelope phase in a femtosecond pulse train from an oscillator [62, 151], recall that a pulse envelope travels at the group velocity $v_g = c/n_g$ while the carrier oscillations travel at the phase velocity $v_p = c/n$. These velocities are different inside a laser cavity due to dispersive elements such as prisms, the laser gain medium, mirrors, and the beam path in air. A round trip of length L of a carrier oscillation therefore takes a time $\tau_p = \int_0^L dz 1/v_p(z)$ while the pulse envelope takes $\tau_g = \int_0^L dz 1/v_g(z)$. The phase shift *difference* between the carrier and the envelope for one round trip is

$$\Delta\phi_{GPO} = \omega(\tau_p - \tau_g) = \int_0^L dz \frac{2\pi}{\lambda}(n_g - n) \tag{2.1}$$

where $(n_g - n)$ can also be expressed as $(n_g - n) = \omega\frac{\partial n}{\partial\omega}$, i.e. it depends on the dispersive properties in the laser cavity. This phase difference between subsequent pulses can be many full cycles. The measurable CEP difference between adjacent pulses is only the sub-cycle part of this large phase slip

$$\Delta\phi_{CE} = \Delta\phi_{GPO} \; mod \; 2\pi \tag{2.2}$$

The carrier envelope offset frequency is defined as the rate of change of the CE phase:

$$f_0 = \frac{1}{2\pi}\frac{d\phi_{CE}}{dt} \tag{2.3}$$

Equation (2.1) shows that f_0 is constant as long as dispersive beam paths in the cavity remain constant. The CE offset can only be measured at time intervals $dt = 1/f_{rep}$, so that we can also express f_0 as

$$f_0 = \frac{\Delta\phi_{CE}}{2\pi} \cdot f_{rep} \tag{2.4}$$

This shows that once the ratio of the two radio-frequencies f_0/f_{rep} is stabilized, one has also stabilized the CE-phase slip in the optical domain.

In practice, there are several sources of CEP noise: All laser parameters that are coupled to the intracavity dispersion contribute. As soon as e.g. beam pointing variations, air pressure fluctuations, pump laser intensity fluctuations occur, the carrier-envelope offset frequency fluctuates. Temperature variations cause long-term drifts. Through the nonlinear index of the gain crystal, the CEP also depends on intra-cavity pulse energy fluctuations [67]. An important contribution to this effect arises from pump laser noise [173].

2.1.3 History and methods of CEP stabilization

There are several ways to measure and/or stabilize the pulse-to-pulse CEP slip. Jones et. al. [76] first demonstrated the carrier-envelope phase stabilization of a Ti:sapphire laser in 2000 employing a method based on frequency domain measurements. This f-2f interferometer is the most widely used method to date to stabilize the CEP slip, and has led to tremendous progress in the field of optical frequency measurements as now a single laser can be used to measure many absolute optical frequencies. It should be emphasized however that this technique does not measure the absolute value of the CEP but only its pulse-to-pulse slip, and additional measurements are required if one wants to fix this absolute value.

The basic idea behind the f-2f nonlinear interferometer (described in more detail below, see Figure 2.1) is this: Produce an octave-spanning, phase-coherent frequency comb. Pass the "red" portion of the comb through a nonlinear crystal, where these modes are phase-coherently up-converted to "green", and combine the original green and doubled red light on a fast photodiode. The original green modes of the frequency comb evolve in time as $\exp(i2\pi(mf_{rep} + f_0)t)$ while the doubled red modes evolve as $\exp(i2\pi(2nf_{rep} + 2f_0)t)$, so the interference signal on the photodiode has components $\cos(2\pi((2n - m)f_{rep} + f_0)t)$. This allows us to measure the beat frequency f_0.

There are two ways to produce a coherent octave-spanning frequency comb: Either a standard Ti:Sapphire laser is used in conjunction with a microstructure fiber as in [76], or the generation of an octave spanning spectrum directly from a modified

Ti:sapphire oscillator [45]. Alternatively, one may use a modified laser [125] in combination with a 2f-3f interferometer, or use difference frequency generation in a PPLN crystal [126]. In addition, new methods are being explored that do not rely on a f-2f interferometer, such as the stabilization of both degrees of freedom of a femtosecond laser to a reference cavity [78].

To actuate on f_0 one can either use feedback on an AOM controlling the pump laser intensity, or use a piezo-actuated tip-tilt mirror in the arm of the laser cavity where the spectrum is dispersed. The AOM method achieves higher bandwidths (150 kHz), while the tip-tilt mirror (tens of kHz bandwidth) avoids the laser intensity fluctuations associated with the AOM method [29].

Of course there are also methods of stabilizing the CEP which employ processes that are directly sensitive to the absolute position of the peaks of the electric field in time domain, such as photoionization with ultrashort pulses. Paulus et al. [118, 119] measured CEP dependent effects in above-threshold ionization (ATI) using a stereo-ATI setup. Here, an ultrashort pulse causes multi-photon above-threshold ionization of a gas target, whereby photoelectrons are preferentially ejected in the direction of the strongest optical half-cycle of the pulse. By measuring the difference in photoelectron yield with two identical detectors placed on opposite sides of the gas target one can measure the absolute CEP.

In a similar way as ATI from a gaseous sample, also photoelectron emission from metals using few-cycle pulses was predicted to be CEP sensitive (Lemell et al. [91]). This effect was later experimentally measured by Apolonski et al. [4].

Roos et al. [132] used interferences between one- and two-photon transitions in a semiconductor to induce a current with a CEP-dependent sign and magnitude that was used to stabilize the CEP. While this experiment still required a microstructure fiber to broaden the spectrum to an octave, with octave spanning lasers and improved signal to noise this method could become an alternative stabilization scheme based entirely on solid-state systems. Similar effects were seen by Mücke et al.[108].

Another highly CEP sensitive process is high-harmonic generation. Durfee et al. observed possible signatures of the CEP in fluctuations of the yield of high-harmonic generation from CEP-unstabilized pulses [71]. Carrier-envelope dependence in the generation of attosecond pulses was reported in [7].

2.1.4 CEP concerns with amplified pulses

The amplification of CEP stabilized pulses through chirped pulse amplification (CPA) [148] poses further challenges. There are two major concerns: First, pulse stretching before amplification and recompression afterwards require the use of strongly dispersive elements. In our setup, this is achieved by a grating-based stretcher and compressor [161]. The first CEP stabilized amplifier had been demonstrated with a material-based stretcher and compressor [7]. Grating-based systems were suspected to be very susceptible to introducing CEP noise [62]. The basic reason is that a beam pointing fluctuation changing the beam position on a grating by just one groove introduces a 2π CEP change [62]. The second concern is CEP changes caused by fluctuations of the nonlinear refractive index in the amplifier gain medium. However such fluctuations are not expected to be very strong, as amplifiers are designed to have a total accumulated nonlinear phase (B-integral) less than 2π. The relevant quantity is again the dispersion of the nonlinear refractive index of the Ti:Sapphire gain medium $(n_g - n) = \omega\frac{\partial n_2}{\partial \omega} = 8 \cdot 10^{-17} cm^2/W$ [62] in equation (2.1). In [62] it is found that about 6% intensity fluctuations should be tolerable for a CEP noise below 100 mrad.

As pointed out above, intensity fluctuations which cause phase changes due to nonlinear refractive index changes might not strongly contribute to CEP changes. Nevertheless cryo-cooling of the amplifier crystal [5] is important to significantly reduce beam pointing fluctuations (leading to large changes in beam path through the amplifier crystal, lenses or beam pointing fluctuations onto the compressor gratings). These effects can be diminished by cryo-cooling. Usually the heat load due to the pump laser creates very strong temperature gradients. Due to the dependence of the sapphire refractive index on temperature this causes thermal-lens aberrations. By cooling the crystal to liquid nitrogen temperatures (77 K), the thermal conductivity increases and the change in index of refraction with temperature decreases, reducing thermal distortions by a factor of 200. Therefore it likely reduces beam pointing effects due to intensity fluctuations from the amplified pulses or pump pulses and therefore decreases CEP noise.

In the following sections I will describe our procedure to demonstrate a CEP stabilized amplifier. First, a microstructure fiber was used to generate an octave spanning spectrum from a portion of the oscillator output, and an f-2f interferometer was used to detect the offset frequency and thereby stabilize the oscillator's carrier-envelope phase. As our next step towards setting up a CEP stabilized amplifier, we analyzed the behavior of a grating-based stretcher and compressor (SC) setup. Our work, as well as the results of Kakehata et al. [80], showed that grating-based chirped pulse amplifiers *can* be stabilized. This work therefore proved that it will be possible to stabilize amplifiers with pulse energies up to several mJ or even into the Joule range [68]. It turned out that stabilization of the oscillator CEP, in combination with the intrinsic CEP stability of a cryogenically cooled amplifier, is sufficient for a rough CEP stabilization of the full amplifier system. After the amplifier at most a slow feedback is required for correcting low frequency noise.

2.2 A CEP stabilized oscillator

In this work, a prism-based oscillator was CEP phase stabilized to serve as the seed oscillator for an amplifier. The CEP slip given by equation (2.4) was measured and locked using a f-2f fiber setup, shown in Figure 2.1. The spectrum of the oscillator was broadened to more than an octave, using self-phase modulation in a ~ 5 cm long microstructure fiber (Crystal Fibre). Typically about ∼ 150 mW were used and the fiber coupling efficiency was ∼ 35 % (Newport microscope objective with numerical aperture 0.65 and 0.85). Infrared and green colors are split using a double pass through a prism pair with a split end mirror. The infrared pulse is then frequency-doubled in a LBO crystal, and is spatially and temporally overlapped on a photodiode with the original green pulse. As described above, this results in a measurement of the beat frequency f_0.

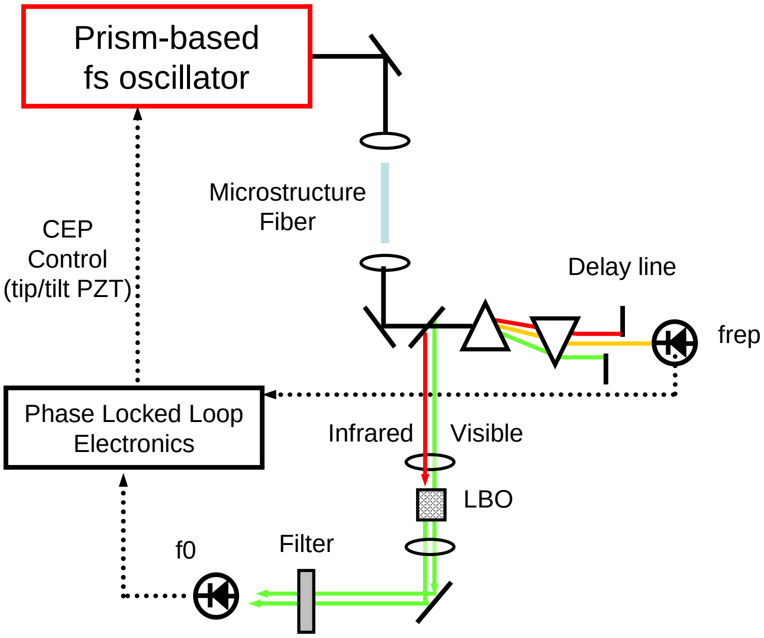

Figure 2.1: Sketch of the f-2f interferometer used to lock the CEP of the amplifier seed oscillator [76, 29]: self-phase modulation in the microstructure fiber broadens the oscillator output to an octave. Infrared and green colors are split and sent through a LBO crystal which causes sum-frequency generation of the near-infrared modes to green. The two green beams are overlapped on a photodiode where their interference produces a radio-frequency beat signal at the carrier-envelope offset frequency f_0. One of the split mirrors at the end of the prism sequence is mounted on a delay stage to optimize the temporal overlap of the two green fields on the photodiode. The prisms are used for dispersion compensation to optimize doubling efficiency of the IR pulse. The laser pulse repetition rate f_{rep} is also recorded. Both signals are fed into the phase-locked loop electronics, which generates a voltage signal for feedback to a tip/tilt PZT mirror inside the laser cavity to lock the ratio f_0/f_{rep}, and hence $\Delta\phi_{CE}$ according to equation (2.4).

Note that different interferometer configurations have been used for oscillator CEP stabilization. The setup of Ref [44] employs an AOM in one interferometer arm. This allows one to shift f_0 to zero (generating a train of identical pulses), but still detect it at the nonzero AOM frequency. In contrast, our setup does not easily allow shifting f_0 to zero, but this is not required for our application (see below). The geometry involving a prism pair with a split end mirror was chosen as it introduces less losses than a Mach-Zehnder interferometer and therefore allows for higher signal to noise beat note detection.

The electronics which is used to process this beat signal is sketched in Figure 2.2. The purpose is to lock f_0 to a pre-set fraction (here 3/8) of f_{rep} using a phase detector and loop filter. The digital phase/frequency detector provides a voltage proportional to the phase difference of the two input signals. The loop filter provides sufficient gain to drive fluctuations of the phase difference to zero. The error signal is sent to a piezo-actuated tilt mirror in the frequency dispersed arm of the oscillator. The bandwidth of this servo loop is approximately 10 kHz (limited by the PZT mirror).

Results for the locked CEP are shown in Figure 2.3. (a) shows the RF spectrum recorded with the "f_0" photodiode, extending from DC to 100 MHz. The pulse repetition rate is visible at $f_{rep} = 96$ MHz. The phase-locked beat note f_0 is visible at 36 MHz. The peak at 60 MHz corresponds to $f_{rep} - f_0$. (b-d) show successively zoomed-in spectra of the beat note at 36 MHz, exhibiting various residual noise features. (e) shows the in-loop CEP noise at frequencies $> f_0$ on a logarithmic scale. The decrease of noise with decreasing frequency below 10 kHz clearly shows that the lock efficiently cancels noise frequencies < 10 kHz.

The rms *in-loop* phase fluctuations for this stabilized oscillator are shown in Figure 2.4, measured with a FFT spectrum analyzer that allows a smaller resolution bandwidth than in the measurements of Figure 2.3. To make this measurement, an electronic reference signal at 3/8 f_{rep} was generated in order to mix f_0 to DC. The phase noise

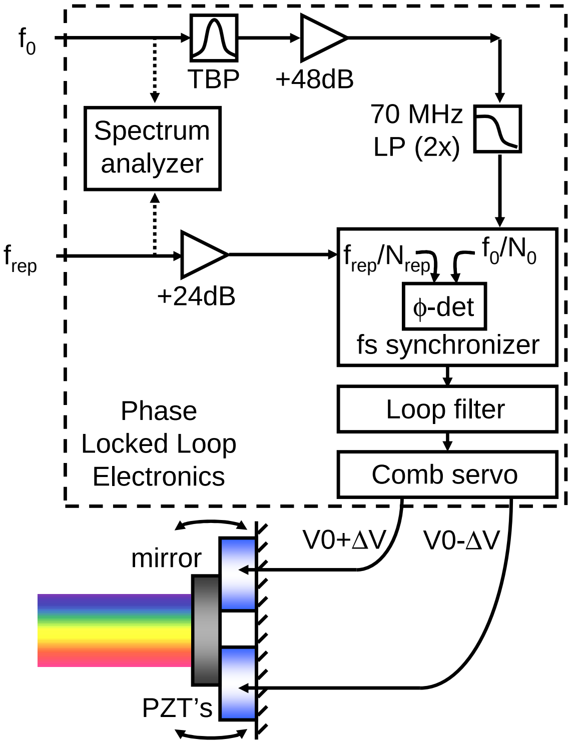

Figure 2.2: Phase-locked loop electronics used to stabilize the CEP slip of the oscillator [29]. f_0 and f_{rep} are recorded as shown in Figure 2.1. f_0 is sent through a tunable bandpass filter (TBP), amplified and sent through two low-pass filters (LP). f_{rep} is also amplified and filtered. Both frequencies are electronically divided by suitable integers (N_0 and N_{rep}, respectively) and compared on a phase detector. Its voltage output, proportional to the phase- (or frequency-) difference serves as the error signal. This is sent to a loop filter, which provides proportional and integral gain, as well as additional low-pass filtering for the error signal. The "comb servo" provides suitable high-voltage signals to drive a piezoelectric tilt-mirror. For our experiments, N_0 and N_{rep} are chosen to yield $f_0/f_{rep} = 3/8$.

accumulates to $\Delta\phi_{CE} \sim 300$ milliradians over 16 seconds (integrated from 63 mHz to 102 kHz). Typical values achieved on a daily basis (as presented in the stretcher/compressor measurements in section 2.3) were $\Delta\phi_{CE} \sim 400$ milliradians.

In practice, for a successful lock, a good signal-to-noise beat note needs to be achieved. Environmental noise needs to be kept at a minimum to obtain a good passive stabilization, before active stabilization is attempted. Noise sources should be identified and removed so that the loop only has to deal with the remaining noise. As the beat

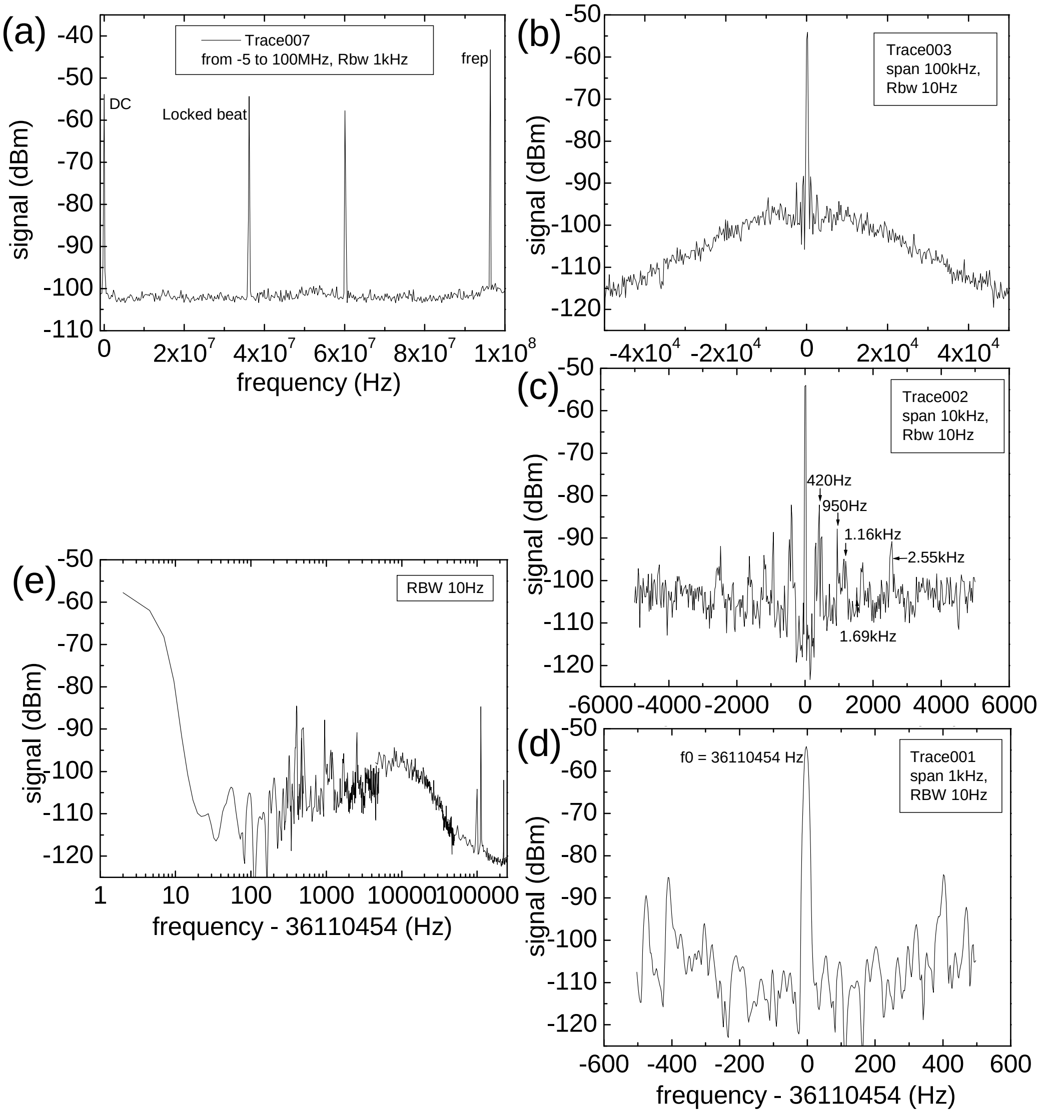

Figure 2.3: Measurement of f_0. (a) shows the RF spectrum recorded with the "f_0" photodiode. (b)-(d) Zooming in on the CEP beat signal. (e) In-loop noise on a log-scale representation at frequencies $> f_0$. The feature below 10 Hz corresponds to the resolution bandwidth limited coherent spike, i.e. it is not a measure of true noise.

note is a very delicate signal, all beam paths should be air tight to avoid air pressure fluctuations - particularly at dispersive elements. Acoustically isolating enclosure boxes for the beam path as well as for noisy equipment are necessary. All elements in the beam path should be mechanically stable (i.e. low and thick mounts). A stable lab temperature is essential, especially at the delicate microstructure fiber. Vibrations from

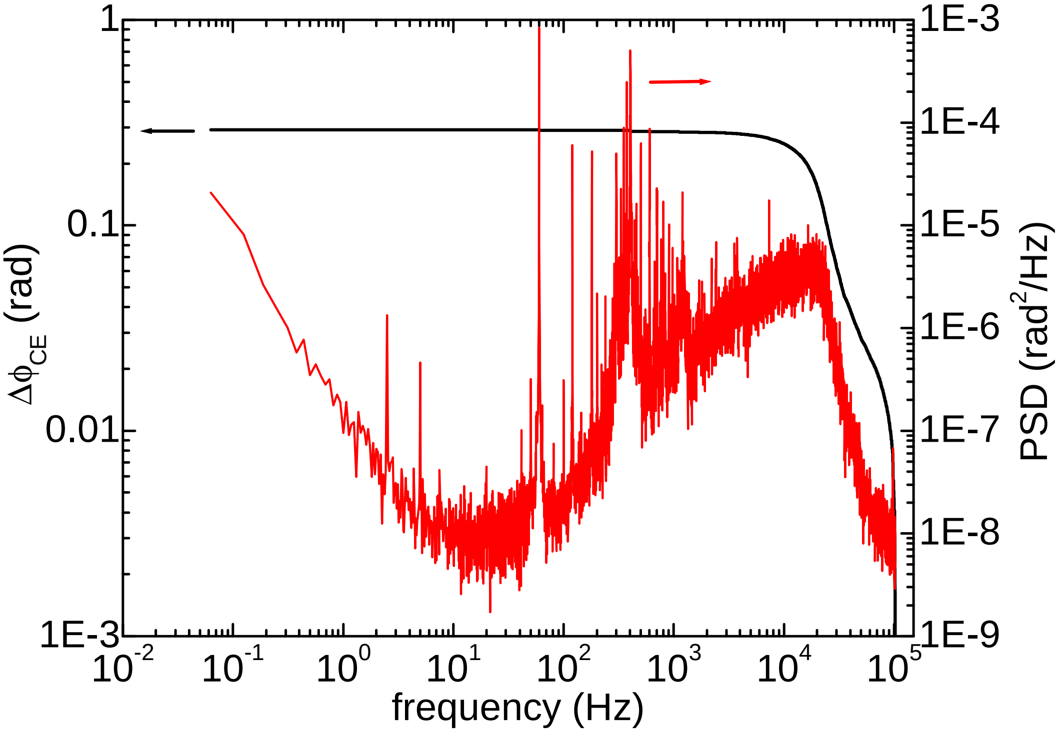

Figure 2.4: Measurement of in-loop oscillator CEP noise using a FFT spectrum analyzer. Red, phase noise power spectral density ($radians^2/Hz$). Black, accumulated root mean square (rms) phase fluctuations $\Delta\phi_{CE}$.

water lines, vacuum pumps, etc need to be damped and isolated. Any noise transmitted to the table needs to be eliminated (floating of the table is one consideration). Another noise source are fans, which can produce physical vibrations, air pressure variations and also electrical noise. Electrical noise sources and ground loops are additional major concerns. Before any equipment was moved into the lab, the room noise and floor vibrations were evaluated by accelerometer measurements.

The work described in this section provides the groundwork for the measurements in the next sections, as well as for the CEP stabilization of a complete amplifier setup.

2.3 Investigation of a grating-based stretcher/compressor for carrier-envelope phase stabilized femtosecond pulses

In this chapter, we experimentally investigate the effect of a grating based pulse stretcher/compressor on the carrier-envelope phase stability of femtosecond pulses. Grating based stretcher-compressor (SC) setups have been avoided in past demonstrations [7] of chirped pulse amplification (CPA) of carrier envelope phase (CEP) stabilized femtosecond pulses, because they were expected to introduce significantly stronger CEP fluctuations than material-based SC systems [62, 162]. The CEP change in a double pass through a grating compressor is [162]

$$\Delta\phi_{CE} = 4\pi\frac{G}{d}\tan(\gamma - \theta(\omega_0)) \tag{2.5}$$

where G is the perpendicular grating distance, d is the groove period, γ is the angle of incidence, and $\theta(\omega_0)$ is the angle between input beam and the diffracted ray of the center frequency. If the path through the compressor is identical for different pulses, their CEP change is identical. However input beam fluctuations $\Delta\gamma$ lead to pulse-to-pulse CEP flucutuations of order $4\pi\frac{G}{d}\Delta\gamma$. Typically $\frac{G}{d} \sim 10^6$ and $\Delta\gamma \lesssim 10^{-6}$ rad, making it conceivable that eq. 2.5 could be significant. It turns out that cancellations between the first and second pass reduce the fluctuations somewhat, allowing grating-based optics to be used for CEP stabilization.

Using a microstructure fiber-based detection setup, we measure CEP fluctuations of $\Delta\Phi_{CE,SC} = 340$ milliradians rms for a frequency range from 63 mHz to 102 kHz for pulses propagating through the SC setup. When bypassing the beam path through the SC, we find CEP fluctuations of $\Delta\Phi_{CE,bypass} = 250$ milliradians rms. These values contain significant contributions from amplitude-to-phase conversion in our microstructure fiber-based detection setup for $\Delta\Phi_{CE}$. Hence, we do not unambiguously measure any added CEP noise intrinsic to the SC setup. To distinguish between intrinsic SC effects and amplitude-to-phase conversion, we introduce controlled beam pointing fluctuations $\Delta\alpha$ and again compare the phase noise introduced when passing through / bypassing the SC. Our measurements do not reveal any intrinsic effects of the SC system, but allow us to place an upper limit on the sensitivity of our SC system of $\Delta\Phi_{CEintrinsic,SC} < 13000$ rad/rad. Our results demonstrate experimentally that there is not a strong coupling mechanism between CEP and beam pointing through a stretcher/compressor , as well as measuring significantly smaller CEP fluctuations than experimental results reported previously.

2.3.1 Introduction

Chirped pulse amplification (CPA)[148] is the most widespread technique for amplification of fs pulses. In this scheme the pulse is stretched before amplification by introducing a positive chirp, and afterwards recompressed by compensating for the positive chirp introduced in the stretcher and gain material with an equally large negative chirp. Amplified CEP stabilized pulses were first produced using stretchers based on material dispersion followed by compression by prism compressors [7]. These systems reach pulse energies of ~ 3 millijoules, limited by the required amount of stretching and recompression [144].

These limitations could be overcome by CPA using grating based stretcher / compressor systems. Such systems however, have been predicted to have a more severe effect on CEP stability than material-based stretcher compressor systems, due to a stronger coupling of beam pointing fluctuations to CEP fluctuations [62].

In this work, we quantitatively investigate the effect of a grating based stretcher compressor setup on CEP stability. We employ two self-referencing setups [29] to detect the root mean square (rms) CEP fluctuations both in the oscillator stabilization loop ($\Delta\Phi_{CE}$) and out of loop ($\Delta\Phi_{CE}^{'}$), as shown in Fig. 2.5. The difference $\Delta\Phi_{CE,SC} := \Delta\Phi_{CE} - \Delta\Phi_{CE}^{'}$ is a direct measure of CEP fluctuations introduced outside

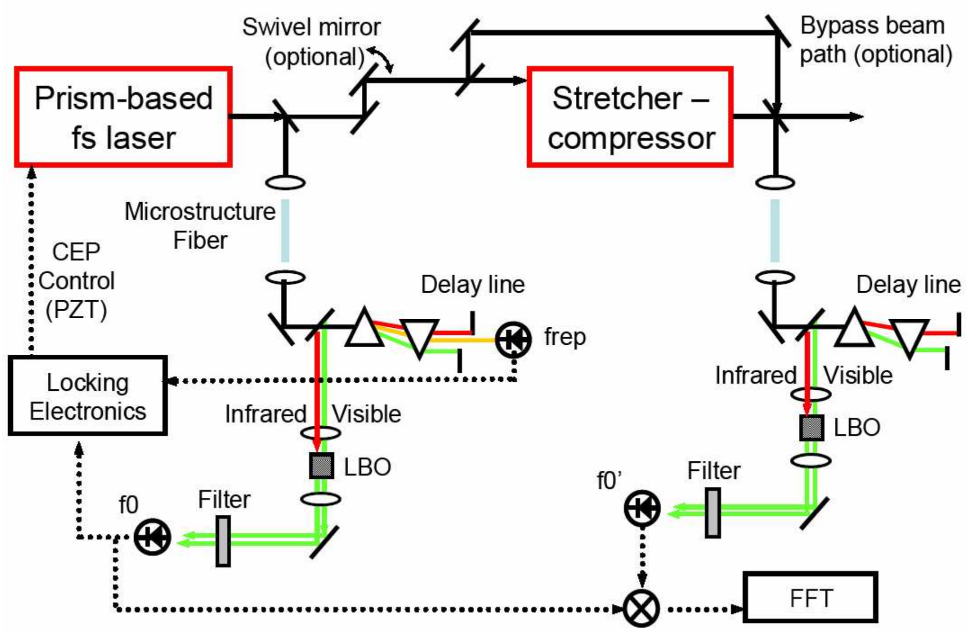

Figure 2.5: The setup consists of a prism-based fs laser coupled into a grating-based stretcher-compressor (SC). Two microstructure-based setups measure the offset frequency of the phase-locked laser spectra, after the oscillator (in-loop, f_0) and after the SC (out of loop, f_0'). These are converted into phase fluctuations using Eq. 2.6. The difference between CEP fluctuations introduced inside and outside the oscillator stabilization loop are measured by mixing $f_0 - f_0'$, and FFT analyzed. Optionally the beam bypasses the SC. A swivel mirror before the SC allows introduction of controlled beam pointing fluctuations.

the oscillator stabilization loop, in the beam path through the stretcher-compressor. We perform the measurement both with pulses that have passed the SC setup ($\Delta\Phi_{CE,SC}$), as well as with pulses that bypass the stretcher compressor ($\Delta\Phi_{CE,bypass}$). Our results, presented below, show quantitatively that the coupling between beam pointing and CEP introduced in our grating based SC setup is sufficiently small to enable phase stabilized amplification using a standard stretcher / compressor CPA system.

This work adds to recent results reported by Kakehata et al.[80] that show CEP stability of oscillator pulses can be retained after amplification to 3.5 mJ using a regenerative plus multipass amplifier system, together with a grating-based stretcher-compressor. Their measurement of CEP changes introduced by beam pointing fluctuations did not separate the effects of CEP fluctuations in the stretcher and compressor from additional CEP fluctuations in the regenerative amplifier and amplifier ring, as well as amplitude-to-phase conversion in the CEP detection setup (using a Krypton gas filled hollow fiber for spectral broadening). Furthermore, in that work it is difficult to distinguish between CEP changes and pulse timing fluctuations, due to the spectral interferometry technique that was used over a limited wavelength range.

Our measurements are based on a different CEP detection method that does not introduce an ambiguity between CEP changes and timing fluctuations. We also take into account amplitude-to-phase conversion in our CEP detection setup by comparing measurements of pulses propagating through, as well as bypassing, the SC setup. Our measurements therefore extend and clarify the results of Ref. [80]. Finally, we demonstrate experimentally that there is not a strong coupling mechanism between CEP and beam pointing through a stretcher/compressor, as well as measuring significantly smaller CEP fluctuations than experimental results reported previously.

2.3.2 Setup and measurement methods

Our setup is shown in Fig. 2.5. It consists of a CEP stabilized prism-based Ti:Sapphire oscillator producing pulses of $\sim$ 25 fs duration, with a repetition rate of $f_{rep} = 96$ MHz and a spectrum centered at 820 nm, with an average power of 850 mW. For CEP detection we use a self referencing setup using a 4.5 cm long air-silica microstructure fiber to broaden the spectrum to an octave. This setup allows direct measurement of the offset frequency f_0 of the modelocked spectrum. The offset frequency f_0 is related to the pulse-to-pulse CEP slip $\Delta\Phi_{CE}$ by

$$\frac{f_0}{f_{rep}} = \frac{\Delta\Phi_{CE}}{2\pi} \tag{2.6}$$

The repetition rate f_{rep} is detected on a separate photodiode. We stabilize $f_0/f_{rep} = p/q$ to 3/8. The ratio $p/q = 3/8$ ensures that every 8^{th} pulse experiences a $3 \cdot 2\pi$ phase slip and is therefore indistinguishable from the 1^{st} pulse. Practically, CEP stabilization is achieved using a piezoelectric tilt mirror, achieving a loop bandwidth around 10 kHz. The measured rms in-loop phase fluctuations are 400 milliradians (integrated from 63 mHz to 102 kHz).

Pulses from this oscillator are then sent through a grating based stretcher in a double pass configuration. It consists of a grating (1200 grooves/mm) and a curved imaging mirror of 406 mm focal length. The stretched pulse duration, at 220 picoseconds, is suitable for amplification up to Joule or higher pulse energy level [169]. Pulse recompression to $\sim$ 35 fs is achieved using a 1200 grooves/mm grating pair in double pass configuration.

Measurement of the offset frequency f_0' of the recompressed pulses is performed using a second self-referencing setup similar to the first one. From the measurement of f_0', the phase noise $\Delta\Phi_{CE}^{'}$ is determined from Eq. 2.6. In order to measure the fluctuations of CEP introduced outside the oscillator stabilization loop, i.e., $\Delta\Phi_{CE,SC} := \Delta\Phi_{CE} - \Delta\Phi_{CE}^{'}$, we mix the f_0 and f_0' photodiode signals to an output signal around DC. The mixer output voltage is $V_{mixer} \sim \cos(\Delta\Phi_{CE,SC} + \phi)$, where ϕ is an arbitrary phase offset. For suitable ϕ and small $\Delta\Phi_{CE,SC}$, $V_{mixer} \sim \Delta\Phi_{CE,SC}$ is proportional to the phase difference to be measured. We take care that the fluctuations $\Delta\Phi_{CE,SC}$ are not larger than $\pi/5$ so that the mixer output is a true representation of the phase noise $\Delta\Phi_{CE,SC}$. The signal is analyzed on an FFT signal analyzer (62.5 mHz to 102.4 kHz range). For each frequency range we take an average over four data sets. The FFT signal V_{rms}^2/Hz is converted to the CEP power spectral density (PSD) $\Delta\Phi_{CE,SC,rms}^2/Hz$ using the mixer output peak-to-peak voltage corresponding to $\Delta\Phi_{CE,SC} = \pi$.

The phase noise $\Delta\Phi_{CE,SC}$ is obtained from the power spectral density by integrating from the upper frequency f_u to the lower limit f_l of the FFT frequency range

$$\Delta\Phi_{CE,SC} = \sqrt{2\int_{f_u}^{f_l} \frac{\Delta\Phi_{CE,SC,rms}^2}{Hz} df} \tag{2.7}$$

2.3.3 Results and discussion

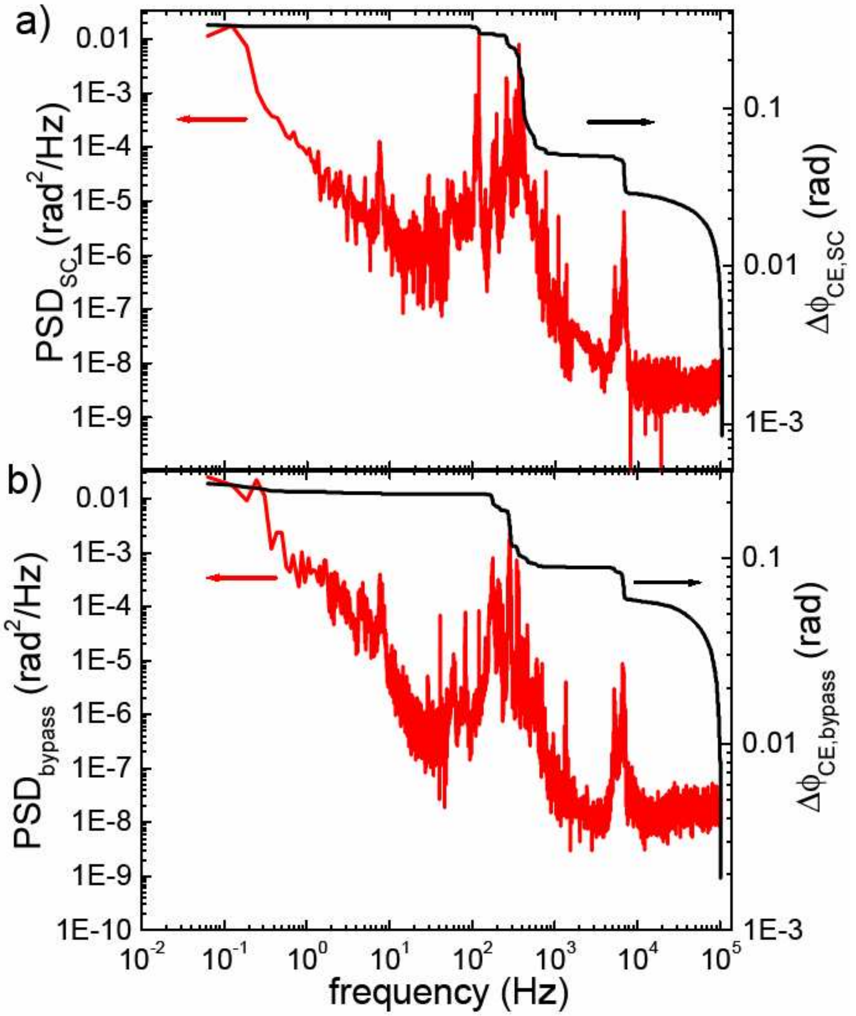

Figure 2.6: Comparison of CEP fluctuations a) passing through the SC, b) bypassing the SC. Red: power spectral density (PSD) $\Delta\Phi^2_{CE,SC,rms}/Hz$, Black: integrated CEP noise given by Eq. 2.7

Figure 2.6 (a) shows the measured power spectral density of phase fluctuations, $\frac{\Delta\Phi^2_{CE,SC,rms}}{Hz}$ (red curve), as well as the RMS phase fluctuations $\Delta\Phi_{CE,SC}$ (black curve) introduced when the pulses propagate through the stretcher compressor. The RMS phase fluctuations $\Delta\Phi_{CE,SC}$ are obtained from the PSD using Eq. 2.7. Figure 2.6 (b) shows the corresponding data measured when the pulses bypass the stretcher compressor.

For pulses passing through the stretcher compressor, we measure $\Delta\Phi_{CE,SC} = 340$ milliradians of CEP fluctuations, whereas we measure $\Delta\Phi_{CE,bypass} = 250$ milliradians for pulses bypassing the stretcher-compressor. Both values are dominated by the effects of mechanical resonances of optical components in the frequency range from 100 Hz to 600 Hz.

We expect that the CEP fluctuations $\Delta\Phi_{CE,bypass}$ of the bypassed beam would be dominated by nonlinear amplitude-to-phase conversion in the detection setup for $\Delta\Phi'_{CE}$ [46, 173]. The slightly larger value of $\Delta\Phi_{CE,SC} = 340$ millirad when passing through the stretcher-compressor, may either be caused by additional CEP fluctuations introduced by stretcher-compressor, but may also be due to slight differences in alignment, lock settings or differing optical mounts and beam paths. The close similarity of the values $\Delta\Phi_{CE,SC}$ and $\Delta\Phi_{CE,bypass}$ therefore does not permit a precise determination of effects intrinsic to the stretcher-compressor. We have measured the RMS beam pointing fluctuations of the laser beam into the SC setup to be $\Delta\alpha_{rms} < 0.1$ microradians, assuming the beam fluctuations to originate from the oscillator Ti:sapphire crystal. We note that this allows us to only set a relatively large upper bound of beam pointing sensitivity of the SC setup, $\Delta\Phi_{CE,SC}/\Delta\alpha_{rms} < 3.4\,10^6 rad/rad$, likely dominated by effects not intrinsic to the SC.

In order to obtain a clearer signature of CEP effects occurring in the stretcher-compressor setup, we artificially introduce a beam pointing oscillation of controlled amplitude. We use a swivel mirror in front of the stretcher compressor, at a distance of 90 cm to the first grating. We again analyze the introduced phase fluctuations $\Delta\Phi_{CE,SC}$ on a FFT signal analyzer. In this way we can separate the spectral component at the swivel frequency 50 Hz from all other CEP fluctuations.

As the beam pointing oscillations inevitably cause amplitude to phase coupling in the second self-referencing setup, we have performed the measurement both for a beam propagating through the SC, and for a beam bypassing it with a similar path length to the second microstructure fiber.

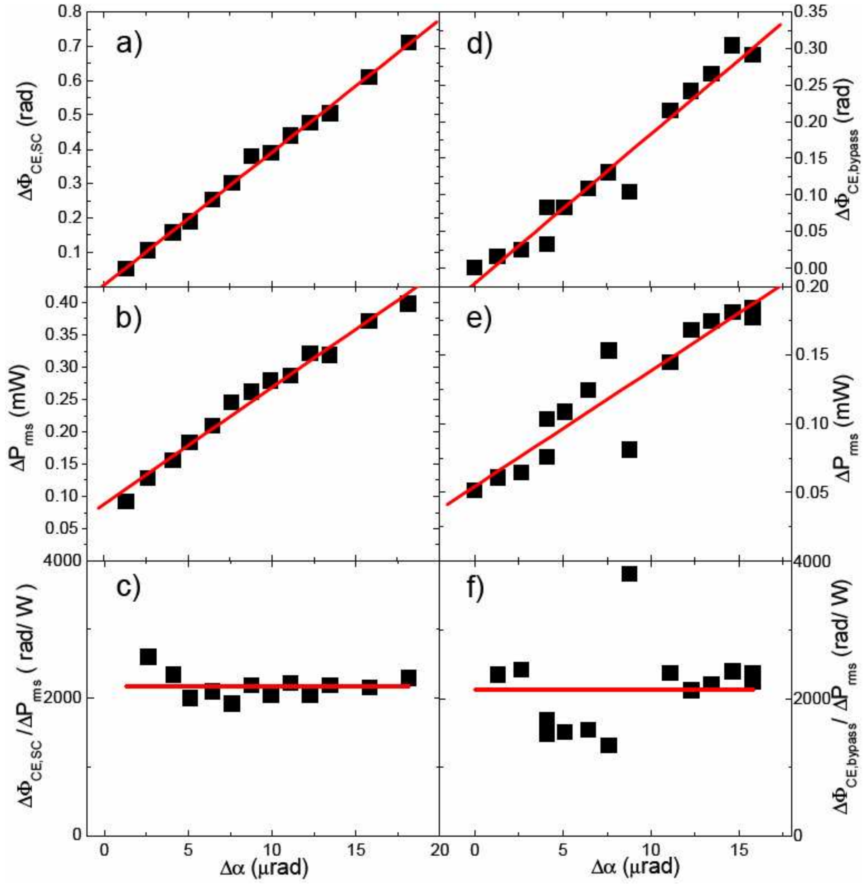

Figure 2.7: Measurements of carrier-envelope phase-fluctuations $\Delta\Phi_{CE}$, power fluctuations ΔP_{rms} and the ratio of both, when beam pointing fluctuations $\Delta\alpha$ are introduced.(a-c): data for stretcher-compressor, (d-f): data for bypassing beam.

Figure 2.7 shows the results of this measurement through the stretcher compressor. Fig. 2.7(a) shows the measured CE phase fluctuations $\Delta\Phi_{CE,SC}$ vs. the beam pointing angle $\Delta\alpha$, defined as the peak-to-peak angle of beam deviations. The data show a clear linear dependence with a slope of $\Delta\Phi_{CE,SC}/\Delta\alpha = 3.9(\pm 0.1)\, 10^4 rad/rad$. As we show, below this value is dominated by amplitude-to-phase coupling in the second self-referencing setup. The beam pointing angle is typically limited to $\Delta\alpha \sim 17$ microradians in order to keep fluctuations $\Delta\Phi_{CE}$ smaller $\sim \pi/5$. In Fig. 2.7(b) we plot the simultaneously measured rms power fluctuations $\Delta P_{rms} = \Delta P_{pp}/(2\sqrt{2})$,where

ΔP_{pp} are the peak-to-peak power fluctuations detected after the second microstructured fiber. Figure 2.7(c) shows $\Delta\Phi_{CE,SC}/\Delta P_{rms}$, where only the power fluctuations due to swiveling are used, i.e., the offset of the linear fit of ΔP_{rms} vs. $\Delta\alpha$ has been subtracted from ΔP_{rms} (this offset results from steady-state beam fluctuations not related to the artificially-induced swiveling). We obtain a value of $\Delta\Phi_{CE,SC}/\Delta P_{rms} = 2170 \pm 180$ rad/W, where the error is the standard deviation of the data points.

The data bypassing the stretcher-compressor are shown in Figs. 2.7(d)-(f). Again a linear dependence of ΔP_{rms} and $\Delta\Phi_{CE,bypass}$ on $\Delta\alpha$ is seen, and again we take the ratio $\Delta\Phi_{CE,bypass}/\Delta P_{rms}$. We expect this value to be equal to the amplitude-to-phase conversion coefficient Cap, and obtain $\Delta\Phi_{CE,bypass}/\Delta P_{rms} = 2130 \pm 630 rad/W$, in approximate agreement with Refs. [46, 173].

Comparing our data obtained by going through the SC and bypassing it, we see that the ratio $\Delta\Phi_{CE}/\Delta P_{rms}$ is identical in both measurements, and we conclude that intrinsic fluctuations due to the SC are not contributing significantly to $\Delta\Phi_{CE,SC}$. From our data, we can place an upper limit on the intrinsic CE phase fluctuations introduced by the stretcher compressor $\Delta\Phi_{CEintrinsic,SC}/\Delta\alpha < 13000 rad/rad$.

We obtain this value by taking the difference

$$\Delta\Phi_{CEintrinsic,SC}/\Delta P_{rms} = \Delta\Phi_{CE,SC}/\Delta P_{rms} - \Delta\Phi_{CE,bypass}/\Delta P_{rms} = 40 \pm 660 rad/W \tag{2.8}$$

We convert to $\Delta\Phi_{CEintrinsic,SC}/\Delta\alpha$ by writing

$$\Delta\Phi_{CEintrinsic,SC}/\Delta\alpha = \Delta\Phi_{CEintrinsic,SC}/\Delta P_{rms} \cdot \Delta P_{rms}/\Delta\alpha \tag{2.9}$$

and take $\Delta P_{rms}/\Delta\alpha = 18.0(+/-0.7)W/rad$ from the slope in Fig. 2.7. This yields $\Delta\Phi_{CEintrinsic,SC}/\Delta\alpha = 740 \pm 12000 rad/rad$, i.e. $< 13000 rad/rad$.

Comparing this to [80] we find our upper limit for the intrinsic CE phase fluctuations introduced by the stretcher compressor to be 2.3 times smaller. The difference is likely due to amplitude-to-phase noise conversion in the hollow fiber and some ambiguity due to contributions from delay changes in the spectral interferometry setup. Contributions due to the amplification process itself are common to all configurations of CPA systems, and have proven to be sufficiently small as to not preclude CEP stabilization [7, 80].

2.3.4 Conclusions regarding grating-based stretcher compressor systems

We have carefully measured CEP fluctuations introduced by grating-based stretcher compressor systems for amplifiers using a standard design of chirped pulse amplification. From our error analysis, we find a very small upper limit on $\Delta\Phi_{CEintrinsic,SC}/\Delta\alpha = 13000 rad/rad$ for our set-up. From our measured steady-state beam pointing fluctuations of $\Delta\alpha_{rms} < 0.1\mu rad$, we would expect intrinsic CEP fluctuations $\Delta\Phi_{CEintrinsic,SC} <$ 3.6 milliradians. Our results confirm and improve upon the conclusion of Kakehata [80] that grating based CPA systems are not a severely limiting factor for amplification of high power CEP stabilized pulses. Since our measured noise is $> 2\times$ smaller than past results, there is considerable future room for improvement. Finally, we also verified experimentally for the first time that there is no severe coupling mechanism between beam pointing in a stretcher/compressor and the CEP.

2.4 Long-term carrier-envelope phase stability from a grating-based, chirped pulse amplifier

Having demonstrated that a grating-based stretcher and compressor do not introduce significant obstacles to CEP stabilization, we now demonstrate a carrier-envelope phase (CEP) stabilized, cryogenically cooled chirped pulse laser amplifier that exhibits greatly improved intrinsic long-term CEP stability compared with that of other amplifiers. Single-shot carrier envelope phase noise measurements are also presented that avoid underestimation of this parameter caused by fringe averaging and represent a rigorously accurate upper limit on CEP noise.

2.4.1 Electronics for CEP stabilized amplifier

Here I briefly describe the electronics that provide a train of CEP-identical seed pulses to the amplifier. The setup is shown in Figure 2.8. The setting $f_0/f_{rep} = 3/8$ chosen in section 2.2 for the oscillator offset frequency means that the n'th pulse in the oscillator train has a CEP slip of $n \cdot 2\pi \cdot 3/8$. In order to provide a train of CEP-identical pulses, the "femtosecond synchronizer" was modified to provide an output at $f_{rep}/8$ synchronized with CEP-identical oscillator pulses. This signal, instead of the conventionally used f_{rep} signal is fed into the "KM board" which picks a suitable integer N and divides the input frequency down to the desired amplifier repetition rate $f_{rep,amp} = f_{rep}/(8N) \sim 1kHz$. The output of the KM board is sent to a delay generator (Stanford research systems DG535) which triggers both the amplifier pump laser and the Pockels cell that selects seed pulses for the amplifier. This setup ensures that only identical pulses can be picked as seed pulses.

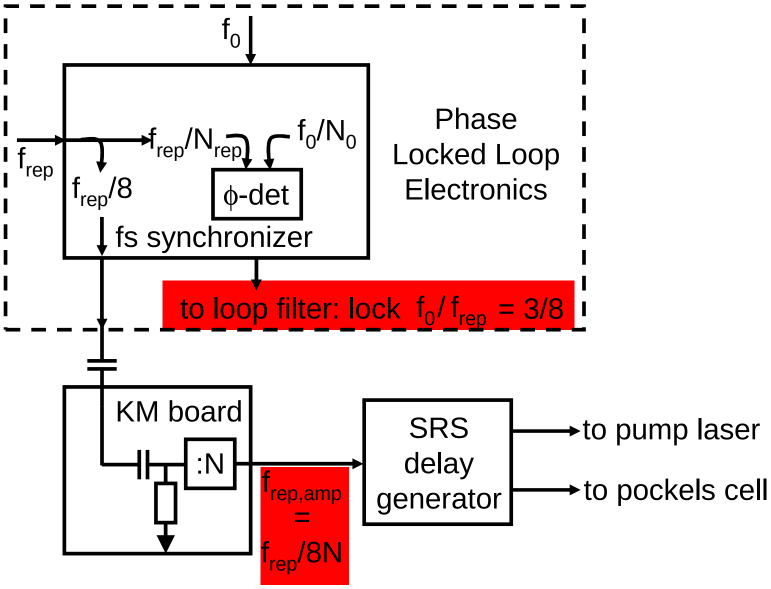

Figure 2.8: Electronics that provide a train of CEP-identical seed pulses to the amplifier. The fs synchronizer is modified to provide a signal at $f_{rep}/8$. This signal, which is synchronized with a subset of CEP-identical oscillator pulses, is divided down to provide the amplifier repetition rate $\sim 1kHz$, and is sent to the Pockels cell and amplifier pump laser.

2.4.2 Measurements and results

Whereas the carrier-envelope phase (CEP) stabilization of femtosecond Ti:sapphire oscillators is now a well-established technology [76, 174, 77], stabilization of laser amplifiers is new, and the technology is still under development. The appeal of high-power stabilized lasers is that they make possible many interesting strong field experiments [134, 31, 32]. Two designs have been demonstrated to date: Baltuska et al.[8] demonstrated a chirped pulse amplifier system[148] that uses material to stretch the pulse and prisms to compress it, while Kakehata et al.[80] showed preliminary work on a grating-based chirped pulse amplifier system. In principle, grating-based amplifier systems can be scaled to much higher output energies than can material- and prism-based systems; therefore it is important to address questions regarding their long-term stability. In previous work[157] in which only a laser oscillator was used, we showed that properly aligned grating-based stretcher compressor pairs do not destroy CEP coherence.

In this work we demonstrate, for the first time to our knowledge, a CEP stabilized amplifier system that exhibits excellent intrinsic long-term coherence, i.e., with coherence time scales of the order of tens of minutes. The shot-to-shot rms phase jitter of pulses from the system is 650 mrad in 0.5 s and appears to be limited primarily by the oscillators CEP lock stability. The slow drift of the CEP can be tracked over long time intervals $>$ 30 min. These results represent an order-of-magnitude improvement for long-term stability and shot-to-shot fluctuations over those reported previously for grating-based amplifier systems. Moreover, the measurements presented here represent to our knowledge the first true shot-to-shot reported characterization of carrier-envelope offset phase from a chirped pulse amplifier system. Previous measurements of carrier-envelope offset from both grating- [80] and material-based [8] systems presented data averaged over 16 30 shots, averaging out nearly all the actual CEP noise. In contrast, we present single-shot measurements, which yield accurate high-frequency phase noise estimates while also demonstrating a long coherence time. This amplifier design presents no barriers to scaling to much higher output energies. Finally, we note that the excellent long-term intrinsic CEP stability demonstrated here obviates the need for a slow feedback on the amplifier system in many situations while avoiding noise that could be introduced in additional feedback systems. Methods used for CEP detection were reported previously [127, 44, 79] and can be implemented by use of either the time- or the frequency-domain setups. Time-domain phase detection and stabilization, used with high repetition rate oscillators, are achieved by beating together two frequency components of an octave-spanning laser pulse. One component is centered at 2f, while the other is the second-harmonic signal of the component centered at f. The time delay between the two beams is set to near zero, and the signal is detected by a photodiode. The signal is

$$S(t) = E_f^2(t) + E_{2f}^2(t) + 2[E_f^2(t)E_{2f}^2(t)]^{1/2}cos[2\phi_f(t) - \phi_{2f}(t) + \phi_0] \tag{2.10}$$

where $\phi_f(t) = n\,f_{rep} + f_0$ and ϕ_0 is the absolute carrier-envelope phase. The offset frequency, f_0, may then be determined from

$$f_0 = \Delta\phi_0 f_{rep}/(2\pi) \tag{2.11}$$

where f_{rep} is the repetition frequency and $\Delta\phi_0$ is the slip in CEP from shot to shot. If the ratio of f_0 to f_{rep} is locked, the pulse-to-pulse CEP slip is fixed.

In frequency-domain detection, which is appropriate for a lower repetition rate pulse train from a laser amplifier, a spectrometer is used to measure the phase by introducing a time delay between the f and 2f beams. The signal is then given by

$$\tilde{S}(\omega) = E_f^2(\omega) + E_{2f}^2(\omega) + 2[\tilde{E}_f^2(\omega)\tilde{E}_{2f}^2(\omega)]^{1/2}cos[2\tilde{\phi}_f(\omega) - \tilde{\phi}_{2f}(\omega) + \phi_0] \tag{2.12}$$

This signal produces an interference fringe pattern. Shifts in the fringe pattern mirror changes in the CEP.

In our experiment, the front end of the laser system consists of a stabilized, prism-based laser oscillator incorporating a piezoactuator-controlled end mirror (see Fig. 2.9). The oscillator output has an average power of approximately 750 mW at 98 MHz. Part of the oscillator beam is used to derive a signal to phase lock the oscillator. When the CEP slip is locked, the out-of-loop rms CEP noise of our oscillator is ≈ 500 mrad for 16 s integration time, under conditions of minimal acoustic noise.

Most of the oscillator energy is used to seed the amplifier system. Timing for the pump laser and a Pockels cell is derived from the offset frequency, f_0 (see Figure 2.8), rather than the repetition rate, f_{rep}, to ensure that a pulse with the same CEP is always injected into the amplifier. A Faraday isolator is also inserted, to prevent optical feedback into the oscillator. The cryogenically cooled amplifier cell is pumped by a diode-pumped YAG laser (Coherent Corona), delivering 14 W of power at 1 kHz, with a power stability better than 1% rms. The output of the amplifier system is 1.4 mJ at a repetition rate of 1 kHz, with a FWHM pulse duration below 35 fs and an rms power stability of 0.8 - 1.2 %.

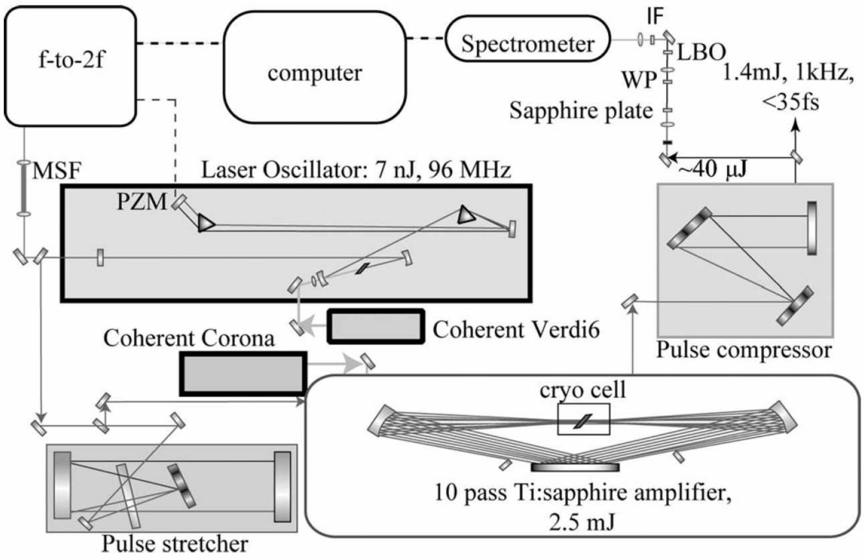

Figure 2.9: Schematic of the CEP stabilized laser amplifier system: MSF, microstructured fiber; PZM, piezoactuated mirror; WP, wave plate; IF, interference filter.

Part of the amplifier output (4%) is used for phase detection (using spectral interferometry, see Figure 2.10) [79]. Frequency-domain detection of the CEP of the high-energy pulse is done by focusing part of the output beam into a 5 mm thick sapphire plate to generate a white-light continuum. A 10 mm lithium triborate (LBO) crystal is then used for doubling the IR component, and the interference signal between the doubled IR and the short wavelength part of the continuum is detected with a high-resolution spectrometer after the wave has passed through an interference filter. The spectrometer s integration time can be varied from 1 ms to 10 s, allowing for single-shot detection at 1 kHz.

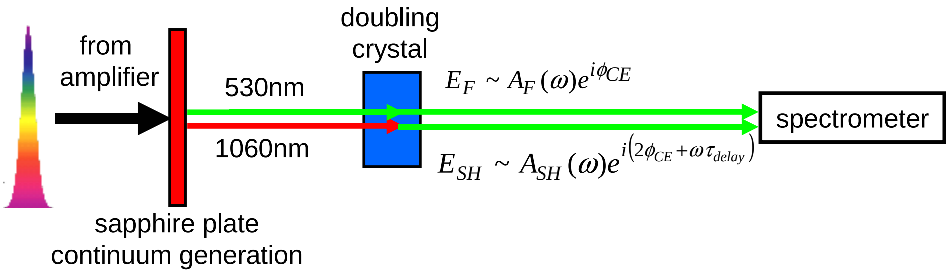

Figure 2.10: Spectral interferometry for the measurement of amplifier carrier-envelope phase fluctuations.

For the following measurements, the detected values of rms CEP noise provide an upper limit, since they include both system and detection noise. Power fluctuations of the amplifier will introduce CEP fluctuations through the self-phase modulation that occurs in the sapphire plate used to broaden the spectrum. Interferometric instabilities will also result in added CEP fluctuations.

Figure 2.11 (top) shows the interference fringes' visibility in the cases when the oscillator was CEP locked and unlocked versus integration time. Figure 2.11 (bottom) shows the corresponding rms CEP noise in the case when the oscillator was CEP locked. The fringe visibility for longer integration times was normalized to single-shot visibility. In these measurements, no active feedback from the output of the amplifier was

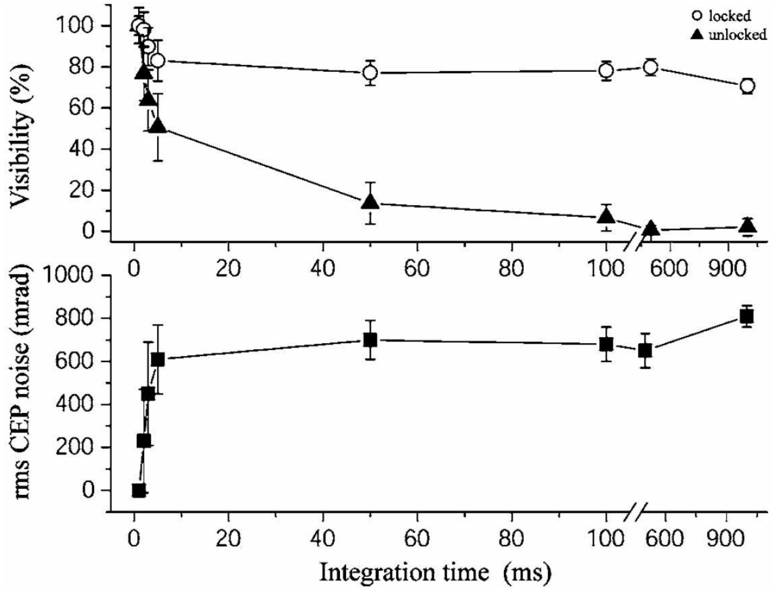

Figure 2.11: Top, fringe visibility versus integration time of the detector for locked and unlocked oscillators. Bottom, accumulated rms CEP noise corresponding to a CEP-locked oscillator.

implemented. Fringe visibility in the unlocked case drops rapidly. In the locked case, after an initial decrease of 1 to 5 ms integration time, it remains constant for as long as 500 ms. Thus most of the phase noise arises from frequencies greater than $\approx$ 200 Hz. The data for 1 s integration time show a modest loss in visibility. However, it should be noted that noise from the detector (power-fluctuation induced CEP noise plus electronic noise) becomes important at such a long integration time.

Next, the phase was monitored over long periods of time. Figure 2.12 (top) shows the evolution of the phase-dependent interference fringes measured for more than 30 min. For a single shot, the inter-fringe distance corresponds to a 2π shift. Each point represents an integration time of 1 ms and was collected at 2 Hz. As was the case for the visibility measurement, the data were collected without active feedback on the amplifier output. Figure 2.12 (bottom) shows the results of using the computer that measures the CEP to supply a sinusoidal voltage signal with a period of $\sim$ 40 s to the oscillator locking electronics. This sinusoidal voltage is added to the error signal by an adder

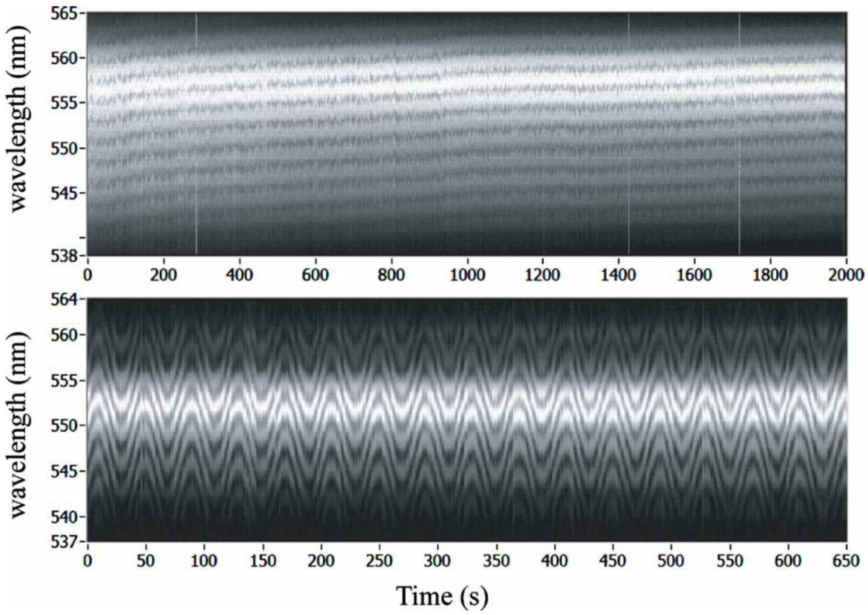

Figure 2.12: Evolution of the fringe pattern derived from the output of the amplifier as a function of time, when (top) the oscillator is phase locked and when (bottom) a sinusoidal voltage is applied to the oscillator locking electronics. This voltage is added to the error signal by an adder electronics box.

electronics box, amplified and sent to the piezo-actuated tilt mirror inside the oscillator. Such a time-domain modulation of the CEP can be used in conjunction with lock-in analysis techniques, with no further long-term stabilization of the CEP. The absence of active feedback in the amplifier simplifies the design considerably without significantly limiting usefulness. It also ensures that no additional noise from the amplifier CEP retrieval algorithm is introduced into the system.

It was also noted during these experiments that long-term stability of the CEP is correlated to the signal-to-noise ratio of the f-to-2f beat note used to stabilize the oscillator. As coupling into the microstructured fiber drifted, the amplifier CEP drifted. This correlation can be seen in Figure 2.13.

Active stabilization of this parameter might thus result in an improvement in long-term CEP stability. We investigated several explanations for the excellent long-term stability of our system compared with previous results. Great care was taken to stabilize

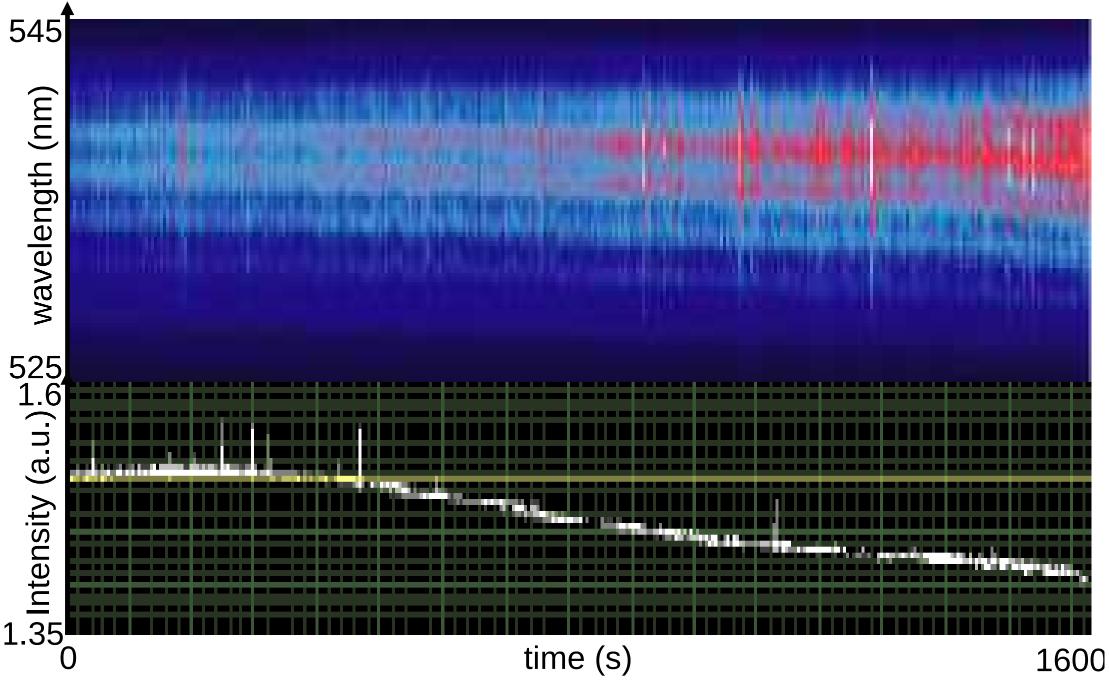

Figure 2.13: Correlation between intensity drop of the beat note from the microstructure fiber used in the oscillator feedback loop and drift of the spectral interference fringes recorded after the amplifier. The intensity drop in the beat note leads to a deterioration of the feedback loop performance.

the pump laser's power output beyond the manufacturer's specifications, and a rms noise of less than 1% was achieved. However, we believe that the main cause of excellent long-term stability is cryogenic cooling of the Ti:sapphire crystal [5], which is unique to this system. It is known that cryogenic cooling reduces thermal lensing (by > 2 orders of magnitude over room temperature) and allows for higher average power. Calculations were made to compare the CEP slip in sapphire at different temperatures that were due to pump power fluctuations [159]. While the effects were an order of magnitude bigger at room temperature than at cryogenic temperature, they were overall 12 orders of magnitude too small to produce a significant change in the CEP. We believe that the more important effect of cryogenic cooling is the reduction of beam pointing fluctuations out of amplifier crystal. As thermal beam pointing drifts can lead to substantial CEP changes in a misaligned compressor, the reduction of this effect could be an explanation for the good long-term stability of our amplifier.

In conclusion, we have presented what is to our knowledge the first demonstration of a CEP stabilized, grating-based amplifier system with excellent intrinsic long-term coherence. The remaining slow drift of the CEP can be easily monitored. We have also reported the first CEP noise measurements for a grating-based chirped-pulse amplification system that includes single-shot measurements as required for accurate estimation of this noise. Finally, we demonstrated an ability to control and modulate the CEP of the amplified pulse. The use of a grating-based stretcher and compressor also allows for scaling to much higher output energies.

Since our work, the CEP stabilization of grating based amplifiers has continued to progress: A slow feedback control of the CEP of a grating-based amplifier was demonstrated, by adjusting the effective distance of the gratings in the stretcher of the amplifier [94]. A CEP stabilized amplifier with improved stability, using a grating-based stretcher-compressor system is now commercially available (KMLabs).

Chapter 3

Generation and temporal characterization of attosecond pulses

This chapter contains materials published in [154] and [152]. In this chapter I present the first temporal characterization of extreme ultraviolet radiation generated in a noble gas-filled hollow-core waveguide. In particular I concentrate on two regimes of EUV radiation which both generate pulse durations in the sub-optical-cycle regime (i.e. radiation shorter than one optical cycle of the driving NIR pulses, which corresponds to 2.66 fs for a center wavelength of 800 nm). In the first regime I describe, we generated and characterized pulses with an envelope of 1.4 femtoseconds, comprised of one or two attosecond pulses - each shorter than 500 attoseconds. This first regime, in addition to its short duration, has the advantage over other sub-optical cycle EUV radiation demonstrated so far, that its energy is spectrally confined to a width of $\sim 1eV$, and therefore can be used without the need for further spectral filtering by lossy EUV optics. This radiation is in addition easily spectrally tunable by adjusting the pressure and intensity in the waveguide. This makes this radiation particularly useful as a pump or probe pulse in experiments that require state-selectivity. In the second regime we investigated, we could show that primarily single isolated attosecond pulses of 200 attosecond duration can be generated using NIR driving pulses of 15 femtosecond duration coupled into a hollow-core waveguide filled with low-pressure Argon gas. Again the driving pulses were not CEP stabilized. These driving pulses are thus significantly longer than shown in previous work – so far the longest NIR driving pulses that showed evidence for the generation of single attosecond pulses of 650 ± 150 attosecond duration were 7.5 fs long [63]. In both regimes we investigated, we thus combined experimental measurements with careful numerical analysis, to demonstrate that even relatively long-duration, $13-15$ fs, carrier-envelope-phase (CEP) unstabilized near-infrared (NIR) pulses can generate extreme-ultraviolet (EUV) radiation confined to sub-optical cycle duration by the dynamically-changing phase matching conditions in a hollow-core waveguide geometry.

The measurements were made using the laser-assisted photoelectric effect to cross-correlate the EUV pulse with the NIR pulse. A FROG CRAB analysis of the resulting traces (photoelectron signal versus photoelectron energy and EUV-NIR delay) was performed using a generalized projections (GP) algorithm, adapted for a wide-angle photoelectron detection geometry and non-CEP stabilized driving laser pulses. In addition, we performed direct FROG CRAB simulations under the same conditions. Such direct simulations allow more freedom to explore the effect of specific pulse parameters on FROG CRAB traces than is possible using the automated GP retrieval algorithm.

3.1 Introduction

To date, sub-femtosecond light pulses have been generated only through the process of high-order harmonic generation (HHG). By the uncertainty principle, sub-femtosecond light pulses require a bandwidth larger than 10^{15}Hz, which is larger than the entire visible range of the spectrum. In HHG an intense ultrashort laser pulse is focused into a gas. The interaction between the atoms and laser field is so strong that a portion of the electron wave packet can escape the atom due to the lowering of the Coulomb potential by the laser electric field. The electron wave packet is then accelerated by the laser electric field, and forced back towards the atom as the sign of the field reverses. The returning electron wave packet can, with a certain probability, recombine with the ion and emit higher harmonics of the fundamental laser frequency [87, 93, 26]. This high-order harmonic upconversion of intense femtosecond laser light results in a tabletop-scale source of coherent light in the extreme ultraviolet (EUV) region of the spectrum. This light source has produced the shortest light pulses measured to-date, making it ideal for observing *electron dynamics* in atoms, molecules and condensed systems on femtosecond (fs= 10^{-15} s) or attosecond (as= 10^{-18} s) timescales. Simple pump/probe geometries are being developed, in analogy to the well-established pump/probe techniques using visible and NIR femtosecond pulses for the study of *nuclear dynamics*.

To date, considerable effort has been devoted to generating isolated attosecond EUV pulses using very short, 5 fs, carrier-envelope-phase stabilized driving laser pulses [141]. Such ultrashort laser pulses need meticulous dispersion control over a large frequency bandwidth, and are challenging to propagate through even one meter of air (which will broaden a 5 fs pulse to 12 fs). Moreover, the EUV spectrum that supports an isolated attosecond pulse consists of a broad continuum. However, many experiments in ultrafast molecular and materials spectroscopy require EUV pulses slightly longer in duration, in the range of ~ 1 fs. This is because such pulses can have a sufficiently narrow spectral bandwidth to either initiate or probe the femtosecond dynamics of specific electronic excited states with reasonable spectroscopic resolution (~ 1 eV). Good spectroscopic resolution is required for obtaining initial-state-specific photoelectron spectra in the typically congested EUV spectra of molecules, molecular clusters, or solids [61, 51, 41, 181, 129, 130, 37]. Therefore, the generation and characterization of sub-optical-cycle EUV pulses with narrow spectral bandwidth is a topic of great interest that has remained unexplored to date.

Not only the generation, but also the characterization of sub-optical-cycle EUV waveforms is challenging. Nearly all current EUV pulse characterization techniques rely on two-color photoionization, in which an atom is simultaneously irradiated with EUV and near-infrared (NIR) laser fields and the energy of the resultant electrons is monitored as a function of the time delay between the laser and EUV fields. In the case of relatively long EUV pulses (> 10 fs), the EUV pulse duration can be deconvolved from the cross correlation measurement provided that the laser pulse duration is accurately characterized. However, in order to extract the pulse duration of a sub-optical cycle EUV field from a cross-correlation measurement, both the laser pulse and the cross-correlation between the EUV and laser fields would need to be measured to an accuracy better than ~ 0.05 fs (which is not feasible). The RABBITT (Reconstruction of Attosecond Beating by Interference of Two-photon Transitions) technique [117] can be used to determine the temporal structure of the individual attosecond bursts - but not the overall envelope. Alternatively, the FROGCRAB (Frequency-Resolved Optical Gating for Complete Reconstruction of Attosecond Bursts) technique [101, 124] has recently been introduced, which in theory allows for reliable deconvolution of an EUV waveform of any duration. However, this measurement technique has to-date been applied only to the case of a single isolated EUV burst of 130 as duration [141], where the isolated nature of the EUV burst considerably simplifies the pulse shape extraction.

Applications of attosecond pulses are only beginning to emerge. Noteworthy examples include an experiment in which an attosecond pump pulse (~ 250 attosecond pulse centered around 90 eV) was used in conjunction with a NIR probe pulse and the Ne^{2+} yield revealed ionization steps on the order of half a driving laser cycle [166]. Another notion of things to come in the future [18] shows that attosecond pulses can also be used in condensed matter systems: Here, an EUV isolated attosecond pump pulse and a NIR femtosecond probe pulse were used to determine a 100 attosecond delay between the emission of photoelectrons from localized core states and from the conduction band.

It should be noted here, that manipulation of electron dynamics on the attosecond time scale does not *require* the use of isolated attosecond pulses (or the use of attosecond pulse trains). Pulse shaping techniques of intense NIR femtosecond pulses can be used to manipulate electron trajectories in the continuum with a precision of 25 attoseconds.

The interference of these electron trajectories in the continuum can lead to a useful outcome such as control over the shape of the produced high order harmonics [11, 21]. Another example is the excitation of correlated nuclear and electronic wave packets in the strong-field ionization of D_2. As for high harmonic generation, the electron returns to the nucleus. Instead of recombining and emitting a photon, it inelastically scatters, leading to the dissociation to $D^+ + D$. The experiment is repeated using several fundamental laser periods, thus changing the recollision time. From the measured energies of the D^+ fragment, the motion of the nuclear wave packet on the D_2^+ $X\Sigma_g$ potential curve can be tracked with $\sim$ 200 attosecond resolution [111].

3.2 Attosecond pulse generation methods

To-date, *single, isolated* attosecond pulses have been generated only using very short-duration, 5-7 fs driving laser pulses. Using these very short-duration laser pulses [22, 58] the cycle-by-cycle electric field of the laser pulse changes significantly. The highest energy EUV radiation is then generated exclusively by the strongest half-cycle (provided the CEP is adjusted appropriately). In this case the discrete harmonic structure disappears at the highest energies and the spectrum broadens into a continuum. Spectrally filtering to allow only the highest energy harmonic light to pass can then produce a single isolated attosecond pulse. This method requires a very short, intense femtosecond pulse to create the amount of continuum bandwidth required for an attosecond pulse in the strongest half cycle alone (as a rule of thumb a 200 attosecond pulse requires a FWHM bandwidth of 9 eV assuming a Gaussian spectral shape). The proposal by Christov et al. [22] showed that 5-fs pulses are required, and indeed isolated pulses of few hundreds of attosecond duration have been experimentally demonstrated. The current record is 80 attoseconds while writing this thesis [58].

A variation of this method adds a rapidly changing ellipticity to the driving laser pulse [141, 20, 25]. The efficiency of high harmonic generation is strong only for linearly polarized driving lasers, and falls strongly with ellipticity. In this scheme only a single half-cycle occurs which has linear polarization and therefore allows generation of high harmonics, whereas the elliptical polarization suppresses HHG in all other half-cycles. This ellipticity scheme was the first proposal to generate isolated attosecond pulses [25], based on earlier suggestions of the attosecond pulse structure of high-harmonic generation [43, 59]. The original proposal suggested that driving pulses of 25 fs duration could be used to generate subfemtosecond pulses. The use of 25 fs driving pulses has proven to be over-optimistic; nevertheless, polarization modulation of a sub-10 fs driving pulse can broaden the region of the spectrum over which a continuum is generated, and thus helps to generate shorter-duration pulses.

Experimentally, all implementations of attosecond pulses to-date have used carrier-envelope phase (CEP) stabilized driving pulses of 5 fs duration, with the exception of some earlier experimental results that showed evidence for the generation of single attosecond pulses of 650 ± 150 as duration using 7.5 fs long driving laser pulses [63]. In detailed theoretical studies [48] the reason for generating a single isolated attosecond pulse using such long driving pulses was explained by "ionization driven spatio-temporal reshaping of the intense driving pulse as it propagates through a long, relatively dense medium leads to XUV radiation which, after spatial and spectral filtering in the far field, yields an isolated attosecond pulse".

As CEP stabilized 5 fs pulses are difficult to work with, there is great interest in generating isolated single attosecond pulses using longer driving pulses e.g. by employing two-color laser driving fields, ionization gating, quasi-phase-matching or long-wavelength driving lasers [102, 104, 122, 17, 23, 49]. So far, these have been theoretical suggestions or spectral measurements, but with no temporal characterization of the emission generated in these longer-duration driving pulse regimes to date.

3.3 Attosecond pulse measurements

Characterizing the time structure of either attosecond pulse trains [98, 100] or isolated attosecond pulses [141, 58] is equally important and technically challenging to the generation process. There are several reasons for this. First, the generated radiation lies in the extreme ultraviolet (EUV) region and therefore is strongly absorbed in air or any material. As a consequence, experiments must be conducted inside a vacuum chamber. Second, as high harmonic generation is a highly nonlinear process, the EUV photon flux is typically low ($\approx 10^9$ photons/pulse at 45 eV). For these reasons, instantaneous nonlinear effects that are commonly used in the visible region are difficult to access in the EUV regime. Therefore nearly [143, 110] all current EUV pulse characterization techniques rely on two-color photoionization, in which an atom is simultaneously irradiated with EUV and near-infrared (NIR) laser fields, and the energy of the resultant electrons is monitored as a function of the time delay between the laser and EUV fields [142, 56]. Here the EUV radiation creates one or several electron wavepackets by single photon photoionization. These wavepackets are then modulated by the electric field of the NIR laser field, leading to sidebands or shifts in the resulting photoelectron spectra (see below). The resulting spectrogram as a function of delay τ and photoelectron energy ω encodes information about the temporal structure of the EUV pulse.

To extract the temporal structure of the attosecond fields from the spectrogram, different methods have been proposed and some of them have been experimentally implemented [117, 73, 27]. For isolated attosecond pulses that are significantly shorter than the driving laser field, the “attosecond streak camera” technique has been used [73]. To reconstruct individual attosecond bursts of long attosecond pulse trains consisting of identical attosecond pulses, the “RABBITT” (Reconstruction of Attosecond Beating By Interference of Two-photon Transitions) technique has been employed. As originally proposed, RABBITT used the sideband structure to extract the relative phase between harmonic orders, which relates directly to an averaged attosecond pulse structure. However it did not attempt to obtain information on the pulse envelope, e.g. through analysis of the detailed shape of the sidebands versus energy and delay. A more generally applicable method is the FROG-CRAB (Frequency Resolved Optical Gating for Complete Reconstruction of Attosecond Bursts) technique. This technique was theoretically proposed in [101, 124] and can in theory characterize attosecond fields of arbitrarily complex temporal structure. We chose this method to characterize recent experimental data [154] because they were exactly in the transition regime between an isolated single attosecond pulse and a train of attosecond pulses. That work demonstrated that, by using pulses of ~ 13 fs duration in a phase-matched hollow-waveguide geometry, EUV pulses with envelope duration of 1.4 fs and individual pulse structure of < 500 as could be generated. This corresponds to an attosecond pulse "train" that could contain $\sim 80\%$ of its energy in a single burst, or consist of two equally strong bursts – the FROG CRAB measurement technique could only determine a pulse envelope and the structure of the individual attosecond bursts (but not their position) in this case of a non-CEP stabilized laser.

Despite all the efforts in characterizing experimental attosecond pulses, there are still unresolved issues in using attosecond pulse retrieval algorithms. Even the most current approaches fail to recover certain pulse parameters, e.g. do not yet give correctly the relative phase of adjacent EUV pulses [52]. Furthermore, so far no algorithm correctly includes the final photoelectron kinetic energy dependence in the FROG trace. This effect can be seen in [141] where the shifted photoelectron energies using the algorithm result in shifts that are too small at high photoelectron energies and too large at low photoelectron energies. The same effect can be seen in our results when we retrieve the attosecond pulse using a GP (Generalized projections) algorithm [163, 164] that neglects the photoelectron kinetic energy dependence. The energy dependence is most important at low photoelectron energies and large ponderomotive shifts. Experiments in molecular dynamics using soft x-ray pulses often employ relatively low energy photons. Thus accuracy in characterizing all wavelength ranges is desirable. We note that inclusion of the photoelectron kinetic energy dependence should be feasible in future implementations of the GP algorithm of FROGCRAB, however is not feasible for the more general PCGP (Principal components generalized projections) algorithm [81].

3.3.1 EUV EUV autocorrelation

EUV pump/ EUV probe experiments are extremely challenging, in contrast to what is routinely done in conventional geometries with visible/NIR femtosecond pulses. Nonetheless, an autocorrelation measurement of the 27^{th} harmonic from a Ti:sapphire laser was performed by the Midorikawa group using two-photon double ionization of Helium [110]. Two-photon ionization cross sections at this energy are $\sigma_2 \sim 10^{-52}\ cm^4\, s$ (and therefore similar to two-photon ionization cross sections in the visible region of the spectrum). The two-photon events/pulse are given by $n\, V\, \sigma_2\, F^2\, \tau_{pulse}$ where $n\, V$ is the number of target atoms in the interaction volume V. Events are limited by the low EUV photon peak flux $F = \frac{number\, of\, photons}{\tau_{pulse} \cdot Area}$. With the currently available low EUV flux most researchers however choose to temporally characterize the EUV pulses using two-color cross-correlation methods, where a strong NIR femtosecond pulse (often the same pulse that generated the EUV radiation) is used to characterize the EUV pulse. These methods will be described in the next sections.

3.3.2 Laser-assisted photoemission

Nearly [143, 110] all current EUV pulse characterization techniques rely on laser assisted photoelectron emission. Such techniques were pioneered by Schins and coworkers, who demonstrated laser assisted Auger decay [142], and by Glover and coworkers, who used the laser assisted photoelectric effect for the first temporal measurements of femtosecond high harmonic radiation [56]. The EUV and fundamental near-infrared fields are focused with an adjustable delay into a gas jet. An EUV photon sets an electron free out of an atom. If at the same time the fundamental laser field is present, the photoelectron energies will be modified, i.e. the fundamental field acts as a phase shifter for the electron wave packet. From the detailed shape of the resulting photoelectron spectrum versus EUV-NIR delay, the temporal structure of the EUV radiation can be retrieved. Roughly speaking, there are two limiting regimes depending on whether the photoelectrons are set free by a long EUV pulse train or an isolated attosecond EUV pulse, as shown in Figure 3.1.

Figure 3.1(a) shows the quantum regime of laser-assisted photoemission: For a long EUV pulse, where long means longer than an optical cycle of the NIR field, then the NIR field periodically modifies the energy of the photoelectron wavepacket in time, and due to interference between portions of the wavepacket set free at different times, sidebands develop in the photoelectron spectrum. These sidebands are spaced by the laser photon energy, so one can think of them as being due to absorption or emission of laser photons during the photionization process. There are two ways in which EUV pulse durations can be obtained in this regime: (a) The non-interferometric cross-correlation: As the delay between EUV pulse and fundamental pulse is varied, the sidebands will be visible as long as the two pulses overlap, i.e. roughly for a range of delays from $-t_{fundamental}/2 - t_{EUV}/2$ to $t_{fundamental}/2 + t_{EUV}/2$. So, if the fundamental pulse duration is well known, the EUV pulse duration can be inferred from the temporal extent of the sidebands. (b) Interferometric cross correlation: Here one makes use of the interference between two pathways leading to the same sideband which causes oscillations in sideband intensity vs. delay. This sideband oscillation carries information on the spectral phase of the EUV pulse. So from the EUV spectrum the amplitudes and from the sideband oscillations the phases are known, and the full pulse structure can be reconstructed. Figure 3.1(b) shows the classical regime of laser-assisted photoemission: For an EUV pulse duration much shorter than half an optical cycle, there is no interference

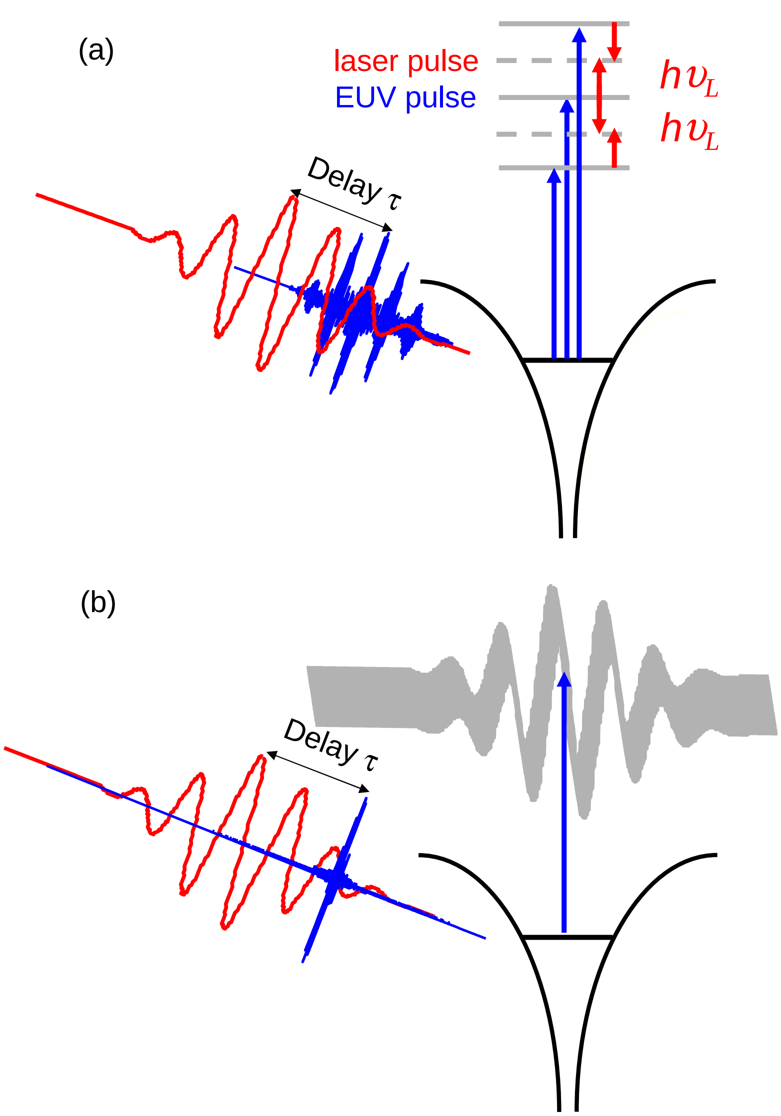

Figure 3.1: Different regimes of laser assisted photoelectron emission. In both cases EUV (blue) and fundamental pulse (red) are focused with adjustable delay into a gas jet. (a) Quantum regime, where the EUV duration is much longer than one cycle of the fundamental light. The photoelectron spectrum (grey) generated by discrete harmonics of EUV light develops sidebands due to emission/absorption of additional fundamental photons. Sideband intensities are modulated versus delay due to interference of the 2 pathways indicated by red arrows. (b) Classical regime for EUV pulses shorter than a fundamental half-cycle. Here the broad photoelectron spectrum is energy-shifted due to the momentum imparted by the fundamental laser field.

between different portions of the photoelectron wavepacket. The freed electron will be accelerated by the laser electric field - this will shift its final momentum (final means when electron is detected at the photoelectron spectrometer, and the laser pulse has long vanished) by an amount $\Delta p(t_r) = \int_{tr}^{\infty} e\, E_L(t')\, dt' = eA(t_r)$, and hence the final photoelectron energy, as shown in Figure 3.1(b).

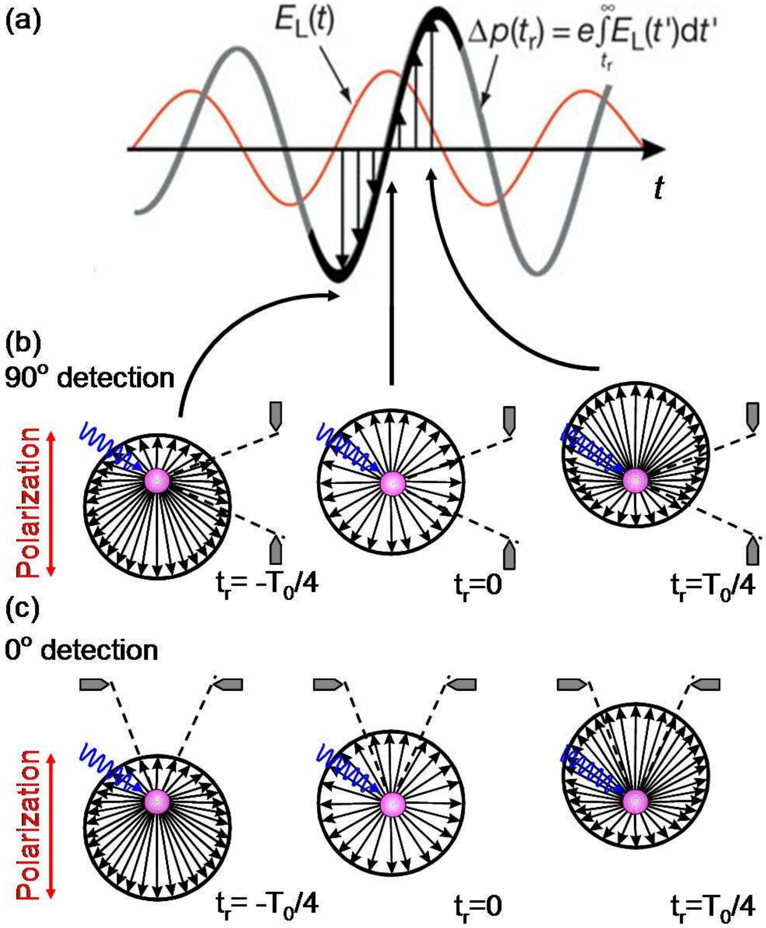

Figure 3.2: (a) Adapted from Ref. [63]. In two-color photoelectron spectroscopy, photoelectrons experience a momentum shift due to the fundamental laser light of $\Delta p(t_r) = \int_{tr}^{\infty} e\, E_L(t')\, dt'$, starting from the time t_r they are released from the atom by the EUV light. This leads to periodic energy shifts with delay between fundamental and EUV light. (b) In 90° detection geometry, periodic downshifts are observed. (c) In 0° detection geometry, up- and downshifts are observed. The $2 - \pi$ detection geometry used in this work includes electrons from both cases.

In Figure 3.2 we take a more detailed look at these momentum shifts: In 3.2(a) the momentum shift is shown as a function of the release time of the photoelectron (delay between the EUV pulse and the laser electric field) - it is 90 degrees out of phase with the electric field. In Figure 3.2(b) and (c) the momentum diagram of the process is shown. The EUV light can eject the electrons according to the differential partial cross section. Assuming the electrons are ejected on an isotropic momentum sphere (as shown for $t_r = 0$), the electric field then shifts the momentum sphere periodically up ($t_r = T_0/4$) and down ($t_r = -T_0/4$) along its polarization direction. The final momentum depends on both - the momentum shift imparted by the fundamental field, as well as the direction of photoelectron momentum w.r.t. fundamental electric field. We specify this direction by the angle θ between final photoelectron momentum and electric field polarization. We will detect these momentum shifts as energy shifts in a photoelectron spectrometer. Figure 3.2(b) shows that for $\theta = 90°$ detection, only energy downshifts are expected (with period $T_0/2$), while for $\theta = 0°$ detection both up- and downshifts are expected (with period T_0). The spectrometer used in this thesis has a $2 - \pi$ detection geometry and thus includes electrons from both cases.

In the following short sections I will briefly review different techniques for attosecond pulse reconstruction based on the principle of laser-assisted photoemission. While the "Attosecond streak camera" technique is suitable for single isolated attosecond pulses, and RABBITT is suited for long attosecond pulse trains, the FROG CRAB technique is generally applicable and will therefore be described in more detail below. "Attosecond SPIDER" is another proposed technique, that opposed to the other methods does not rely on the generation of a photoelectron wave packet as a replica of the EUV pulse, but therefore requires the generation of a replica of the EUV pulse itself.

3.3.3 Attosecond streak camera

This method [73, 84] is suited for the characterization of an isolated attosecond pulse. The principle is shown in Figure 3.3. The delay between a single EUV pulse and the fundamental field is adjusted such that the EUV pulse sits at a maximum of the fundamental electric field. At this position the vector potential has a maximum positive slope and "streaks" the photoelectron energies: photoelectrons generated at the beginning of the attosecond pulse are energy downshifted, while at the end of the attosecond pulse they are energy upshifted. If the attosecond pulse is chirp-free, the photoelectron spectrum is broadened. A positively chirped pulse is broadened, while a negatively chirped pulse is narrowed. This relation can be reversed by repeating the experiment $T_f/2$ later, where the vector potential has maximum negative slope.

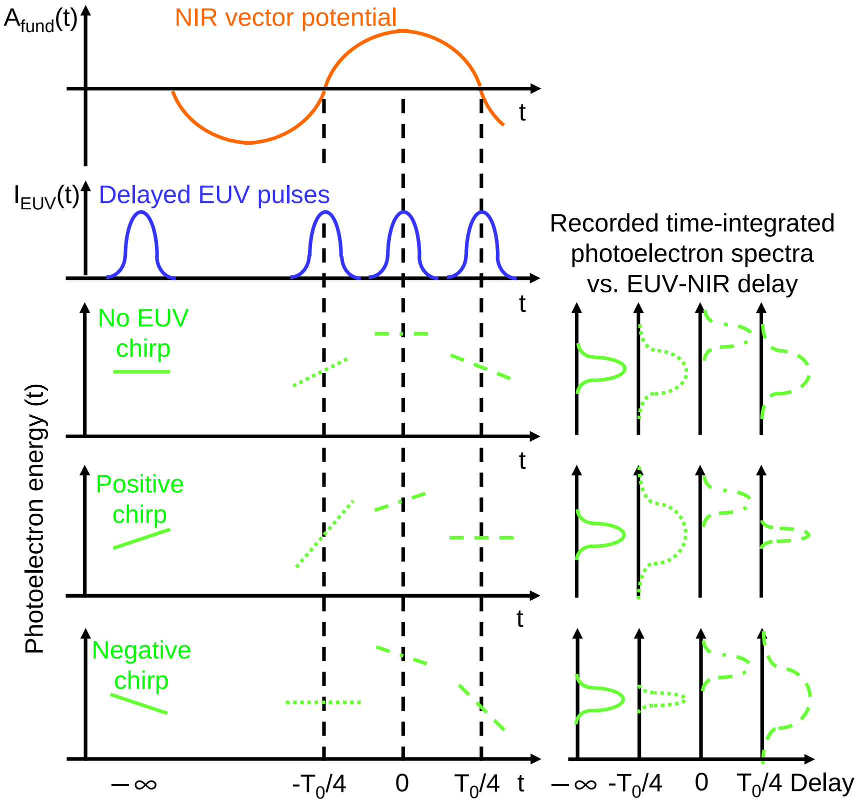

Figure 3.3: Determination of EUV pulse structure from photoelectron spectra in the attosecond streak camera measurement. Red: fundamental vector potential. Blue: EUV pulse, shown at various delays w.r.t. fundamental pulse. In green, the center frequencies of photoelectron spectra are shown versus time. For each delay, the experiment records time-integrated photoelectron spectra, shown to the right. An additional positive/negative EUV chirp leads to further broadening and narrowing of photoelectron spectra, revealing the sign of the EUV chirp.

3.3.4 RABBITT

RABBITT is short for "Reconstruction of Attosecond Beating By Interference of Two-photon Transitions" [109, 117]. RABBITT has been successfully applied to attosecond pulse trains. Here, the EUV electric field in time can be expanded as a sum of harmonics q: $E_{x-ray}(t) = \sum A_q \exp(i(\omega_q t + \phi_q))$. To reconstruct the time structure one needs the amplitudes A_q (which are simply obtained with an x-ray CCD camera) and phases ϕ_q for all harmonic orders q that make up the pulse. One overall phase is irrelevant, i.e. one only needs to measure all relative phase differences between harmonics. Laser-assisted photoelectron emission with interferometric stability between the EUV pulse and NIR pulse allows one to measure these phases from the time dependence of the sideband intensity, which oscillates as $\cos(2\omega_{fundamental}\tau + (\phi_q - \phi_{(q-2)}))$ where τ is delay between EUV and fundamental pulse and $(\phi_q - \phi_{(q-2)})$ is the phase difference between q^{th} and $(q-2)^{th}$ harmonic.

3.3.5 XUV SPIDER

This technique was proposed in [27]. SPIDER is short-hand for "spectral phase interferometry for direct electric-field reconstruction". For this technique one generates two replicas of the attosecond pulse, delays and spectrally shifts one of them (by τ and $\delta\omega$, respectively). These two pulses are then detected with an x-ray CCD camera. From the resulting interferogram $S(\omega, \tau) = |E(\omega) + E(\omega + \delta\omega)\exp(-i\omega\tau)|^2$ which contains a term $\propto \cos(\phi(\omega) - \phi(\omega + \delta\omega) + \omega\tau)$, the spectral phase $\phi(\omega)$ of the attosecond pulse can be retrieved. The amplitude $|E(\omega)|$ of the EUV pulse is measured simply from the spectrum. An inverse Fourier transform of $|E(\omega)|\exp(i\phi(\omega))$ then allows reconstruction of the time structure of the EUV pulse.

A variation of this technique is SEA (spatially encoded attosecond) SPIDER [27], where the two spectrally shifted pulses are interfered in space. An x-ray spectrometer then records spatial interference patterns versus EUV wavelength. This geometry has the advantage that the required spectral resolution of the x-ray spectrometer can be low, as no spectral fringes need to be resolved. Because SEA spider does not use a *time-delayed* replica, it eliminates concerns about distortions of the replica which travels through the high harmonic generation medium previously ionized by the first pulse.

3.3.6 Frequency-Resolved Optical Gating for Complete Reconstruction of Attosecond Bursts (FROG CRAB)

FROG CRAB [101, 124] is a generalized method for the reconstruction of attosecond pulses and contains the RABBITT technique and the attosecond streak camera technique as limiting cases. The idea is to record a photoelectron spectrogram (electron counts versus energy and EUV-NIR delay) in the presence of the fundamental laser field. The spectrogram is analyzed using a generalized projections (GP) code to retrieve the time structure of the EUV pulse. FROG CRAB is the method of choice in this thesis, and will therefore be described in detail in the following sections.

3.4 Theoretical background: EUV photoionization in the presence of a NIR driving laser field

FROG CRAB is inspired by the temporal characterization technique FROG, which is well established for the characterization of short laser pulses in the mid-IR to UV region of the spectrum [163, 164]. Ultrashort laser pulses in the visible/ NIR can be straightforwardly measured by making use of nonlinear-optical materials for this spectral region that operate at easily achievable intensities and have an instantaneous response. A commonly used nonlinear process is second-harmonic-generation (SHG). There a beamsplitter is used to split the pulse into two pulses i.e. one creates a replica of the pulse. This replica can then be delayed w.r.t the pulse in the other arm using a delay stage. The replica thereby serves as a temporal gate, sampling the spectrum of the pulse at varying delay steps. A two-dimensional trace of spectra versus delay steps is the result. This spectrogram $S(\omega,\tau)$ can be mathematically written as

$$S(\omega,\tau) = \left| \int_{-\infty}^{+\infty} E(t) g(t-\tau) \exp\left(-i\omega t\right) dt \right|^2 \tag{3.1}$$

where $E(t)$ is the electric field and $g(t-\tau)$ is the gate function which is simply $E(t-\tau)$ in the case of SHG FROG. From the measured spectrogram the complete electric field can be determined using iterative Fourier-transform algorithms.

As first discussed in [101, 124], FROG CRAB extends FROG to the EUV and for attosecond pulses. For completeness we include here the main results of Quéré et. al. [101, 124] where they describe photoionization of atoms by EUV pulses in the presence of low-frequency driving pulses. The derivation assumes the strong field approximation (i.e. neglects the effect of the ionic potential on the motion of the electron after ionization) and the single active electron approximation. First, EUV radiation creates one or several electron wavepackets by single photon photoionization, which are then modulated by the electric field of the NIR laser leading to sidebands or shifts in the generated electron wavepackets. Mathematically the transition amplitude of the electron wavepacket $a_{\mathbf{v}}(\tau)$ at a delay time τ from the ground state to the final continuum state $|\mathbf{v}>$ with final electron velocity $\mathbf{v}$ is given by

$$a_{\mathbf{v}}(\tau) = -i \int_{-\infty}^{+\infty} \mathbf{d}_{\mathbf{p}(t)} \cdot \mathbf{E}_{xray}(t-\tau) \exp\left(i \left[I_p t - \int_t^{+\infty} \frac{p^2(t')}{2} dt' \right] \right) dt \tag{3.2}$$

Here $\mathbf{d}_{\mathbf{p}(t)}$ is the dipole transition matrix element from the ground state to the continuum state $|\mathbf{p}>$, $\mathbf{p}(t) = \mathbf{v} + \mathbf{A}(t)$ is the instantaneous momentum of the free electron in the laser field. Here $\mathbf{A}(t)$ is the vector potential such that $\mathbf{E}_{LASER}(t) = -\frac{\partial \mathbf{A}}{\partial t}$, and $\mathbf{E}_{xray}(t-\tau)$ is the electric field of the EUV pulse and I_p is the ionization potential of the atom. The term in the exponential is the acquired phase in the ground state until ionization at time t, and the Volkov phase i.e. the integral of the instantaneous energy of a free electron in the laser field.

Because there is no general description of the dipole transition matrix element $\mathbf{d}_{\mathbf{p}(t)}$, it is expedient to assume that it takes a constant value independent of energy. However this could lead to a photoelectron amplitude versus energy being different from the EUV pulse amplitude. Therefore the ionization cross section versus energy should ideally be taken into account in the fit process, or the EUV spectrum should be independently measured by a x-ray spectrometer. The EUV spectrum and photoelectron spectrum might also differ in phase if there is a phase dependence of the transition dipole matrix element as a function of energy (e.g. resonances in the continuum).

We can rewrite the amplitude of the electron wavepacket

$$a_{\mathbf{v}}(\tau) = -i \int_{-\infty}^{+\infty} \exp\left(i\Phi(t)\right) \mathbf{d}_{\mathbf{p}(t)} \cdot \mathbf{E}_{xray}(t-\tau) \exp\left(i(I_p + W)t\right) dt \tag{3.3}$$

where

$$\Phi(t) = -\int_{t}^{+\infty} \left(\mathbf{v} \cdot \mathbf{A}(t') + \frac{\mathbf{A}^2(t')}{2} \right) dt' \tag{3.4}$$

Since we are measuring photoelectron probabilities, the modulus square of the amplitude of the electron wavepacket, $|a_{\mathbf{v}}(\tau)|^2$ needs to be compared to the spectrogram $S(\omega, \tau)$. The one-by-one comparison shows that the gate function $g(t-\tau)$ of $S(\omega, \tau)$ corresponds to the $\exp\left(i\Phi(t)\right)$ term in $|a_{\mathbf{v}}(\tau)|^2$:

$$g(t) = \exp\left(i\Phi(t)\right) \tag{3.5}$$

This term corresponds to a phase modulation of the electron wavepacket induced by the NIR dressing laser, which serves as a temporal phase gate for measuring the duration of the EUV pulse.

Finally we express the phase with experimental observables as a sum of three contributions:

$$\Phi(t) = \Phi_1(t) + \Phi_2(t) + \Phi_3(t) \tag{3.6}$$

$$\Phi_1(t) = -\int_t^{+\infty} U_p(t)dt \tag{3.7}$$

$$\Phi_2(t) = \frac{\sqrt{8WU_p(t)}}{\omega_L}\cos(\theta)cos(\omega_L t - \phi_{CE}) \tag{3.8}$$

$$\Phi_3(t) = -\frac{U_p(t)}{2\omega_L}\sin(2\omega_L t - 2\phi_{CE}) \tag{3.9}$$

where

$$U_p(t) = \frac{E^2}{4\omega_L^2}\exp(-4\ln 2(t/\tau)^2) \tag{3.10}$$

is the ponderomotive potential, W is the final photoelectron kinetic energy, ω_L is the laser angular frequency, and ϕ_{CE} is the fundamental carrier envelope phase, θ is the angle between the laser polarization direction and the final photoelectron velocity.

3.5 Generalized projections (GP) algorithm for FROGCRAB

We start by using the generalized projection (GP) algorithm to retrieve the EUV electric field. This iterative Fourier-transform algorithm converges to a solution by iteratively optimizing between two constraints - one in the frequency and one in the time domain. In the frequency domain, the calculated FROG trace amplitude is replaced by the square root of the experimental trace $S(\omega, \tau)$, and in the time domain a new guess for the electric field is obtained by minimizing the error between a newly created signal field $E_{sig}(t, \tau)$ and the signal field obtained in the last iteration $E'_{sig}(t, \tau)$.

A schematic of the procedure is shown in Figure 3.4.

First, a random $E_{xray}(t)$ is generated. Second, a signal field

$$\mathbf{E}_{sig}(t, \tau) = E_{xray}(t - \tau)\exp(i\Phi(t)) \tag{3.11}$$

is generated. It is important to note here that all current implementations of the GP algorithm, including ours, replace the final photoelectron kinetic energy W in Eq.

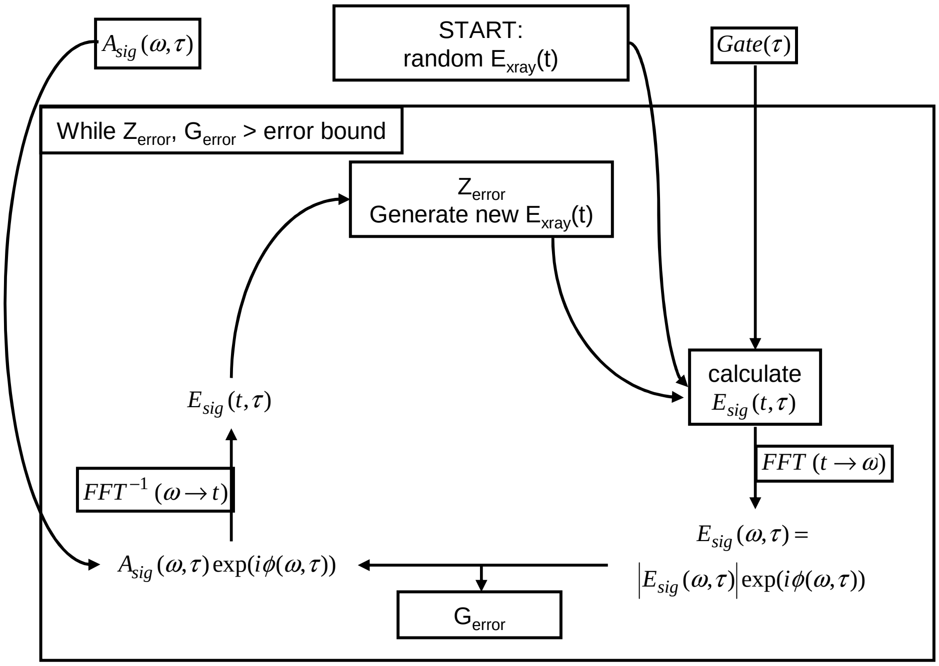

Figure 3.4: Basic schematic of GP algorithm.

(3.8) by W_0, the photoelectron center energy - we will discuss consequences of this approximation below. Third, Fourier-transforming into the frequency domain yields $E_{sig}(\omega,\tau)$. Fourth, the amplitude of $E_{sig}(\omega,\tau)$ is replaced by the amplitude $A_{sig}(\omega,\tau)$ of the experimental Frog trace data $S(\omega,\tau)$. Fifth, we perform the inverse Fourier-transform back into time domain $E'_{sig}(t,\tau)$. Sixth, we improve our guess for $E_{xray}(t)$ by minimizing the error between a newly created signal field and the signal field obtained in the last iteration. Seventh, the newly generated $E_{xray}(t)$ is used as input for a new signal field, which brings us back to the second step of the loop. The retrieval algorithm is run until the errors in the frequency domain

$$G_{err} = \sqrt{\frac{1}{N^2}\sum_{i,j=1}^{N}\left|A_{sig}^2(\omega_i,\tau_j) - \mu|E_{sig}(\omega_i,\tau_j)|^2\right|^2} \tag{3.12}$$

and in the time domain

$$Z_{err} = \sum_{i,j=1}^{N} \left| E_{sig}(t_i, \tau_j) - E'_{sig}(t_i, \tau_j) \right|^2 \tag{3.13}$$

are lower than a specified limiting value. Here μ is a real normalization constant that minimizes G_{err} and $N x\, N$ is the array size.

3.6 Modifications to the GP algorithm

Our experimental setup described above uses a magnetic bottle time-of-flight spectrometer that collects a large range of final electron momenta corresponding to angles from 0 to 90 degrees. Furthermore, the CEP of the pulses is not stabilized. Both these features require modifications to the GP algorithm. The reason lies in the dependence of the gate function (3.5) on the angle θ and on the carrier-envelope phase of the NIR pulse, as seen in equations (3.3) to (3.10) in section 3.4. So, in essence one must run the algorithm with different gate functions in parallel, and do appropriate averaging when comparing with experimental data. In addition, the resolution of the photoelectron spectrometer should be included to take into account any broadening of the spectrum which leads to retrieved pulse durations systematically shorter than the actual pulse duration. In this experimental work, we use a very conservative value for this resolution, and thus obtain a result that is a realistic upper limit of pulse duration. The lower limit can be determined by the transform limit of the EUV spectrum.

Figure 3.5 shows how the GP algorithm is modified to take into account the $2-\pi$ detection geometry and non-CEP stabilized NIR pulses.

First, to take into account the fact that we make no attempt to CEP-stabilize our driving laser pulses, we take into account two gate functions - one with the absolute phase set to zero degree and one with the absolute phase set to 180 degrees. These CEP values correspond to "cosine" and "minus cosine" IR pulses which lead to identical conditions for HHG generation in a noble gas. Our results below show that the experi-

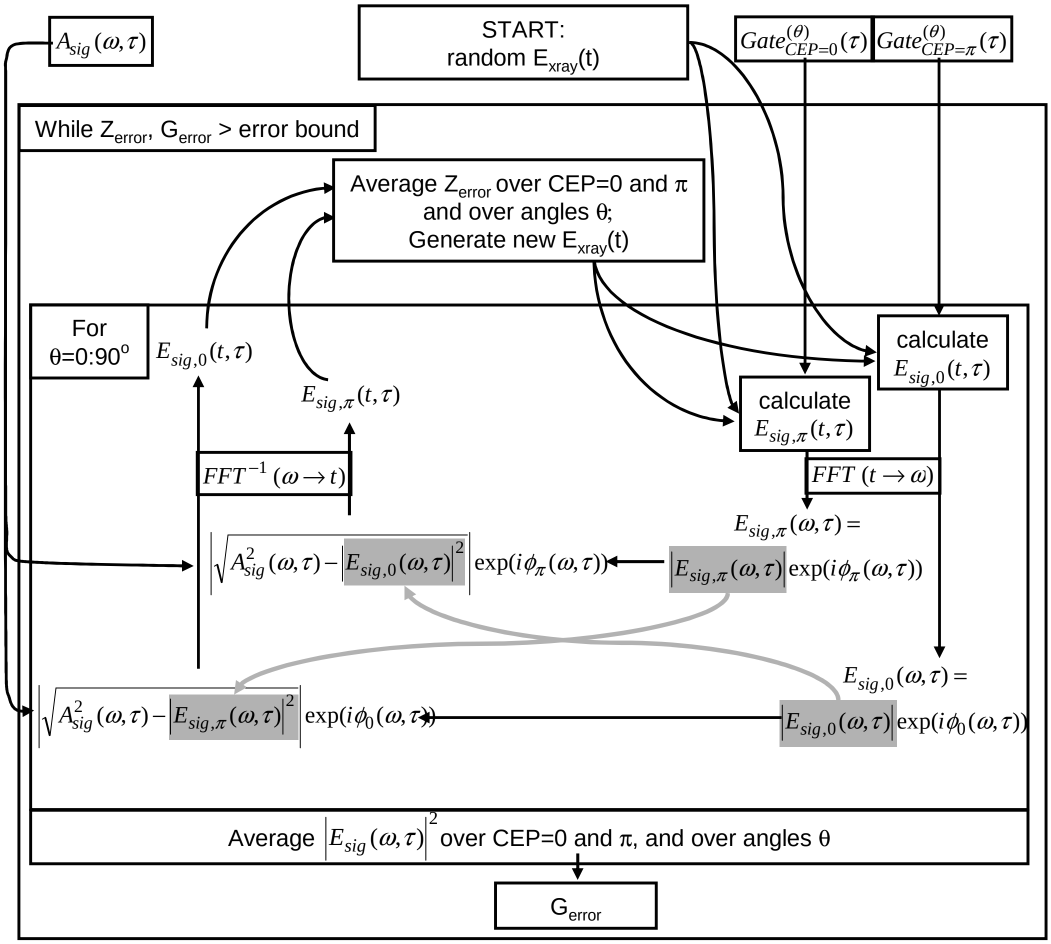

Figure 3.5: Schematic of GP algorithm adapted to wide-angle photoelectron detection geometry and non-CEP stabilized driving laser pulses.

mental data are quite well described by this procedure. The reason why only these two values of CEP are required to achieve good agreement is that the NIR beam (which is the same beam that generated the EUV radiation) is temporally synchronized with the EUV radiation due to the EUV generation process itself. However if multiple EUV bursts are present, their relative strengths (amplitudes, not their timing) could change with CEP. In our case, if for certain CEP values multiple bursts were generated, we would observe this as a modulation of the photoelectron spectrum, as shown in the simulations presented in Fig. 3.22. Experimentally however, we observe only a very small amount of modulation (see Fig. 3.17 and Fig. 3.22), meaning either that only in a small fraction of laser shots multiple EUV bursts are generated, or that in every shot only very small side bursts are generated along with the main burst. The synchronization is also well-demonstrated by the fact that we clearly see interferometric modulation of the photoelectron energy data versus delay (see Fig. 3.19 (a)). This is also not any more of an approximation than that used in any other attosecond pulse measurement. All measurements, whether they be for isolated pulses or pulse trains, show this interferometric synchronization [100, 63]. Furthermore, at the level of the instantaneous electric field of the driving laser, CEP fluctuations look identical to intensity fluctuations in the laser pulse, and recent theoretical calculations have corroborated the insensitivity of the pulse generation process to intensity variations [141]. Thus, our presumption that the attosecond pulses in the train are well-synchronized with the fundamental electric field, with the exception that the direction of the field oscillations may flip randomly, is well justified. The remaining question, which we address below, is whether the averaging over 2 CEP phases creates significant deconvolution ambiguities compared with a CEP-stabilized case.

We therefore apply the algorithm simultaneously to two signal fields - one with the CEP set to 0 degrees and one with CEP 180 degrees. Instead of replacing the amplitude of $\mathbf{E}_{sig}(\omega, \tau)$ by the amplitude of the experimental FROG CRAB trace $A_{sig}(\omega, \tau)$, we replace the amplitude of the signal field with CEP 0 radians $|E_{sig,0}(\omega, \tau)|$ with an expression containing the amplitude of the experimental FROG CRAB trace $A_{sig}(\omega, \tau)$ and the amplitude of the signal field with CEP π radians $\left|\sqrt{A_{sig}(\omega, \tau)^2 - |E_{sig,\pi}(\omega, \tau)|^2}\right|$. An analogous replacement is made for $|E_{sig,\pi}(\omega, \tau)|$. This is the essential step of driving both signal fields to converge to a combined signal field describing the experimental FROG CRAB data. To obtain the G_{err} we calculate the rms error between the combined signal field

$$|E_{sig}(\omega, \tau)|^2 = \frac{1}{2}\left(|E_{sig,0}(\omega, \tau)|^2 + |E_{sig,\pi}(\omega, \tau)|^2\right) \tag{3.14}$$

and the experimental FROG CRAB trace. In the next step we Fourier-transform both signal fields back into time domain, yielding $E_{sig,0}(t,\tau)$ and $E_{sig,\pi}(t,\tau)$. Two new guesses for the EUV field $\mathbf{E}_{xray}(t)$ are calculated. The average of the two EUV fields is taken and used to construct two new signal fields $E'_{sig,0}(t,\tau)$ and $E'_{sig,\pi}(t,\tau)$. The Z_{err} is calculated for both CEP 0 and π according to Equation (3.13), and is then averaged.

Next we discuss how to adapt the algorithm to include the dependence of the gate on the angle between the laser polarization and the final photoelectron velocity. To this end we implement a for-loop in which for each angle, both signal fields $|E_{sig,0}(\omega,\tau)|$ and $|E_{sig,\pi}(\omega,\tau)|$ are calculated. The G_{err} is then calculated with the average signal field calculated as a sum over different angles

$$E_{sig,CALC}(\omega,\tau) = \sqrt{\sum_{\theta} \left(|E^{\theta}_{sig,0}(\omega,\tau)|^2 \cdot prob(\theta) + |E^{\theta}_{sig,\pi}(\omega,\tau)|^2 \cdot prob(\theta) \right)} \tag{3.15}$$

where

$$prob(\theta) = \sin(\theta) \cdot \sigma(\theta) / \sum_{\theta} \sin(\theta) \cdot \sigma(\theta) \tag{3.16}$$

is the probability containing the geometrical weight factor $\sin(\theta)$ for the photoelectron distribution as well as the differential partial cross section $\sigma(\theta)$ for the detection gas used [13]. We also generate a for-loop to calculate the Z_{err} for all angles and we average the Z_{err} by calculating

$$Z_{err} = \sum_{\theta} Z_{err}(\theta) \cdot prob(\theta) \tag{3.17}$$

The $E_{xray}(t)$ is also averaged

$$E_{xray}(t)_{ave} = \sum_{\theta} E_{xray}(t,\theta) \cdot prob(\theta) \tag{3.18}$$

The resolution of the spectrometer can be included as follows. After calculating the new signal fields $E_{sig,0}(t,\tau)$ and $E_{sig,\pi}(t,\tau)$ in time, they are fourier-transformed into the frequency domain and convolved with the square root of the resolution function of the photoelectron spectrometer. The convolved signal fields are Fourier-transformed back into the time domain. When in the next step the magnitude of $|E_{sig}(\omega,\tau)|$ is replaced (see Fig. 3.5), the information about the convolution is preserved in the phase of $E_{sig}(\omega, \tau)$, which remains unchanged. Empirically we found two further methods for improving the convergence of the algorithm: for every iteration, we vary the delay of the experimental trace by a fixed number of single delay steps to minimize the G_{err}. We also change the sign of the spectral phase of E_{xray} every ≈ 100 iterations. Only the center 90% of the delay range of the calculated FROG CRAB trace is used to calculate the G_{err}. This is done to avoid numerical artifacts that occur at the calculated edges.

3.6.1 Atto- and harmonic chirp

Before turning to experimental results, I briefly review two kinds of phase contributions which exist for EUV radiation, called attochirp and harmonic chirp [167].

The harmonic chirp is associated with the second order temporal phase of an EUV pulse, which for harmonic order q is defined as $b_j^q = -\frac{\partial^2 \phi_j^q}{\partial t^2}$ (j refers to EUV radiation generated from the short or long electron trajectory) and is given by

$$b_j^q \approx q b_{fund} + 8(\ln 2) \frac{I_0}{\tau_0^2} \frac{\partial \phi_j^q}{\partial I} \tag{3.19}$$

Here, b_{fund} is the quadratic temporal phase of the fundamental light defined by $\phi_{fund}(t) = -\omega t - b_{fund} t^2/2$, I_0 and τ_0 are the fundamental intensity and duration, respectively. The harmonic chirp is then given by the second order spectral phase

$$\frac{\partial^2 \phi}{\partial \Omega^2} = \frac{b_j^q}{(b_j^q)^2 + 16(\ln 2)^2/(\Delta t)^4} \tag{3.20}$$

(Δt is the EUV pulse duration). The harmonic chirp thus has the same sign as b_j^q. In the absence of a fundamental chirp it is the same sign as $\frac{\partial \phi_j^q}{\partial I}$, which is negative, both for the short (small negative value) and long (large negative value) trajectory (Figure 1 in Ref. [167]). On the other hand, if the fundamental chirp term is dominant, then the harmonic chirp will have the same sign as the fundamental chirp.

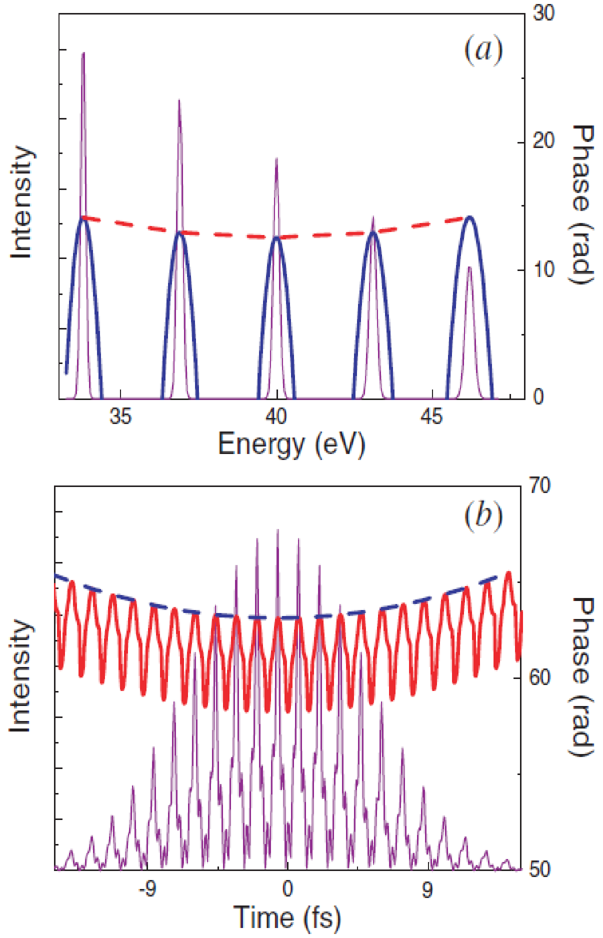

Figure 3.6: Taken from Varju et al. [167]: Harmonic and atto chirps in frequency and time domain. (a) Spectral intensity (purple, left scale) and phase (solid blue, right scale) for a group of 5 harmonics. (b) Corresponding temporal intensity (purple, left scale) and phase (solid red, right scale). The harmonic chirp corresponds in frequency domain to a quadratic behaviour around each harmonic (solid blue line), and in time domain to a slow quadratic drift of the central phase (dashed blue line). The atto chirp corresponds to a quadratic drift of the spectral phase from one harmonic to the next (dashed red line), and a fast quadratic variation in time domain around each attosecond pulse (solid red line).

The atto chirp is given by

$$b_{atto} = \frac{\frac{\partial^2 \phi_j^q}{\partial q^2}}{(\frac{\partial^2 \phi_j^q}{\partial q^2})^2 + 16(\ln 2)^2/(\Delta\Omega)^4} \tag{3.21}$$

where $\Delta\Omega$ is the spectral bandwidth of the EUV pulse. $\frac{\partial^2 \phi_j^q}{\partial q^2}$, and hence the attochirp, is positive for the short trajectory, and negative for the long trajectory (Figure

2 in Ref. [167]). The two kinds of chirps are illustrated in Figure 3.6, taken from [167].

3.7 Experimental setup and photoelectron detection geometry

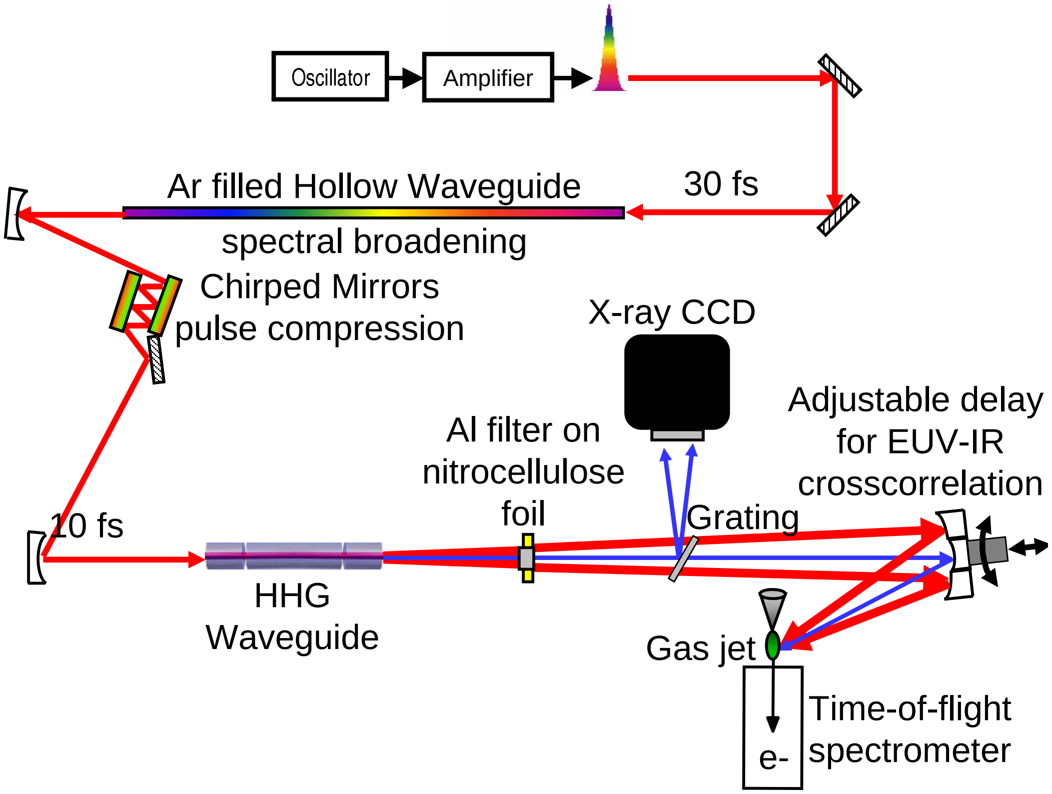

Figure 3.7: Experimental setup for EUV pulse generation and temporal characterization via photoelectron energy resolved two-color cross-correlation using a NIR pulse.

Our experiment, shown in Fig. 3.7, starts with 30 fs, 2 mJ laser pulses from a cryogenically-cooled 2 kHz Ti:Sapphire laser amplifier [5]. We use a 1 m long, 400 μm diameter hollow waveguide filled with Argon gas to broaden the laser spectrum by self phase modulation (SPM fiber) [113, 149]. To prevent defocusing of the laser pulses at the entrance of the SPM fiber, we use a pressure gradient of 0 Torr at the input and $\sim$ 300 Torr at the output of the fiber. We then temporally compress the pulses using commercially-available negatively chirped mirrors (Layertec $-40\ fs^2$ per mirror bounce). We obtain pulses of $10 - 15$ fs duration centered at $\lambda \approx 740\,nm$, and focus them into a 150 μm diameter, 3.5 cm long hollow-core waveguide (including two 0.5 cm long end sections for differential pumping) filled with Argon gas [135], in which the high harmonic radiation is generated. We estimate an intensity in the fiber of $\sim 5.7 \cdot 10^{14}$ W/cm^2, and the Argon pressure was $\approx$ 10 torr [152]. We note that the coupling of the fundamental light into the fiber was well-optimized (80% coupling efficiency) [152], resulting in very small power loss inside the fiber, and an excellent near-TEM_{00} output mode. This indicates near-perfect coupling to the fundamental EH_{11} fiber mode. The spectra of the fundamental radiation after the fiber showed only a small amount of blue-shift compared to the one before the fiber, indicating that only a small amount of temporal reshaping of the fundamental pulse took place in this low-pressure regime.

To temporally characterize the EUV pulse, we employ an interferometric, photoelectron energy resolved EUV - NIR cross correlation geometry [36]. The EUV and fundamental driving pulse are focused into a Neon gas jet, and a cross-correlation signal is obtained from the generated photoelectron spectra as the relative delay between the two pulses is varied. The delay line makes use of the different divergences of the fundamental and the EUV beam exiting the HHG fiber. The low divergence, central EUV beam passes through a small circular Al filter suspended in a Kapton filter. The annular fundamental beam, which passes around the Al filter, is reflected by an annular mirror, while the central EUV beam is reflected by a Mo/Si mirror that is mounted on a closed loop piezoelectric transducer (S-325 tip/tilt piezo and z-axis positioner, Physik Instrumente). The two time-delayed light fields are then focused onto a Neon gas jet.

The photoelectrons ejected from Neon by the EUV beam are then detected using a magnetic bottle time-of-flight spectrometer [86] and a multichannel plate (MCP) detector in a Chevron configuration. This spectrometer has a 2 π detection solid angle i.e. photoelectrons parallel and perpendicular to the laser polarization (which points towards the MCP) are detected. To characterize the EUV spectrum separately, we use a home-built spectrometer consisting of a concave grating (ROC 1 m, 1200 gr/mm) and an x-ray CCD camera (100 x 1340 pixels, Roper Scientific), directly following the high harmonic generation hollow-core waveguide.

3.7.1 Magnetic bottle time-of-flight spectrometer, electronics and data acquisition

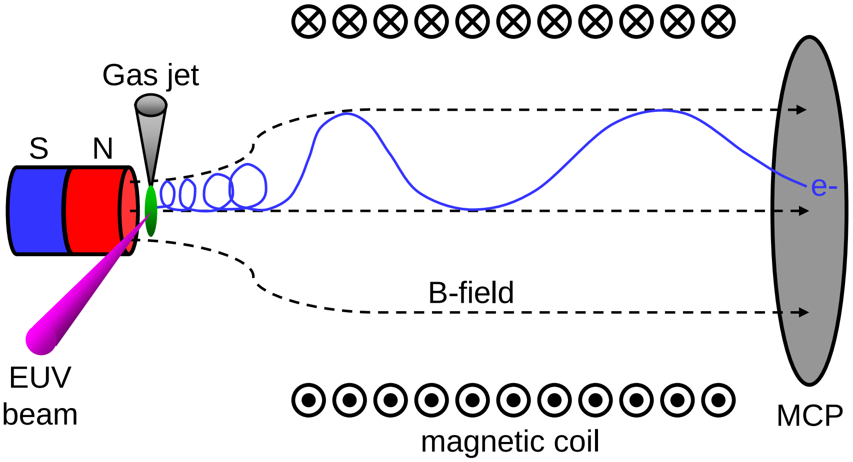

Figure 3.8: Magnetic bottle time of flight spectrometer. Electrons from photoionization in a gas jet are guided towards a MCP detector by inhomogeneous fields. The field geometry ensures adiabatic parallelization (see text) of all trajectories that had an initial velocity component towards the MCP, providing $2-\pi$ collection and a time-of flight proportional to the initial photoelectron energy.

Here the principle of the magnetic bottle time-of flight spectrometer used in this chapter is described [86] (see Figure 3.8). This type of spectrometer was chosen as it allows time-of-flight detection of electrons emitted into $2-\pi$ solid angle, allowing fast data acquisition even under conditions where in total few electrons per laser shot are created. It has been rebuilt based on the design in Emily Gibson's thesis [55]. However, an additional larger coil was added on the top of the spectrometer. The additional coil had $\sim$ 100 windings (Kapton insulated square wire gauge 14) and an inner diameter of 16 cm. The reason for this additional coil is that without it, the magnetic field drops toward zero at the MCP detector (see Figure 3.9). The additional coil lead to an increase of electron counts by one order of magnitude.

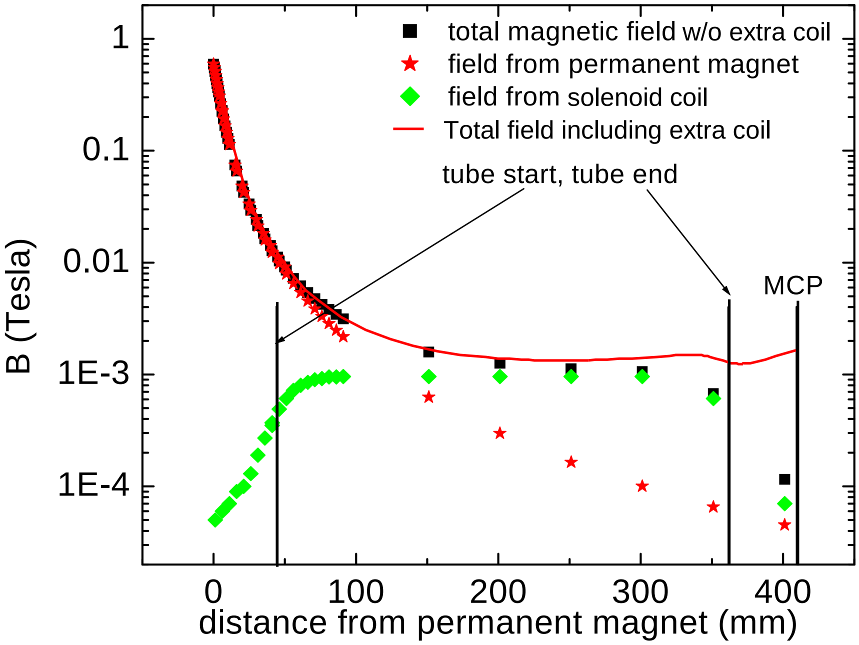

Figure 3.9: Magnetic fields of the time-of-flight photoelectron spectrometer (in log scale). Black symbols: Total magnetic field without additional coil. Red line: calculated total field including the extra coil. The drop-off at the MCP position is avoided, enhancing electron counts by a factor of 10.

The setup is shown in Figure 3.8. To achieve $2-\pi$ collection and time-of-flight detection simultaneously, the gas jet is placed in an inhomogeneous magnetic field created by a strong permanent magnet (NdFeB). This magnetic field goes over into a homogeneous field created by a solenoid, which extends through the time of flight tube to the electron detector, two microchannel plate (MCP) detectors in a Chevron configuration. This total magnetic field configuration initially forces the photoelectrons on tight circular orbits in the plane transverse to the axis towards the detector, with the electron trajectory radii given by $r_i = mv_{perpendicular}/(eB)$. As the field decays away from the permanent magnet and becomes homogeneous, the electron trajectories are bent adiabatically to become almost parallel to the field lines, with the final electron radii given by $r_f = r_i \cdot \sqrt{B_i/B_f}$. The parallelization can be understood from the conservation of energy, as well as of angular momentum about the field axis:

$L_z = mv_{perp}r = const$, where $v_{perp} = \omega r$ with the cyclotron frequency $\omega = eB/m$. It follows that $v_{perp}^2/B = const$, i.e. v_{perp} decreases with decreasing B. Energy conservation then demands that $v_z = \sqrt{v^2 - v_{perp}^2}$ increases with decreasing B, and the electron trajectories get parallelized. The "parallelized" electrons have the same time-of-flight for the same total velocity v. Good energy resolution is thus ensured if the parallelization takes much less time than the time spent in the drift tube.

Care has to be taken that the adiabaticity parameter is kept below unity. It is defined by $\chi = \frac{2\pi mv}{eB_z^2}|\frac{dB_z}{dz}|$, which is the fractional change in the field that the electron experiences in one cyclotron orbit. In the design a compromise has to be found between a low adiabaticity value (large B_f preferred), good energy resolution (low B_f preferred) and that the electrons hit the active area of the detector (large B_f preferred). The adiabaticity parameter in the final design remained below 1.5 everywhere inside the spectrometer.

The laser polarization for all experiments in this chapter was chosen parallel to the time-of-flight axis.

In figure 3.10 I show a sketch of the TOF apparatus and the electronics for processing of photoelectron counts from the MCP detector. The MCP signal was separated from the high-voltage in a bias tee. A $1.1\,\mu s$ delay was inserted using a low loss/low dispersion coaxial cable to temporally separate the signal from electromagnetic noise, associated with the pockels cell switching for the amplifier pulse. An electronic amplifier/timing discriminator provided the "stop" signal for the ACAM timing board (the "start" signal was provided by a fast photodiode recording scattered light from the amplifier pulse). The data collected with the ACAM PC board were acquired and displayed with a user interface written in Labview. This program also controlled the position (delay) of the closed-loop piezoelectric transducer, as well as allowing for the optimization of photoelectron counts using the tip/tilt degrees of the piezo. After alignment was completed the program allowed automated acquisition of a full FROG CRAB

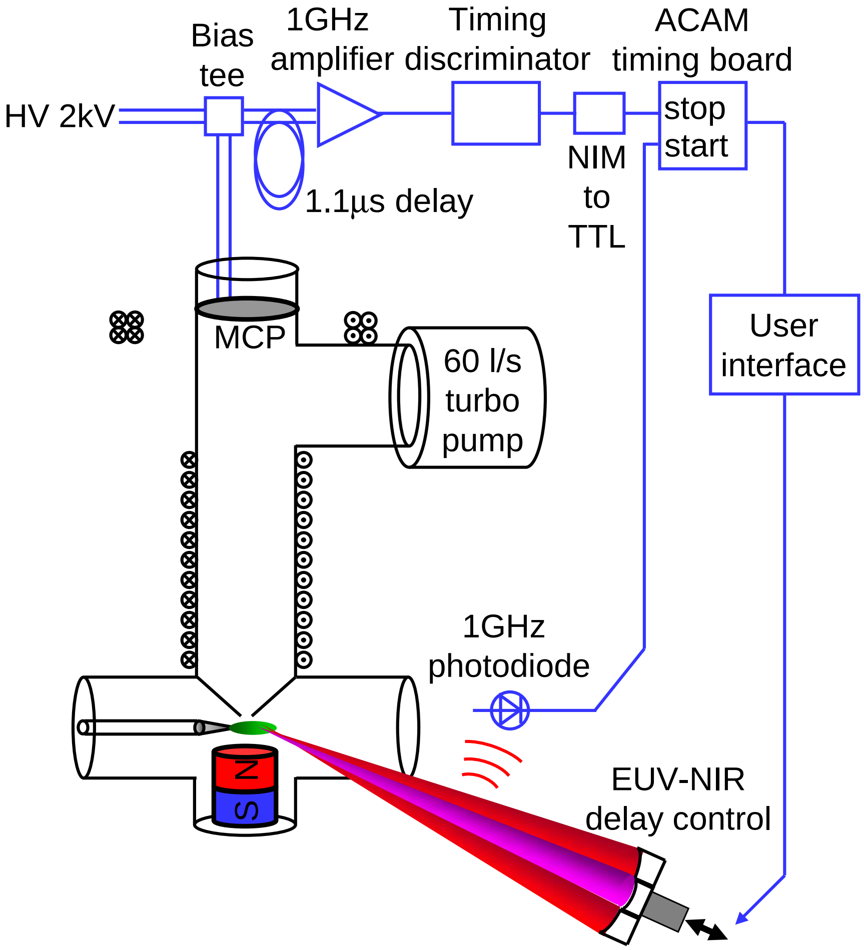

Figure 3.10: Electronics following the photoelectron spectrometer setup.

spectrogram. Figure 3.11 shows the Labview interface for Windows XP.

Figure 3.12 shows an example of a photoelectron spectrogram demonstrating the good resolution of the spectrometer. To quantify the resolution, the widths of photoelectron peaks were compared to the widths of the corresponding harmonics recorded simultaneously using an x-ray CCD camera in a separate measurement. This yielded an estimate of the photoelectron spectrometer resolution of 0.73 eV.

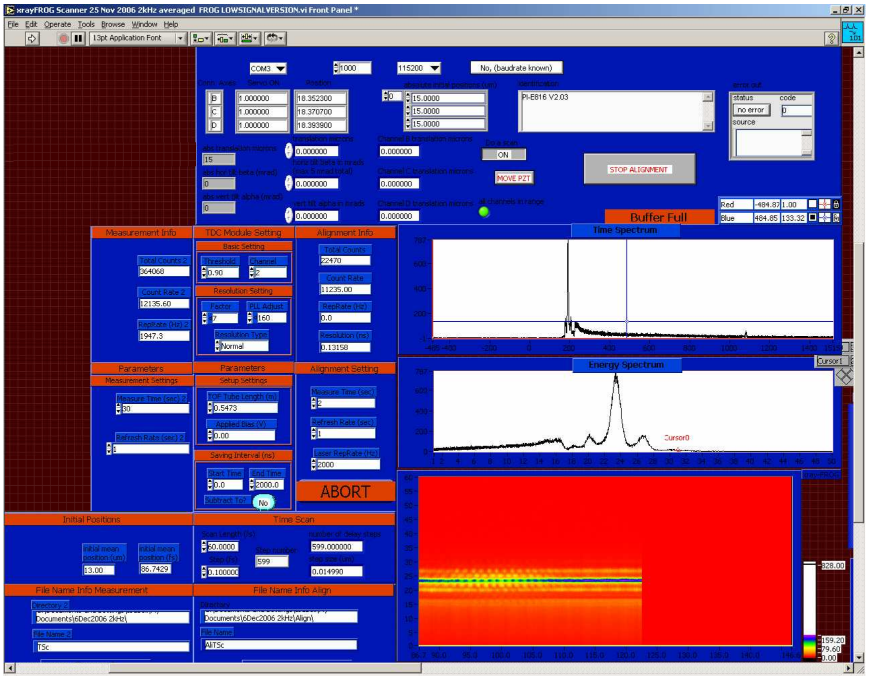

COM3
1000
115200
No, (baudrate known)

Conn. Axes	Servo ON	Position
B	1.000000	18.352300
C	1.000000	18.370700
D	1.000000	18.393900

absolute initial positions (um): 15.0000, 15.0000, 15.0000
Identification: PI-E816 V2.03
error out: status: no error; code: 0; source:
abs translation microns: 15
abs hor tilt beta (mrad): 0
abs vert tilt alpha (mrad): 0
translation microns: 0.000000
horiz tilt beta in mrads (max 5 mrad total): 0.000000
vert tilt alpha in mrads: 0.000000
Channel B translation microns: 0.000000
Channel C translation microns: 0.000000
Channel D translation microns: 0.000000
Do a scan: ON
all channels in range

Red	-484.87	1.00
Blue	484.85	133.32

Total Counts 2: 364068
Count Rate 2: 12135.60
RepRate (Hz) 2: 1947.3
Basic Setting: Threshold: 0.90; Channel: 2
Resolution Setting: Factor: 7; PLL Adjust: 160; Resolution Type: Normal
Total Counts: 22470
Count Rate: 11235.00
RepRate (Hz): 0.0
Resolution (ns): 0.13158
Measurement Settings: Measure Time (sec) 2: 30; Refresh Rate (sec) 2: 1
Setup Settings: TOF Tube Length (m): 0.5473; Applied Bias (V): 0.00
Saving Interval (ns): Start Time: 0.0; End Time: 2000.0; Subtract To?: No
Measure Time (sec): 2
Refresh Rate (sec): 1
Laser RepRate (Hz): 2000
initial mean position (um): 13.00
initial mean position (fs): 86.7429
Scan Length (fs): 60.0000
Step (fs): 0.100000
Step number: 599
number of delay steps: 599.000000
step size (um): 0.014990
Directory 2: Documents\6Dec2006 2kHz\
File Name 2: TSc
Directory: Documents\6Dec2006 2kHz\Align\
File Name: AliTSc

Figure 3.11: Labview interface for automated acquisition of photoelectron spectrograms in Windows XP.

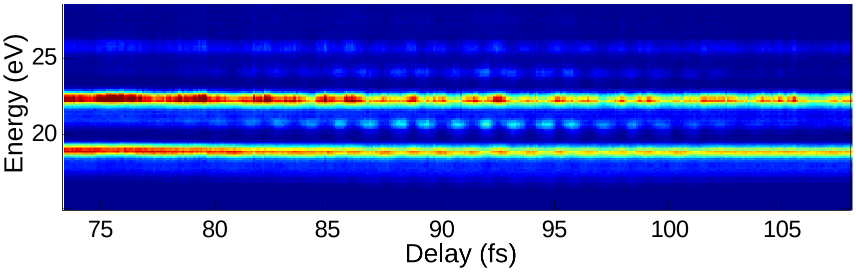

Figure 3.12: Photoelectron spectrogram demonstrating the good resolution ($\approx 0.7\,eV$ at $\approx 22\,eV$ determined in a separate measurement) of the spectrometer: Sidebands and individual harmonics are clearly separated.

3.8 Temporal characterization of attosecond waveforms in the sub-optical cycle regime

In this section, I present the first temporal characterization of sub-optical cycle EUV pulses generated in a hollow waveguide [154, 140]. This new generation scheme allows us to use significantly longer driving laser pulses, of 13 fs in duration, than have been used for sub-optical-cycle EUV generation to date. Such 13 fs driving pulses can be generated by standard ultrafast laser pulse compression techniques. We use two independent techniques to extract the complex EUV field: an iterative step-by-step reconstruction based on a constrained number of physical parameters and error minimization between the experimental FROG CRAB trace and a simulation based on the expression given in [101, 124], and an unrestricted FROG CRAB pulse retrieval algorithm. Both methods independently show that the generated EUV pulse consists of a very short train of moderately-chirped 470 attosecond pulses, with bursts spaced by $\sim$ 1.3 fs with the total energy contained within a 1.4 fs FWHM (full-width at half-maximum) pulse envelope. Moreover, we show that the EUV field is near the Fourier-transform limit, with a narrow spectral bandwidth where $\sim$ 64% of the energy is contained within a single harmonic peak of 1.1 eV FWHM. Finally, the EUV pulse can be tuned over an energy range between 38 eV and 48 eV by adjusting the driving laser intensity and the gas pressure in waveguide. Because of the sub-optical-cycle pulse duration, narrow bandwidth, ease of tunability, and greatly simplified generation scheme, this source will have many applications in probing electron dynamics with state selectivity in molecular systems and materials.

I would like to note here that the generation of such spectrally narrow EUV spectra, consisting predominantly of a single harmonic, is not restricted to short driving pulses. I have observed such spectra even with extremely long driving pulses (transform-limit of 45 fs). In this case individual harmonics become very narrow, indicating a very long EUV pulse envelope. The generation of such spectra appears to be related to the details of the alignment of the fundamental beam into the HHG fiber, and hence maybe to the spatial mode profile in the fiber. The negative dispersion of the EUV radiation that I observed in [154] could be consistent with phase matching of the long trajectory, that maybe occurs under special conditions in the fiber.

Our experiment starts with 30 fs laser pulses from a cryogenically-cooled 2 kHz

Ti:Sapphire laser amplifier, similar to the ultrafast laser amplifier systems present in hundreds of labs worldwide. We use a 1 m long, 400 micron diameter hollow waveguide filled with Argon gas to broaden the laser spectrum, and temporally compress the pulses using commercially-available negative chirped mirrors. We then focus the 13 fs, $2 \times 10^{14}\, Wcm^{-2}$ pulses into a 2.5 cm long, 150 micron diameter hollow-core waveguide [135] filled with Argon gas, in which the high harmonic radiation is generated. To temporally characterize the EUV pulse, we employ an interferometric EUV - NIR cross correlation geometry [36]. The EUV and fundamental driving pulse are focused into a Helium gas jet, and a cross-correlation signal is obtained from the generated photoelectron spectra as the relative delay between the two pulses is varied. The delay line makes use of the different divergences of the fundamental and the EUV beam. The low divergence, central EUV beam passes through a small circular Al filter suspended in a nitrocellulose filter. The annular fundamental beam, which passes around the Al filter, is reflected by an annular mirror, while the central EUV beam is reflected by a Mo/Si mirror that is mounted on a piezoelectric transducer to introduce a variable delay between the fundamental beam and the EUV beam. The Mo/Si mirror reflectivity is centered at ~ 47 eV with a FWHM ~ 13 eV, so that all harmonics generated in the waveguide are reflected. The photoelectrons ejected from Helium by the EUV beam are then detected using a magnetic bottle time-of-flight spectrometer and a multichannel plate (MCP) detector. This spectrometer has a $2 - \pi$ detection solid angle[86] i.e. photoelectrons parallel and perpendicular to the laser polarization (which points towards the MCP) are detected.

Figure 3.13(a) shows the experimental cross-correlation data. At large time delays between the EUV and NIR pulses, the photoelectron spectra are generated by the EUV light alone. The photoelectron peak generated by the dominant harmonic is clearly visible, as well as two adjacent smaller photoelectron peaks generated by the two adjacent weaker harmonics. When both EUV and fundamental beams are present,

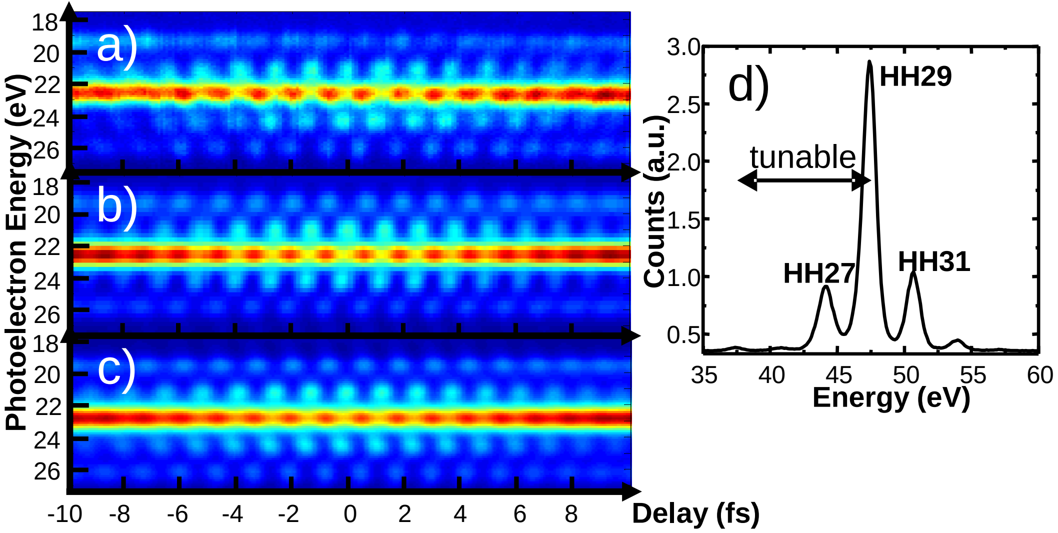

Figure 3.13: (a) Experimental photoelectron spectrum as a function of time delay between the EUV and IR pulses, when these pulses are focused simultaneously into He gas. (b) FROGCRAB simulation of the data in (a) based on theory presented in [101, 124]. (c) FROGCRAB trace obtained from a generalized projections (GP) algorithm. (d) EUV spectrum of the pulse that generated the photoelectron spectrum shown in (a). The energy tuning range is indicated. Tuning of the energy is achieved by changing the pressure and intensity inside the HHG waveguide.

sidebands occur due to the absorption of an EUV photon simultaneous with absorption or emission of a fundamental photon. The sidebands are modulated at a period corresponding to half the fundamental laser cycle. In the following, we use the FROG CRAB technique for a careful analysis of our data. FROG CRAB is inspired by the temporal characterization technique FROG, which is well established for the characterization of short laser pulses in the mid-IR to UV region of the spectrum [**?**, 164]. The temporal gate for FROG is usually an amplitude gate. Instead of an amplitude gate, FROG CRAB uses the fundamental field as a phase gate that modulates the electron wave packet ionized by the EUV beam. It is established that for most conventional FROG techniques [163], spectrograms will have a certain shape depending on the phase of the E-field to be measured. One might expect that the phase-gate used in FROG CRAB might generate nonintuitive traces [101, 124]. However, as we show below, this is not the case.

First, to gain intuitive insight in the properties of the generated radiation, as well as in the characteristic features of the FROG CRAB trace, we perform an iterative error minimization between the experimental FROG CRAB trace and a simulation. The results of this first analysis will be later fully confirmed by a second, independent analysis using an unrestricted pulse retrieval algorithm. To generate simulated FROG CRAB traces, we employed the strong-field-approximation expression given in [101, 124]. We adapted it to our experimental case where photoelectrons are detected over a $2-\pi$ solid angle, by averaging the photoelectron distribution for different angles including both a geometrical weighting as well as the differential partial cross section for detecting photoelectrons from Helium. Our FROG CRAB trace is the addition of two traces for the fundamental light, a cosine and minus cosine waveform. The reason is that we do not need phase stabilized laser pulses, and the conditions for generating high harmonics (phase-matching and recollision) are the same for both waveforms. For each delay step, photoelectrons are acquired for multiple laser shots, and therefore can contain signal from both waveforms.

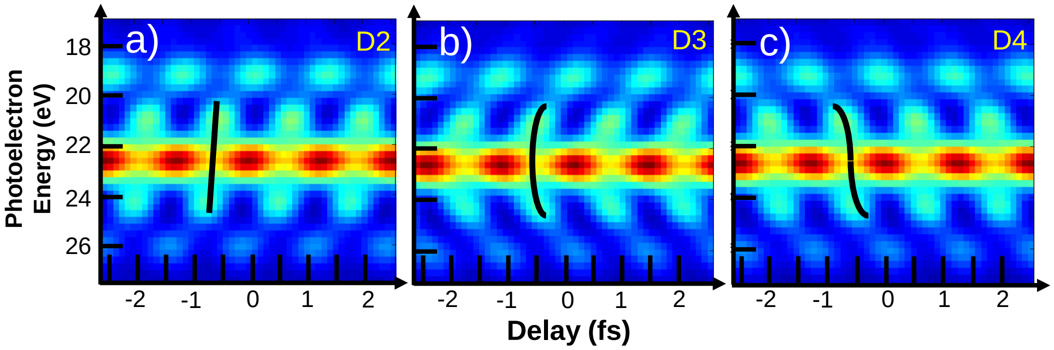

Figure 3.14: Simulated FROGCRAB data, when higher dispersion orders are artificially introduced into the EUV field: (a) 2nd order D2, (b) 3rd order D3, (c) 4th order D4 dispersion. Intuitively, the sideband shape shows the group delay of the EUV light, indicated by black lines.

Before turning to a detailed analysis of our EUV radiation using FROGCRAB, we first show that, although FROG CRAB uses a seemingly complex phase modulation gate, considerable intuition about pulse characteristics can be obtained from the shape of the sidebands. To demonstrate this, we apply individual dispersion orders to artificially constructed EUV bursts, similar to those generated in our experiment. Sample results of FROG CRAB traces are shown in Fig. 3.14, plotted over a delay range of two fundamental laser cycles. Figures 3.14(a) to 3.14(c) show that the shape of the sidebands changes significantly depending on whether 2^{nd} order phase D2 (Fig. 3.14(a)), 3^{rd} order phase D3 (Fig. 3.14(b)) or 4^th order phase D4 (Fig. 3.14(c)) is added. FROG CRAB traces can also indicate the sign of the dispersion order, because for opposite signs of dispersion, the sidebands are inverted along the time delay axis.

We now turn to a detailed analysis of our experimental FROG CRAB data. To construct the EUV electric field for the simulated FROG CRAB trace, we start with the EUV spectrum shown in Fig. 3.13(d), recorded using an x-ray spectrometer and CCD camera. This EUV spectrum is then deconvolved with the Gaussian x-ray spectrometer resolution function of 0.38 eV FWHM, determined by a separate measurement using spectrally narrow harmonics. (Using the measured EUV spectrum without deconvolution would underestimate the pulse duration by $\sim 5\%$). The deconvolved EUV spectrum is then multiplied by the transfer functions that relate the measured EUV spectrum to that incident on the detection gas. A spectral phase, described below, is added to the EUV spectrum $E(\omega)$, before transforming into the time domain. The calculated FROGCRAB trace is finally convolved with the measured photoelectron spectrometer resolution function of width $\Delta E = 0.7$ eV. This photoelectron spectrometer resolution E imposes an upper limit of approximately $h \cdot 0.44/\Delta E$ (h is Planck's constant) on the envelope duration that can reliably be measured. With the current resolution, we can characterize pulse durations up to 2.5 femtoseconds.

As shown above, we can retrieve higher order spectral phases with FROG CRAB. Therefore, in Fig. 3.15(a), we vary the 2nd order phase and compare the RMS (root-mean-square) deviation of the experimental and calculated FROG CRAB trace within

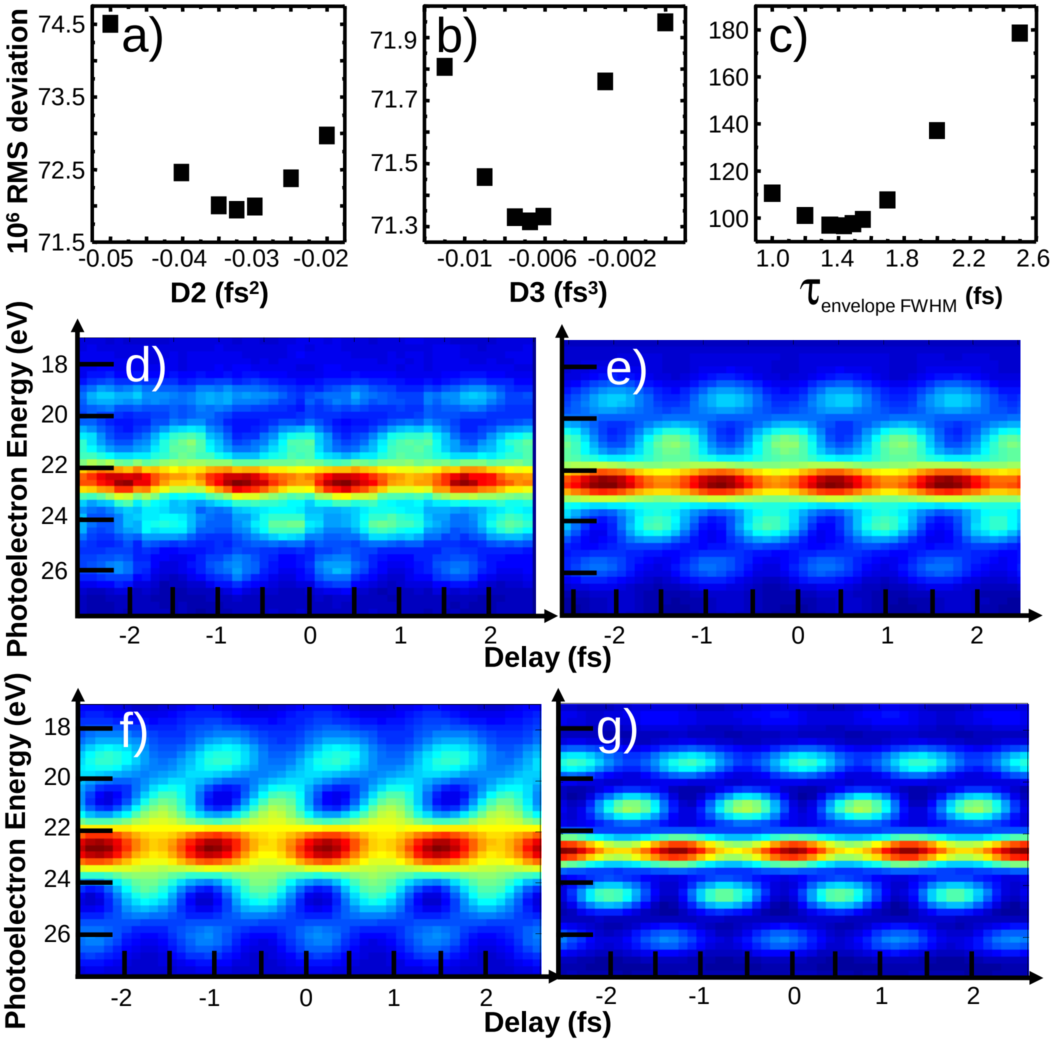

Figure 3.15: RMS deviation between the FROG CRAB simulation and the experimental cross-correlation trace as the parameters of the simulated pulse are varied: (a) Varying the linear chirp D2, (b) Varying the quadratic chirp D3, (c) Varying the EUV pulse envelope. (d) experimental FROG CRAB data, (e) FROG CRAB data simulated using the optimized values of D2, D3 and EUV pulse envelope of 1.4 fs. (d, e) are zoom-ins of the centers of Fig. 3.13 (a, b). (f), (g) simulated FROG CRAB data using the optimized values of D2, D3 but when the EUV pulse envelope is changed from the optimized value of 1.4 fs to 1 fs and 2.5 fs respectively. These traces do not match the experimental data.

the central 2 NIR field cycles. We obtain a 2^{nd} order phase of $D2 = -0.033\, fs^2$. Using the same procedure we obtain a minimum RMS deviation for third order dispersion at $D3 = -0.007\, fs^3$ in Fig. 3.15(b). The atomic phase of the detection gas, as well as contributions from the EUV mirror and the Al filters, are negligible at the EUV energies considered. Using the best values for the second and third order dispersions found in this way, we construct the simulated FROG CRAB trace, shown in Fig. 3.15(e). This agrees very well and in detail with the experimental trace in Fig. 3.15(d). The full simulated FROG CRAB trace is shown in Fig. 3.13(b), and compares excellently with the experimental trace shown in Fig. 3.13(a).

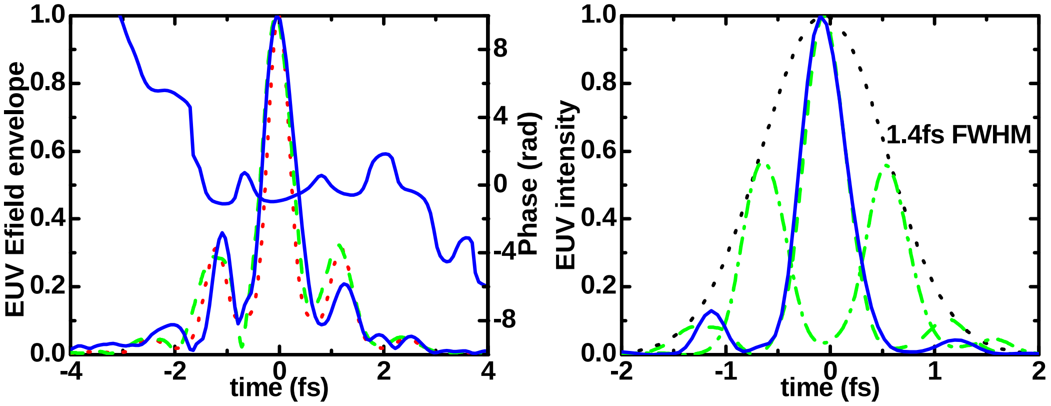

Figure 3.16: (a) Chirped EUV electric field envelope vs. time: (Dashed green) obtained from optimized fit shown in Fig. 3.13(b); magnitude (solid blue) and phase (solid blue) retrieved from a GP algorithm; (dotted red) transform limited pulse for comparison. (b) (Solid blue, dashed green): EUV intensities vs. time corresponding to the chirped pulses shown in (a); (dash-dotted green): intensity of a double pulse with the same envelope; (dotted black) intensity envelope of the extracted EUV field.

With the above analysis, we can now plot the correct chirped EUV electric field envelope, shown in dashed green in Fig. 3.16(a). For comparison, the transform-limited electric field envelope is also shown in dotted red. Figure 3.16(b) shows the intensity versus time of the chirped EUV pulse (dashed green), as well as the envelope corresponding to the transform-limited center harmonic for comparison (dotted black line). Figure 3.16 shows that the attosecond bursts are broadened from their transform-limited value of 360 attoseconds, to a chirped value of 470 attoseconds, while the total EUV radiation is contained in an overall intensity envelope of 1.4 ± 0.2 fs FWHM. This corresponds to a single burst with two $\sim 10\%$ sidelobes in the case of a cosine pulse. However, distinguishing a cosine from a sine pulse with two equivalent intensity bursts (dash-dotted green line in Fig. 3.16(b)) is not possible (Note that the two cases could be distinguised if a CEP stabilized NIR driving pulse was used for the temporal characterization - see Fig. 3.23). This is because the two FROG CRAB traces are equivalent - see Fig. 3.23. To validate the temporal FWHM EUV envelope extracted from our analysis, we also explored the effect of varying the envelope duration in our simulated FROG CRAB traces. We found that varying the pulse envelope also changes the widths and the shape of the FROG CRAB sidebands, as can be seen in the simulated FROG CRAB data for varying EUV pulse envelope in Fig. 3.15(e), (f), (g) for 1.4 fs, 1 fs and 2.5 fs respectively. A plot of the RMS deviation between the simulated and experimental FROG CRAB traces versus the EUV pulse duration is shown in Fig. 3.15(c). The best agreement is found for an EUV pulse duration of 1.44 fs (FWHM), in very good agreement with the duration of the EUV field reconstructed from the CCD spectrum for dispersions of $D2 = -0.033\, fs^2$ and $D3 = -0.007\, fs^3$. Furthermore we checked that including an additional quadratic phase around each harmonic (harmonic chirp [167]) leads to a worse agreement between the data and the fit.

To validate the results of our previous analysis, we performed an independent, unrestricted pulse retrieval using a Generalized Projections (GP) FROG CRAB algorithm. This algorithm has been adapted to our experimental situation in the same way as was discussed above for the simulated FROG CRAB traces, to take into account photoelectron collection over a $2-\pi$ solid angle, as well as the addition of two traces for the fundamental pulse, a cosine and minus cosine waveform, by calculating multiple FROG CRAB traces, and comparing an appropriately averaged trace to the experimental data. Calculated data are convolved with the photoelectron spectrometer resolution function. The detailed implementation of this algorithm will be the subject of a forthcoming publication [152]. The resulting reconstructed FROG CRAB trace is shown in Fig. 3.13(c) and shows excellent agreement with the experimental trace. The RMS error is 1%. The retrieved temporal electric field profile agrees quantitatively with the one extracted from our first analysis, and is shown in solid blue in Fig. 3.16(a). Analysis of the spectral phase of the retrieved electric field (not shown) yields second and third order dispersion coefficients $D2 = -0.032\,fs^2$ and $D3 = -0.025\,fs^3$ in excellent agreement with our first analysis, and in addition shows a small amount of harmonic chirp, but second (third) order terms around all harmonics are smaller than $0.1\,fs^2$ $(0.03\,fs^3)$, respectively. Such small amounts of harmonic chirp do not measurably influence the overall EUV pulse envelope, as confirmed by the EUV field retrieved by the GP algorithm, shown in Fig. 3.16(a), and by the analysis in [167].

Finally, we note that in earlier work [140], simulations predict a dynamically phase matched gated HHG regime, in which the EUV emission of one harmonic should be localized within an optical cycle, which is consistent with our present measurements. Numerical calculations of single-atom radiation on the other hand, predict EUV pulse durations of 6 fs or longer for our experimental parameters, suggesting the importance of a temporal phase matching that is reducing the EUV pulse duration in our geometry.

In conclusion, we have characterized the amplitude and phase of a complex extreme ultraviolet field with attosecond sub-structure. Using a hollow waveguide geometry we generate sub-optical-cycle pulses from relatively long 13 fs driving laser pulses. Using the FROG CRAB pulse measurement technique, we extracted the extreme ultraviolet waveform consisting of chirped 470 attosecond bursts, spaced by ~ 1.3 fs, within a 1.4 fs intensity envelope. We also showed that the sub-optical-cycle EUV pulses are near transform-limited, with a relatively narrow bandwidth of ~ 1 eV, making this source ideal for ultrafast state-selective molecular and materials spectroscopy. In this difficult temporal regime, where the laser fundamental cycle of 2.6 fs is comparable in duration to the EUV pulse, we have demonstrated that the FROGCRAB technique can be successfully used to bridge the gap in EUV pulse measurement capabilities between simple non-interferometric cross-correlation measurements, and RABBITT, which determines the time structure of individual attosecond bursts but not the overall envelope. Finally, we have shown that considerable intuition about the EUV pulse characteristics can be obtained directly from the FROGCRAB trace.

3.9 Characterizing isolated attosecond pulses from hollow-core waveguides using multi-cycle driving pulses

This section describes a second set of experiments, in which it is shown that an isolated pulse with duration of ≈ 200 attoseconds can result from CEP unstabilized, high intensity ≈ 15 fs multi-cycle driving pulses coupled into a hollow-core waveguide filled with low-pressure Argon gas.

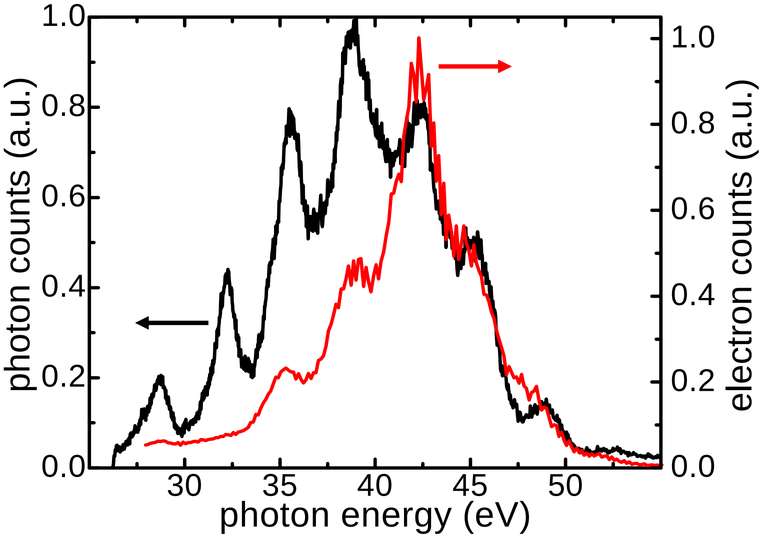

Figure 3.17: EUV spectrum recorded with an x-ray spectrometer (black), and corresponding photoelectron spectrum upshifted by the ionization potential (red). The difference in spectral shape is due to EUV mirror reflectivity (which is low at the lower photon energies).

In Figure 3.17 we show an experimental EUV spectrum using this x-ray spectrometer. The CCD spectrum shows a quasicontinuum centered around the 23^{rd} harmonic. We also show the corresponding unstreaked photoelectron spectrum, upshifted by the ionization potential of the gas. The difference in shape is due to the mirror reflectivity of Mo/Si EUV mirror used for focusing into the Neon detection gas jet (Mo/Si multilayer mirror centered at $\approx 47\,eV$ with a FWHM $\approx 13\,eV$). This mirror therefore provides a spectral filtering which suppresses the lower harmonics and results in a continuum centered around the 25^{th} harmonic.

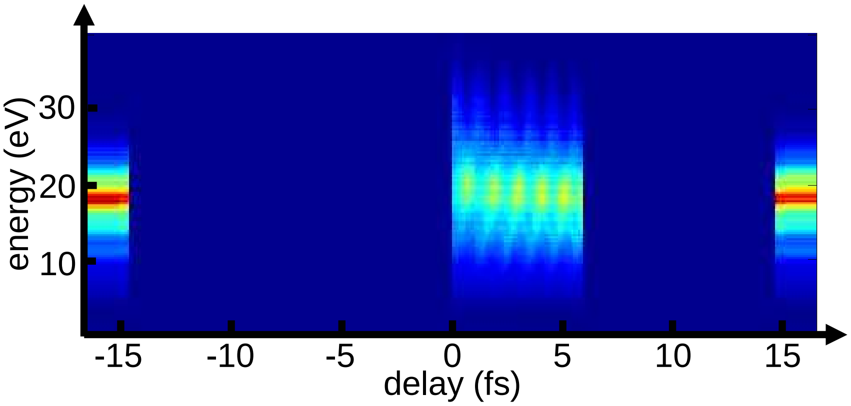

Figure 3.18: Retrieval of a partial FROG CRAB trace. Experimentally, a small range $(0-6$ fs) of delay steps were taken with high temporal resolution. In order to retrieve the EUV pulse, the data are embedded into a larger array with zeros, with "unstreaked" spectra (recorded without the fundamental light present) attached at large delays.

To accurately retrieve an EUV pulse, we obtained high temporal resolution data for 2.5 laser cycles near to zero delay, with delay steps of 100 attoseconds. For such a "partial" FROG CRAB trace to converge, however, it is necessary to terminate the trace with a range of "unstreaked" spectra. Therefore we used a photoelectron spectrum generated by the EUV radiation alone and attached it at the edges (around ±15 fs delay) of the experimental FROG CRAB trace as seen in figure 3.18. The convergence errors are calculated only for regions where data actually exist.

Figure 3.19 shows the experimental photoelectron energy resolved two-color cross-correlation and the FROG CRAB trace retrieved using the GP algorithm, as well as the EUV reconstructed electric field and intensity. Here, the G_{error} was 1.7%. The retrieved single isolated attosecond pulse has a FWHM pulse duration of 210 attoseconds with negligible ($\sim 5\%$ electric field amplitude) sidebursts, and a second-order dispersion of 0.009 fs^2. The agreement in the central energy range is good, while at high energies,

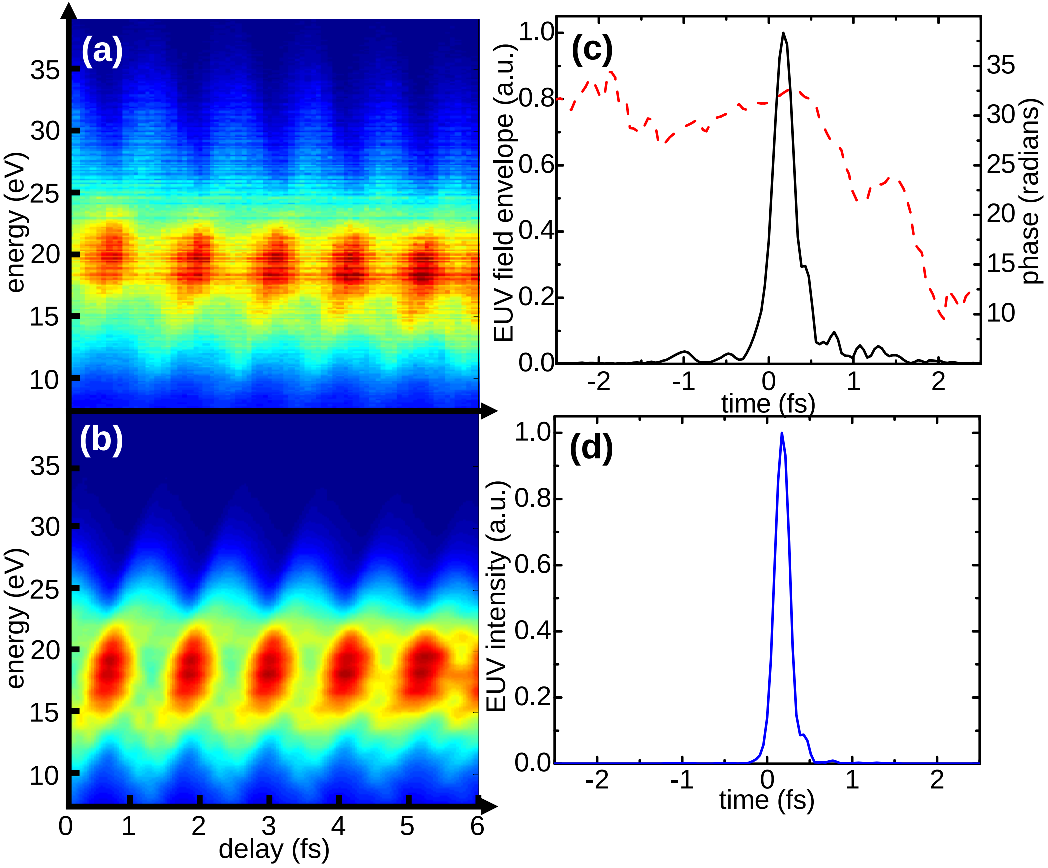

Figure 3.19: (a) Zoom-in on the experimental photoelectron energy resolved two-color cross-correlation shown in Fig. 3.18. (b) FROG CRAB trace retrieved using the GP algorithm. (c) Reconstructed EUV electric field envelope and temporal phase. (d) Reconstructed EUV intensity yielding a FWHM pulse duration of 210 attoseconds.

the ponderomotive shifts are not correctly recovered using the algorithm. This is due to the approximation of the W-dependence in Eq. (3.8) by W_0, as we will show below.

3.9.1 Direct simulations of FROG CRAB traces

In this section we employ directly simulated FROG CRAB traces. We first show that such direct simulations can reproduce the experimental two-color cross-correlation spectrogram shown in Figure 3.19(a). Such direct simulations allow more freedom to explore the effect of specific pulse parameters on FROG traces, or to address specific concerns regarding the retrieved pulse, than is possible using the automated GP retrieval algorithm. We then turn to a more general discussion, showing that in almost all situations, the EUV electric field can be retrieved without carrier-envelope phase stabilization, with one important exception that we point out explicitly. Finally, we show that in direct simulations, which in contrast to the GP algorithm do not make use of the approximation $W \to W_0$ in Eq. (3.8), the large ponderomotive upshifts seen in the experimental trace are reproduced correctly.

To simulate FROG CRAB traces, we employed the theory described in section 3.4, and adapted it to our experimental situation, again by appropriately weighting FROG CRAB traces obtained for different angles θ, and for CEP $= 0$ and CEP $= \pi$. All simulated traces were convolved with the experimentally measured photoelectron spectrometer resolution function, a Gaussian of 0.73 eV FWHM.

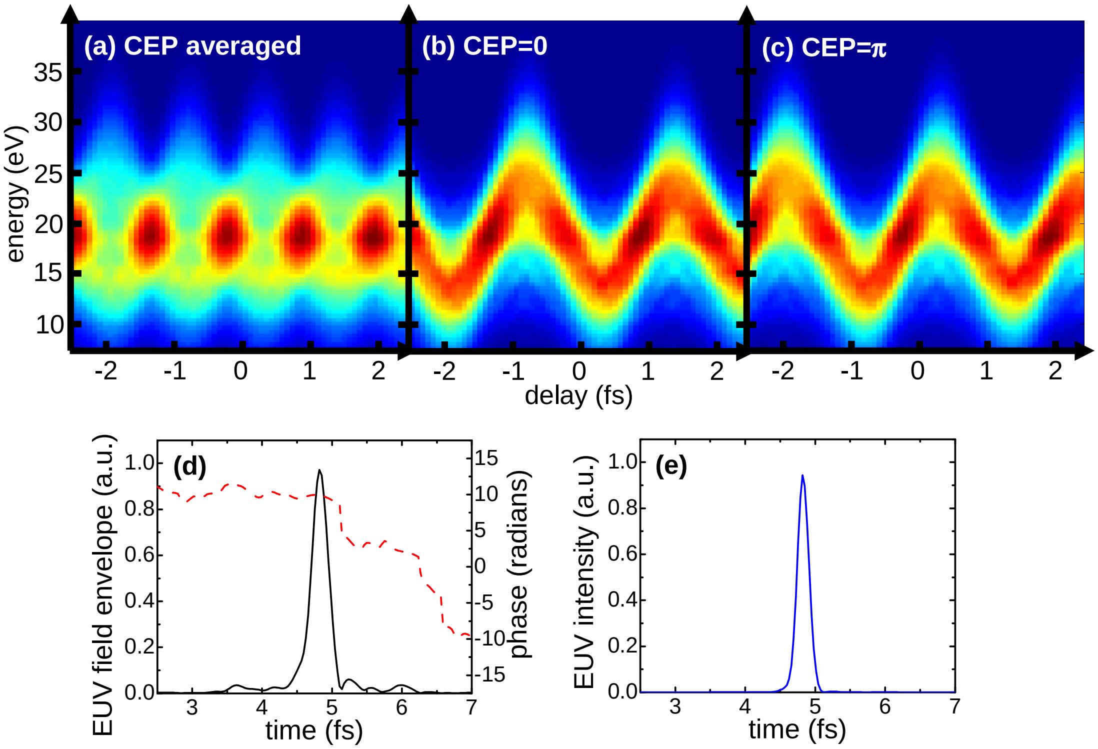

Figure 3.20: Simulations for (a) averaged CEP, (b) CEP $= 0$, (c) CEP $= \pi$, (d) retrieved EUV field envelope and phase, (e) intensity of 200 attoseconds FWHM pulse duration.

In Fig. 3.20 we show the results of the direct simulations yielding the best fit to the experimental data shown in Figure 3.19(a). In addition to the final averaged trace (Fig. 3.20(a)), we also show the individual traces for CEP $= 0$ and CEP $= \pi$ (Fig. 3.20(b) and (c)). The retrieved single isolated attosecond pulse has a FWHM pulse duration of 200 ± 25 attoseconds, in good agreement with the result from the algorithm, and a second-order dispersion of 0.005 fs^2. The error in the pulse duration was determined by an observation of a clearly visible discrepancy between measured and simulated FROG traces. The Fourier limited duration was 185 as. We again point out that in these direct simulations we do *not* make the approximation $W- > W_0$ in Eq. (3.8), yielding improved agreement in the strongly streaked regions compared to the GP algorithm (Fig. 3.19).

To generate the FROG CRAB trace above, first the gate function (i.e. the fundamental field) was obtained by optimizing agreement between simulation and full trace experimental data taken at larger delay steps of 300 attoseconds. These data are shown in Fig. 3.21. The retrieved fundamental pulse has a FWHM pulse duration of $15fs$, $U_p = 0.54eV$ and a linear chirp of $\Gamma_2 = 0.0185fs^{-2}$.

Secondly, the simulated FROG CRAB traces were optimized with respect to the experimental FROG CRAB traces through a progressive fitting procedure by minimizing the root-mean-square (RMS) deviation between the simulated and experimental FROG CRAB traces. To this end, we include spectral phase terms describing the attochirp [167] resulting in a chirped x-ray field in time which is used as input in the simulations.

We used direct simulations to explore the question whether the measured FROG CRAB trace might be explained by an attosecond pulse train, as opposed to a single burst. In the case of an unchirped pulse train, already the CCD spectrum would reveal a comb of well resolved harmonics, contrary to what we observe in Figure 3.17. Therefore we explored the possibility of a pulse train with a significant femtochirp [167, 19]. In this case subsequent portions of the train would generate energy-shifted harmonic combs, such that the time-integrated measured spectrum appears as a continuum. We explored

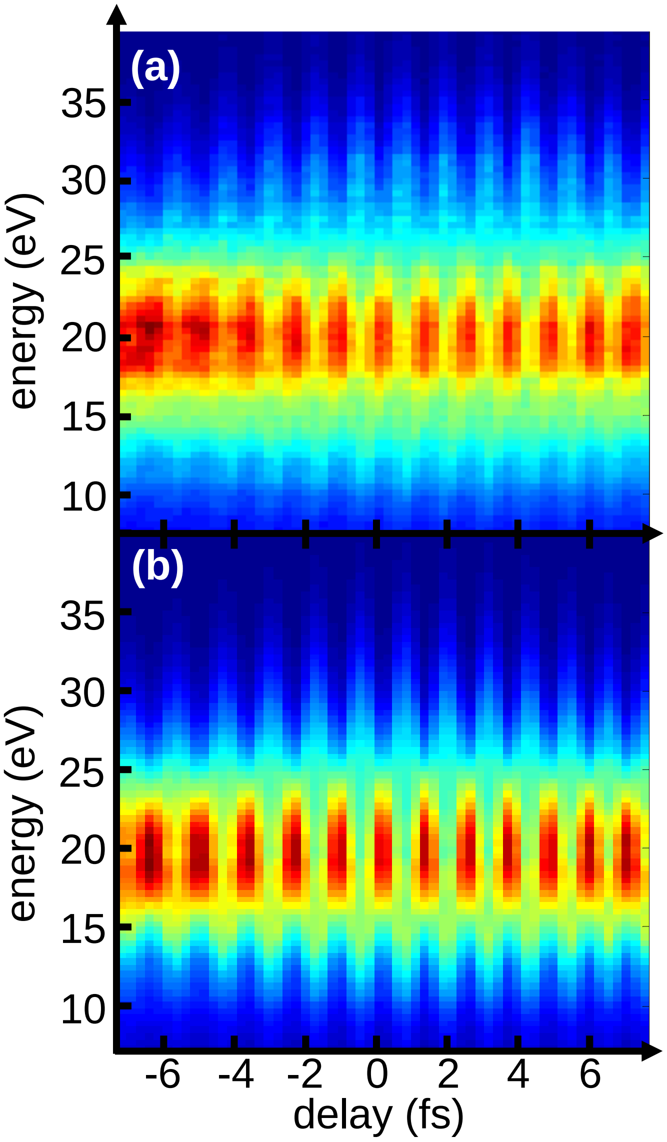

Figure 3.21: (a) Experimental data of complete FROG CRAB trace (b) Simulations of experimental data shown in (a), used to extract NIR fundamental pulse parameters.

a wide range of values for Γ_2, and find that such FROG CRAB traces are always significantly modulated. Representative simulated data are shown in Figure 3.22. From the amount of modulation in the calculated FROG CRAB traces, in comparison to experiment, we can set an upper limit on the energy contained in possible side bursts, of about 5%. Although it is impossible to test for all possible chirp patterns, our results strongly suggest that our experimental data are incompatible with a strongly chirped attosecond pulse train.

A last point of concern is the following: A number of measurements so-far have shown that the harmonic peaks in a spectrum can under certain conditions shift with the CEP value [7, 112]. However these observations were all made with very short driving pulses of ~ 6 fs duration. We have calculated the phase that the electron acquires while in the continuum (harmonic phase) using the classical electron trajectory for the short quantum path. It is the difference in this phase between the two dominant half-cycles contributing to radiation (see Fig. 3.25 below) that determines the spectral position of harmonic peaks. We calculate this harmonic phase difference for different values of the CEP, and find that for our harmonics in the plateau region the corresponding shifts of harmonic peaks in frequency are negligible (~ 0.2 eV) [112]. This is in agreement with earlier calculations using the saddle-point approximation that find strong effects of CEP on high harmonic generation in the high-plateau and cutoff region only when very short driving pulses are used [112], whereas the amount of CEP-dependent spectral shift of the harmonic peaks decreases upon increasing the driving pulse duration.

We now turn to a more general discussion of the possible ambiguities in CEP unstabilized vs. stabilized FROG CRAB traces. The left column of Figure 3.23 shows simulated FROG CRAB traces for a single gate of CEP=0 radians, as would be measured in an experiment with CEP stabilized pulses, while the right column shows FROG CRAB traces averaged over two gates (CEP $= 0$ and CEP $= \pi$ radians). The figure shows that both for isolated attosecond bursts (Fig. 3.23(a)) as well as for attosecond pulse trains containing more than 2-3 bursts (Fig. 3.23(d)), the CEP does not need to be stabilized for reconstruction of the temporal structure of the EUV field. Only when working in the regime intermediate between a single isolated attosecond pulse with small $\approx 10\%$ intensity pre- and post pulses, (Fig. 3.23(b)) and a double pulse (Fig. 3.23(c)) there exists an ambiguity in the FROG CRAB traces. This is the intermediate regime we studied in [154]. This ambiguity can be removed by stabilizing the CEP of

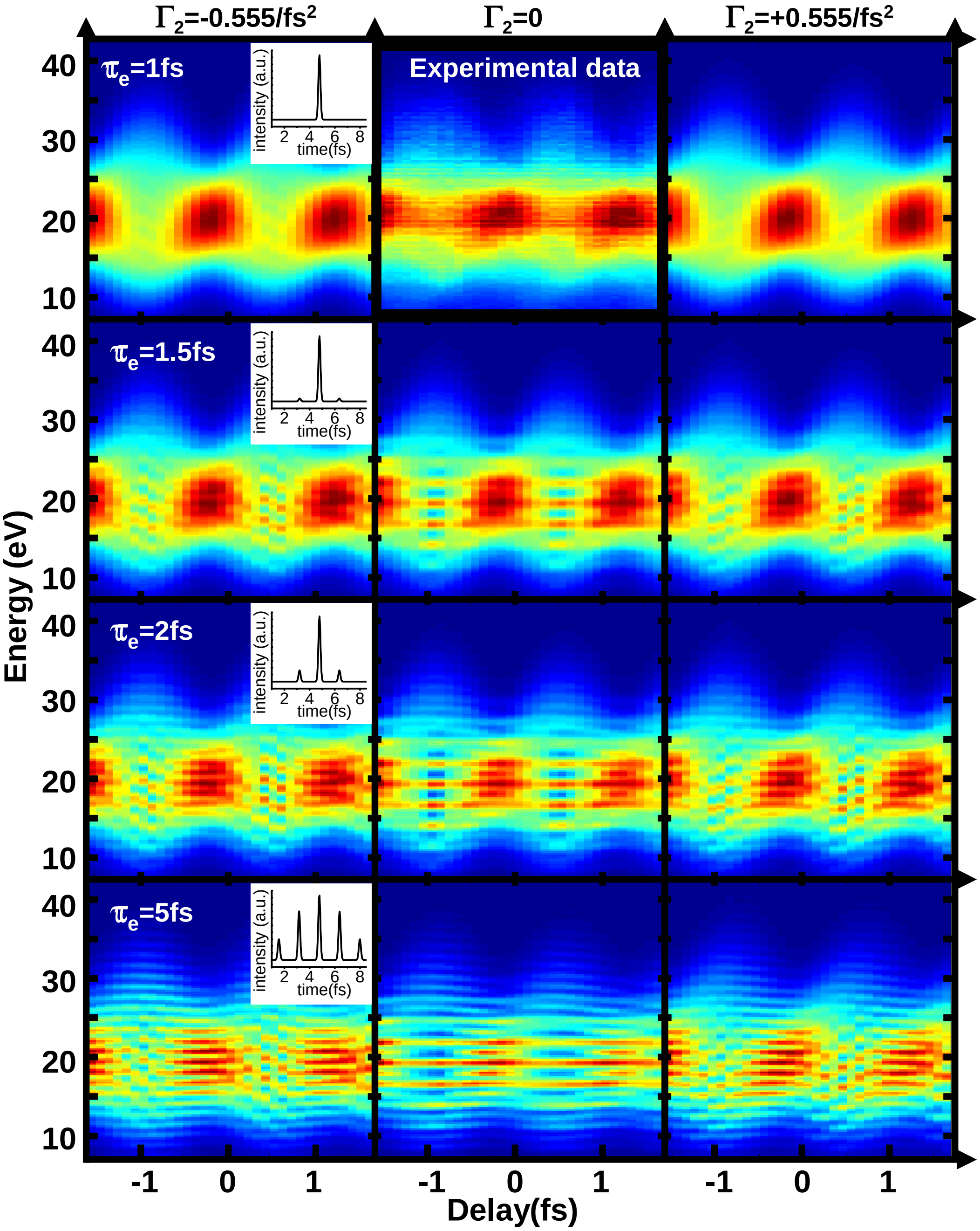

Figure 3.22: Simulations of chirped attosecond pulse trains. Top row center: experimental data for comparison. Γ_2: femtochirp parameter in $1/fs^2$. τ_e: envelope of the simulated EUV pulse trains (see insets). First row: $\tau_e = 1$ fs corresponds to an isolated attosecond pulse with two, 10^{-3} intensity side bursts. $\tau_e = 1.5$ fs: two, 5% intensity side bursts. All simulated traces with $\tau_e > 1.5$ fs show significantly more spectral modulation than the experimental data. Simulated traces have been convoluted with the experimental photoelectron spectrometer resolution function.

the fundamental laser pulse. While the position of the burst(s) underneath the envelope cannot be determined without CEP stabilization, the attosecond pulse structure of the individual attosecond bursts, as well as the overall intensity envelope, can be retrieved [154].

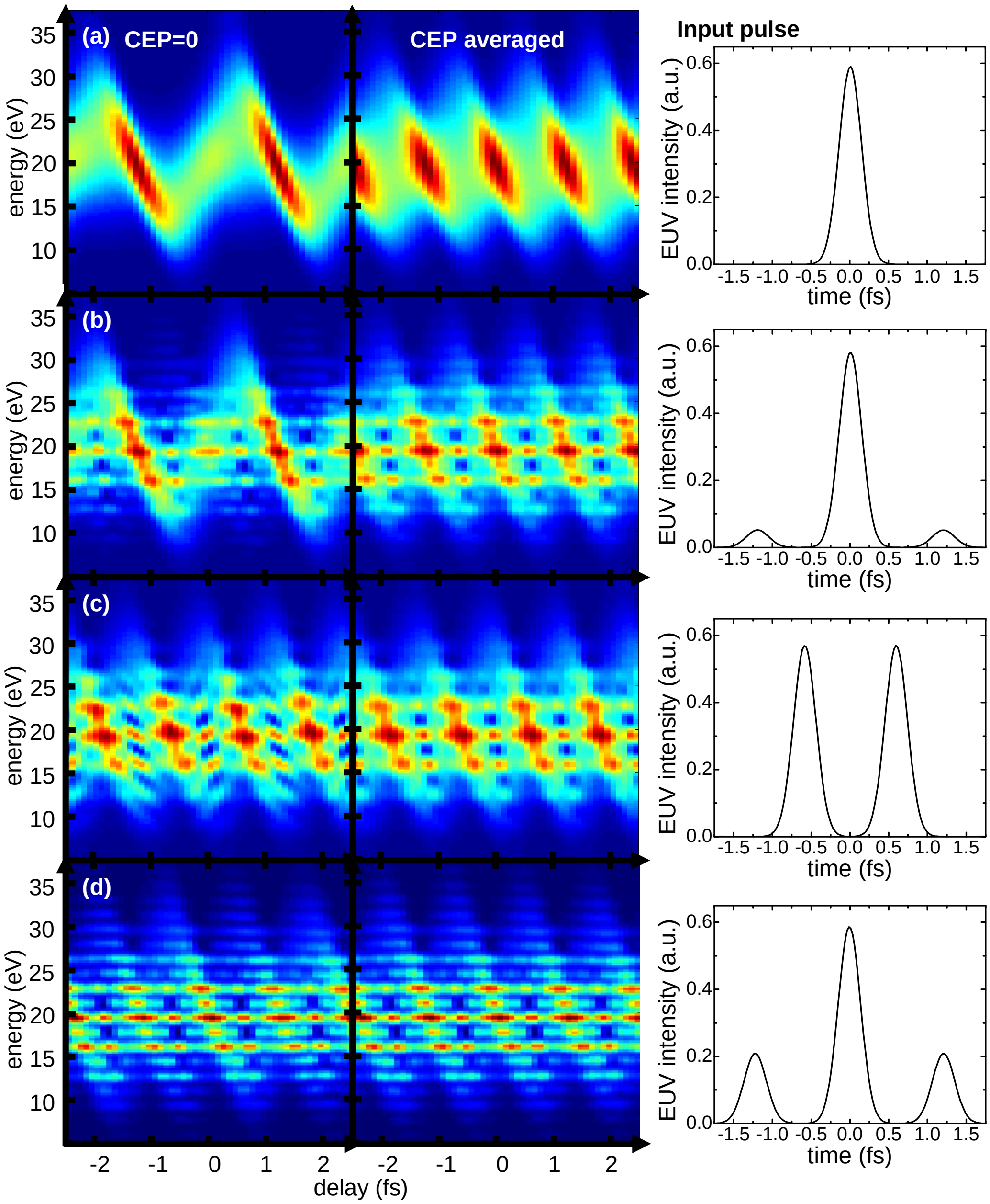

Figure 3.23: Simulations of FROG CRAB traces for different number of EUV bursts. Left column: CEP stabilized traces; middle column: CEP unstabilized traces obtained by averaging over CEP 0 and π; right column: EUV intensity of input pulses.

Lastly, we compare the reconstructed traces using the GP algorithm (Fig. 3.24 (b)) which does not contain the dependence on final photoelectron kinetic energy, with the progressive fitting simulation code (Fig. 3.24 (c)) which contains the final photoelectron kinetic energy dependence. Visually it is obvious that the simulation code achieves a better agreement with the experimental trace Fig. 3.24 (a) than the GP algorithm with the $W \rightarrow W_0$ approximation. Also, in the simplified geometry (2° photoelectron detection angle and CEP stabilized) of [141] there is a systematic error between experimental and reconstructed trace due to this neglected energy dependency, which leads to ponderomotive shifts that are too weak at high photoelectron energies and too strong at low photoelectron energies. It was found [101] that this energy dependence is only negligible if the bandwidth of the attosecond pulse is small compared to the center energy, which is not fulfilled in [141] and the data presented here.

Thus it would be desirable that reconstruction algorithms such as the GP and PCGP [81] include the energy dependence in future implementations.

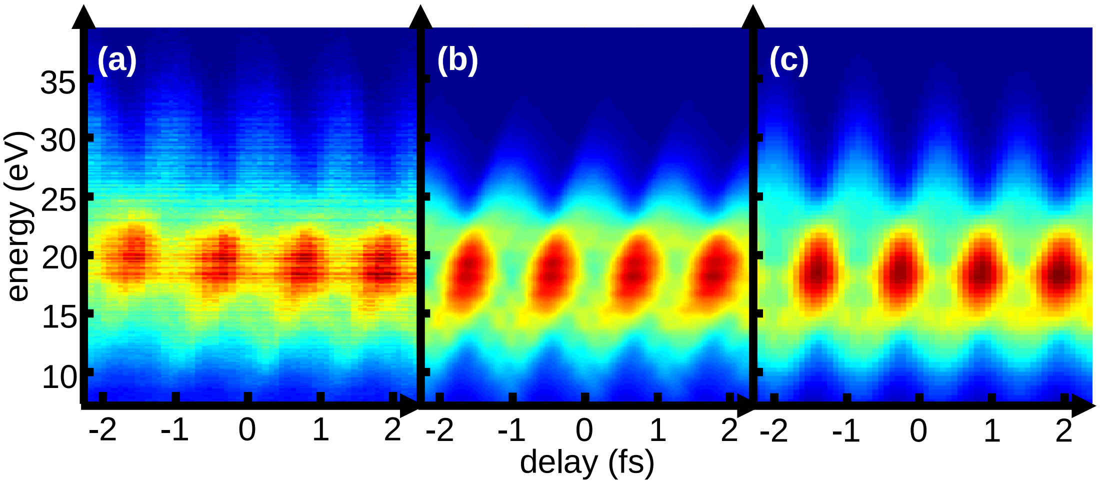

Figure 3.24: Comparison of (a) experimental data, (b) GP algorithm, and (c) direct simulations of FROG CRAB traces using optimized EUV pulse parameters.

3.9.2 Interpretation of single attosecond pulse generation mechanism

In this section we give a qualitative explanation for the main experimental result described in section 3.9, which demonstrates the generation of a single isolated attosecond pulse from a ≈ 15 fs, CEP unstabilized driving pulse. In essence, under our experimental conditions, efficient EUV generation is only possible on the leading edge of the driving pulse, before the coherence length gets too short due to the rapidly rising time-dependent ionization caused by the high-intensity driving pulse.

On the leading edge of a femtosecond pulse, every consecutive half-cycle has a higher instantaneous intensity, so that in each half-cycle a new spectral range of EUV radiation with a higher cutoff than in the previous half-cycle can be generated, see Fig. 3.25 (a). This has been described in [60, 22, 122] and recently named "half-cycle cutoffs". If now from one half-cycle to the next, high harmonic generation can be suppressed, then the last half-cycle produces a spectral continuum corresponding to the bandwidth of radiation that was not accessed in the previous half-cycle. If lower-energy emission produced in more than one half-cycle is spectrally filtered out, a single isolated attosecond pulse remains.

In our case, a dynamic phase mismatch between driving laser and EUV radiation provides the mechanism that rapidly shuts off EUV generation. The phase mismatch is given by

$$\Delta k(t) = q \cdot k_{laser}(t) - k_q \tag{3.22}$$

where k_q is the wave vector of the q'th harmonic, and the fundamental laser wave vector $k_{laser}(t)$ is given by [135]

$$k_{laser}(t) \approx 2\pi/\lambda + \frac{2\pi N(1-\eta(t))\delta(\lambda)}{\lambda} - N\eta(t)r_e\lambda - \frac{u_{nm}^2\lambda}{4\pi a^2} \tag{3.23}$$

Here, N is the total gas density (neutral gas plus plasma), $\eta(t)$ is the time-

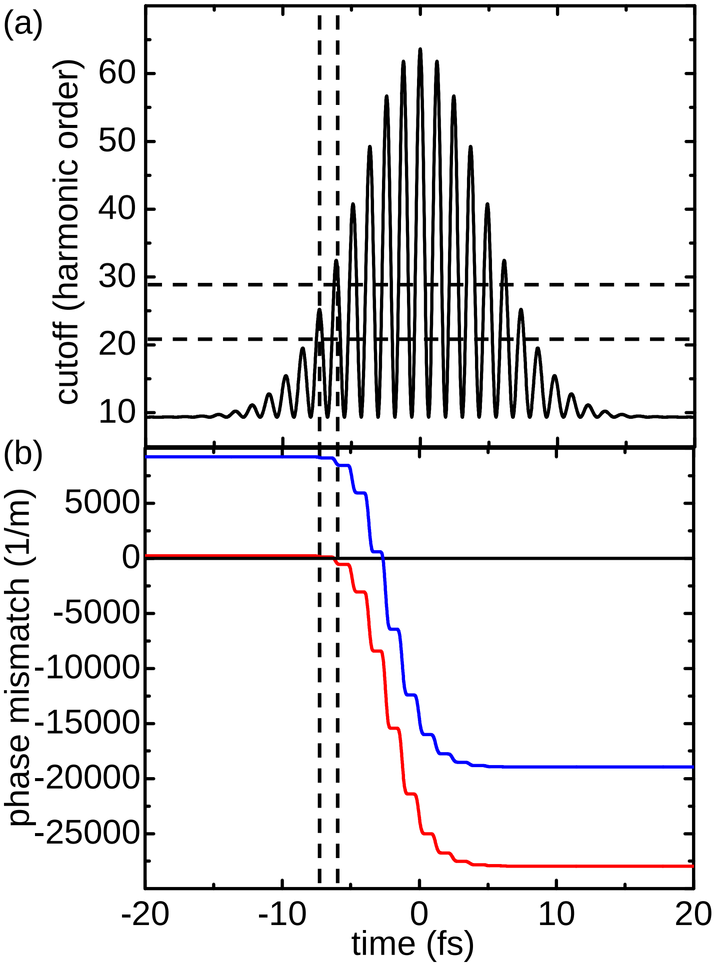

Figure 3.25: (a) EUV cutoff harmonic as a function of time, determined from instantaneous intensity. (b) phase mismatch [135, 54] for the 25^{th} harmonic versus time for straight fiber (red), effect of employing a QPM fiber for same pulse parameters (blue). Horizontal dashed lines: region of experimentally generated EUV spectrum. Vertical dashed lines: guides to the eye highlighting the half-cycles in which efficient EUV generation is possible: Earlier, the instantaneous intensity is too low to generate the experimental spectrum (lower harmonics are absorbed in the generating Argon gas, and not reflected by EUV mirror). Later, large phase mismatch prevents coherent build-up of EUV radiation.

dependent ionization fraction, $\delta(\lambda)$ describes the dispersive characteristics of the atom, r_e is the classical electron radius, a is the waveguide radius, and u_{nm} is the m^{th} root of the $(n-1)^{th}$ Bessel function of the first kind and depends on the transverse modes coupled into the waveguide. The EUV radiation is not significantly affected by any of the three dispersion contributions, and its wave vector k_q in Eq. 3.22 is only slightly modified from its vacuum value. In our low-pressure Argon, as shown in Fig. 3.25 (b), initially the phase mismatch is small, and EUV generation can occur. As soon as the intensity starts to increase rapidly on the leading edge of the pulse, it generates a very rapidly increasing plasma density. This growing plasma contribution sweeps the phase mismatch through zero and then to large negative values, such that high harmonic generation is suppressed for all later half-cycles.

The spectral filtering of lower harmonics (produced in several of the early half-cycles), required to isolate a single attosecond pulse, is achieved by the Mo/Si EUV mirror focusing the radiation into the detection gas jet. In addition, low harmonics are already strongly absorbed in the Argon gas. Note that there could also be some spatial filtering by the small EUV mirror [48], similarly as in the experiment of Ref. [63].

To further support the ionization gating mechanism we performed propagation simulations for the driving laser with the purpose of finding the best pressure and laser peak intensity parameters for ensuring phase matching at a specific time window. The propagation equation we used is a one dimensional version of the extreme-nonlinear optics propagation equation developed by Geissler et al.[53] modified to include neutral gas dispersion and waveguide dispersion. The ionization of the medium was calculated using an ADK-based model[145]. As the generated high harmonics propagate with virtually no dispersion they can be considered to propagate at the speed of light. Because the propagation equation is calculated in a frame moving at the speed of light the degree of overlap of the laser pulse as it propagates in the medium with the one at the beginning of the medium is a measure for the temporal phase mismatch: at those times where there is perfect overlap the generation of the high harmonics would be completely phase matched. A similar approach was used to explain the generation of sub-optical cycle, CEP insensitive, EUV pulses [140]. To find the best parameters for our case we defined a phase-matching-criterion: the temporal overlap in the desired time-window divided by the temporal overlap outside this time window, integrated over the propagation coordinate, should be as large as possible. The time window was defined as the interval between the moment the laser intensity is high enough for generation of the 21st harmonic to the moment it is high enough for the generation of the 29th harmonic (as indicated in Fig. 3.25). Plots of this phase-matching-criterion are shown in Fig. 3.26 a-b for two different values of CEP. Warmer colors correspond to better phase-matching-criterion. We note that the best pressure is almost the same for the two different CEP values while the best peak intensity changes by $\sim 10\%$ indicating only a small sensitivity to the CEP value. The estimated best peak intensity is different by only ten percent from the one estimated in the experiment while the estimated best pressure is about half of that estimated in the experiment which at such low pressures (~ 10 Torr) could be within the experimental estimation error. In Fig. 3.26 c-d the laser pulse at the end of the medium overlapped over the pulse at the beginning of the medium is shown for the two CEP cases for the best parameter values. As can be seen the overlap is optimized at the desired time window.

The numerical results of Fig. 3.26 indicate a blue-shift in the spectrum. This does not agree with measurements of the spectrum before and after the fiber, which showed only a small amount of reshaping. The reason for this discrepancy is that we used here one-dimensional simulations relevant only to the center of the radial laser intensity profile where the nonlinear conversion process is most efficient. Taking into account the radial intensity distribution combined with the low pressure within the fiber would wash out this blue-shift in a spectral measurement. For example, simulations we did indicate that once the field amplitude reduces to 60% of its peak value the spectral blue shift is only around 10% of the spectrum FWHM. In addition, the simulation assumed the same pressure conditions all along the fiber, while in the experiment a pressure gradient towards the end of the fiber could also reduce the spectral distortion. While the radial averaging reduces the spectral distortion, it does not destroy the dynamic phase-matching mechanism: the length scale needed for this mechanism is on the order

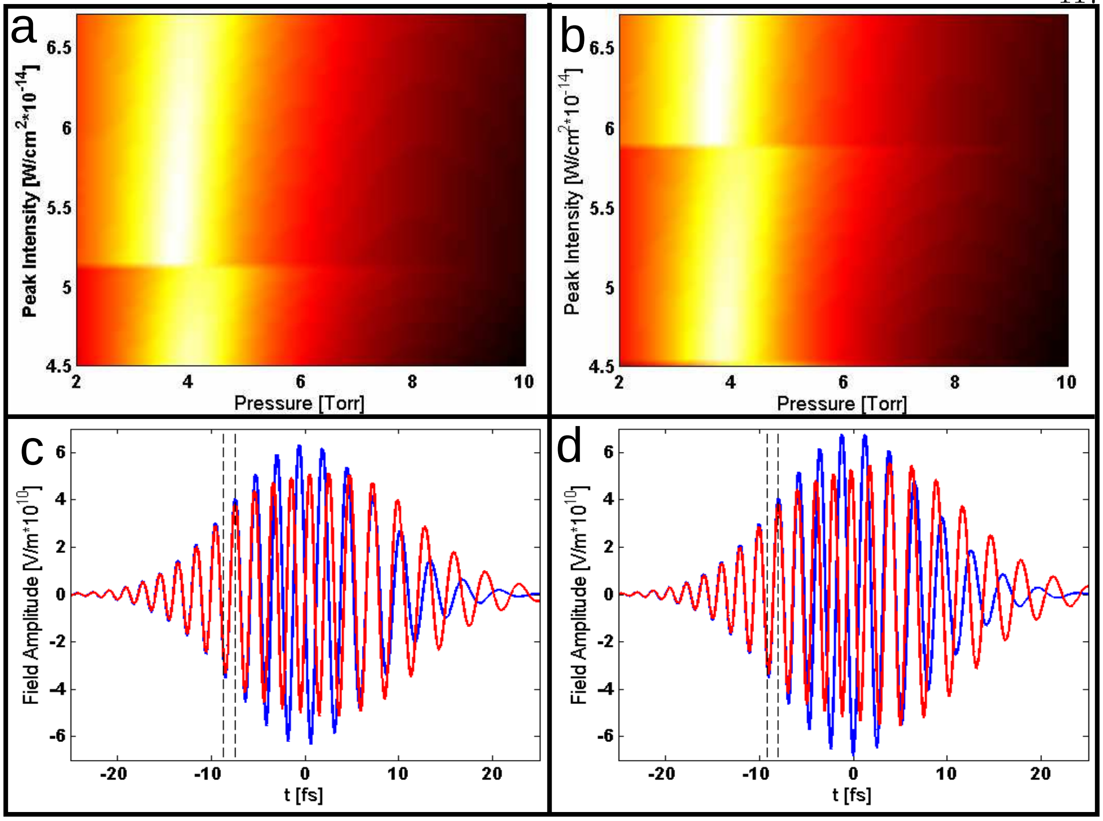

Figure 3.26: Phase matching conditions for ionization gating. Phase-matching-criterion for the time window in which the 21st-29th harmonics are first generated as a function of the laser peak intensity and gas pressure for (a) $CEP = \pi/2$ (b) $CEP = 0$. Warmer colors represent better phase matching. The corresponding temporal overlap of the laser pulse at the end of the medium (red) over the pulse at the beginning of the medium (blue) is shown in (c) and (d).

of several coherence lengths (a few mm).

3.9.3 Conclusion and Outlook

In Section 3.8 [154] we reported a technically simplified method for generating sub-optical cycle EUV radiation, consisting of either a single attosecond burst with a small pre-and post-pulse, or a double attosecond burst. The radiation was spectrally narrow (~ 1 eV) and energy-tunable simply by changing pressure and intensity in the hollow waveguide, making it a very useful tool for future investigations of state-selective molecular and materials dynamics.

In the other EUV regime studied [152], we have shown experimentally that it is possible to generate a single isolated attosecond pulse with ≈ 15 fs driving pulses, by using dynamic phase-matching in a noble-gas filled hollow-core waveguide combined with spectral filtering.

To temporally characterize the attosecond pulses, we have used photoelectron energy resolved two-color cross-correlation and both a GP algorithm and direct simulations of the FROG CRAB traces. These were both extended from the conventional, angularly restricted photoelectron detection and CEP stabilized fundamental pulses, to a more efficient $2-\pi$ detection scheme and CEP unstabilized pulses. Both reconstruction methods agree very well on the temporal structure of the EUV pulse, finding a near-transform limited isolated EUV burst of ≈ 200 attoseconds FWHM (Section 3.9). The generation mechanism in this case is limited to the energy range we observed: as the pressure in the waveguide is increased, the quasicontinuous spectrum evolves towards separated harmonics. Adjustment of other parameters such as e.g. the pulse energy may make it possible to extend this study to the generation of attosecond pulses with tunable center wavelength. In addition, the use of different generation gases in the hollow-core waveguide and spectral filtering with EUV mirrors may allow for tuning. While the position of individual harmonics is only weakly CEP dependent in our regime, it remains to be studied if tunability of the spectral envelope (i.e. center energy) could be achieved in a hollow-core waveguide by changing the CEP of the driving pulse, as was shown for a 2 mm gas cell [122].

We believe that macroscopic effects [49, 3] are an important parameter for single attosecond pulse generation and can be used to generate tunable isolated attosecond pulses from multi-cycle driving laser pulses. One possible route to change the center wavelength of the attosecond pulse would be to employ quasi-phase-matching (QPM) methods [23]. In QPM one employs e.g. periodically modulated fibers to add a constant offset to the phase mismatch. This offset is tunable by changing the modulation period, and allows to shift the phase-matching window in time (see figure 3.25), and thereby one could phase-match half-cycles of different instantaneous intensities. This could create a very short temporal window closer to the maximum intensity of the laser pulse and therefore could lead to the generation of a continuum at higher energies.

Alternatively, the use of spatiotemporal shaped driving pulses for isolated attosecond pulse generation could be investigated [168, 49]. This technique produces fundamental pulses with a fast rising edge, which should be well suited for generating isolated attosecond pulses.

Finally we note that the spatial mode profile of the driving laser in the hollow-core waveguide is a very important parameter in determining the spectral and temporal structure of the generated EUV radiation, and that therefore it is worth studying the separate contributions from the spatial mode profile and temporal profile of the fundamental pulse in detail [172].

Chapter 4

Combining femtosecond-EUV pulses with the COLTRIMS technique as a novel spectroscopy method in molecular physics

This chapter contains material published in [156].

4.1 Introduction

While the previous chapters dealt with the generation and temporal characterization of high harmonics, in this chapter we turn our attention to applications of table-top extreme ultraviolet pulse sources.

The unique properties of EUV radiation, such as good coherence [12], short wavelength (allowing for imaging with high spatial resolution) [138], femtosecond and even attosecond time resolution, high brightness, high repetition rate, tunability, compactness and the temporal synchronization with the NIR driving pulse, make it a unique source for time-resolved pump-probe spectroscopy. Recently, pump-probe experiments using high harmonic radiation have led to the tomographic reconstruction of the highest occupied molecular orbital of N_2 [72] and proton dynamics in molecules as well as structural rearrangement after removal of an electron was probed [6]. The excellent time resolution of high harmonic radiation also makes it an exquisite source to study highly excited molecular states, which have been difficult to study so far. Excited states can either be emerging from inner valence shell excitations or outer valence excitations that can occur in combination with shakeup processes (where one photon excites one electron into the continuum and a second electron into a higher lying state). Near-infrared femtosecond pulses can also be used in combination with EUV radiation to perform pump-probe experiments. NIR pulses are used e.g. for the study of strong-field phenomena [120] or to create aligned molecular samples[146].

Combining the exquisite time resolution obtained with femtosecond near-infrared pulses or EUV pulses, with sensitive detection techniques such as a COLTRIMS (COLd Target Recoil Ion Momentum Spectroscopy) apparatus (which provides single-particle sensitivity, coincidence capabilities, and 3D momentum imaging, as presented below), creates a very powerful tool for molecular physics. New information can be gained about unknown excited states, arising from inner- or outer valence shell excitation, as was e.g. demonstrated in [51], where the potential curve of a shake-up state was determined by means of a known Coulomb explosion channel. Very fast dynamics of inner-valence excitations such as from an Auger decay [106, 37] or other autoionization processes can be time-resolved. The coincidence detection of electrons and ions and their respectively complete momenta allows for the measurement of molecular-frame photoelectron angular distributions, which are very complex and reveal detailed information e.g. about theoretically challenging correlated multi-electron dynamics in molecules [30].

In the following I will describe a pump probe experiment using few femtosecond EUV pulses and a COLTRIMS apparatus to answer a very basic open question in molecular physics: What is the orientational dependence of molecular photoionization (see artist's impression in Fig. 4.1)? To this end, first an aligned sample of gas-phase molecules must be created. In our experiment, molecules are impulsively aligned by means of intense femtosecond pump pulses. The excited molecular rotational wavepacket experiences revivals even a long time after the pump pulse has left. During such revivals the molecular axes change their orientation from parallel to perpendicular with respect to the polarization of the pump pulse within a few 100 femtoseconds. Therefore photoionization by femtosecond EUV pulses with variable delay during a re-

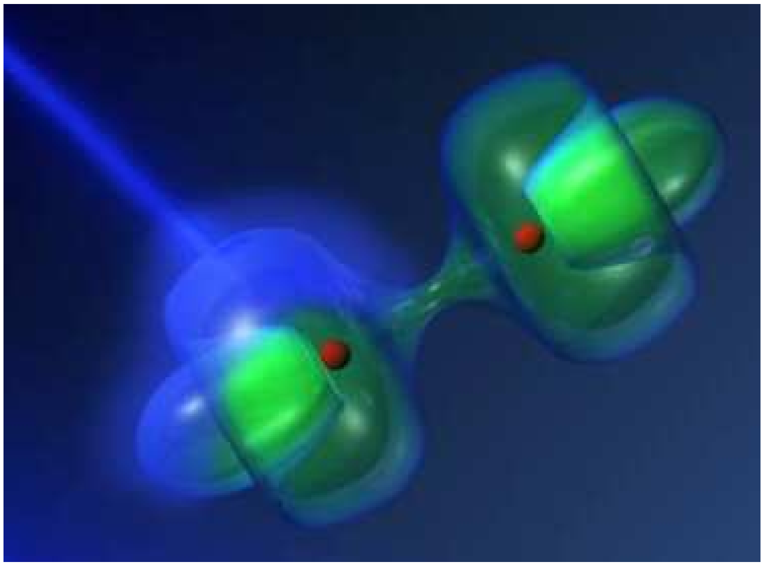

Figure 4.1: Artist's impression of molecular photoionization. Credit: Greg Kuebler

vival is equivalent to photoionization of molecules with different orientation. The high energy (here $\sim$ 42 eV) of the probe pulses leads to the ionization of molecules into non-dissociating and dissociating channels, whereby for both channels the angle-dependent probability for single-photon photoionization could be measured. With this novel spectroscopic method the orientational dependence of single-photon photoionization of N_2 and CO_2 into non-dissociating channels, as well as a long-lived state of CO_2 could be measured for the first time.

In the following I will therefore introduce the COLTRIMS technique (Sections 4.2 and 4.3), give an introduction to molecular alignment (Section 4.4), and present our experimental results on the angular dependence of photoionization (Section 4.5).

4.2 The COLTRIMS technique

The COLTRIMS technique [34, 39] permits the coincidence detection and reconstruction of the full 3D momentum vectors of all charged particles (electrons and ions) which result from one individual molecular reaction. In the simplest case, the reaction could be the fragmentation of an individual molecule under irradiation with ultrashort intense laser pulses or EUV pulses, or collision with an energetic particle. Importantly, the COLTRIMS technique has multi-hit, coincidence capability and reconstructs the full 3D momenta. In contrast, e.g. the velocity map imaging (VMI) technique only records a 2D image and reconstructs the full momentum by an inverse Abel transform for systems with cylindrical symmetry [40], limiting studies to a fraction of systems containing cylindrical symmetry. A disadvantage of the COLTRIMS technique, or any technique measuring coincidences, is that the event rate of generated electron-ion pairs per laser pulse needs to be much smaller than one to avoid false coincidences. COLTRIMS was developed in Frankfurt (Germany) by Horst Schmidt-Böcking and coworkers starting in the '70s and has been commercialized in the '90s by Roentdek [34, 39]. It has been applied to systems in the gas phase as well as to surfaces.

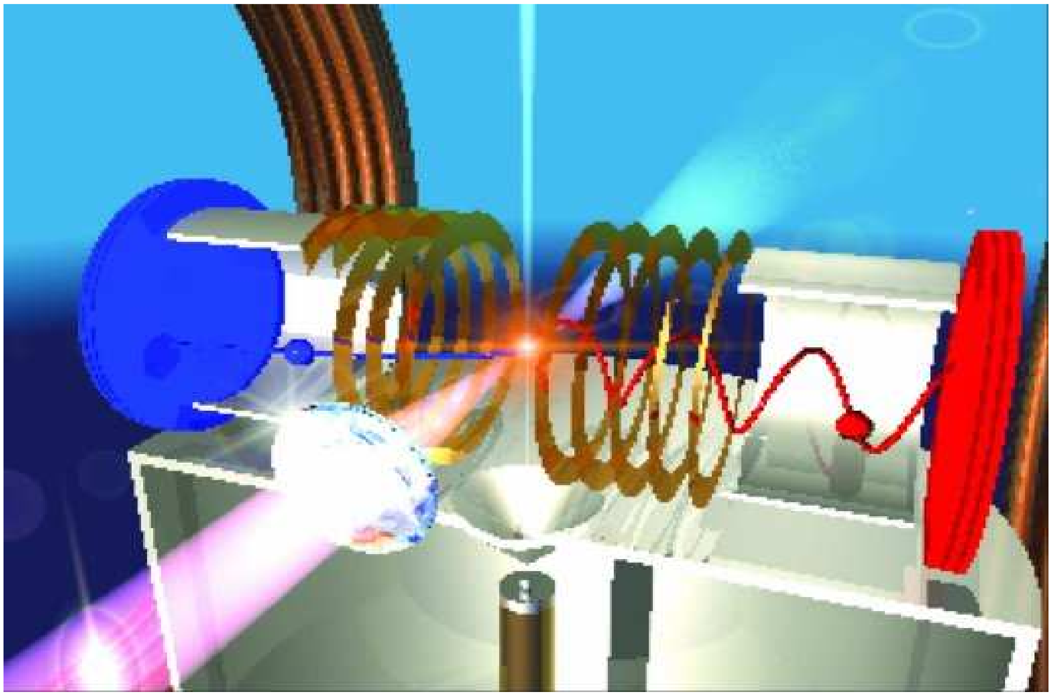

Figure 4.2: The COLTRIMS setup. A light source is focused onto a gas jet in the center of the apparatus. The ion (blue trajectory) and electron (red trajectory) are guided to opposite time-and position sensitive detectors (red, blue) by electric and magnetic fields. Taken from [1].

Figure 4.2 shows a schematic of the COLTRIMS setup: A light source is focused into a supersonically cooled gas jet where it causes a single ionization event. The ion (blue trajectory) and electron (red trajectory) are guided to opposite time-and position sensitive detectors by electric and magnetic fields, where they are detected in coincidence. All electrons and ions emitted into the full $4-\pi$ solid angle are collected. From time and position of the hit, the full three-dimensional initial momentum can be reconstructed, as will be described below.

In the following we give a short overview of the physical components of a COLTRIMS apparatus, the electronics used for reading out the detectors, available software for acquiring and analyzing the data and the setup of pump/probe beam lines.

4.3 Components of a COLTRIMS apparatus

4.3.1 Supersonic gas jet and COLTRIMS chamber

For gas-phase experiments, the target source is provided by a supersonic jet, shown in Fig. 4.3. This source provides a narrow initial translational velocity spread of target molecules as required for best spectroscopic resolution. In addition, internal degrees of freedom, i.e. rotations and vibrations, are cooled to have easier interpretable spectra. Lastly, it allows a small interaction volume with the laser beam - this is required, as the COLTRIMS does not provide focusing of particles generated at different positions transverse to the axis toward the detectors.

The COLTRIMS apparatus is built up around this gas jet. It consists of three main vacuum chambers at different operating pressures: a gas jet chamber, a detector chamber and a catcher. A steel tubing (1/4 inch) delivers the gas through an in-line filter to a 30 micron diameter nozzle, which is situated inside the gas jet chamber. The gas line tubing is backed by ~ 1 atmosphere of pressure, whereas the gas jet chamber on the other side of the nozzle is kept at $\sim 10^{-4}$ Torr by means of a 2000 l/s MAG

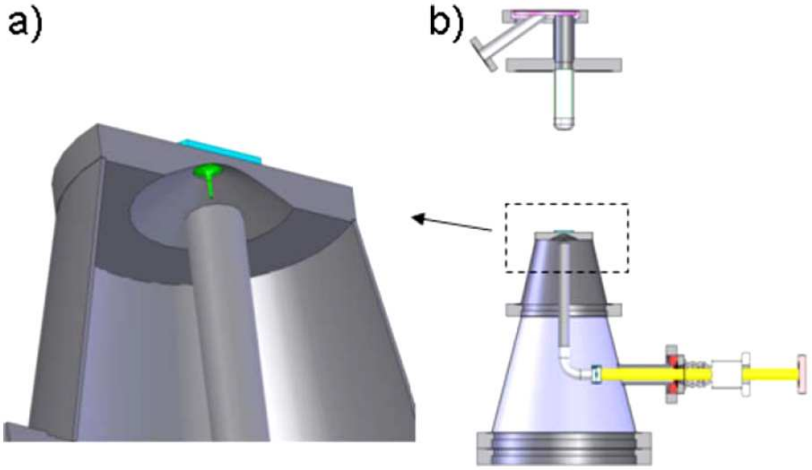

Figure 4.3: Setup of the supersonic gas jet. (a) green: the skimmer, located above the nozzle in which supersonic expansion and cooling occurs, transmits the central, transversely cold region of the jet, to the interaction region above. (b) gas delivery setup, and catcher (top). From [39].

turbo pump from Leybold backed by a rotary vane pump (Leybold HV Chemical (Trivac D65BCS), 75 m^3/hour). The pressure drop through the nozzle produces a supersonic expansion of the gas which cools it (This explains the "COLd Target" in the acronym COLTRIMS). Supersonic expansion happens even for expansion into a vacuum of 10^{-4} mbar. The position of the nozzle is adjustable via a 3-axis manipulator. The gas jet is then skimmed by a 300 micron diameter skimmer (13 mm downstream from the nozzle [39]) to further reduce its temperature and size. Thereby one selects the "zone of silence" (see Figure 4.4) which is the region where the gas reaches supersonic speed

$$v_{jet} = \alpha\sqrt{k_B T_0/m} \tag{4.1}$$

where $\alpha = \sqrt{7}$ for diatomic gases and $\sqrt{5}$ for atoms and T_0 is the temperature of the gas before the expansion. The gas jet exits through the skimmer into the detection chamber and reaches a diameter of 6 mm and internal temperature generally on the order of 100 mK ($T_{int} = \frac{5}{2}\frac{T_0}{S^2}$ where S is the speed ratio depending on the gas, temperature T_0 as well as nozzle diameter and the stagnation pressure p_0, see Fig. 4.4.).

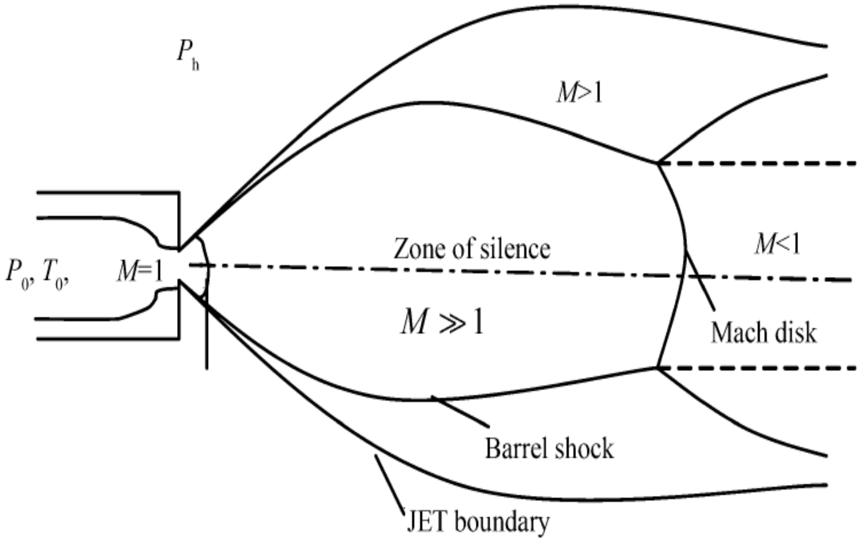

Figure 4.4: Schematic of a supersonic gas jet. The gas expands from the backing pressure region (left) into the supersonic zone of silence. The Mach number is the ratio of gas speed to the speed of sound. Adapted from [107].

The size of the gas jet limits the momentum resolution along the x-axis, which limits the total momentum resolution. The uncertainties of momenta along the y- and z- axes are smaller as they are given by the diameter of the EUV and NIR laser beams intersecting with the gas jet. The pressure in the detector chamber reaches 3×10^{-9} Torr without gas and $\sim 10^{-7}$ Torr with gas [39]. To maintain the high vacuum inside the detection chamber a catcher for the gas jet is brought as close as possible to the interaction region (limited by the dimensions of the electrodes that create an electric field around the interaction region). The catcher has a $250\,l/s$ turbo pump by Varian attached to it, backed by a TriScroll 600 pump from Varian (pumping speed $30m^3/hr$).

4.3.2 Electric and magnetic fields

Here I describe the electric and magnetic fields that guide the charged particles from the interaction region to the detectors. The electrons and ions generated in the interaction region are separated by a homogeneous electric field along the spectrometer axis, such that they are accelerated to opposite detectors (HEX-detector for electrons,

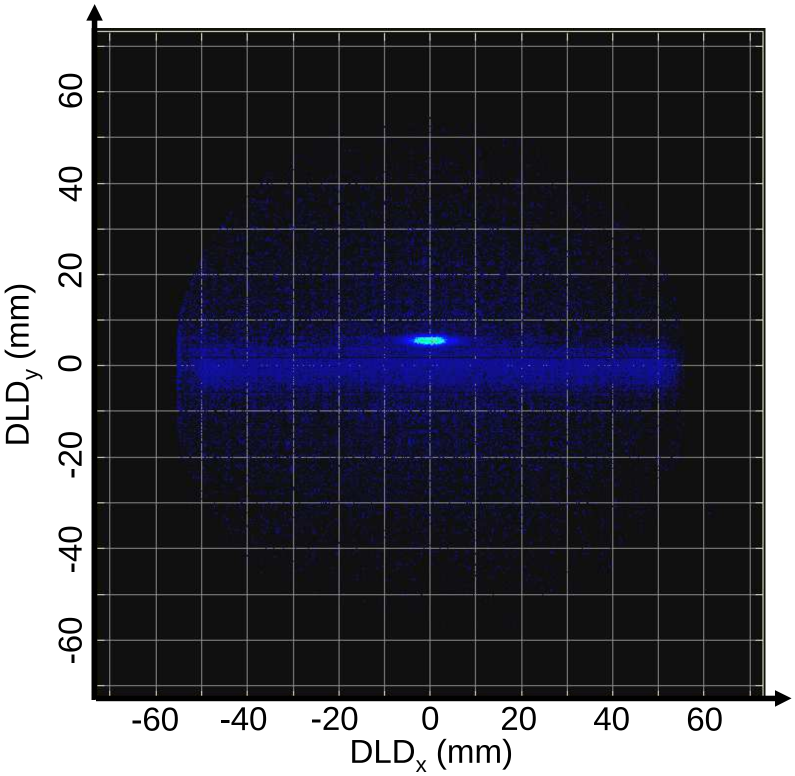

Figure 4.5: Ionization events from gas jet (intense spot) and background gas (diffuse band). The vertical offset, together with the time of flight, gives the gas jet velocity (4.1).

DLD-detector for ions, see below). This electric field is generated by applying a voltage over a chain consisting of alternating resistors (100 kOhm) and Copper square electrodes (41 electrodes with a center hole of 13 cm diameter spaced by 0.5 cm). The homogeneous electric field is properly terminated by transmission meshes (each about 80% grid transmission efficiency) in front of the detectors. While the ions only pass through an acceleration region of length $\sim$ 11.6 cm, the electrons traverse in addition to the acceleration region a field free drift region generated by two transmission meshes at the same potential. The drift region is twice as long (24.2 cm) as the acceleration region (12.1 cm). This design makes sure that electrons that are generated at slightly different positions in the interaction volume *along the spectrometer axis* arrive at the detector at the same time (Wiley McLaren time-lag focusing [171]).

In order to confine electron detection to the size of even the largest commercially available detectors, a magnetic field is required. This contrasts with the ions, for the following reason: Assume only an electric field E guides the electrons. The detector needs to be larger than a typical hit position $x_{hit} = v_{ini} \cdot TOF$. Inserting the time of flight TOF found from $L_{TOF} = \frac{1}{2}\frac{qE}{m}TOF^2$ gives $x_{hit} = v_{ini}\sqrt{\frac{2mL_{TOF}}{qE}} \sim v_{ini}\sqrt{m}$. Now compare the hit position on the detector x_{hit} for electrons and ions: Using momentum conservation in the ionization process $m_e v^e_{ini} = m_{ion} v^{ion}_{ini}$ one gets $x^e_{hit} = \sqrt{m_{ion}/m_e} x^{ion}_{hit}$. This means that electrons would require a detector $\sqrt{m_{ion}/m_e} \sim \sqrt{1836} \sim 40$ times larger than that required for the lightest ion!

An additional homogeneous magnetic field along the spectrometer axis is therefore used to confine electrons with large perpendicular momentum mv_{perp} to a cyclotron radius of $R = mv_{perp}/(qB)$. The strength of the B field is chosen to fill a good fraction of the electron detector. This magnetic field in principle affects the ions too, but the cyclotron period for ions $T_{cyc} = 2\pi m_{ion}/(qB)$ is in general much larger than the ion time of flight, so that the ion image is hardly affected.

The magnetic field is generated by two identical coated copper coils (10 gauge square copper wire with 100 turns) which are separated by a distance equal to the radius of the coils (Helmholtz geometry). Two coils with smaller radius are added at the far ends to extend the region of the homogenous magnetic field. In addition to these large coils creating a magnetic field along the z-axis, a set of 4 additional coils made out of 37 turns of computer cable are used to shield the COLTRIMS apparatus from the earth's magnetic field (~ 0.32 Gauss) and other laboratory generated magnetic fields (one pair of coils along the x-axis and one pair along the y-axis).

The experimentally chosen electric field strengths (typically several 100's V/m) and magnetic field strengths (typically $5 - 10$ Gauss) vary depending on the ions and electrons investigated in a reaction. As the electric field strength is the dominant parameter affecting the ions, its strength is generally adjusted such that a significant fraction of the ion detector is covered by the ion hits of interest. The magnetic field is then chosen such that electron hits fill the electron detector. However, one has to avoid electron flight times corresponding to integer multiples of the cyclotron period when all electron trajectories return to the initial transverse position irrespective of their momentum - this would severely degrade momentum resolution (see below). In general one needs to find a compromise between the spread of arrival times of the electrons with different kinetic energies (Does one want to look at only one electron or detect a second electron in coincidence?). In addition one wants to assure that all generated ions and electrons in the reaction are hitting the detector.

4.3.3 Electron and ion trajectories

4.3.3.1 Equations of motion for ions

In the following we will give the equations of motion for ions and electrons in an electric field E and a magnetic field B, both parallel along the z-axis. We will see that we can determine the complete initial momentum vector for any charged particle, by measuring its time of flight and its coordinates on a two dimensional position detector. Solving the equations of motion for ions, we find that the initial momentum components can be measured from the hit position $(x(TOF), y(TOF))$ on the detector as well as the time of flight (TOF) from the gas jet to the detector:

$$p_x = m \cdot \frac{x(TOF) - x(0)}{TOF} \tag{4.2}$$

$$p_y = m \cdot \frac{y(TOF) - y(0)}{TOF} - m \cdot v_{jet} \tag{4.3}$$

$$p_z = \frac{m \cdot L}{TOF} - \frac{q \cdot E \cdot TOF}{2} \tag{4.4}$$

where m is the mass of the fragment, and $x(0)$ is the x-position of the gas jet. For the initial momentum in y-direction we have to subtract the upward velocity of the supersonic gas jet v_{jet}. For p_z we have L which is the length from gas jet to detector and q the electric charge of the ion.

4.3.3.2 Equations of motion for electrons

For the electrons we also have to consider the B-field:

Starting with the equations of motion for x and y for the electrons

$$m\ddot{x} = -e\dot{y}B \tag{4.5}$$

$$m\ddot{y} = +e\dot{x}B \tag{4.6}$$

We can then define a new variable $\dot{\varphi} = \dot{x} + i\dot{y}$. Choosing the correct Ansatz $\dot{\varphi} = A \cdot \exp i\omega t$ the new variable $\dot{\varphi}$ and initial condition $\dot{\varphi}(0) = A = \dot{x}(0) + i\dot{y}(0)$, we can integrate $\dot{\varphi}$. This gives us the equations for the position hits on the detector, x and y, which can finally be solved for the initial momentum components p_x and p_y of the electron:

$$p_x = m\frac{b \cdot x - a \cdot y}{a^2 + b^2} \tag{4.7}$$

$$p_y = m\frac{a \cdot x + b \cdot y}{a^2 + b^2} \tag{4.8}$$

where $a = \frac{cos(\omega t)-1}{\omega}$ with $\omega = \frac{eB}{m}$ the cyclotron angular frequency and $b = \frac{sin(\omega t)}{\omega}$ and t is the time-of-flight.

Equations (4.7) and (4.8) show that the transverse momenta cannot be determined under the condition when $a^2 + b^2 = 0$. This is the case when the electron TOF is an integer i number of full cyclotron orbits ($\omega \cdot TOF = i \cdot 2\pi$) and all electrons return to their initial transverse position independent of their initial momentum, leading to a characteristic "fish" structure in the x-position/y-position vs. TOF image (see Figure 4.6). It is important to adjust the magnetic field strength B such that these "nodes" in the electron trajectories occur outside the range of electron momenta accessed in a given experiment.

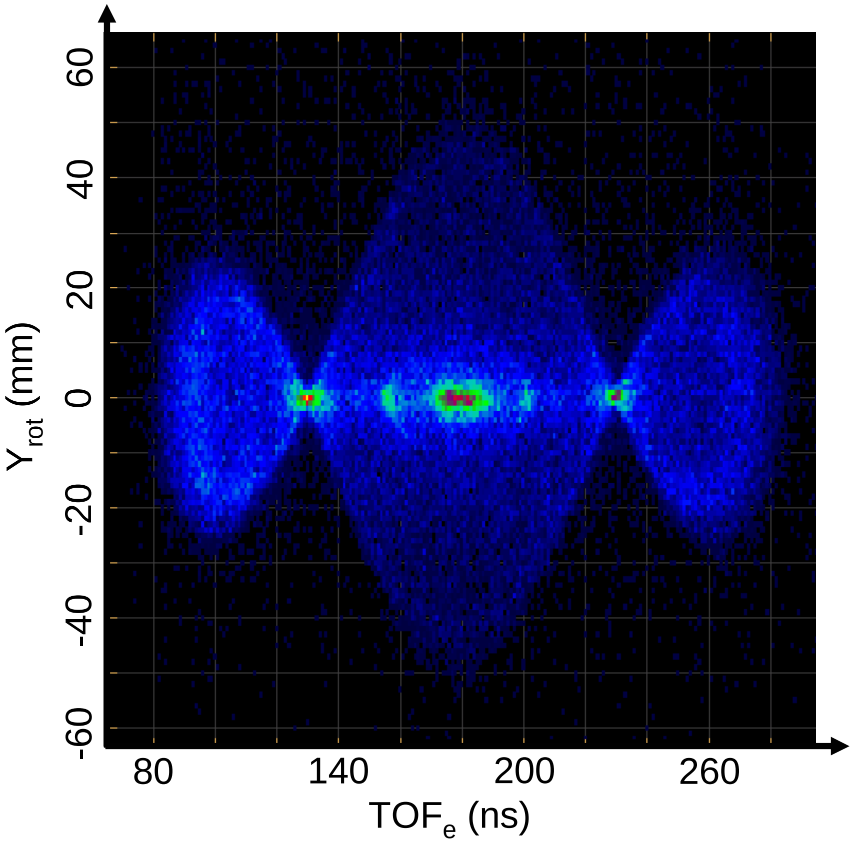

Figure 4.6: Magnetic field calibration using "fish" images (transverse electron hit position Y_{rot} versus time of flight). The time between the two nodes gives the cyclotron period and hence the magnetic field strength.

To calculate the initial momentum component p_z along the spectrometer axis we have to consider the motion in the electric field along the acceleration region and subsequent motion in the drift region. Solving the equation of motion in the acceleration region gives us:

$$m \cdot L_a = p_z^{initial} \cdot TOF_a - eE\frac{TOF_a^2}{2} \tag{4.9}$$

with L_a the acceleration region and TOF_a the time of flight in the acceleration region.

The equation of motion in the drift region gives us:

$$m \cdot (L_a + L_{drift}) = m \cdot L_a + (p_z^{initial} - e\,E\,TOF_a \cdot (TOF - TOF_a) \tag{4.10}$$

where L_{drift} is the drift region and TOF is the measured total time-of-flight. With the two above equations we can solve for the two unknowns $p_z^{initial}$ and TOF_a.

4.3.4 Detectors and electronics

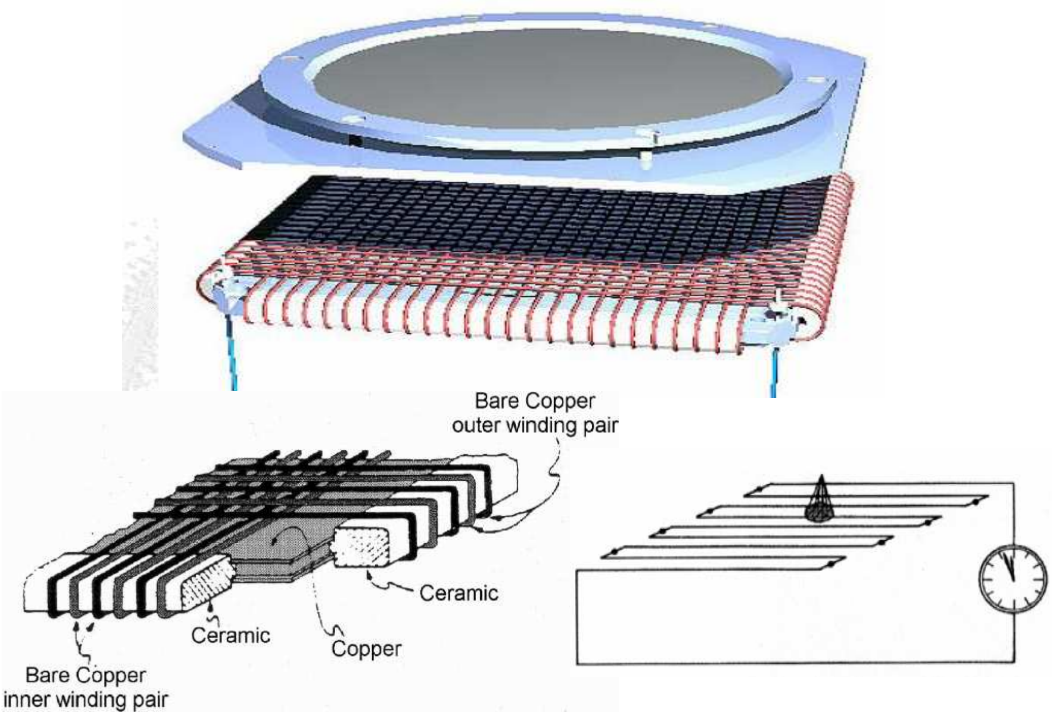

Figure 4.7: The DLD detector, taken from [57]. On top is a multichannel plate which amplifies an incident electron to a charge cloud that exits on the back side. The position of this cloud is recorded by a two-dimensional delay-line anode (one vertical and one horizontal wire wound into a grid). Position-sensitivity is achieved by measuring the time difference of two signals traveling on the delay line in opposite directions of the vertical and horizontal wire, respectively.

The core pieces of a COLTRIMS apparatus are the time- and position- sensitive detectors for the electron and ion fragments. The detector used for the ions was a 2-dimensional delay-line-detector including microchannel plates (MCPs in Chevron configuration) with an active area of 12 cm ($DLD120$ Roentdek), shown in Fig. 4.7. The detection principle is as follows: First an ion or an electron hits the microchannel plates (MCP) (MCP front biases can be varied from -4 kV to $+1$ kV). Along the microchannels this hit leads to a cascade of secondary electron emission. This amplified electron pulse gives the measured time-of-flight signal. Behind the MCP plates are the delay-line anodes which measure the position of the hit: The charge pulse created by the electron in the microchannel plate exits the back side of the MCP, where two wires are wound into a grid (see Fig. 4.7). Each wire provides spatial information in one dimension. The position of an electron hit is measured from the time difference of the charge pulses traveling to opposite ends of the wire [1] . In practice a pair of wires is used – a signal and a reference wire – where the signal wire is at a slightly higher potential of +40 V and therefore carries the electron pulse. The signal and reference wire create a transmission line that has the advantage of minimizing losses and dispersion of the current pulse, and is usually used for the transmission of high frequency pulses. It also allows to amplify only the differential signal and therefore to reject any noise picked up along the way on both wires. The signals are coupled out over an RC element and are then amplified. Even though the distance between adjacent wire windings is ~ 1 mm, the position resolution of the detectors is < 100 microns. This is because one can determine the center of charge of the electron cloud hitting the anode grid more precisely than the wire spacing. The spatial resolution is therefore really limited by the interaction volume defined by the gas jet and the laser beam widths. The count rate of detector can be 1 MHz but is limited by the attached electronics (see below). The time resolution is ~ 500 picoseconds.

The electrons are detected with a 2-dimensional Hexanode detector ($HEX120$) with the same properties as the ion detector, except that it includes a third layer of delay line wire offering redundant information which can be useful in cases where multiple electrons with similar time of flights or positions are detected in coincidence. This HEX detector is shown in Fig. 4.8.

The signals from the MCPs and delay-line-anodes are amplified and then constant

---

[1] Note that the wires traveling in the y-direction determine the x-position of the hit.

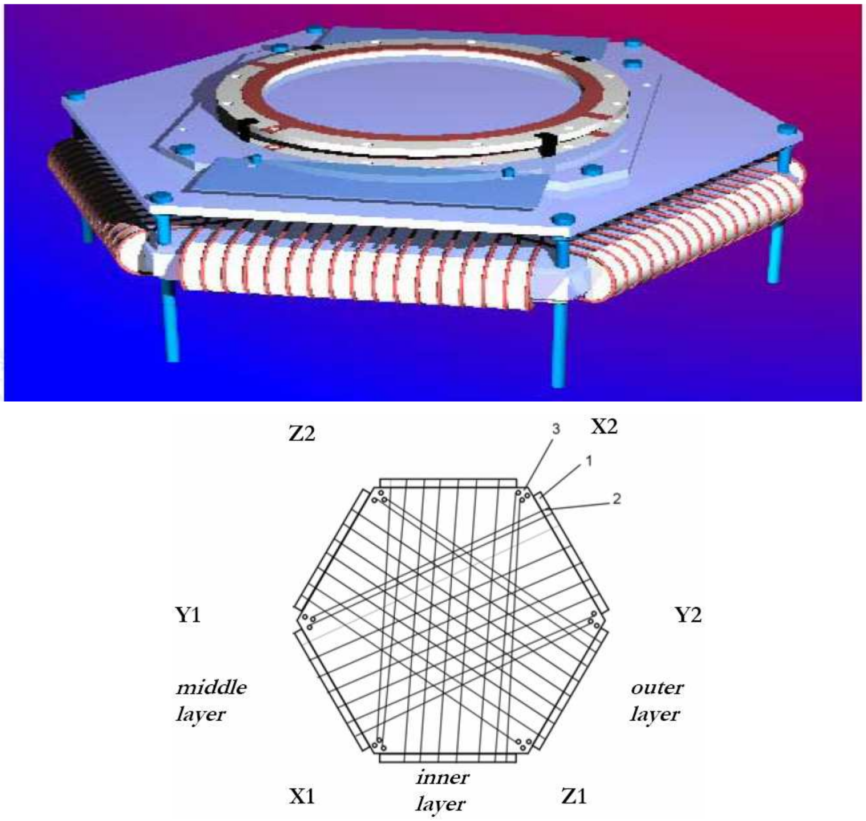

Figure 4.8: The HEX detector, taken from [57]. The principle is the same as for the DLD detector, with the exception of a third delay line offering redundant information for improved multi-hit performance.

fraction discriminators are used to create NIM (Nuclear Instrumentation Module) pulses (ATR19 Roentdek). A constant fraction discriminator takes input pulses and converts them independently of their peak height fluctuations into pulses that contain the accurate timing information of the input pulses, i.e. it creates a pulse output always at the same fraction of the input pulse. It also allows to set a threshold for the input signals and the created output NIM pulse has a precise shape and height of -0.9 Volts. The NIM signals are then fed into two synchronized time-to-digital converter boards ($TDC8PCI2$ Roentdek). Each TDC board has 8 channels (based on the LeCroy $MTD133B$ chip), can acquire data for a $32\mu s$ range with 500 ps resolution (16-bit dynamic range). It has multi-hit capabilities up to 16 hits with a multi-hit dead time of $\sim$ 10 ns. Data

Table 4.1: Typical potential settings for COLTRIMS electric field.

DLD				
Signal/Reference	Holder	MCP back	MCP front	Mesh
180 V	100 V	0 V	-2100 V	-450 V
HEX				
Mesh	MCP front	MCP back	Holder	Signal/Referece
-200 V	-50 V	2150 V	2250 V	2330 V

acquisition speed can be 25 kHz for 1 hit per channel, but decreases for more hits.

4.3.5 Data analysis

For acquisition and analysis the CoboldPC software from Roentdek is used. A data acquisition program written in C++ and a command file are used for data acquisition. All events are saved in list-mode format. In a list-mode file each individual event is stored with its position and timing information, so that the full information is available for re-analysis at any time.

In addition the list-mode file can be loaded later using a data analysis program also written in C++ with which it is possible to reanalyze the data using filters on events and extracting momenta and energy information as well as coincidence information.

4.3.6 Coincidence detection

For coincidence detection of several charged fragments the question one needs to pose is what event rate can one afford to ensure true coincidences. Therefore one typically uses the system in a mode, where $\ll 1$ event per pulse is detected. Generally speaking, one needs to determine the final number of events per pulse in the gas jet, and make sure that two of these events per pulse occur with a significantly lower probability than one event. As a rule of thumb, by making sure the event of interest is happening only every tenth laser pulse, this also ensures that the ratio of double events to single events is only about 10%. In general this has not yet been of much concern in our setup, as cross sections (typically on the order of $10^{-19} cm^2$), gas jet density (on the order of $10^{11}/cm^3$) and photon flux in the COLTRIMS target region ($N_p \sim 3 \cdot 10^6$ photons per pulse at $\sim$ 45 eV at the gas target) are not very high. Event probabilities are $nL\sigma N_p \sim 1\%$ per pulse for a $L \sim 3$ mm gas jet.

4.3.7 COLTRIMS detection efficiency and optics efficiency

Not all events produced in the gas jet are also detected. The number of ions and electrons detected are strongly reduced by the use of meshes ($\sim$ 80% transmission efficiency) in the COLTRIMS detection setup (These meshes provide a more homogenous electric field). Two of those meshes are at the beginning and end of the drift region for the electrons and one mesh is used in front of the ion detector. In addition the efficiency of the MCP and delay line anode is only $\sim$ 30%.

The EUV photon flux ($\sim 10^8$ photons per pulse out of the generation waveguide) is also reduced by the usage of 2 EUV mirrors and an Aluminum filter. The Aluminum filter is used to reflect the NIR driving pulses. The COLTRIMS beamline consists of two Mo/Si (molybdenum-silicon) EUV multilayer mirrors in a z-fold configuration with a reflectivity of $20 - 25\%$ at $\sim$ 43 eV and an Aluminum filter of 200 nm thickness with a transmission of $\sim$ 64% at $\sim$ 43 eV ($0.22 \cdot 0.22 \cdot 0.64 = 0.03$). This reduces the EUV photon flux to $\sim 3 \cdot 10^6$ photons per pulse.

4.4 Molecular alignment methods

Here I give an introduction to molecular alignment, as this experimental technique is used later in this thesis to determine the angle-dependent photoionization of molecules. There exist two distinct regimes of molecular alignment: The first regime, referred to as "adiabatic alignment" [114, 136], requires a very strong static electric field (10's of kV/cm) or a long laser pulse (picosecond to nanosecond), that slowly turns on and off compared to the molecular rotational period, and aligns the molecular axes along the electric field/ laser polarization by exerting a torque on the permanent dipole $\mathbf{d}$ or the induced dipole $\mathbf{d} = \alpha\,\mathbf{E}$, where α is the polarizability tensor. The interaction energy is given by:

$$V = -\frac{\mathbf{d} \cdot \mathbf{E}}{B} \tag{4.11}$$

here B is the rotational constant, E the electric field and d the dipole moment. A review can be found in [146], where results of adiabatic alignment of iodine (using a noble gas as buffer gas to further lower the rotational temperature) with an alignment cosine (see below) of 0.85 were demonstrated. The highest degree of alignment ($< \cos^2 \Theta >= 0.92$) using 9-nanosecond long pulses has been shown in iodobenzene by Kumarappan [88].

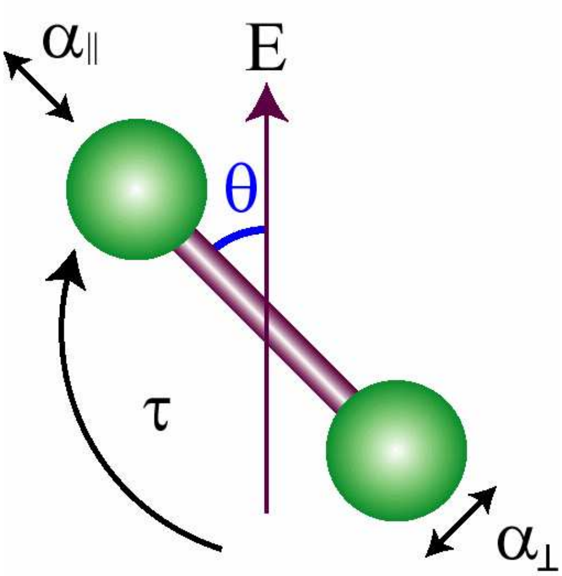

Figure 4.9: Definition of molecular polarizabilities $\alpha_{||}$ along and $\alpha_{\perp}$ perpendicular to the molecular axis. The alignment field E torques the molecule towards the field axis.

The second regime is referred to as "non-adiabatic alignment". It employs a short laser pulse to impulsively excite a coherent rotational wave packet, which undergoes periodic dephasing and rephasing (revivals) and transiently aligns the molecules. These field-free alignment revival structures allow probing the aligned molecules while unperturbed by external fields and therefore are attractive for studying the interaction between non-perturbed free molecules and photons. This is the regime which we use below for the alignment of molecules with femtosecond pulses.

4.4.1 Field free (nonadiabatic) molecular alignment

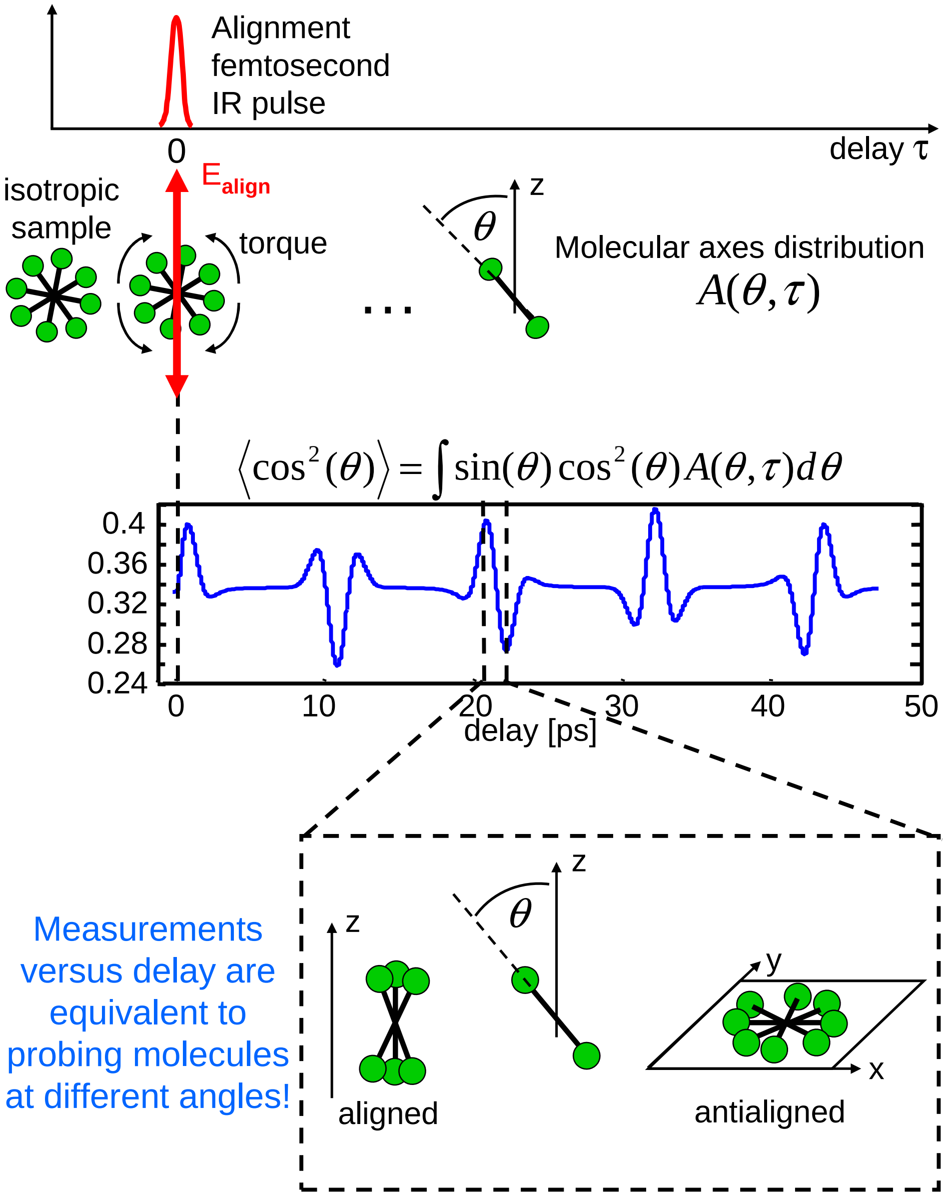

Figure 4.10: Molecular alignment: A femtosecond laser pulse impulsively torques the molecular axes towards its polarization direction. The molecular axes distribution $A(\theta, \tau)$ experiences periodic revivals, as demonstrated by peaks and dips in the alignment cosine $< \cos^2(\theta) >$. During the half-revival around 21 ps for CO_2 the axes distribution changes from aligned to antialigned.

For the experiments described here we use nonadiabatic alignment to align the molecular sample. In this case the employed alignment pulses are much shorter than the rotational period of the studied molecules. For example for the molecules CO_2 and N_2 the full revivals occur for $\sim$ 42.6 ps and $\sim$ 8.4 ps, respectively. Around the half revival the molecular axis distribution changes from aligned to antialigned in $\sim$ 1.5 ps for CO_2 and $\sim$ 700 fs for N_2.

For nonadiabatic alignment, the electric field of the alignment pulse torques the molecular axes towards its polarization axis. This torque creates a brief initial alignment in which the axes are aligned parallel to the electric laser field shortly after time zero. Then the molecular axis distribution dephases and the sample becomes almost isotropic. However periodic transient molecular alignment revivals (rephasing) occur long after the end of the excitation pulse. This has the advantage that the laser pulse is long gone before the molecular sample experiences revivals, which are therefore happening unperturbed from external fields. The delay times at which revivals occur are determined by the rotational constant of the molecule. How these revival structures occur is best explained quantum mechanically: The spectrum of the short alignment pulse contains many frequency components. Therefore pairs of frequencies can drive many Raman transitions (spaced by the selection rule $\Delta J = +/-2, 0$). This cascaded Raman process creates a coherent superposition of rotational levels a rotational wave packet:

$$\Psi(t) = |0> exp(i0t/\hbar) + |2> exp(iE_2t/\hbar) + |4> exp(iE_4t/\hbar) + ... \tag{4.12}$$

where $|J\rangle$ is the rotational state and $E_J = BJ(J+1)$ the rotational energy and $B = \hbar^2/(2I)$ is the rotational constant of the molecule with I the moment of inertia. The different components of the wavepacket evolve in time according to their energies, and periodically come into phase again. After time $T_{rot} = h/2B$, the full revival occurs where all rotational levels are in phase. Less strong revivals occur at fractions of the full revival time.

4.4.2 Quantum mechanical description of rotational coherent wave packets

For a quantum mechanical treatment we refer to the work of Ortigoso and coworkers [114]. Briefly, we start with a molecule in the laser field where the interaction energy is given by

$$E_{interact} = -\mathbf{d} \cdot \mathbf{E} \tag{4.13}$$

Here the dipole can be either a permanent electric dipole $\mathbf{d}$, as e.g. in a heteronuclear molecule, or an induced dipole

$$\mathbf{d} = \alpha \cdot \mathbf{E} \tag{4.14}$$

where

$$\alpha = \begin{pmatrix} \alpha_{\perp} & 0 & 0 \\ 0 & \alpha_{\perp} & 0 \\ 0 & 0 & \alpha_{||} \end{pmatrix} \tag{4.15}$$

is the polarizability tensor with $\alpha_{||}$ and $\alpha_{\perp}$ the polarizabilities along the molecular axis and perpendicular to the molecular axis.

For a linear or symmetric top molecule we can write an effective Hamiltonian describing the interaction of the laser field with the dipole as well as a term for the molecular rotational energy:

$$H_{eff}(t) = B \cdot \mathbf{J^2} - \frac{1}{2}E^2(t)[(\alpha_{||} - \alpha_{\perp})cos^2\theta + \alpha_{\perp}] \tag{4.16}$$

The time evolution of the wavefunction describing the molecular axis orientation is described by

$$i\frac{\hbar}{B}\frac{\partial\psi(t)}{\partial t} = \frac{H(t)}{B}\psi(t) \tag{4.17}$$

The Ansatz for the rotational wavepacket is

$$\psi(\Delta\omega(t)) = \sum_J d_J(\Delta\omega(t)) Y_{J,M} \tag{4.18}$$

where

$$\Delta\omega(t) = (\alpha_{||} - \alpha_{\perp}) \cdot \frac{E^2(t)}{2B} \tag{4.19}$$

and $Y_{J,M}$ are the spherical harmonics. One can solve for the time-dependent coefficients d_J by inserting (4.18) into the time-dependent Schroedinger equation for the rotational wavepacket (4.17).

Under the influence of the laser pulse an initial state $|J_i, M_i\rangle$ evolves into a time-dependent molecular axis distribution $A(\theta,\tau)^{(J_i,M_i)}$ given by the probability of the rotational wavepacket $|\psi(\Delta\omega(t))|^2$. However even in a supersonically cooled gas jet there are several states $|J_i, M_i\rangle$ populated and therefore have to be thermally averaged to calculate the expectation value of the molecular axis distribution:

$$A_{thermal}(\theta,\tau) = \frac{1}{Q_{rot}} \sum_{J_i=0}^{J_i=max} \omega_{J_i} \exp^{-\frac{E_{J_i}}{kT}} \sum_{M_i=-J_i}^{+J_i} \langle \psi(\Delta\omega(\tau)) | \psi(\Delta\omega(\tau)) \rangle^{(J_i,M_i)} \tag{4.20}$$

where the rotational partition function is given by

$$Q_{rot} = \sum_{J_i=0}^{J_i=\infty} \omega_{J_i} (2J_i + 1) \exp^{-\frac{E_{J_i}}{kT}} \tag{4.21}$$

and ω_{J_i} are factors giving the relative populations of the rotational levels due to nuclear spin statistics.

In the case of CO_2 only even J values are occupied, whereas for N_2 even and odd J values are occupied.

A good parameter to describe the degree of alignment is the ensemble-average of $cos^2\theta$, called the alignment cosine (see Figure 4.10):

$$< cos^2(\theta)(\tau) >= \int cos^2(\theta) A_{thermal}(\theta,\tau) \sin(\theta) d\theta / \int A_{thermal}(\theta,\tau) \sin(\theta) d\theta \tag{4.22}$$

where $\sin(\theta)$ is the geometrical weight factor in spherical coordinates and $A_{thermal}(\theta)$ is the axis probability distribution. It is shown in Figure 4.10 for CO_2 versus delay after the alignment pulse. The higher $< cos^2\theta >$, the larger the number of molecules aligned parallel to the polarization of the alignment laser. $< cos^2\theta >= 1$ would correspond to a fully aligned sample, $< cos^2\theta >= 0$ would be fully antialigned (i.e. all axes perpendicular to the alignment laser polarization) and an isotropic sample has a $< cos^2\theta >= 1/3$. Note that for the isotropic sample $A(\theta, \tau) = 0.5$.

4.4.3 Practical considerations for strong molecular alignment

From the above considerations and from others [180] we find that the bigger the polarizability anisotropy and the stronger the electric field of the alignment pulse, the stronger the alignment will be. Of course the maximum intensity that can be used in the alignment pulse is limited by the onset of ionization, i.e. determined by the molecule's ionization potential. In general, less polarizable molecules can withstand higher intensities (as the nonresonant ionization rate scales with the polarizability), compensating for their smaller polarizability. The only other quantity that influences alignment is the temperature/rotational constant ratio T/B which gives the number of initially populated rotational states. For a stronger alignment we want as few states as possible to be initially populated. Therefore we can increase the degree of alignment by decreasing the molecular rotational temperature. To achieve this, it can be useful to seed the molecules with another gas (buffer gas) [146] to further cool the sample in a supersonic expansion. This will not only increase the variation between minimum and maximum of $< cos^2\theta >$, but also increase the delay between alignment maximum and minimum in a revival. The background alignment between the revivals also increases with decreasing temperature.

We also find that with increasing laser intensities the minima and maxima of $< cos^2\theta >$ increase, as shown in Figure 4.11. However we need to keep the laser intensity

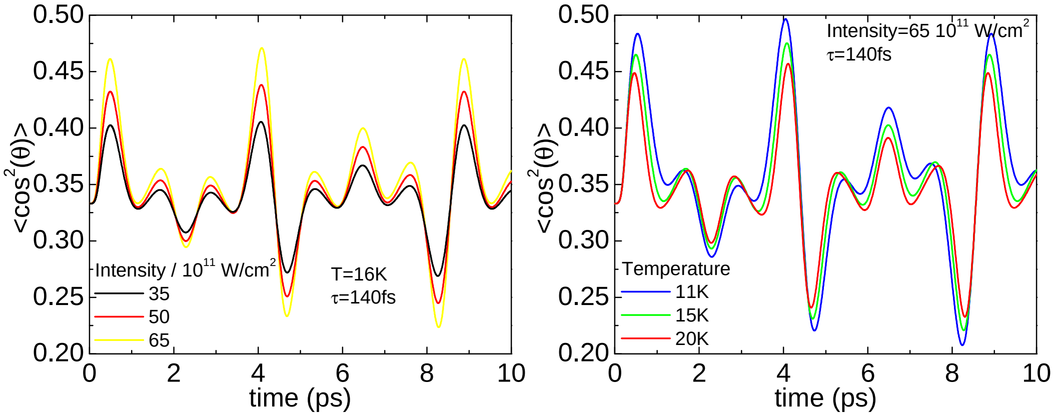

Figure 4.11: Calculated alignment cosine for N_2 versus time after alignment pulse. Left: dependence on alignment pulse intensity at fixed rotational temperature. Right: dependence on temperature at fixed alignment pulse intensity.

low enough to not ionize the molecules by multiphoton ionization. This can be especially critical in a COLTRIMS apparatus where a large number of false coincidences can occur due to these unwanted ionizations from the alignment beam. Of course, the method of field-free molecular alignment is restricted to molecules with anisotropic polarizability i.e. there must be a large difference in polarizability along and perpendicular to the molecular axis. However, this is generally true for molecules for which alignment is meaningful, i.e. not spherically symmetric molecules.

Another method to improve the degree of molecular alignment is the use of several pulses for alignment. Using two-pulse alignment [90] an improvement of the alignment cosine of $\sim 20\%$ was achieved.

4.5 Measuring neutral-to-ionic transition dipoles: Angular Dependence of the Single-Photon Ionization of Aligned N_2 and CO_2

We demonstrate a new method which allows us to measure the orientation of the transition dipole for nondissociative ionizations using single photon photoionization for the first time. It also allows to measure dissociative ionizations which do not fulfill the axial recoil approximation for the first time and may be used in future experiments to examine the validity of the axial recoil approximation in detail.

4.5.1 Motivation for this experiment

Why are we interested in measuring the angular orientation of molecular neutral to- ionic transition dipoles? In any system in which we want to control ionization and make it happen efficiently, we need to assure that at least a portion of the transition dipole is parallel to the ionizing field. This transition dipole $\mathbf{d}$ is given by the matrix element of the dipole operator $e \cdot \mathbf{x}$ between an initial, neutral molecular state $|\psi_{neutral}\rangle$, and the final state $\langle\psi_{ionic}|$, consisting of the ion and the leaving photoelectron $\langle\psi_{ionic}|e\mathbf{x}|\psi_{neutral}\rangle$. When the transition dipole is parallel to the molecular axis, then the angular dependence of the ionization cross section is $\cos^2\theta$ and the ionization yield is maximized for an aligned sample, whereas for a perpendicular dipole it is $\sin^2\theta$ and the yield is maximized for molecular axes perpendicular to the ionizing field (θ is the angle between the polarization of the light source and the molecular axis). Knowledge of the molecular frame transition dipole $\langle\psi_{ionic}|e\mathbf{x}|\psi_{neutral}\rangle$ between neutral and ionic states of molecules is thus fundamental to understanding photoionization of molecules. The calculation of transition dipole moments is substantially more difficult for bound-free transitions than for bound-bound transitions. This is because in contrast to calculating transition dipole moments for neutral-to-neutral transitions (provided the electronic structure for initial and final state is known), a correct treatment of the continuum wave function of the free electron is required [97].

The difficulty in measuring molecular-frame transition dipoles arises because gaseous molecules are isotropically oriented. In addition, relatively short femtosecond duration NIR pulses for alignment and EUV probe pulses for probing the angular dependence of photoionization of molecules are needed. This is because the time duration between alignment and antialignment of molecular axes during a fractional revival of the rotational wave packet is on the order of $100's$ of femtoseconds. Of course these measurements also require a low pulse-to-pulse timing jitter of the EUV pulse with respect to the IR alignment pulse so that the delay between pump and probe is well defined. This is one reason why this experiment is difficult to implement at current synchrotron or free electron laser facilities, as the EUV pulses there have large timing jitters on the order of femtoseconds or even picoseconds.

By combining amplified femtosecond pulses to create field-free molecular alignment, with ionizing few-femtosecond EUV pulses, and momentum imaging of the resulting molecular fragment ions and photoelectrons using a COLTRIMS reaction microscope, we map the angular dependence of molecular photoionization yields for the first time for a non-dissociative molecule. The observed modulation in ion yield as a function of molecular alignment is attributed to the molecular frame transition dipole moment of single-photon ionization to the X, A and B states of N_2^+ and CO_2^+. Our data show that the transition dipoles for single-photon ionization of N_2 and CO_2 at 43 eV have larger perpendicular components than parallel ones. A direct comparison with published theoretical partial wave ionization cross-sections confirm these experimental observations - which are the first results to allow such comparison with theory for bound cation states. These results also provide the first step towards a novel method for measuring molecular frame transition dipole matrix elements. As a side, we will also show the orientational dependence of the transition dipole from IR strong-field ionization, which is a multiphoton process.

4.5.2 Past measurements on transition dipoles

In past work, molecular frame neutral-to-ionic transition dipoles have been measured e.g. for molecules adsorbed on surfaces. In the case of CO, it is possible to monitor the intensity of a particular shape resonance as a function of x-ray polarization to determine if the molecule is lying flat or perpendicular to the surface [147]. However a surface can perturb the adsorbed molecules.

Transition dipoles have also been measured for dissociative ionization channels, by coincidence measurement of "fixed-in-space" photoelectron angular distributions following dissociative ionization [176]. In the simplest case of linear molecules, the fragment ions recoil along the molecular axis and we can measure the momentum of the fragment ions. The angular distribution of photoelectrons with respect to the molecular axis defined by the recoiling ions allows then to determine the molecular-frame transition dipole. This approach has been applied to both valence- [131] and inner-shell [131, 33, 175] ionization, but is limited to systems in which the ions dissociate rapidly, i.e. faster than it would take the molecule to rotate between ionization and dissociation. This condition is called the axial recoil approximation.

Note also that fragmentation processes into dissociating channels only make up a few percent of the total ionization yield, so that a large fraction of ionizations cannot be studied using this method. For example for CO_2 the ratio of nondissociative ionizations into CO_2^+ to the dissociative channel $O^+ + CO$ is $\sim 3 : 1$. Therefore, measurements of molecular frame transition dipoles for states undergoing non-dissociative ionization have to date been very limited.

Experimental molecular frame transition dipole matrix elements for photoionization have also been determined previously by measurements of rotationally resolved photoelectron angular distributions [128, 65, 66, 89, 115]. To date, this approach has only been applied to hydride molecules and to the photoionization of selected high rotational levels of diatomic molecules, where the rotational spacings of the ion are sufficiently large to resolve.

While all these approaches have produced beautiful and enlightening results, both methods have their limitations. Thus, complementary approaches for determining molecular frame transition dipole matrix elements are highly desirable.

It has long been proposed [131] that a perfectly aligned molecular sample ($< cos^2\theta >= 1$) would enable the direct measurement of the molecular frame transition dipoles for states undergoing non-dissociative ionization, which is the dominant process in photoionization. In the case of gas phase molecules, adiabatic and non-adiabatic alignment methods have been extensively studied over the past decade [133, 47, 146]. Adiabatic alignment requires a very strong static electric field or a long laser pulse (picosecond to nanosecond), that slowly aligns the molecular axes along the laser polarization by exerting a torque on the induced dipole. Adiabatic alignment has recently been used in an x-ray absorption experiment to study CF_3Br [121]. Non-adiabatic alignment employs a short laser pulse to excite a coherent rotational wave packet, which undergoes periodic rephasing (revivals) and transiently aligns the molecules. This approach has the advantage of being field free and therefore more attractive for studying the interaction between non-perturbed free molecules and photons. Non-adiabatic alignment has been used in a recent experiment, to probe alignment effects using EUV [92]. Suzuki and coworkers [165] demonstrated the possibility of generating a rotational wave packet by using a one-photon transition. The issue with this type of experiment lies in the low degree of alignment they can produce in molecules. The theoretical limiting value of $< cos^2\theta >$ is 0.6 for a pure parallel transition (Note that this value is only true for the fraction of molecules that were excited. Most of the molecules however remain in the ground state.). However, the adiabatic and non-adiabatic alignment does not have such limit. For example, a very high degree of alignment ($< cos^2\theta >= 0.92$) has been achieved in iodobenzene by Kumarappan et al.[88]. Experimental conditions such as molecular rotational temperature and laser intensity can be optimized to increase the degree of alignment. Of course, the method of field-free alignment is restricted to molecules with anisotropic polarizability.

In this work we show that by combining non-adiabatic alignment using strong femtosecond pulses with a reaction ”microscope”– molecular imaging apparatus, we can use femtosecond EUV pulses to measure the relative single-photon ionization cross-section as a function of molecular alignment. As a result, we can directly obtain the ratio between the parallel and perpendicular molecular frame transition dipoles. We also compare the angular dependence of single-photon ionization with soft x-rays to the angular dependence of multiphoton ionization by an intense femtosecond infrared (IR) laser field. We find that the N_2^+ and CO_2^+ multiphoton ionization ion yields are maximized when the molecules are aligned with the polarization axis of an intense NIR field. In contrast, for single-photon non-dissociative ionization by EUV pulses, the ion yields maximize when the molecules are aligned perpendicular to the polarization of the x-rays. These measurements indicate that the ionizing transitions are predominantly perpendicular for single-photon EUV ionization, and allow a direct comparison with theory for the first time for these systems. Finally, we show that the single-photon dissociative ionization channels $N2 \rightarrow N^+ + N + e^-$ and $CO_2 \rightarrow O^+ + CO + e^-$ are maximized when the molecules are aligned parallel to the EUV polarization, in contrast to the non-dissociative ionization channels. These results provide the first step towards direct measurement of molecular frame transition dipoles from highly aligned molecules in the laboratory frame.

Lepine et al. [92] have performed similar experiments using a combination of short NIR pulses to align N_2 and CO_2, and EUV light produced by high-harmonic generation to probe the alignment. The principal difference between their work and our experiment is that their EUV beam was not energy-selected, but consisted of all harmonic orders between $\sim$ 20 eV and 55 eV. In our experiment, we use multilayer mirrors to select a single harmonic order - the 27^{th} harmonic at $\sim$ 43 eV - with a few eV bandwidth. This difference is important because the molecular frame transition dipoles, and thus the relative amplitudes of the parallel and perpendicular transitions, are energy dependent. Thus, the larger bandwidth of the previous measurements is expected to smooth out any variations. In addition, although the potential of the approach for threshold (non-dissociative) photoionization was discussed, the earlier measurements focused on dissociative ionization processes, and no parent cation yield modulation was observed. Their attempt to observe an alignment dependence of the angular-resolved photoelectron spectrum of N_2 was unsuccessful.

4.5.3 Experimental setup and technique for measuring angle dependent photoionization of molecules

Our experiment begins with a gaseous sample of molecules which are isotropically oriented. To create field-free alignment in the molecular sample we employ a strong but non-ionizing fs NIR laser pulse ($\sim 4 \cdot 10^{12} W/cm^2$) to impulsively excite a coherent molecular rotational wavepacket. We then use few-femtosecond EUV pulses to measure the yield of single-photon ionization as a function of time as the molecules undergo field-free alignment. This method to measure molecular neutral ionic transition dipoles is widely applicable - the only requirement is that the molecules can be aligned. It is applicable to nondissociative ionizations, as well as dissociative ionizations that do not fulfill the axial recoil approximation.

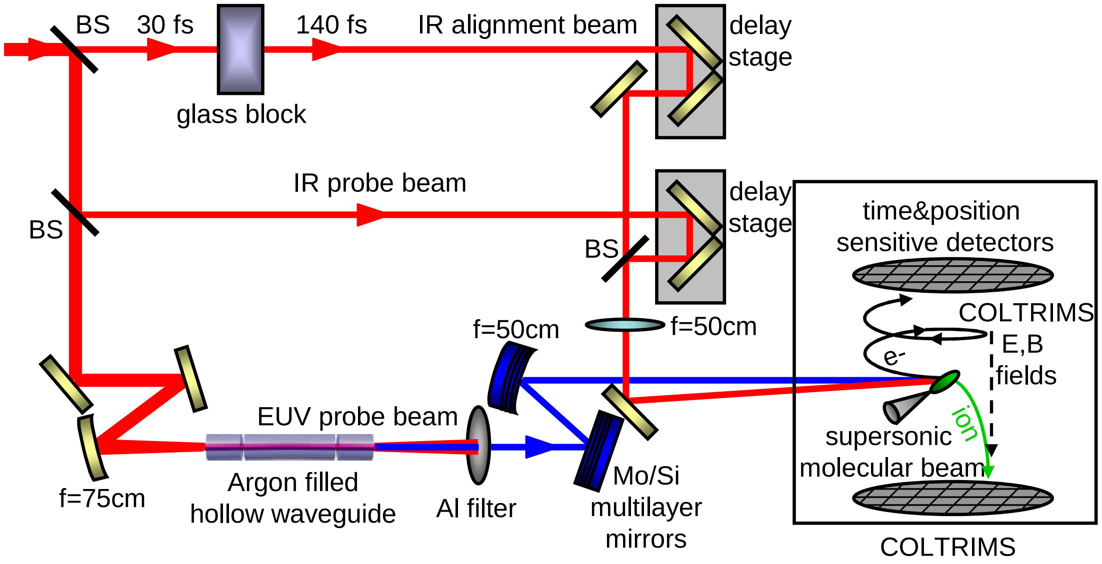

Figure 4.12: Experimental setup. An NIR (800 nm) alignment pulse of duration 140 fs first aligns the supersonically cooled N_2 and CO_2 molecules. Aligned molecules are then ionized by either a delayed, 35 fs, NIR pulse or a $\sim$ 10 fs, 43 eV energy, EUV pulse (blue).

To measure the single-photon ionization yield during a rotational wave packet revival in a small molecule, sub-picosecond EUV pulses are needed because of the short duration of the revival. Therefore, in this experiment we use high harmonic generation by a femtosecond laser to produce ultrafast ($\sim$ 10 fs) EUV pulses as the source of ionizing radiation. The experimental setup is shown in Figure 4.12. We use a Ti:sapphire amplifier system producing 2 mJ pulses, at a 2 kHz repetition rate, and with 35 fs pulse duration, and split the output into pump and probe beams. The pump pulse, with intensity $\sim 4 \cdot 10^{12}\, W/cm^2$, is stretched to 140 fs to impulsively align the molecules by creating a rotational wave packet, which periodically exhibits macroscopic field-free alignment around the polarization axes of the pump aligning pulse [114]. The probe beam, with energy 1 mJ, is focused into an argon-filled hollow waveguide to produce a comb of phase matched harmonics [135]. Using two Mo/Si multilayer mirrors and an Aluminum filter (200 nm thick), we preferentially select soft x-ray harmonics centered at $\sim$ 43 eV (27^{th} harmonic), which are then focused non-collinearly with the pump beam into the molecular sample. The soft x-ray photon flux is estimated to be $\sim 10^6 photons/pulse$. The relatively large bandwidth of the EUV light precludes the resolution of vibrational (and even electronic) structure in the photoelectron spectra of the N_2^+ and CO_2^+, which have vibrational spacing of $\sim 0.1 - 0.4$ eV. Alternatively, we can use NIR light as the probe beam to ionize the molecule using multiphoton strong-field ionization that occurs at laser intensities around $3 \cdot 10^{13}\, W/cm^2$. Since multiphoton ionization is a more sensitive probe of alignment, we first used the strong field ionization signal to verify our alignment conditions.

To extract the angle dependent ion yield, a molecular supersonic gas jet is placed in a COLTRIMS (Cold Target Recoil Ion Momentum Spectroscopy) reaction microscope [51], which allows reconstruction of the full momentum vectors of all charged particles resulting from ionization, with coincidence measurement capability. We exploit the COLTRIMS coincidence and momentum imaging capabilities to distinguish different ionization channels. We measure the kinetic energy E_{pe} of photoelectrons detected in coincidence with the respective ions. This allows determination of the ion channel by its vertical ionization energy $E_{ion} = h\nu_{EUV} - E_{pe}$.

The ion yield was probed during the first half-revival for N_2 (4.2 ps) and CO_2 (21.0 ps), where the molecular axis distribution changes from aligned to anti-aligned. The variation of the angular distribution with delay during a rotational revival is effectively the same as varying the angle between pump and probe polarization at a fixed time delay corresponding to maximum molecular axis alignment. However, by using parallel polarizations in the alignment and ionizing pulses, azimuthal symmetry is maintained at all times, which simplifies the analysis.

4.5.4 Experimental Results: Angular Dependence of the Strong-Field Ionization of Aligned N_2 and CO_2

In a first experiment we used strong field ionization to verify our method of extracting angle-dependent photoionization. As this is a multiphoton process, the angular cross section can be more strongly peaked than for single photon ionization. This can be seen in the yield of N_2^+, which peaks rather sharply around the aligned point, and takes a rather broad dip around the antialigned point (see inset 4.14 (a)). From the observed behavior of the ion yield we can immediately infer that the ionization cross section is sharply peaked around 0 degrees and suppressed for all other angles. From a fit of the ion yield versus delay we quantitatively extract the angle-dependent cross section. An analogous analysis can be done for CO_2.

4.5.5 Experimental Results: Angular Dependence of the Single-Photon Ionization of Aligned N_2 and CO_2

For single photon ionization the cross section is simply proportional to $1 + \beta \cdot P_2$, where P_2 is the second order Legendre polynomial and β is the parameter we extract from our measurements. A β of 2 corresponds to a parallel dipole. This means that molecules are most efficiently ionized when the axis is parallel to the ionizing field. For β of -1 we have a perpendicular dipole which means the ionization is most efficient for axis perpendicular to the ionizing field.

Figure 4.13 shows the photoelectron spectra of N_2 and CO_2, measured in coincidence with N_2^+ and N^+, and CO_2^+ and O^+, respectively, following ionization by 43 eV photons. Within our experimental resolution, these spectra agree with published photoelectron spectra of CO_2 and N_2, showing that single-photon ionization of N_2 results primarily in the population of the $X\,^2\Sigma_g^+$, $A\,^2\Pi_u$ and $B\,^2\Sigma_u^+$ states of N_2^+, and that ionization of CO_2 results primarily in the population of the $X\,^2\Pi_g$, $A\,^2\Pi_u$, $B\,^2\Sigma_u^+$, and $C\,^2\Sigma_g^+$ states of CO_2^+. The ionization energy of N_2 is 15.6 eV, and the dissociation energy of N_2^+ is 8.7 eV, resulting in a dissociative ionization threshold of 24.3 eV [69]. Thus, with a 43 eV photon, photoelectrons with kinetic energy greater than $\sim$ 18.7 eV are expected to be correlated with stable N_2^+, while photoelectrons with kinetic energy less than $\sim$ 18.7 eV are expected to be correlated with N^+ fragments. Given our experimental resolution, this assumption is consistent with Figure 4.13 (a). Similarly, the ionization potential of CO_2 is 13.8 eV and the dissociation energy of CO_2^+ is $\sim$ 5.3 eV, resulting in a dissociative ionization threshold of $\sim$ 19.1 eV. Photoelectrons with kinetic energy greater than $\sim$ 23.9 eV should therefore be correlated with stable CO_2^+. While this is generally consistent with our observations, in contrast to N_2, some CO_2^+ appears unstable for photoelectron energies up to $\sim$ 30 eV. This result may simply reflect the bandwidth of the high-harmonic light. In addition, some CO_2^+ appears to be stable for photoelectron energies down to about 18 eV. This observation may simply result from the larger number of internal degrees of freedom in CO_2^+, resulting in a longer lifetime before dissociation, and enabling competing non-dissociative decay mechanisms such as fluorescence to stabilize the parent ion. This observation is also consistent with the relatively long dissociation timescale inferred below for the CO_2^+ C state.

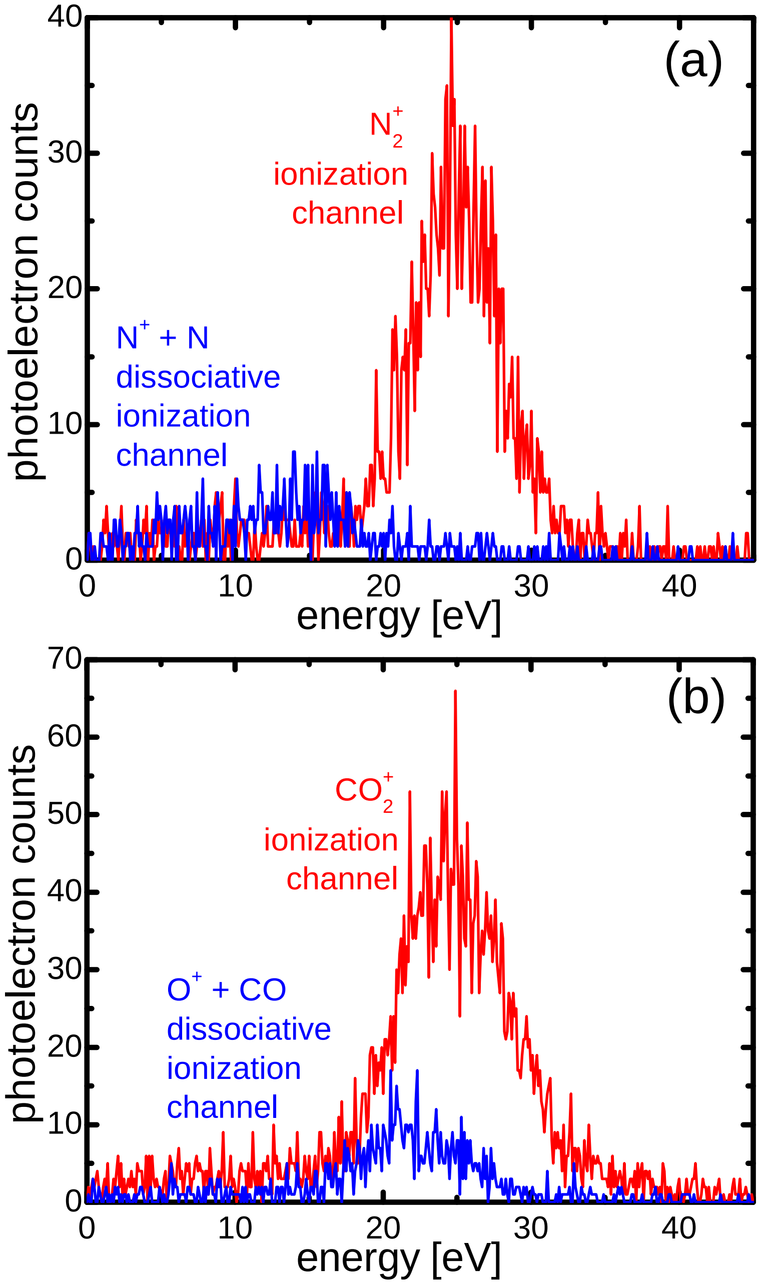

Figure 4.13: Photoelectron spectra in coincidence with (a) N_2^+ (red) and N^+ (blue) (b) CO_2^+ (red) and O^+ (blue). With coincidence measurement, N_2^+ and CO_2^+ are found at X, A and B state. N^+ is from N_2^+ inner valence states with binding energy > 24 eV. O^+ is from CO_2^+ C dissociative state (~ 19 eV).

The yields for singly ionized N_2 and CO_2 as a function of time delay between the alignment and EUV ionizing pulses, again in the region around the half revival,

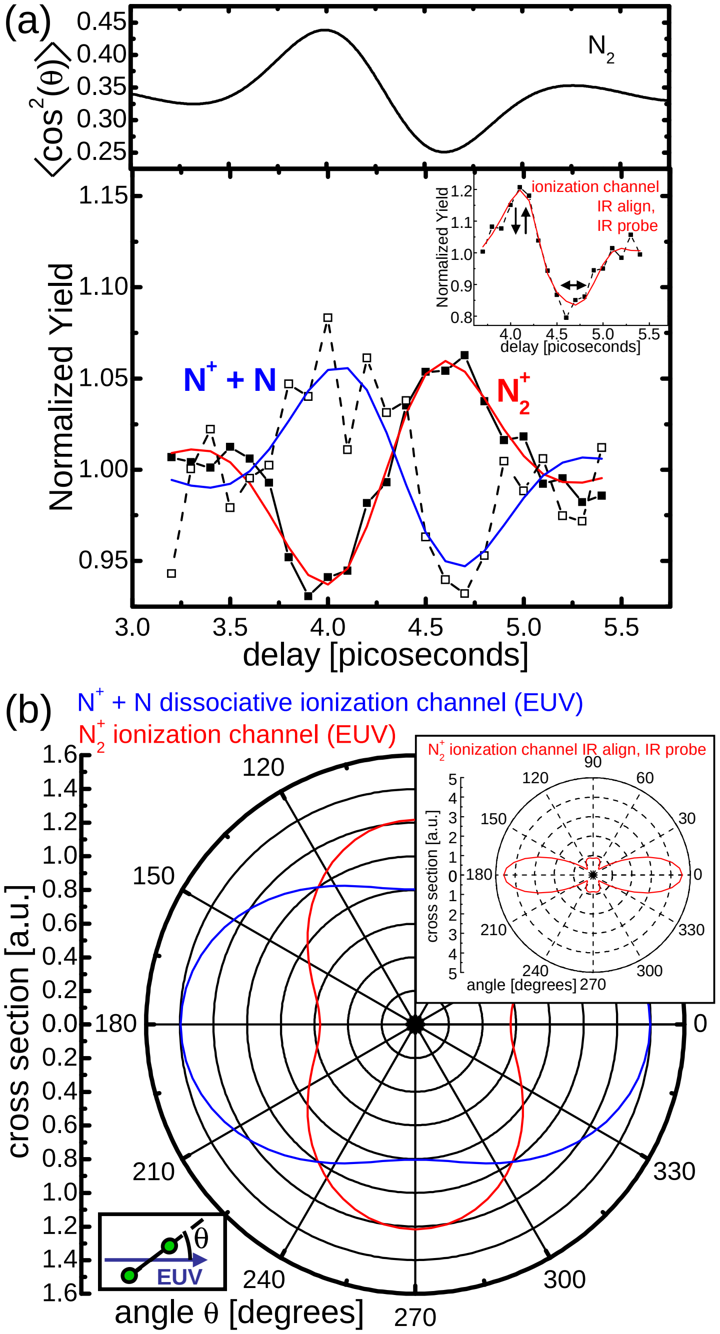

Figure 4.14: (a) Upper panel: calculated alignment cosine (see text) for N_2 versus time delay. Main panel: EUV ionization yields from transiently aligned N_2. Solid (hollow) symbols: N_2^+ ($N^+ + N$ dissociation). Lines: numerical fitting. Inset: multiphoton (NIR) ionization yield of N_2^+ and its numerical fitting. (↓↑: aligned sample; ↔: antialigned sample). (b) Extracted angular dependence of the EUV photoionization cross section to N_2^+ and N_2^+ dissociative states (N^+). Inset: extracted angular dependence of multiphoton (IR) ionization of N_2. These angular dependencies were extracted, as described in the text, from a fit to the delay-dependent yield data shown in (a).

are shown in Figure 4.14 and 4.15. The insets of these figures also show the ion yields resulting from multiphoton ionization by an intense femtosecond NIR field. For the case of multiphoton ionization, the N_2^+ and CO_2^+ yields are highest when the molecules are aligned with the polarization of the NIR field. However, for the case of single-photon EUV ionization, the ion yield is at minimum when the EUV polarization is parallel to the molecular axis. This surprising contrast clearly demonstrates the difference between multi-photon and single-photon ionization. However, the origin of such difference is not trivial, since the mechanism of multi-photon ionization is still an area of intense investigation [120].

4.5.6 Discussion

Electronic transitions in linear molecules are generally classified as parallel or perpendicular according to whether the dipole is parallel or perpendicular to the molecular axis, with the corresponding selection rule for the electronic angular momentum, Λ, of $\Delta\Lambda = 0$ and $\Delta\Lambda = \pm 1$, respectively. Note that for the final state in photoionization,Λ includes the electronic angular momentum of the ion and photoelectron. When the molecule is aligned parallel to the polarization axis of the light, parallel transitions are enhanced, and perpendicular transitions are diminished, while the opposite is true if the molecule is aligned perpendicular to the polarization axis of the light. Thus, the time- (angular-) dependence of the ionization yield is a sensitive probe of the character of the transition dipole, and the angle-dependent yield can be directly related to the molecular frame dipole. Note, however, that limited resolution can complicate the process of extracting the direction of molecular frame dipoles, as several continua can contribute at a given photon energy. For example, if the photoelectron energy resolution is insufficient to resolve different final electronic states, the $N_2\ X\,^1\Sigma_g^+ \rightarrow N_2^+\ X\,^2\Sigma_g^+ + \epsilon p\sigma_u$ or $\epsilon f\sigma_u$ and $N_2\ X\,^1\Sigma_g^+ \rightarrow N_2^+\ B\,^2\Sigma_u^+ + \epsilon' s\sigma_g$ or $\epsilon' d\sigma_g$ photoionization processes, which all have the same overall symmetry, will overlap.

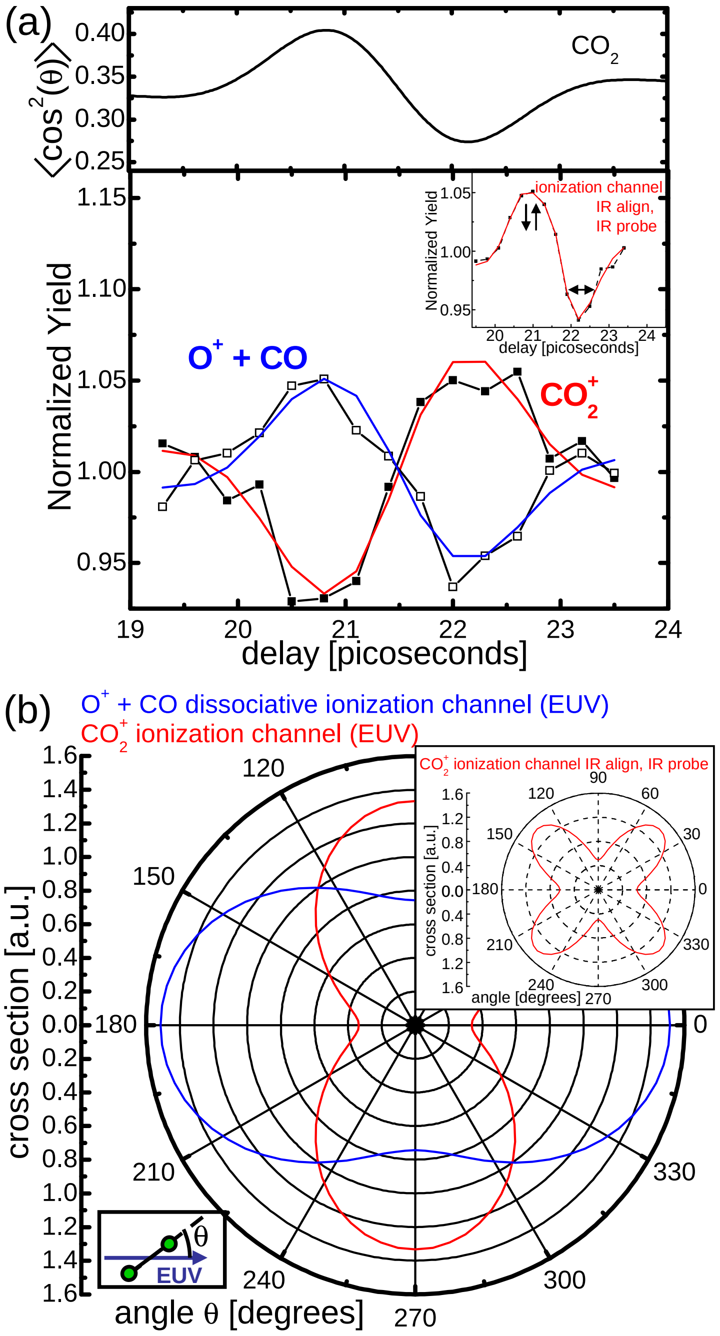

Figure 4.15: (a) Upper panel: calculated alignment cosine (see text) for CO_2 versus time delay. Main panel: EUV ionization yields from transiently aligned CO_2. Solid (hollow) symbols: CO_2^+ ($O^+ + CO$ dissociation). Lines: numerical fitting. Inset: multiphoton (IR) ionization yield of CO_2^+ and its numerical fitting. (↓↑: aligned sample; ↔: antialigned sample). (b) Extracted angular dependence of the EUV photoionization cross section to CO_2^+ and CO_2^+ dissociative states (O^+). Inset: extracted angular dependence of multiphoton (IR) ionization of CO_2.

To quantitatively determine the angular dependence of EUV photoionization, we first calculate the time dependence of the angular probability distribution $A(\theta, \tau)$ of molecular axes for the rotational revival following the method developed by Ortigoso et al.[114]. We use the experimental parameters for alignment pulse duration and laser intensity of 140 fs, $3.5 \cdot 10^{12}\ W/cm^2$ for CO_2, and 140 fs, $5 \cdot 10^{12}\ W/cm^2$ for N_2. The degree of alignment of the sample is given by the alignment cosine, i.e. the average of $cos^2(\theta)$ over the calculated molecular axis distribution:$< cos^2(\theta) >= \int cos^2(\theta) A(\theta, \tau) \sin(\theta) d\theta / \int A(\theta, \tau) \sin(\theta) d\theta$. The calculated alignment cosine for the conditions of the EUV single-photon ionization experiment is given for N_2 and CO_2 in Fig. 4.14 (a) and 4.15 (a), upper panel, respectively. Then the ionization yield versus delay τ is given by an angle integral: $Yield(\tau) = \int A(\theta, \tau) \sigma(\theta) \sin(\theta) d\theta$, where θ is the angle between the direction of polarization of the light and the molecular axes. We expand the angular dependence of the ionization cross-section in terms of Legendre polynomials $\sigma(\theta) = C \cdot (1 + \beta P_2(\cos(\theta)) + \gamma P_4(\cos(\theta)) + ...)$. For single-photon ionization, the ionization cross-section only contains the second order term: $\sigma(\theta) = C \cdot (1 + \beta P_2(\cos(\theta))$. Note, the β value in the equation is different from the one extracted from photoelectron angular distributions. It simply represents the anisotropy of angular dependence of the ionization cross-section. To remove the effect of possible EUV intensity fluctuations, the yield in the presence of the alignment beam is normalized by the yield without the alignment pulse present. We obtained $\beta = -0.43 \pm 0.13$ by fitting to the N_2^+ ion yield data shown in Figure 4.14. A theoretical value ($\beta_{theory} = -0.46$) for this parameter can be derived from the results of recent calculations on the photoionization of N_2 at this energy [16]. To do this, we used the equation: $\beta = (2 - \sigma_{perp}/\sigma_{para})/(1 + \sigma_{perp}/\sigma_{para})$. σ_{perp} and σ_{para} are the total cross-sections of perpendicular transitions and parallel ones taken from the reference. The theoretical calculations [16] indicate that at 43 eV, photoionization to the A state makes up more than half of the total ionization cross-section and is strongly perpendicular in character, while photoionization to the X and B states has mixed parallel and perpendicular character, resulting in overall perpendicular character for the unresolved continua.

In Figure 4.14 we also show the N^+ yield from the dissociative channel leading to $N^+ + N$. This process can be separated into transitions leading to two final states - the $F\,^2\Sigma_g^+$ and $(2\sigma_g)^{-1}\ ^2\Sigma_g^+$ state - with the $F\,^2\Sigma_g^+$ state dominant. These channels can be separated in our experiment, and thus we can characterize the orientation of their transition dipoles separately: N^+ ions were measured in coincidence with photoelectrons, and energy filters were applied. For the $F\,^2\Sigma_g^+$ state, the ion energy filter was between $0.08-1.84$ eV, and the electron energy filter was between $8-20$ eV. For the $(2\sigma_g)^{-1}\ ^2\Sigma_g^+$ state, the ion energy filter was between $1.84 - 5.32$ eV, while the electron energy filter was between $3.5 - 13.5$ eV. We find the β values for the $F\,^2\Sigma_g^+$ state and $(2\sigma_g)^{-1}\ ^2\Sigma_g^+$ states are 0.47 ± 0.20, and 0.18 ± 0.20, respectively. These correspond to ratios between the perpendicular and parallel dipole contributions of ~ 1 and 1.54 respectively using $\sigma_{perp}/\sigma_{para} = (2 - \beta)/(1 + \beta)$. These two dissociative channels leading to $N^+ + N$ are the only ones relevant to this study that have been accessible in previous studies using momentum imaging techniques. In experiments with 40.8 eV photons, Hikosaka and Eland [64] have measured a transition ratio $\sigma_{perp}/\sigma_{para}$ of 0.23 for the $F\,^2\Sigma_g^+$ state, and a ratio $\sigma_{perp}/\sigma_{para}$ of 0.6 for the $(2\sigma_g)^{-1}\ ^2\Sigma_g^+$ state. Although the ratio for the $(2\sigma_g)^{-1}$ $^2\Sigma_g^+$ state is higher than that for the $F^2\Sigma_g^+$ state in both experiments, the absolute values are quite different. This discrepancy may result in part from the different photon energies in the two experiments.

In Figure 4.15, we show the O^+ yield from the dissociative channel leading to $O^+ + CO$, as well as the non-dissociative CO_2^+ yield. It is obvious that the dissociative process results from a predominantly parallel transition, while the non-dissociative process results from a predominantly perpendicular one. As in the case of N_2, our results for CO_2 are in agreement with theoretical results ($\beta_{theory} = -0.43$) [15]. Specifically, at 43 eV, perpendicular transitions are expected to dominate photoionization to the X, A, and B states of CO_2^+, while parallel transitions are expected to dominate photoionization to the C state, of CO_2^+ , which mainly predissociates into $O^+ + CO$. We find a β value of -0.67 ± 0.19 for the data shown in Figure 4.15. These data are for CO_2^+ ions detected in coincidence with electrons in the energy range from 20 to 30 eV which was done to remove the signal from the NIR alone. Because of its low ionization potential of 13.78 eV, CO_2 can even be ionized by the alignment NIR pulse. However, since these ions are generated in coincidence with low energy electrons, they therefore can be filtered from the data. We also studied the electron yield for comparison. For electrons with energy between 20 eV and 30 eV, which are formed in coincidence with both CO_2^+ and $O^+ + CO$, we find a value of -0.36 ± 0.10. This observation is consistent with the fact that the parallel component for the transition to the C state of CO_2^+ is stronger than the perpendicular component. This results in a larger value than is observed by monitoring CO_2^+ ions, for which the C state does not contribute.

We also obtain the angular dependence of the photoionization cross-section for the dissociative channel $O^+ + CO$. We find a β value of $+0.51 \pm 0.15$ (see Figure 4.15). The $O^+ + CO$ channel likely proceeds by dissociation from the $C\,4\sigma_g$ channel of CO_2^+ [92, 15, 96]. The angular ionization cross section of this dissociative channel could thus not be measured before.

Although the O^+ ion signal shows a strong dependence on the alignment of the molecular axis, the O^+ angular distribution at a given delay (or given alignment of the molecular axis to the polarization axis) is essentially isotropic at all delays. This observation is consistent with the results of Lepine et al. [92]. In particular, the long lifetime of the intermediate state in this dissociation channel therefore appears to violate axial recoil approximation, leading to an isotropic momentum distribution and making it impossible to determine the transition dipole with conventional methods. However, Dowek et al. [35] reported an anisotropic parameter of ~ 1 for O^+ angular distribution from CO_2 dissociative ionization at 35 eV. Even though this discrepancy between their and our results might be due to the photon energy difference, it needs further investigation to clarify. Theoretically [15, 99] it has been predicted that a broad shape resonance structure contributes to the ionization to the C state between 30 and 45 eV. The corresponding continuum orbital is of σ_u symmetry, making this a parallel transition. The experimental β parameter is in agreement with the theoretical value at 43 eV of $\beta_{theory} = 0.84$, which was obtained as described above for N_2. The other partial wave contribution $\sigma_g -> \pi_u$ is a perpendicular transition and is not affected by the shape resonance. Thus, our method provides a direct way to probe this otherwise elusive shape resonance [14] in free CO_2 molecules.

We summarize extracted experimental anisotropy parameters for different ionization channels and their theoretical values in the following table.

Table 4.2: Comparison of Anisotropy Parameters (β) between Experiment and Theory

molecules	ionization channels	$\beta_{experiment}$	β_{theory}
	N_2^+(X,A,B)	-0.43 ± 0.13	-0.46
N_2	$N_2^+\ (F\,^2\Sigma_g^+, N^+ + N)$	$+0.47 \pm 0.20$	-/-
	$N^+\ (2\sigma_g)^{-1}\ {}^2\Sigma_g^+, N^+ + N)$	$+0.18 \pm 0.20$	-/-
CO_2	CO_2^+(X,A,B)	-0.67 ± 0.19	-0.43
	$CO_2^+(C\,4\sigma_g, O^+ + CO)$	$+0.51 \pm 0.15$	+0.84

4.5.7 Conclusion and Outlook

In conclusion, we have developed a novel method for measuring the direction of molecular transition dipoles. This new method does not require fragmentation of the molecule to determine the direction of the transition dipole, and allows measurement of non-dissociative bound-free transitions in N_2^+ and CO_2^+ for the first time. Moreover, our approach also allows determination of the direction of the transition dipoles for dissociative ionization, where for example, the excited lifetime of the state is comparable to or longer than the molecular rotation period i.e. where the axial recoil approximation breaks down, as we show for the $O^+ + CO$ channel. The method presented here should be also applicable to larger and more complicated molecules, and can be extended to measurements of excited molecular states. With increased electron energy resolution, future experiments should also allow selective measurements for individual final states. Finally, as pointed out in the Introduction, a particularly interesting extension of this method will be to measure photoelectron angular distributions of highly aligned molecules. Such measurements will ultimately allow the determination of both quantitative molecular-frame transition dipole matrix elements and their phase-shift differences, i.e. a "complete" ionization experiment [83].

4.6 Towards molecular-frame photoelectron angular distributions

This section describes progress towards the measurement of molecular-frame photoelectron angular distributions, including electrons from nondissociative ionization channels. For a strongly aligned sample, the lab frame is identical to the molecular frame, and molecular frame photoelectron angular distributions can be measured. These measurements become more difficult for lower degree of alignment, where molecular-frame information gets blurred in the lab-frame. Here we describe some initial results in obtaining molecular-frame photoelectron angular distributions.

This work is related to the work by Tsubouchi and Suzuki. They created a rotational wave packet of NO molecules in an excited electronic state using a femtosecond laser pulse. From a detailed analysis of the time-dependent lab-frame photoelectron angular distribution, photoionization transition dipole moments were determined [165].

We measure the angular dependence of photoelectrons from the *nondissociative* ionization channel N_2^+ and CO_2^+ from aligned and antialigned molecules. To date, attempts to see such effects have been unsuccessful [92]. Fig. 4.16 shows a typical *lab frame* electron momentum distribution. Figure 4.17 (a) shows the difference in lab-frame photoelectron counts for an aligned versus isotropic molecular sample for CO_2 (black

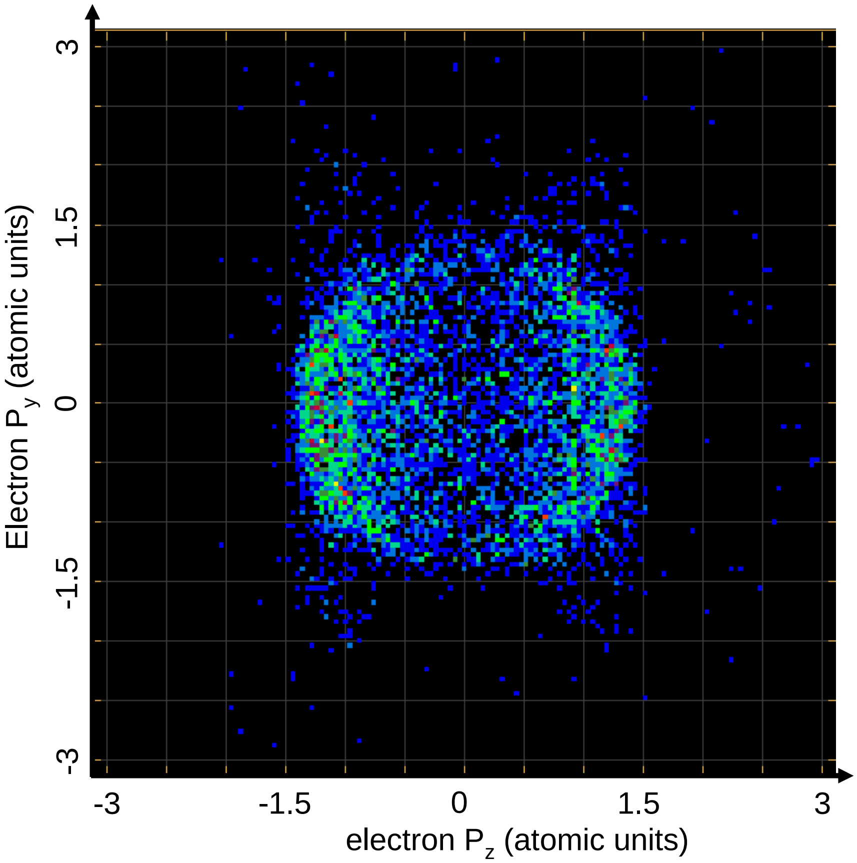

Figure 4.16: 2D projection of lab frame momentum distribution of photoelectrons from N_2.

symbols) and N_2 (red symbols), and Fig. 4.17(b) shows difference in photoelectron counts for an antialigned versus isotropic sample for CO_2 and N_2. The plotted angle here is between photoelectron emission and EUV polarization, which is parallel to the NIR alignment beam polarization. For the aligned case there is an overall negative difference because the nondissociative ionization channel is suppressed for the aligned sample, as discussed above for the ion yield. Around 90° however the difference tends toward zero again in agreement with above results on the ion yield. For the antialigned case in Fig. 4.17(b) we expect to see a positive yield and an increase of photoelectrons at 0°. Indeed we observe evidence of this in the case of CO_2 (Note that the data contain geometrical $sin(\theta)$ factor. The reason why it does not completely go to zero at zero degrees is that the data were more averaged along the x-axis), perhaps due to its higher anisotropic polarizability, but not for N_2.

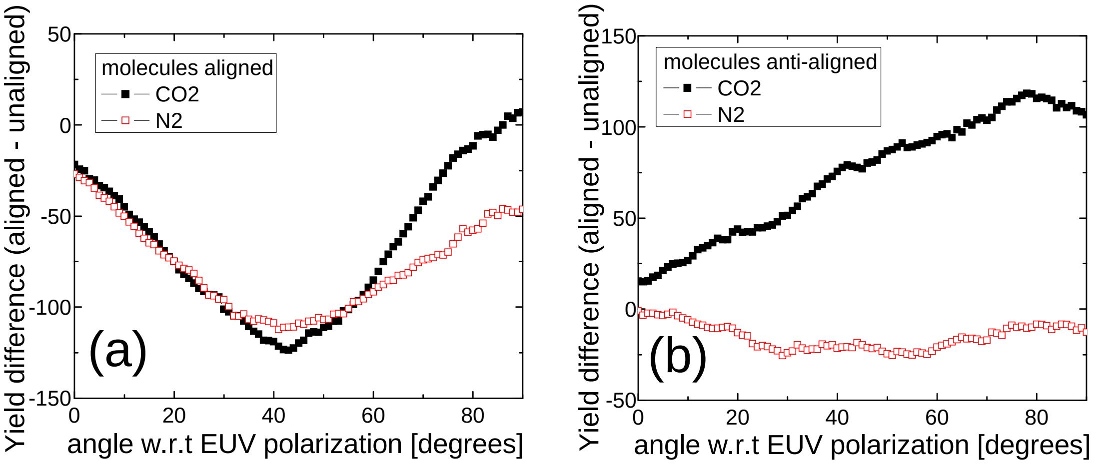

Figure 4.17: Difference in photoelectron angular distributions for aligned (a) and anti-aligned (b) molecules [155].

In future experiments we would like to extract the molecular frame photoelectron angular distribution from observables measurable with the COLTRIMS reaction microscope and the photoelectron angular distribution in the lab frame. To this end, COLTRIMS acquisition and analysis codes and a Matlab program were implemented for future experiments.

Figure 4.18 shows the relevant coordinates. We are particularly interested in photoelectron angular distributions from molecular nondissociative ionizations using the experimental techniques described above. We can measure the photoelectron distribution in the lab frame, $Counts(\theta_{ez})$ where θ_{ez} is the angle between the measured electron momentum and the lab z-axis (equal to the polarization axis of the alignment pulse and ionization pulse). The photoelectron distribution in the laboratory frame is given by

$$Counts(\theta_{ez}) = \sin(\theta_{ez}) \int d\varphi_e \int d\theta_i \sin(\theta_i) \cdot A(\theta_i, \tau) \cdot \sigma(\theta_i) \cdot B(\theta_{ez}, \varphi_e, \theta_i) \tag{4.23}$$

Here, $\sin(\theta_{ez})$ is a geometrical weighting factor, $A(\theta_i, \tau)$ is the angular probability

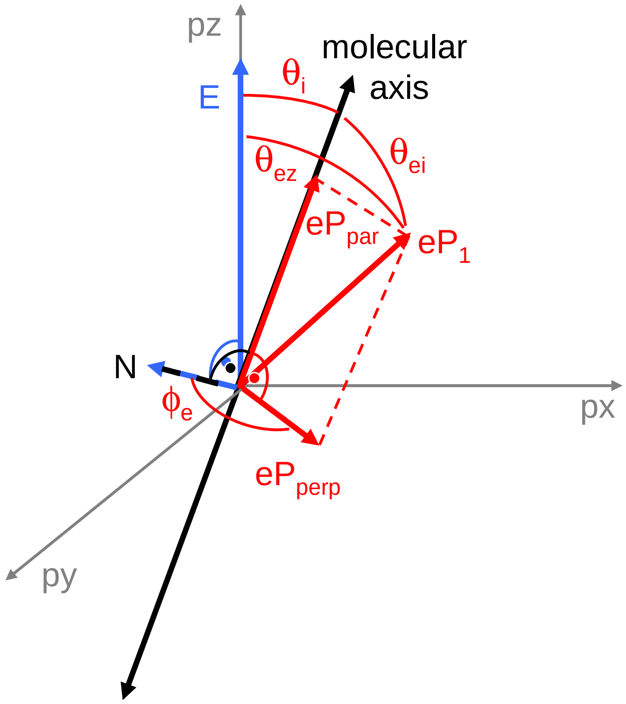

Figure 4.18: Coordinates used for the description of molecular-frame photoelectron angular distributions: The EUV electric field points in the lab-frame z-axis. The black arrow defines the molecular axis - here at an angle θ_i w.r.t. the lab frame z-axis. eP_1 is the momentum of an electron detected at an angle θ_{ez} w.r.t. the lab frame z-axis. The electron emission angles in the molecular frame are θ_{ei} and ϕ_e (defined w.r.t the normal N on the plane spanned by E and the molecular axis).

distribution of molecular axes, which is calculated [114], and θ_i is the angle of the molecular axis in the lab frame. The angular dependence of the ionization cross section $\sigma(\theta_i)$ is expressed in terms of Legendre polynomials,

$$\sigma(\theta_i) = C \cdot (1 + \beta \cdot P_2(\cos(\theta_i))) \tag{4.24}$$

and β gives the orientation of the transition dipole, which can be obtained in a separate measurement (as was described in section 4.5 above). $B(\theta_{ez}, \varphi_e, \theta_i)$ is the photoelectron angular distribution (PAD) in the molecular frame. We express $B(\theta_{ez}, \varphi_e, \theta_i)$ through Legendre polynomials,

$$B(\theta_{ez}, \varphi_e, \theta_i) = A \cdot (1 + \beta^{'} \cdot P_2(\cos(\theta_{ei})) + \gamma^{'} \cdot P_4(\cos(\theta_{ei}))) \tag{4.25}$$

Here $\beta^{'}$, $\gamma^{'}$ are fit parameters (more than two fit parameters can be easily included if necessary), and θ_{ei} is the angle between the momentum of the photoelectron and the molecular axis. As we want to express $B(\theta_{ez}, \varphi_e, \theta_i)$ as a function of lab frame angle θ_{ez}, we express the angle θ_{ei} in the molecular frame by angles in the lab frame (see Figure 4.18):

$$\cos(\theta_{ei}) = \vec{i} \cdot \vec{e} = \sin(\theta_i) \cdot \sin(\theta_{ez}) \cdot \cos(\varphi_e) + \cos(\theta_i) \cdot \cos(\theta_{ez}) \tag{4.26}$$

The ion axis is chosen in the lab xz-plane (which is possible, as the ion distribution is azimuthally symmetric) $\vec{i} = (\sin(\theta_i), 0, \cos(\theta_i))$, and the electron momentum direction is $\vec{e} = (\sin(\theta_{ez})\cos(\varphi_e), \sin(\theta_{ez})\sin(\varphi_e), \cos(\theta_{ez})$. The expression for $Counts(\theta_{ez})$ can be understood as follows: the integral $\int d\theta_i \sin(\theta_i) \cdot A(\theta_i, \tau) \cdot \sigma(\theta_i) \cdot B(\theta_{ez}, \varphi_e, \theta_i)$ averages the PAD over all possible molecular axis orientations, weighted with the probability of finding a molecule with a given angle, $A(\theta_i, \tau)$, and weighted with the probability of ionizing such a molecule, $\sigma(\theta_i)$. The integral $\int d\varphi_e$ finally sums over all azimuthal electron angles, as we do not expect any azimuthal dependence of the electron distribution, because the alignment (and therefore the molecular axes distribution) and ionization geometries are azimuthally symmetric. The information about the PAD is given by the fit parameters $\beta^{'}$, $\gamma^{'}$. Of course, the ansatz 4.25 is oversimplified, and can only provide a very limited amount of information on the actual molecular-frame PAD. However it is straightforward to replace the right-hand side with a more general expression in terms of spherical harmonics [128].

4.7 Other results obtained with COLTRIMS

This section shows unfinished results of several other molecules peeked at with the COLTRIMS reaction microscope.

4.7.1 Coulomb explosion following photoionization of N_2O at 43 eV

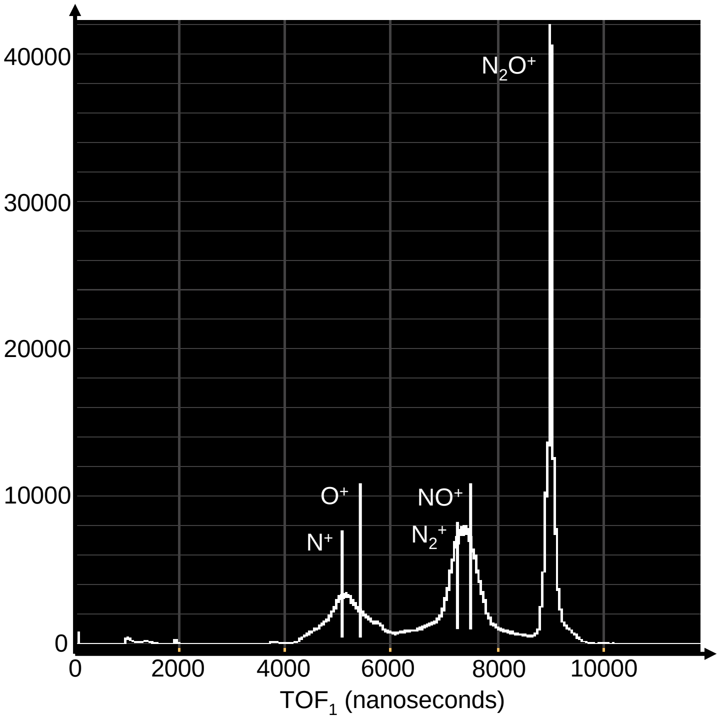

Figure 4.19: Time of flight spectrum of all charged fragments of N_2O irradiated with 43 eV light. N_2O^+: nondissociative ionization. All other fragments may arise from dissociative ionization $O^+ + N_2$ and $N^+ + NO$, or from Coulomb explosion $O^+ + N_2^+$ or $N^+ + NO^+$.

Figures 4.19 - 4.21 show results obtained on the EUV photoionization of N_2O at 43 eV. Importantly, Figure 4.21 shows a projection of the ion angular distribution of NO^+ from the Coulomb explosion of doubly ionized $N_2O^{2+} \rightarrow NO^+ + N^+$. Surprisingly, this ion angular distribution is almost isotropic. From earlier results we had expected a very anisotropic distribution $\beta \sim 1.5$ [2]. However the data in [2] show a missing data point exactly at 43 eV. In addition, Eland and coworkers [150] showed evidence

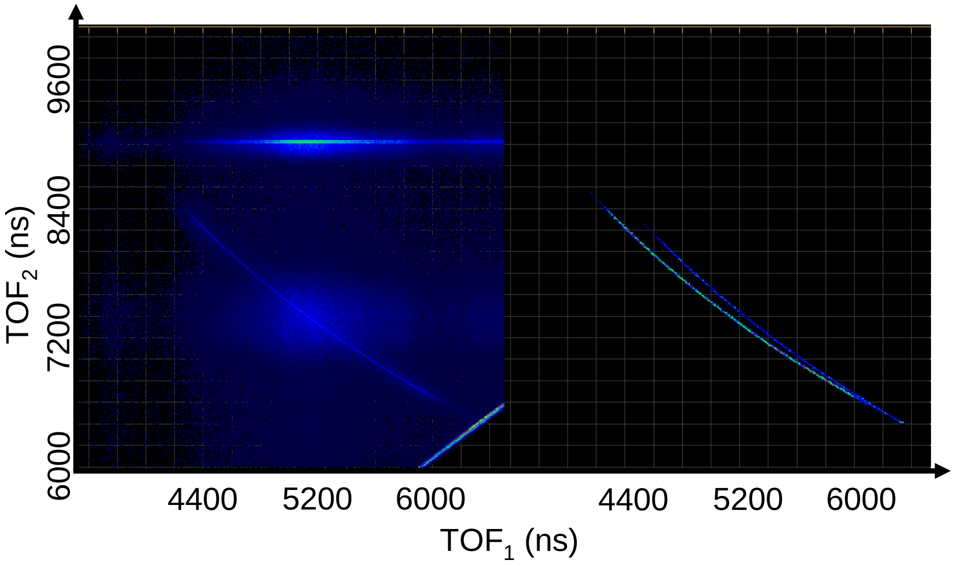

Figure 4.20: Coincidence filters applied. Left: unfiltered TOF_2 vs TOF_1 image of two ion fragments detected in coincidence from the fragmentation of N_2O. Right: The Coulomb-explosion channels of interest, $N_2O \rightarrow NO^+ + N^+$ and $N_2O \rightarrow N_2^+ + O^+$ are selected out by a filter relating TOF_2 and TOF_1 via the momentum conservation in the Coulomb explosion.

of a "probable" metastable state of the N_2O^{2+} dication, assigned as $2\,^3\Pi$ at 42.5 eV, a "somewhat surprising" finding given multiple potential curve crossings in this energy region. A metastable state with a lifetime longer than a rotational period would be consistent with an isotropic angular distribution of fragments.

4.7.2 EUV photoionization of O_2 at 43 eV

Figure 4.22 shows the O^+ fragment from the photoionization of O_2. This fragment shows multiple dissociation channels: The assignment of ion channels in the figure caption follows Vrakking and coworkers [75].

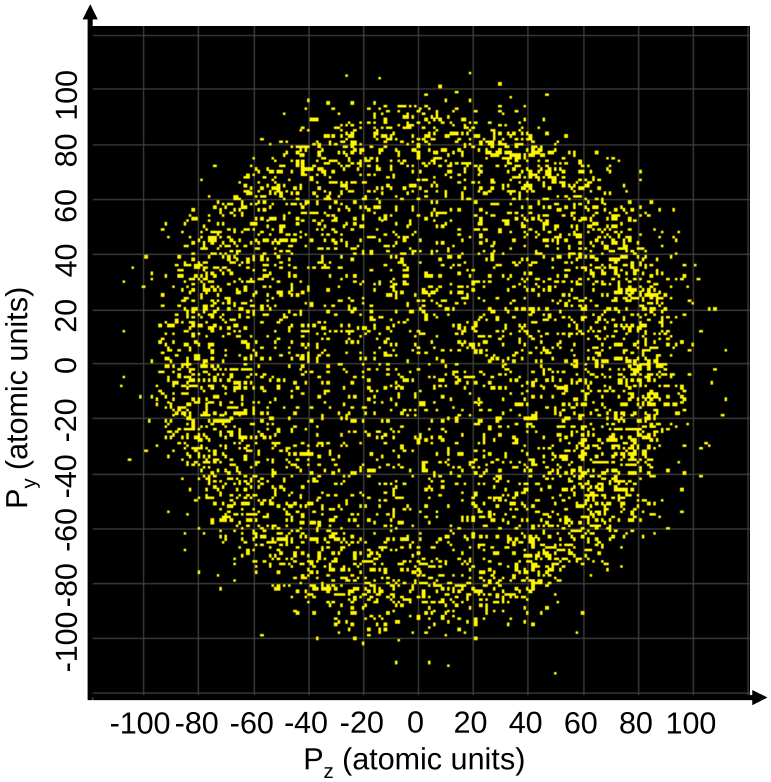

Figure 4.21: 2D projection of the momentum image of NO^+ from the Coulomb explosion $N_2O \rightarrow NO^+ + N^+$.

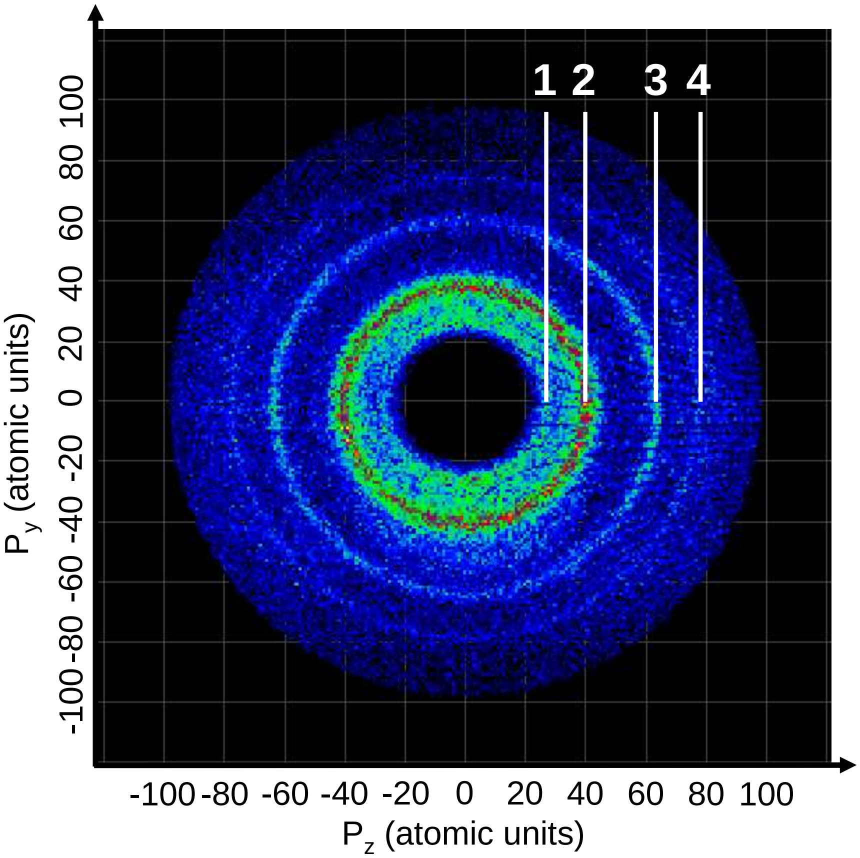

Figure 4.22: The momentum image of O^+ following dissociative ionization of O_2 shows 4 dissociation channels, 1: $O^+(^2P) + O(^3P)$, 2: $O^+(^4S) + O(^3P)$, 3: $O^+(^4S) + O^*(^1D)$, 4: $O^+(^4S) + O(^3P)$.

Chapter 5

Outlook

The results described in this thesis can be a starting point for many future experiments. The combination of ultrafast EUV and NIR radiation with the coincidence capabilities of the COLTRIMS detection technique is a powerful tool for the study of time-resolved correlations of electrons and ions. While the experiments using the COLTRIMS apparatus done so far in our group have employed EUV pulses which are several femtoseconds in duration, future experiments could well benefit from the attosecond duration EUV pulses presented in Chapter 3, enabling attosecond spectroscopy experiments.

It has become clear that future EUV experiments in molecular physics would greatly benefit from state resolution. In general, the use of lower EUV photon energies and EUV mirrors with narrower reflectance bandwidth will allow better energy resolution. The easily energy-tunable EUV radiation produced in this thesis, together with a setup for easy exchange between mirrors for selecting different harmonics will thus be useful for experiments in molecular and materials experiments. Part of this has already been implemented by designing a setup consisting of 2 EUV mirrors in a z-configuration. The two rotatable EUV mirrors consist of pie slices, each coated for different center energies. Such a setup will essentially create a "table-top synchrotron", and will e.g. allow one to measure the orientation of the transition dipole (and transition dipole matrix elements) with state resolution, as opposed to the averaged results presented in this thesis. In addition it will simplify the analysis of photoelectron angular distributions.

Overall, I am convinced that the field of attosecond science is just at its beginning, and that there are exciting times to come for ultrafast EUV radiation. Isolated attosecond pulses generated from long driving pulses using waveguide geometries will be useful for the study of fast electron dynamics. Easily energy-tunable single-femtosecond, near Fourier transform limited pulses will be an excellent source for the study of the coupled motion of nuclei and electrons, as it occurs e.g. near conical intersections in molecules. Sophisticated pump-probe experiments in combination with NIR pulses or electron wave packets, together with more and more sensitive detection techniques, and the utilization of coherent EUV imaging techniques, will open up more and more applications for this unique table-top light source.

Bibliography

[1] http://hsb.uni-frankfurt.de/web/research/atomic/COLTRIMS/.

[2] M. Alagia, P. Candori, S. Falcinelli, M. Lavollée, F. Pirani, R. Richter, S. Stranges, and F. Vecchiocattivi. Anisotropy of the angular distribution of fragment ions in dissociative double photoionization of n_2o molecules in the 30-50 eV energy range. JCP, 126:201101, 2007.

[3] Carlo Altucci, Valer Tosa, and Raffaele Velotta. Beyond the single-atom response in isolated attosecond-pulse generation. Phys. Rev. A, 75:061401(R), 2007.

[4] A. Apolonski, P. Dombi, G.G. Paulus, M. Kakehata, R. Holzwarth, Th. Udem, Ch. Lemell, K. Torizuka, J. Burgdörfer, T.W. Hänsch, and F. Krausz. Observation of light-phase-sensitive photoemission from a metal. Phys. Rev. Lett., 92:073902, 2004.

[5] S. Backus, R. Bartels, S. Thompson, R. Dollinger, H. C. Kapteyn, and M. M. Murnane. High-efficiency, single-stage 7-kHz high-average-power ultrafast laser system. Opt. Lett., 26:465, 2001.

[6] S. Baker, J. S. Robinson, C. A. Haworth, H. Teng, R. A. Smith, C. C. Chirilă, M. Lein, J. W. G. Tisch, and J. P. Marangos. Probing proton dynamics in molecules on an attosecond time scale. Science, 312:424, 2006.

[7] A. Baltuska, T. Udem, M. Uiberacker, M. Hentschel, E. Goulielmakis, C. Gohle, R. Holzwarth, V. S. Yakoviev, A. Scrinzi, T. W. Hänsch, and F. Krausz. Attosecond control of electronic processes by intense light fields. Nature, 421:611–615, 2003.

[8] A. Baltuska, M. Uiberacker, E. Goulielmakis, R. Kienberger, V. S. Yakovlev, T. Udem, T. W. Hänsch, and F. Krausz. Phase controlled amplification of few-cycle laser pulses. IEEE J. Sel. Top. Quantum Electron., 9:972, 2003.

[9] Albrecht Bartels, Nathan R. Newbury, Isabell Thomann, Leo Hollberg, and Scott A. Diddams. Broadband phase-coherent optical frequency synthesis with actively linked Ti:sapphire and Cr:forsterite femtosecond lasers. Opt. Lett., 29:403–405, 2004.

[10] R. Bartels, S. Backus, I. Christov, H. Kapteyn, and M. Murnane. Attosecond time-scale feedback control of coherent X-ray generation. Chem. Phys., 267:277–289, 2001.

[11] R. Bartels, S. Backus, E. Zeek, L. Misoguti, G. Vdovin, I. P. Christov, M. M. Murnane, and H. C. Kapteyn. Shaped-pulse optimization of coherent emission of high-harmonic soft X-rays. Nature, 406:164–166, 2000.

[12] Randy A. Bartels, Ariel Paul, Hans Green, Henry C. Kapteyn, Margaret M. Murnane, Sterling Backus, Ivan P. Christov, Yanwei Liu, David Attwood, and Chris Jacobsen. Generation of spatially coherent light at extreme ultraviolet wavelengths. Science, 297:376, 2002.

[13] U. Becker and D. Shirley. VUV And Soft X-Ray Photoionization. Plenum Press.

[14] C. E. Brion and K. H. Tan. Partial oscillator strengths for the photoionization of N_2O and CO_2 (20-60 ev). Chem. Phys., 34:141, 1978.

[15] I. Cacelli, R. Moccia, and R. Montuoro. Influence of the channel interaction on the photoabsorption and photoionization spectra of carbon dioxide. Phys. Rev. A, 63:012512, 2001.

[16] Ivo Cacelli, Roberto Moccia, and Antonio Rizzo. Gaussian-type-orbital basis sets for the calculation of continuum properties in molecules: The differential photoionization cross section of molecular nitrogen. Phys. Rev. A, 57(3):1895–1905, Mar 1998.

[17] Wei Cao, Peixiang Lu, Pengfei Lan, Xinlin Wang, and Guang Yang. Single-attosecond pulse generation with an intense multicycle driving pulse. Phys. Rev. A, 74:063821, 2006.

[18] A. L. Cavalieri, N. Müller, Th. Uphues, V. S. Yakovlev, A. Baltuska, B. Horvath, B. Schmidt, L. Blümel, R. Holzwarth, S. Hendel, M. Drescher, U. Kleineberg, P. M. Echenique, R. Kienberger, F. Krausz, and U. Heinzmann. Attosecond spectroscopy in condensed matter. Nature, 449:1029, 2007.

[19] Z. Chang, A. Rundquist, H. Wang, I. Christov, H. C. Kapteyn, and M. M. Murnane. Temporal phase control of soft-x-ray harmonic emission. Phys. Rev. A, 58:30(R), 1998.

[20] Zenghu Chang. Single attosecond pulse and xuv supercontinuum in the high-order harmonic plateau. Phys. Rev. A, 70:043802, 2004.

[21] I. P. Christov, R. Bartels, H. C. Kapteyn, , and M. M. Murnane. Attosecond time-scale intra-atomic phase matching of high harmonic generation. Phys. Rev. Lett., 86:5458–5461, 2001.

[22] I. P. Christov, M. M. Murnane, and H. C. Kapteyn. High-harmonic generation of attosecond pulses in the “single-cycle” regime. Phys. Rev. Lett., 78:1251–1254, 1997.

[23] Ivan Christov, Henry Kapteyn, and Margaret Murnane. Quasi-phase matching of high-harmonics and attosecond pulses in modulated waveguides. Opt. Express, 7(11):362–367, 2000.

[24] Ivan P. Christov, J. Zhou, J. Peatross, A. Rundquist, M. M. Murnane, and H. C. Kapteyn. Nonadiabatic effects in high-harmonic generation with ultrashort pulses. Phys. Rev. Lett., 77:1743, 1996.

[25] P. B. Corkum, N. H. Burnett, and M. Y. Ivanov. Subfemtosecond pulses. Opt. Lett., 19:1870, 1994.

[26] P.B. Corkum. Plasma perspective on strong-field multiphoton ionization. Phys. Rev. Lett, 71:1994, 1993.

[27] Eric Cormier, Ian A. Walmsley, Ellen M. Kosik, Adam S. Wyatt, Laura Corner, and Louis F. DiMauro. Self-referencing, spectrally, or spatially encoded spectral interferometry for the complete characterization of attosecond electromagnetic pulses. Phys. Rev. Lett., 94:033905, 2005.

[28] K. L. Corwin, I. Thomann, T. Dennis, R. W. Fox, W. Swann, E. A. Curtis, C. W. Oates, G. Wilpers, A. Bartels, S. L. Gilbert, L. Hollberg, N. R. Newbury, S. A. Diddams, J. W. Nicholson, and M. F. Yan. Absolute-frequency measurements with a stabilized near-infrared optical frequency comb from a Cr:forsterite laser. Opt. Lett., 29:397–399, 2004.

[29] S. T. Cundiff and J. Ye. Colloquium: Femtosecond optical frequency combs. Rev. Mod. Phys., 75:325–342, 2003.

[30] A. Czasch, D. Akoury, O. Jagutzki, J. B. Williams, N. A. Cherepkov, S. K. Semenov, C. W. McCurdy, T. N. Rescigno, C. L. Cocke, T. Osipov, S. Lee, M. H. Prior, A. Belkacem, A. L. Landers, H. Schmidt-Böcking, Th. Weber, and R. Dörner. Ultrafast probing of core hole localization in N_2. Science, 320:920, 2008.

[31] A. de Bohan, P. Antoine, D. B. Milošević, and B. Piraux. Phase-dependent harmonic emission with ultrashort laser pulses. Phys. Rev. Lett., 81:1837, 1998.

[32] P. Dietrich, F. Krausz, and P. B. Corkum. Determining the absolute phase of a few-cycle laser pulse. Opt. Lett., 25:16, 2000.

[33] Dan Dill. Fixed-molecule photoelectron angular distributions. The Journal of Chemical Physics, 65(3):1130–1133, 1976.

[34] R. Dörner, V. Mergel, O. Jagutzki, L. Spielberger, J. Ullrich, R. Moshammer, and H. Schmidt-Böcking. Cold target recoil ion momentum spectroscopy: a 'momentum microscope' to view atomic collision dynamics. Physics Reports, 330:95–192, 2000.

[35] D. Dowek, M. Lebecha, J.C. Houvera, and R.R. Lucchese. J. Electron Spectrosc. Relat. Phenom., 141:211, 2004.

[36] M. Drescher, M. Hentschel, R. Kienberger, G. Tempea, C. Spielmann, G. A. Reider, P. B. Corkum, and F. Krausz. X-ray pulses approaching the attosecond frontier. Science, 291:1923–1927, 2001.

[37] M. Drescher, M. Hentschel, R. Kienberger, M. Uiberacker, V. Yakovlev, A. Scrinzi, Th. Westerwalbesloh, U. Kleineberg, U. Heinzmann, and F. Krausz. Time-resolved atomic inner-shell spectroscopy. Nature, 419:803, 2002.

[38] C. G. Durfee, A. Rundquist, S. Backus, Z. Chang, C. Herne, H. C. Kapteyn, and M. M. Murnane. Guided-wave phase-matching of ultrashort-pulse light. J. Nonlinear Opt. Phys. Mat., 8:211–234, 1999.

[39] A. Paul K. Hagen A. Czasch T. Jahnke P. Ranitovic C. L. Cocke B. Walker M. M. Murnane E. Gagnon, A. S. Sandhu and H. C. Kapteyn. Time-resolved momentum imaging system for molecular dynamics studies using a tabletop ultrafast extreme-ultraviolet light source. Rev. Sci. Instr., 79:063102, 2008.

[40] A.T.J.B. Eppink and D.H. Parker. Velocity map imaging of ions and electrons using electrostatic lenses. Rev. Sci. Instr., 68:3477–3484, 1997.

[41] P. Erman, A. Karawajczyk, E. Rachlew-Källne, J. Rius i Riu, M. Stankiewicz, K. Yoshiki Franzén, A. Weider Moen, and L. Veseth. Non franck-condon effects in photoionization of molecular oxygen. Phys. Script., 62:294, 2000.

[42] G. Korn F. A. Weihe, S. K. Dutta and P. L. Shkolnikov D. Du, P. H. Bucksbaum. Polarization of high-intensity high-harmonic generation. Phys. Rev. A, 51:3433, 1995.

[43] Gy. Farkas and Cs. Tóth. Proposal for attosecond light pulse generation using laser induced multiple-harmonic conversion processes in rare gases. Phys. Lett. A, 168:447 – 450, 1992.

[44] T. M. Fortier, D. J. Jones, J. Ye, and S. T. Cundiff. Long-term carrier-envelope phase coherence. Opt. Lett., 27:1436, 2002.

[45] T. M. Fortier, David J. Jones, and S. T. Cundiff. Phase stabilization of an octave-spanning ti:sapphire laser. Opt. Lett., 28:2198–2200, 2003.

[46] Tara M. Fortier, Jun Ye, Steven T. Cundiff, and Robert S. Windeler. Nonlinear phase noise generated in air-silica microstructure fiber and its effect on carrier-envelope phase. Opt. Lett., 27(6):445–447, 2002.

[47] Bretislav Friedrich and Dudley Herschbach. Alignment and trapping of molecules in intense laser fields. Phys. Rev. Lett., 74(23):4623–4626, Jun 1995.

[48] M. B. Gaarde and K. J. Schafer. Opt. Lett., 31:3188, 2006.

[49] Mette B Gaarde, Jennifer L Tate, and Kenneth J Schafer. Macroscopic aspects of attosecond pulse generation. J. Phys. B: At. Mol. Opt. Phys., 41:132001, 2008.

[50] E. Gagnon, I.Thomann, A. Paul, A. L. Lytle, S. Backus, M. M. Murnane, H. C. Kapteyn, and Arvinder S. Sandhu. Long-term carrier-envelope phase stability from a grating-based, chirped pulse amplifier. Opt. Lett., 31:1866, 2006.

[51] Etienne Gagnon, Predrag Ranitovic, Xiao-Min Tong, C. L. Cocke, Margaret M. Murnane, Henry C. Kapteyn, and Arvinder S. Sandhu. Soft X-ray-Driven Femtosecond Molecular Dynamics. Science, 317(5843):1374–1378, 2007.

[52] J. Gagnon, E. Goulielmakis, and V.S. Yakovlev. The accurate FROG characterization of attosecond pulses from streaking measurements. Appl. Phys. B, 92:25–32, 2008.

[53] M. Geissler, G. Tempea, A. Scrinzi, M. Schnürer, F. Krausz, and T. Brabec. Light propagation in field-ionizing media: Extreme nonlinear optics. Phys. Rev. Lett., 83:2930–2933, 1999.

[54] E. A. Gibson, A. Paul, N. Wagner, R. Tobey, D. Gaudiosi, S. Backus, I. P. Christov, A. Aquila, E. M. Gullikson, D. T. Attwood, M. M. Murnane, and H. C. Kapteyn. Coherent soft X-ray generation in the water window with quasiphase matching. Science, 302:95, 2003.

[55] Emily Gibson. Quasi-Phase Matching of Soft X-ray Light fromHigh-Order Harmonic Generation using Waveguide Structures. PhD thesis, University of Colorado (Boulder), 2004.

[56] T.E. Glover, R.W. Schoenlein, A.H Chin, and C.V. Shank. Observation of laser assisted photoelectric effect and femtosecond high order harmonic radiation. Phys. Rev. Lett., 76:2468–2471, 1996.

[57] Roentdek GmbH. Mcp delay line detector manual.

[58] E. Goulielmakis, M. Schultze, M. Hofstetter, V. S. Yakovlev, J. Gagnon, M. Uiberacker, A. L. Aquila, E. M. Gullikson, D. T. Attwood, R. Kienberger, F. Krausz, and U. Kleineberg. Single-cycle nonlinear optics. Science, 320:1614–1617, 2008.

[59] S.E. Hands, J.J Macklin, and T.W. Haensch. Atomic scale temporal structure inherent to high-order harmonic generation. Opt. Comm., 100:487–490, 1993.

[60] C. A. Haworth, L. E. Chipperfield, J. S. Robinson, P. L. Knight, J. P. Marangos, and J. W. G. Tisch. Half-cycle cutoffs in harmonic spectra and robust carrier-envelope phase retrieval. Nature Physics, 3:52–57, 2007.

[61] Feng He, Camilo Ruiz, and Andreas Becker. Control of electron excitation and localization in the dissociation of H_2^+ and its isotopes using two sequential ultrashort laser pulses. Physical Review Letters, 99(8):083002, 2007.

[62] F. W. Helbing, G. Steinmeyer, J. Stenger, H. R. Telle, and U. Keller. Carrier-envelope-offset dynamics and stabilization of femtosecond pulses. Appl. Phys. B, 74:S35–S42, 2002.

[63] M. Hentschel, R. Kienberger, Ch. Spielmann, G. A. Reider, N. Milosevic, T. Brabec, P. Corkum, U. Heinzmann, M. Drescher, and F. Krausz. Attosecond metrology. Nature, 414:509–513, 2001.

[64] Y Hikosaka and J H D Eland. Molecular-frame photoelectron angular distributions in inner-valence photoionization of N_2. J. Phys. B: At. Mol. Opt. Phys., 33(16):3137, 2000.

[65] Paul Hockett, Adrian K. King, Ivan Powis, and Katharine L. Reid. Complete determination of the photoionization dynamics of a polyatomic molecule. I. experimental photoelectron angular distributions from $\tilde{a}^1\ A_u$ acetylene. The Journal of Chemical Physics, 127(15):154307, 2007.

[66] Paul Hockett and Katharine L. Reid. Complete determination of the photoionization dynamics of a polyatomic molecule. II. determination of radial dipole matrix elements and phases from experimental photoelectron angular distributions from [a-tilde] [sup 1]a[sub u] acetylene. The Journal of Chemical Physics, 127(15):154308, 2007.

[67] K.W. Holman, R.J Jones, A. Marian, S.T. Cundiff, and Jun Ye. Detailed studies and control of intensity-related dynamics of femtosecond frequency combs from mode-locked ti:sapphire lasers. IEEE Journal of Selected Topics in Quantum Electronics, 9:1018–24, 2003.

[68] Kyung-Han Honga, Jongmin Lee, Bixue Hou, John A. Nees, Erik Power, and Gerard A. Mourou. Carrier-envelope phase stabilization of high-contrast femtosecond laser pulses with a relativistic intensity. Appl. Phys. Lett., 89:031113, 2006.

[69] K. P. Huber and G. Herzberg. Constants of Diatomic Molecules. Van Nostrand Reinhold.

[70] Yong Ho Cha Jung-Hoon Kim Kyung Han Hong Hyun Joon Shin, Dong Gun Lee and Chang Hee Nam. Nonadiabatic blueshift of high-order harmonics from ar and ne atoms in an intense femtosecond laser field. Phys. Rev. A, 63:053407, 2001.

[71] Charles G. Durfee III, Andy R. Rundquist, Sterling Backus, Catherine Herne, and Margaret M. Murnaneand Henry C. Kapteyn. Phase matching of high-order harmonics in hollow waveguides. Phys. Rev. Lett., 83:2187, 1999.

[72] J. Itatani, J. Levesque, D. Zeidler, Hiromichi Niikura, H. Pépin, J. C. Kieffer, P. B. Corkum, and D. M. Villeneuve. Tomographic imaging of molecular orbitals. Nature, 432:867, 2004.

[73] J. Itatani, F. Quéré, G. L. Yudin, M.Yu. Ivanov, F. Krausz, and P. B. Corkum. Attosecond streak camera. Phys. Rev. Lett., 88:173903, 2002.

[74] M. Ivanov, T. Zuo P. B. Corkum, and A. Bandrauk. Routes to control of intense-field atomic polarizability. Phys. Rev. Lett., 74:2933, 1995.

[75] P. Johnsson, W. Siu, A. Gijsbertsen, J. Verhoeven, A.S. Meijer, W. van der Zande, and M.J.J. Vrakking. Velocity map imaging of atomic and molecular processes at the free electron laser in hamburg (flash). J. Mod. Opt., 15:26932709, 2008.

[76] D. Jones, S. Diddams, J. Ranka, A. Stentz, R. Windeler, J. Hall, and S. Cundiff. Carrier-envelope phase control of femtosecond mode-locked lasers and direct optical frequency synthesis. Science, 288:635–639, 2000.

[77] R. J. Jones, J.-C. Diels, J. Jasapara, and W. Rudolph. Stabilization of the frequency, phase, and repetition rate of an ultra-short pulse train to a Fabry-Perot reference cavity. Opt. Commun., 174:409, 2000.

[78] R. Jason Jones, Isabell Thomann, and Jun Ye. Precision stabilization of femtosecond lasers to high-finesse optical cavities. Phys. Rev. A, 69:051803(R), 2004.

[79] M. Kakehata, H. Takada, Y. Kobayashi, K. Torizuka, Y. Fujihira, T. Homma, and H. Takahashi. Single-shot measurement of the carrier-envelope phase changes by spectral interferometry. Opt. Lett., 26:1436, 2001.

[80] Masayuki Kakehata, Hideyuki Takada, Yohei Kobayashi, Kenji Torizuka, Hiroaki Takamiya, Kazuki Nishijima, Tetsuya Homma, Hideo Takahashi, Katsuaki Okubo, Shinki Nakamura, and Yahei Koyamada. Carrier-envelope-phase stabilized chirped-pulse amplification system scalable to higher pulse energies. Opt. Express, 12(10):2070–2080, 2004.

[81] D. J. Kane. Principal components generalized projections: a review. J. Opt. Soc. Am. B, 25:120, 2008.

[82] Henry C. Kapteyn, Margaret M. Murnane, and Ivan P. Christov. Extreme nonlinear optics: Coherent x rays from lasers. Physics Today, 58:39, 2005.

[83] J. Kessler. Comments At. Mol. Phys., 10:47, 1981.

[84] R. Kienberger, E. Goulielmakis, M. Uiberacker, A. Baltuska, V. Yakovlev, F. Bammer, A. Scrinzi, T. Westerwalbesloh, U. Kleineberg, U. Heinzmann, M. Drescher, and F. Krausz. Atomic transient recorder. Nature, 427:817–821, 2004.

[85] M. F. Kling, Ch. Siedschlag, A. J. Verhoef, J. I. Khan, M. Schultze, Th. Uphues, Y. Ni, M. Uiberacker, M. Drescher, F. Krausz, and M. J. J. Vrakking. Control of electron localization in molecular dissociation. Science, 312:246, 2006.

[86] P Kruit and F H Read. Magnetic field paralleliser for 2π electron- spectrometer and electron-image magnifier. J. Phys. E: Sci. Instrum., 16:313, 1983.

[87] K. Kulander, K. Schafer, and J. Krause. Dynamics of short-pulse excitation, ion- ization, and harmonic conversion, in 'Super-intense laser-atom physics', B. Piraux, A. L'Huillier, and K. Rzazewski, Eds., Plenum, Han-sur-Lesse, Belgium. Super-Intense Laser-Atom Physics, 316:95–110, 1993.

[88] V. Kumarappan, C. Z. Bisgaard, S. S. Viftrup, L. Holmegaard, and H. J. Stapelfeldt. Role of rotational temperature in adiabatic molecular alignment. J. Chem. Phys., 194309:125, 2006.

[89] David J. Leahy, Katharine L. Reid, and Richard N. Zare. Complete description of two-photon (1+1[script ']) ionization of NO deduced from rotationally resolved photoelectron angular distributions. The Journal of Chemical Physics, 95(3):1757–1767, 1991.

[90] K F Lee, I V Litvinyuk, P W Dooley, M Spanner, D M Villeneuve, and P B Corkum. Two-pulse alignment of molecules. J. Phys. B: At. Mol. Opt. Phys., 37:L43–L48, 2004.

[91] C. Lemell, X. Tong, F. Krausz, and J. Burgdörfer. Electron emission from metal surfaces by ultrashort pulses: Determination of the carrier-envelope phase. Phys. Rev. Lett., 90:076403, 2003.

[92] F. Lepine, M. F. Kling, Y. F. Ni, J. Khan, O. Ghafur, T. Martchenko, E. Gustafsson, P. Johnsson, K. Varju, T. Remetter, A. LHuillier, and M. J. J. Vrakking. Short XUV pulses to characterize field-free molecular alignment. J. Mod. Opt., 54:953, 2007.

[93] M. Lewenstein, Ph. Balcou, M. Yu. Ivanov, Anne L'Huillier, and P.B. Corkum. Theory of high-harmonic generation by low-frequency laser fields. Phys. Rev. A, 49:2117–2132, 1994.

[94] Chengquan Li, Eric Moon, Hiroki Mashiko, Christopher M. Nakamura, Predrag Ranitovic, Chakra M. Maharjan, C. Lewis Cocke, Zenghu Chang, and Gerhard G. Paulus. Precision control of carrier-envelope phase in grating based chirped pulse amplifiers. Optics Express, 14:11468, 2006.

[95] W Li, X Zhou, R Lock, S Patchkovskii, A Stolow, H Kapteyn, and M Murnane. Time-resolved dynamics in N_2O_4 probed using high harmonic generation. Science, 322:1207, 2008.

[96] J. B. Liu, W. W. Chen, M. Hochlaf, X. M. Qian, C. Chang, and C. Y. Ng. Photoemission in the molecular frame using the vector correlation approach: from valence to inner-valence shell ionization. J. Chem. Phys., 118:149, 2003.

[97] T. Lohmuller, M. Erdmann, O. Rubner, and V. Engel. Determination of transition dipole moments from time-resolved photoelectron spectroscopy. Eur. Phys. J. D, 25:95, 2003.

[98] Rodrigo Lopez-Martens, Katalin Varju, Per Johnsson, Johan Mauritsson, Yann Mairesse, Pascal Salieres, Mette B. Gaarde, Kenneth J. Schafer, Anders Persson, Sune Svanberg, Claes-Goran Wahlstrom, and Anne L'Huillier. Amplitude and phase control of attosecond light pulses. Physical Review Letters, 94(3):033001, 2005.

[99] Robert R. Lucchese and Vincent McKoy. Studies of differential and total photoionization cross sections of carbon dioxide. Phys. Rev. A, 26(3):1406–1418, Sep 1982.

[100] Y. Mairesse, A. de Bohan, L. J. Frasinski, H. Merdji, L. C. Dinu, P. Monchicourt, P. Breger, M. Kovačev, R. Taïeb, B. Carré, H. G. Muller, P. Agostini, and P. Salières. Attosecond synchronization of high-harmonic soft X-rays. Science, 302:1540–1543, 2003.

[101] Y. Mairesse and F. Quere. Frequency-resolved optical gating for complete reconstruction of attosecond bursts. Physical Review A (Atomic, Molecular, and Optical Physics), 71(1):011401, 2005.

[102] Hiroki Mashiko, Steve Gilbertson, Chengquan Li, Eric Moon, and Zenghu Chang. Optimizing the photon flux of double optical gated high-order harmonic spectra. Phys. Rev. A, 77:063423, 2008.

[103] M. Meckel, D. Comtois, D. Zeidler, A. Staudte, D. Pavicic, H. C. Bandulet, H. Pépin, J. C. Kieffer, R. Dörner, D. M. Villeneuve, and P. B. Corkum. Laser-induced electron tunneling and diffraction. Science, 320:1478 – 1482, 2008.

[104] Hamed Merdji, Thierry Auguste, Willem Boutu, J.-Pascal Caumes, Bertrand Carré, Thomas Pfeifer, Aurélie Jullien, Daniel M. Neumark, , and Stephen R. Leone. Isolated attosecond pulses using a detuned second-harmonic field. Opt. Lett., 32:3134–3136, 2007.

[105] L. Miaja-Avila, G. Saathoff, S. Mathias, J. Yin, C. La o vorakiat, M. Bauer, M. Aeschlimann, M. M. Murnane, and H. C. Kapteyn. Direct measurement of core-level relaxation dynamics on a surface-adsorbate system. Phys. Rev. Lett., 101:046101, 2008.

[106] L. Miaja-Avila, G. Saathoff, S. Mathias, J. Yin, C. La o vorakiat, M. Bauer, M. Aeschlimann, M. M. Murnane, and H. C. Kapteyn. Direct measurement of core-level relaxation dynamics on a surface-adsorbate system. Phys. Rev. Lett., 101:046101, 2008.

[107] D. Miller. “Free jet sources,” in Atomic and Molecular Beam Methods (G. Scoles, ed.) vol. 1, pp. 1453. Oxford University Press.

[108] Oliver D. Mücke, Thorsten Tritschler, Martin Wegener, Uwe Morgner, Franz X. Kärtner, Galina Khitrova, and Hyatt M. Gibbs. Carrier-wave Rabi flopping: role of the carrier-envelope phase. Opt. Lett., 29:2160, 2004.

[109] H.G. Muller. Reconstruction of attosecond harmonic beating by interference of two-photon transitions. Appl. Phys. B, 74:S17S21, 2002.

[110] Yasuo Nabekawa, Hirokazu Hasegawa, Eiji J. Takahashi, and Katsumi Midorikawa. Production of doubly charged helium ions by two-photon absorption of an intense sub-10-fs soft X-ray pulse at 42 eV photon energy. Phys. Rev. Lett., 94:043001, 2005.

[111] H. Niikura and P.B. Corkum. Attosecond and angstrom science. Adv. At. Mol. Opt. Phys., 54:511, 2007.

[112] M. Nisoli, G. Sansone, S. Stagira, S. De Silvestri, C. Vozzi, M. Pascolini, L. Poletto, P. Villoresi, and G. Tondello. Effects of carrier-envelope phase differences of few-optical-cycle light pulses in single-shot high-order-harmonic spectra. Phys. Rev. Lett., 91:213905, 2003.

[113] M. Nisoli, S. De Silvestri, O. Svelto, R. Szipöcs, K. Ferencz, Ch. Spielmann, S. Sartania, , and F. Krausz. Compression of high-energy laser pulses below 5 fs. Optics Express, 22:522–524, 1997.

[114] Juan Ortigoso, Mirta Rodríguez, Manish Gupta, and Bretislav Friedrich. Time evolution of pendular states created by the interaction of molecular polarizability with a pulsed nonresonant laser field. The Journal of Chemical Physics, 110(8):3870–3875, 1999.

[115] Hongkun Park and Richard N. Zare. Photoionization dynamics of the NO $a^2\ \sigma^+$ state deduced from energy- and angle-resolved photoelectron spectroscopy. The Journal of Chemical Physics, 99(9):6537–6544, 1993.

[116] A. Paul, R. A. Bartels, R. Tobey, H. Green, S. Weiman, I. P. Christov, M. M. Murnane, H. C. Kapteyn, and S. Backus. Quasi-phase-matched generation of coherent extreme-ultraviolet light. Nature, 421:51–54, 2003.

[117] P. M. Paul, E. S. Toma, P. Breger, G. Mullot, F. Auge, Ph. Balcou, H. G. Muller, and P. Agostini. Observation of a Train of Attosecond Pulses from High Harmonic Generation. Science, 292(5522):1689–1692, 2001.

[118] G. G. Paulus, F. Grasbon, H. Walther, P. Villoresi, M. Nisoli, S. Stagira, E. Priori, and S. De Silvestri. Absolute-phase phenomena in photoionization with few-cycle laser pulses. Nature, 414:182–184, 2001.

[119] G.G. Paulus, F. Lindner, H.Walther, A. Baltuska, E. Goulielmakis, M. Lezius, and F. Krausz. Measurement of the phase of few-cycle laser pulses. Phys. Rev. Lett., 91:253004, 2003.

[120] D. Pavicic, K. F. Lee, D. M. Rayner, P. B. Corkum, and D. M. Villeneuve. Direct measurement of the angular dependence of ionization for N_2, O_2, and CO_2 in intense laser fields. Phys. Rev. Lett., 98:243001, 2007.

[121] E. R. Peterson, C. Buth, D. A. Arms, R. W. Dunford, E. P. Kanter, B. Krässig, E. C. Landahl, S. T. Pratt, R. Santra, S. H. Southworth, and L. Young. An x-ray probe of laser-aligned molecules. Applied Physics Letters, 92(9):094106, 2008.

[122] Thomas Pfeifer, Aurélie Jullien, Mark J. Abel, Phillip M. Nagel, Lukas Gallmann, Daniel M. Neumark, and Stephen R. Leone. Generating coherent broadband continuum soft-x-ray radiation by attosecond ionization gating. Opt. Express, 15:17120–17128, 2007.

[123] Anne L'Huillier Philippe Balcou, Pascal Salières and Maciej Lewenstein. Generalized phase-matching conditions for high harmonics: The role of field-gradient forces. Phys. Rev. A, 55:3204, 1997.

[124] F. Quere, Y. Mairesse, and J. Itatani. Temporal characterization of attosecond XUV fields. J. Mod. Opt., 52:339, 2005.

[125] T. M. Ramond, S. A. Diddams, L. Hollberg, and A. Bartels. Phase-coherent link from optical to microwave frequencies by means of the broadband continuum from a 1-ghz ti:sapphire femtosecond oscillator. Opt. Lett., 20:1842–1844, 2002.

[126] J. Rauschenberger, T. Fuji, M. Hentschel, A.-J. Verhoef, T. Udem, C. Gohle, T.W. Hänsch, and F. Krausz. Carrier-envelope phase-stabilized amplifier system. Laser Physics Letters, 3:3742, 2006.

[127] J. Reichert, R. Holzwarth, Th. Udem, and T. W. Hänsch. Measuring the frequency of light with mode-locked lasers. Opt. Commun., 172:59, 1999.

[128] K. L. Reid. Photoelectron angular distributions. Annual Review of Physical Chemistry, 54:397–424, 2003.

[129] F. Remacle and R. Levine. An electronic time scale in chemistry. PNAS, 103:6793, 2006.

[130] F. Remacle and R. D. Levine. The time scale for electronic reorganization upon sudden ionization of the water and water-methanol hydrogen bonded dimers and of the weakly bound NO dimer. The Journal of Chemical Physics, 125(13):133321, 2006.

[131] A. M. Rijs, M. H. M. Janssen, E. t. H. Chrysostom, and C. C. Hayden. Femtosecond coincidence imaging of multichannel multiphoton dynamics. Phys. Rev. Lett., 92(12):123002, Mar 2004.

[132] P. A. Roos, Xiaoqin Li, R. P. Smith, Jessica A. Pipis, T. M. Fortier, and S. T. Cundiff. Solid-state carrier-envelope phase stabilization via quantum interference control of injected photocurrents. Opt. Lett., 30:735, 2005.

[133] F. Rosca-Pruna and M. J. J. Vrakking. Revival structures in picosecond laser-induced alignment of I_2 molecules. I. experimental results. The Journal of Chemical Physics, 116(15):6567–6578, 2002.

[134] V. Roudnev, B. D. Esry, and I. Ben-Itzhak. Controlling $HD+$ and H_2+ dissociation with the carrier-envelope phase difference of an intense ultrashort laser pulse. Phys. Rev. Lett., 93:163601, 2004.

[135] Andy Rundquist, III Durfee, Charles G., Zenghu Chang, Catherine Herne, Sterling Backus, Margaret M. Murnane, and Henry C. Kapteyn. Phase-Matched Generation of Coherent Soft X-rays. Science, 280(5368):1412–1415, 1998.

[136] H. Sakai, C. P. Safvan, J. J. Larsen, K. M. Hilligsøe, K. Held, and H. Stapelfeldt. Controlling the alignment of neutral molecules by a strong laser field. J. Chem. Phys., 10235:110, 1999.

[137] Pascal Salières, Philippe Antoine, Armelle de Bohan, and Maciej Lewenstein. Temporal and spectral tailoring of high-order harmonics. Phys. Rev. Lett., 81:5544, 1998.

[138] Richard L. Sandberg, Ariel Paul, Daisy A. Raymondson, Steffen Hädrich, David M. Gaudiosi, Jim Holtsnider, Raanan I. Tobey, Oren Cohen, Margaret M. Murnane, Henry C. Kapteyn, Changyong Song, Jianwei Miao, Yanwei Liu, and Farhad Salmassi. Lensless diffractive imaging using tabletop coherent high-harmonic soft-X-ray beams. Phys. Rev. Lett., 99:098103, 2007.

[139] A Sandhu, E Gagnon, R Santra, V Sharma, W Li, P Ho, P Ranitovic, C Cocke, M Murnane, and H Kapteyn. Observing the creation of electronic Feshbach resonances in soft X-rayinduced O_2 dissociation. Science, 322:1081, 2008.

[140] Arvinder S. Sandhu, Etienne Gagnon, Ariel Paul, Isabell Thomann, Amy Lytle, Tracy Keep, Margaret M. Murnane, Henry C. Kapteyn, and Ivan P. Christov.

Generation of sub-optical-cycle, carrier-envelope-phase—insensitive, extreme-uv pulses via nonlinear stabilization in a waveguide. Physical Review A (Atomic, Molecular, and Optical Physics), 74(6):061803, 2006.

[141] G. Sansone, E. Benedetti, F. Calegari, C. Vozzi, L. Avaldi, R. Flammini, L. Poletto, P. Villoresi, C. Altucci, R. Velotta, S. Stagira, S. De Silvestri, and M. Nisoli. Isolated single-cycle attosecond pulses. Science, 314:442–446, 2006.

[142] J. M. Schins, P. Breger, P. Agostini, R.C. Constantinescu, H.G. Muller, G. Grillon, A. Antonetti, and A. Mysyrowicz. Observation of laser-assisted Auger decay in Argon. Phys. Rev. Lett., 73:2180–2183, 1994.

[143] Taro Sekikawa, Atsushi Kosuge, Teruto Kanai, and Shuntaro Watanabe. Nonlinear optics in the extreme ultraviolet. Nature, 432:605–608, 2004.

[144] Jzsef Seres, Alexander Müller, Enikö Seres, Kevin O'Keeffe, Miklós Lenner, Richard F. Herzog, Daniel Kaplan, Christian Spielmann, and Ferenc Krausz. Sub-10-fs, terawatt-scale Ti:sapphire laser system. Opt. Lett., 28(19):1832–1834, 2003.

[145] C. Spielmann, C. Kan, N. Burnett, T. Brabec, M. Geissler, A. Scrinzi, M. Schnurer, and F. Krausz. Near-keV coherent X-ray generation with sub-10-fs lasers. IEEE Journal of Selected Topics in Quantum Electronics, 4:249–265, 1998.

[146] Henrik Stapelfeldt and Tamar Seideman. Colloquium: Aligning molecules with strong laser pulses. Rev. Mod. Phys., 75(2):543–557, Apr 2003.

[147] J. Stöhr, K. Baberschke, R. Jaeger, R. Treichler, and S. Brennan. Orientation of chemisorbed molecules from surface-absorption fine-structure measurements: CO and NO on Ni(100). Phys. Rev. Lett., 47(5):381–384, Aug 1981.

[148] D. Strickland and G. Mourou. Compression of amplified chirped optical pulses. Opt. Commun., 56:219–221, 1985.

[149] Akira Suda, Masatoshi Hatayama, Keigo Nagasaka, and Katsumi Midorikawa. Generation of sub-10-fs, 5-mj-optical pulses using a hollow fiber with a pressure gradient. Appl. Phys. Lett., 86:111116, 2005.

[150] S. Taylora, J. H. D. Eland, and M. Hochlaf. Fluorescence and metastability of N_2O^{2+}: Theory and experiment. JCP, 124:204319, 2006.

[151] H. R. Telle, G. Steinmeyer, A. E. Dunlop, J. Stenger, D. H. Sutter, and U. Keller. Carrier-envelope offset phase control: A novel concept for absolute optical frequency measurement and ultrashort pulse generation. Appl. Phys. B, 69:327 – 332, 1999.

[152] I. Thomann, A. Bahabad, X. Liu, R. Trebino, M. M. Murnane, and H. C. Kapteyn. Characterizing isolated attosecond pulses from hollow-core waveguides using multi-cycle driving pulses. Submitted to Optics Express.

[153] I. Thomann, A. Bartels, K. L. Corwin, N. R. Newbury, L. Hollberg, Scott A. Diddams, J. W. Nicholson, and M. F. Yan. 420-MHz Cr:forsterite femtosecond ring laser and continuum generation in the 1-2- μm range. Opt. Lett., 28:1368–1370, 2003.

[154] I. Thomann, E. Gregonis, X. Liu, R. Trebino, A. S. Sandhu, M.M. Murnane, and H. C. Kapteyn. Temporal characterization of attosecond wave forms in the sub-optical-cycle regime. Phys. Rev. A, 78:011806(R), 2008.

[155] I. Thomann, R. Lock, E. Gagnon, A. Sandhu, H. Kapteyn, M. Murnane, and W. Li. Angular-dependence of molecular photoionization cross-sections studied by time-resolved EUV spectroscopy. Conference on Lasers and Electro-Optics (CLEO), pages JFF1 p. 1–2, 2008.

[156] I. Thomann, R.Lock, V. Sharma, E. Gagnon, S. T. Pratt, H. C. Kapteyn, M. M. Murnane, and W. Li. Direct measurement of the angular dependence of the single-photon ionization of aligned N_2 and CO_2. J. Phys. Chem. A, 112:9382, 2008.

[157] Isabell Thomann, Etienne Gagnon, R. Jones, Arvinder Sandhu, Amy Lytle, Ryan Anderson, Jun Ye, Margaret Murnane, and Henry Kapteyn. Investigation of a grating-based stretcher/compressor for carrier-envelope phase stabilized fs pulses. Opt. Express, 12(15):3493–3499, 2004.

[158] Isabell Thomann, Leo Hollberg, Scott A. Diddams, and Randy Equall. Chromium-doped forsterite: dispersion measurement with white-light interferometry. Applied Optics, 42:1661–1666, 2003.

[159] M. E. Thomas, S. K. Anderson, R. M. Sova, and R. I. Joseph. Frequency and temperature dependence of the refractive index of sapphire. Infrared Phys. Technol., 39:235, 1998.

[160] X.M. Tong and Shih-I Chu. Theoretical study of multiple high-order harmonic generation by intense ultrashort pulsed laser fields: A new generalized pseudospectral time-dependent method. Chem. Phys., 217:119, 1997.

[161] E. B. Treacy. Optical pulse compression with diffraction gratings. J. Quantum Electron., 5:454–458, 1969.

[162] E.B. Treacy. Optical pulse compression with diffraction gratings. IEEE J. Quantum Electron., QE-5:454, 1969.

[163] R. Trebino. Frequency-Resolved Optical Gating: The Measurement of Ultrashort Laser Pulses. Kluwer Academic Publishers.

[164] R. Trebino, K. W. DeLong, D. N. Fittinghoff, J. N. Sweetser, M. A. Krumbügel, , and D. J. Kane. Measuring ultrashort laser pulses in the time-frequency domain using frequencyresolved optical gating. Rev. Sci. Instrum., 68:3277, 1997.

[165] Masaaki Tsubouchi and Toshinori Suzuki. Photoelectron kinetic energy dependence in near threshold ionization of NO from A state studied by time-resolved photoelectron imaging. The Journal of Chemical Physics, 121(18):8846–8853, 2004.

[166] M. Uiberacker, Th. Uphues, M. Schultze, A. J. Verhoef, V. Yakovlev, M. F. Kling, J. Rauschenberger, N. M. Kabachnik, H. Schröder, M. Lezius, K. L. Kompa, H.-G. Muller, M. J. J. Vrakking, S. Hendel, U. Kleineberg, U. Heinzmann, M. Drescher,

and F. Krausz. Attosecond real-time observation of electron tunnelling in atoms. Nature, 446:627, 2007.

[167] K. Varjú, Y. Mairesse, B. Carré, M. B. Gaarde, S. Kazamias P. Johnsson, R. López-Martens, J. Mauritsson, K. J. Schafer, PH. Balcou, A. L'huillier, and P. Salières. Frequency chirp of harmonic and attosecond pulses. J. Mod. Opt., 52:379 – 394, 2005.

[168] Nicholas L. Wagner, Emily A. Gibson, Tenio Popmintchev, Ivan P. Christov, Margaret M. Murnane, and Henry C. Kapteyn. Self-compression of ultrashort pulses through ionization-induced spatiotemporal reshaping. Phys. Rev. Lett., 93:173902, 2004.

[169] H. Wang, S. Backus, Z. Chang, R. Wagner, K. Kim, X. Wang, D. Umstadter, T. Lei, M. Murnane, and H. Kapteyn. Generation of 10-W average-power, 40-TW peak-power, 24-fs pulses from a Ti:sapphire amplifier system. J. Opt. Soc. Am. B, 16(10):1790–1794, 1999.

[170] Th. Weber, H. Giessen, M. Weckenbrock, G. Urbasch, A. Staudte, L. Spielberger, O. Jagutzki, V. Mergel, M. Vollmer, and R. Dörner. Correlated electron emission in multiphoton double ionization. Nature, 405:658, 2000.

[171] W.C. Wiley and I.H. McLaren. Time-of-flight mass spectrometer with improved resolution. Rev. Sci. Inst., 26:1150, 1955.

[172] Carsten Winterfeldt, Christian Spielmann, and Gustav Gerber. Colloquium: Optimal control of high-harmonic generation. Rev. Mod. Phys., 80:117–140, 2008.

[173] S. Witte, R. T. Zinkstock, W. Hogervorst, and K.S.E. Eikema. Control and precise measurement of carrier-envelope phase dynamics. Appl. Phys. B, 78:5–12, 2004.

[174] L. Xu, C. Spielmann, A. Poppe, T. Brabec, F. Krausz, and T. W. Hänsch. Route to phase control of ultrashort light pulses. Opt. Lett., 21:2008, 1996.

[175] A. Yagishita, K. Hosaka, and J. I. Adachi. Photoelectron angular distributions from fixed-in-space molecules. J. Electron Spectrosc. Relat. Phenom., 142:295, 2005.

[176] Akira Yagishita, Hideki Maezawa, Masatoshi Ukai, and Eiji Shigemasa. Angular distributions of molecular photofragments emitted following K-shell excitation of N_2. Phys. Rev. Lett., 62(1):36–39, Jan 1989.

[177] E. Zeek, R. Bartels, M. M. Murnane, H. C. Kapteyn, S. Backus, and G. Vdovin. Adaptive pulse compression for transform-limited 15-fs high-energy pulse generation. Opt. Lett., 25(8):587–589, 2000.

[178] Erik Zeek, Kira Maginnis, Sterling Backus, Ulrich Russek, Margaret Murnane, Gérard Mourou, Henry Kapteyn, and Gleb Vdovin. Pulse compression by use of deformable mirrors. Opt. Lett., 24(7):493–495, 1999.

[179] Ahmed H. Zewail. Femtochemistry: Recent progress in studies of dynamics and control of reactions and their transition states. J. Phys. Chem., 100:12701–12724, 1996.

[180] Z. X. Zhao, X. M. Tong, and C. D. Lin. Alignment-dependent ionization probability of molecules in a double-pulse laser field. Phys. Rev. A, 67:043404, 2003.

[181] J. Zobeley, L. S. Cederbaum, and F. Tarantelli. Highly excited electronic states of molecular clusters and their decay. The Journal of Chemical Physics, 108(23):9737–9750, 1998.